Tectonophysics 723 (2018) 309–448

Contents lists available at ScienceDirect

Tectonophysics

journal homepage: www.elsevier.com/locate/tecto

Review Article

Atlas of the underworld: Slab remnants in the mantle, their sinking history, and a new outlook on lower mantle viscosity

Douwe G. van der Meer[a,b,*], Douwe J.J. van Hinsbergen[a], Wim Spakman[a,c]

[a] Department of Earth Sciences, Utrecht University, Heidelberglaan 2, 3584 CS Utrecht, The Netherlands
[b] Nexen Petroleum UK Ltd, 97 Oxford Road, Uxbridge, Middlesex UB8 1LU, United Kingdom
[c] Center for Earth Evolution and Dynamics (CEED), University of Oslo, Sem Saelands vei 24, NO-0316 Oslo, Norway

ARTICLE INFO

Keywords:
Subduction
Slab
Mantle
Atlas
Orogeny
Underworld

ABSTRACT

Across the entire mantle we interpret 94 positive seismic wave-speed anomalies as subducted lithosphere and associate these slabs with their geological record. We document this as the *Atlas of the Underworld*, also accessible online at www.atlas-of-the-underworld.org, a compilation comprising subduction systems active in the past ~300 Myr. Deeper slabs are correlated to older geological records, assuming no relative horizontal motions between adjacent slabs following break-off, using knowledge of global plate circuits, but without assuming a mantle reference frame. The longest actively subducting slabs identified reach the depth of ~2500 km and some slabs have impinged on Large Low Shear Velocity Provinces in the deepest mantle. Anomously fast sinking of some slabs occurs in regions affected by long-term plume rising. We conclude that slab remnants eventually sink from the upper mantle to the core-mantle boundary. The range in subduction-age versus – depth in the lower mantle is largely inherited from the upper mantle history of subduction. We find a significant depth variation in average sinking speed of slabs. At the top of the lower mantle average slab sinking speeds are between 10 and 40 mm/yr, followed by a deceleration to 10–15 mm/yr down to depths around 1600–1700 km. In this interval, in situ time-stationary sinking rates suggest deceleration from 20 to 30 mm/yr to 4–8 mm/yr, increasing to 12–15 mm/yr below 2000 km. This corroborates the existence of a slab deceleration zone but we do not observe long-term (> 60 My) slab stagnation, excluding long-term stagnation due to compositional effects. Conversion of slab sinking profiles to viscosity profiles shows the general trend that mantle viscosity increases in the slab deceleration zone below which viscosity slowly decreases in the deep mantle. This is at variance with most published viscosity profiles that are derived from different observations, but agrees qualitatively with recent viscosity profiles suggested from material experiments.

1. Introduction

Seismic tomography has provided a breakthrough in the analysis of plate tectonic history by allowing to trace now-subducted ancient lithosphere in the Earth's mantle, where they appear as plate-like positive seismic wave-speed anomalies in the upper mantle and often more amorphous structures in the lower mantle (e.g., Spakman et al., 1988; Van der Hilst et al., 1991; Zhao et al., 1992; Fukao et al., 1992, 2001; Grand et al., 1997; van der Hilst et al., 1997; Bijwaard et al., 1998; Widiyantoro et al., 2000; Zhao and Lei, 2004; Fukao and Obayashi, 2013). Since the earliest detection of positive wavespeed anomalies in the deep mantle (Dziewonski, 1984) their interpretation was almost exclusively in terms of remnants of ancient subduction. Only recently, however, this presupposed link was corroborated as being statistically significant at the 99% confidence level for subduction of the past ~120 Myr reaching mantle depths of ~2300 km (Domeier et al., 2016).

Research into linking detailed plate tectonic history to present-day mantle structure started around 1990 (e.g. Spakman et al., 1988; Richards and Engebretson, 1992; van der Hilst and Seno, 1993; De Jonge et al., 1994; Carminati et al., 1998a,b; Lithgow-Bertelloni and Richards, 1998). Improved global mantle tomography models led to interpretations of lower-mantle slab structure which initially focussed on the large Farallon and Tethys anomalies (e.g. Grand et al., 1997; van der Hilst et al., 1997; Bijwaard et al., 1998; Van der Voo et al., 1999a; Hafkenscheid et al., 2006) and the Mongol-Okhotsk (Van der Voo et al., 1999b) as third important anchor slab for linking deep mantle structure to plate tectonic evolution. A major jump was made by van der Meer et al. (2010) who linked present-day lower mantle structure to the paleo-location of 28 ancient subduction zones, of which the geological

* Corresponding author at: Department of Earth Sciences, Utrecht University, Heidelberglaan 2, 3584 CS Utrecht, The Netherlands.
E-mail address: douwevdm@gmail.com (D.G. van der Meer).

https://doi.org/10.1016/j.tecto.2017.10.004
Received 28 January 2017; Received in revised form 13 June 2017; Accepted 1 October 2017
Available online 18 October 2017

artefacts have moved away by plate motion. van der Meer et al. (2010, 2012) used geological dating for the start and end of subduction (e.g. van Hinsbergen et al., 2005) combined with a detailed relative plate-motion model (Torsvik et al., 2008a; Steinberger and Torsvik, 2008) to identify slab remnants in the lower mantle that effectively comprised ~250 Myr of global subduction history. They also derived a first-order estimate of the average sinking rate of slabs through the lower mantle (12 ± 3 mm/yr), a range consistent with later estimates (Butterworth et al., 2014; Sigloch and Mihalynuk, 2013; Domeier et al., 2016), which was also used as a novel constraint on mantle viscosity (Cízková et al., 2012; Bower et al., 2013). Importantly, the identification of slab remnants that subducted at 28 paleosubduction zones provided the first step towards establishing a mantle reference frame based on subduction (van der Meer et al., 2010) that proved to be relatively close to absolute plate motion models that are primarily based on hot spot tracks (e.g. Doubrovine et al., 2012).

Recently major progress occurred on linking geological history to slab remnants imaged in the mantle at regional scale (e.g. Shephard et al., 2013; Sigloch and Mihalynuk, 2013; van Hinsbergen et al., 2014; Hall and Spakman, 2015; Zahirovic et al., 2016). By invoking absolute plate motion models, relatively isolated slab remnants in the deep mantle, of which the geological evidence is meanwhile displaced by thousands of kilometres, could be identified (e.g. Schellart et al., 2009; Schellart and Spakman, 2015; Shephard et al., 2016; Vissers et al., 2016). New approaches use imaged slabs directly as a novel basis for plate kinematic restorations by “surfacing” slab anomalies (Lister et al., 2012; Wu et al., 2016).

Furthermore, mapped slab remnants were correlated with the location of seismic scatterers in the lower mantle (e.g., Hutko et al., 2006; Kaneshima, 2013; van der Meer et al., 2012; Ma et al., 2016) and with Pacific LLSVP topography (He and Wen, 2009; van der Meer et al., 2012). Global interpretation of mantle structure has led to estimates of paleo-subduction zone lengths through time that provided constraints for global plate tectonic activity impacting atmospheric CO_2 (van der Meer et al., 2014; Mills et al., 2014; Kashiwagi, 2016), strontium isotope ratios (van der Meer et al., 2014, 2017) and sea level (van der Meer et al., 2017).

Encouraged by all these new developments, we have expanded our analysis of mantle structure to the identification of 94 slabs throughout the upper and lower mantle. This review constitutes our geological interpretation of these imaged slab remnants by linking them to geological records of subduction. The compilation is summarized in what we call the *Atlas of the Underworld*, for which we also developed an online version at www.atlas-of-the-underworld.org that is fully searchable and includes discussion forums for each interpreted slab to facilitate post-publication peer review. This catalogue is intended to provide a new basis for future studies in the fields of orogenesis, mantle convection and plate tectonic reconstruction, and as a first and extensive global framework for interpretation of present-day global mantle structure and its physical properties and how that relates to our planet's dynamic evolution of the past ~300 Myr.

2. Methods

We aim to provide a succinct documentation of many positive seismic wavespeed anomalies in the mantle as remnants of subducted lithosphere of which we interpret plate tectonic provenance and the timing of subduction from the global continental geological record of subduction. We expand on our previous work (van der Meer et al., 2010) by (1) incorporating upper mantle slab anomalies, (2) by identifying contributions within major mantle anomalies (particularly below North America) from individual paleo-subduction events, and (3) by incorporating lower mantle anomalies that were not yet subject to interpretation in terms of subducted lithosphere, if possible.

Our previous compilation (van der Meer et al., 2010) suggested that the deep mantle contains slab remnants that may have subducted 200–300 Myr ago. Whilst actively subducting upper mantle slabs are straightforwardly linked to the active orogenesis and to overlying arcs, correlating such deep, detached slabs to geological records is not straightforward. Any detached lower mantle slab may, when viewed in isolation, be associated with a large number of geological records, since post-detachment plate motions may have displaced these records over thousands of kilometres relative to the location where its slab remnant sinks in the mantle. One way of assessing this problem is by investigating the past location of a particular geological subduction record in an ‘absolute’ mantle reference frame which potentially may restore the record above a candidate slab remnant in the underlying mantle (e.g. Schellart et al., 2009; Schellart and Spakman, 2012; van der Meer et al., 2012; Sigloch and Mihalynuk, 2013; Schellart and Spakman, 2015; Vissers et al., 2016). However, with the exception of two slab anomalies (Malpelo and Mesopotamia), here we refrain from using absolute plate models as an identification guide because we ultimately aim to use the imaged slab remnants as a constraint on such absolute plate motion models. Instead, we took the following approach in our correlation attempt, which is independent of any absolute plate motion frame.

1) We identified positive P-wave speed anomalies in the mantle that occur in the UU-P07 tomography model (Amaru, 2007, where it was called P06; also described in Hall and Spakman, 2015 and available on the Atlas website) as well as in S-wave anomaly models that are independent of model UU-P07 in terms of both seismological data-type used and inversion methodology. For the lower mantle we examined S40RTS (Ritsema et al., 2011) while for the upper mantle we used the surface wave model SL2013sv (Schaeffer and Lebedev, 2013). Occurrence of positive anomalies in these independent models, albeit with different spatial resolution, was taken as a strong indication of the existence of corresponding mantle heterogeneity. Although here we compare only one P-model to one independent S-model in the upper and lower mantle, we note that a thorough comparison of the structural content of 14 recent P- and S-models, including UU-P07 and S40RTS, through the construction of detailed voting maps (Lekic et al., 2012) is currently underway (Shephard et al., 2017). A preliminary comparison shows an overall match between these voting maps with the anomalies presented here in the Atlas of the Underworld (G. Shephard, personal communication).

Following the approach of Hafkenscheid et al. (2006) and van der Meer et al. (2010), we then estimated the depth range of tops and bases of slabs for P-wave anomaly amplitudes > 0.2% in the UU-P07 model. We label each slab by the name of the geographic region under which the mantle anomalies occur so as to avoid an a priori paleogeographic interpretation of an anomaly and also allow for future corrections of our interpretations, which then needs not involve the anomaly name.

As outlined above, correlation of detached slab anomalies to geological records becomes more difficult with increasing depth. In the Atlas of the Underworld (Section 3), we aimed to provide concise descriptions of our correlations, citing the pertinent literature, while avoiding description of the geological records to which we did not correlate the slab under discussion. Our interpretation strategy starts in the upper mantle with generally well-identifiable slabs. We work our way down in the mantle and side-ways by considering new anomalies in the same, or wider, region occuring at comparable or larger depth. Viable interpretations are next considered in the geological context of previously identified slabs for the same region, or in a wider region if necessary. Clearly, such interpretation process requires stepping backward (questioning previous interpretations at comparable or shallower depth) and forward (evaluating all possible candidate subduction zones).

In more detail, the geological interpretation of slabs was carried out as follows:

2) We first interpreted slabs that are still associated with active subduction zones, orogens, and arcs. From these geological records, we estimated the age range of the onset of these subduction zones using a combination of the following data types: the onset of accretion of thin-skinned nappes or an accretionary prism, the onset of a period of arc volcanism that lasts until today, the oldest high-pressure, low-temperature metamorphic rocks found in an accretionary orogen, and, in the case of subduction below oceanic lithosphere preserved as ophiolites, the ages of metamorphic soles and supra-subduction zone ophiolites. For each individual anomaly, the Atlas provides documentation of the geological data that were used for their interpreted age of subduction.
3) Subsequently, detached slabs were interpreted, whereby we emphasize that we made no assumption on slab sinking rates. We do assume, however, that regionally adjacent slabs did not undergo significant lateral motions relative to each other after slab break-off. This means that we assume slabs to sink dominantly vertically after detachment, as recently shown viable by Domeier et al. (2016). Progressively deeper slabs were generally correlated to progressively older geological records of subduction. In the interpretation process of a particular slab anomaly we used other slabs in the region at shallower or comparable depth as a guide for locating the corresponding geological record. Particularly in the lower half of the mantle, identification of several slab remnants depends in this way on the identification of slab remnants at shallower depth. These interpretation links are made explicit in several schematic figures: Fig. 1 for the Tethyan realm, Fig. 2 for the American realm, and Fig. 3 for the Australasian realm. Unavoidably, to give direction to our search for suitable candidate records we initially assume that shallower slabs have generally younger subduction ages than deeper slabs, and that slabs residing at similar mantle depths may have roughly similar subduction ages, although the range in subduction age we strictly adopt from the literature and may comprise up to 100 Myr for slabs at a particular depth. Generally, slabs are correlated to the youngest possible record of subduction that was not yet associated with shallower slab remnants. (See Fig. 4.)
4) Age ranges for slab break-off are based on a combination of the following data types: the end of accretion in an orogen, the end of deformation in a plate boundary zone associated with an orogen, the arrest of volcanism, or the type of volcanism (e.g., adakites), or the arrest of convergence reconstructed from published plate tectonic reconstructions.

We illustrate this approach by the following example of slab anomalies in the mid-mantle below northwest Africa. For literature references to stated ages and descriptions of the associated subduction records, we refer to the sections in which the slabs are described. Below NW Africa, the Algeria slab (Section 3.4) is a N–S trending body at ~1300–2400 km depth located below Algeria and Mali, and the small Reggane slab (Section 3.71) is located between 1500 and 1900 km depth to the west of the Algeria slab. For correlating these slab anomalies to their geological records we continue on the regional analysis we made for associating slab anomalies at the same depth or shallower to their respective orogens. To the north of the Algeria and Reggane slabs lie upper mantle slabs of Gibraltar (Section 3.34), the Kabylides slab below northern Algeria (Section 3.46), and the Calabrian slab in southern Italy (Section 3.20). These slabs have a record of subduction in their associated circum-Mediterranean orogens dating back to ~45–85 Ma, depending on the literature. This precludes correlation of the Algeria and Reggane lower mantle slabs to the active circum-Mediterranean orogens, where high-temperature metamorphic rocks in Calabria and the Betic Cordillera provided Eocene, ~45 Ma ages demonstrating that subduction was underway by this time.

To the northeast of the Algeria slab, the Aegean slab (Section 3.1) is found down to depth of ~1300–1500 km, i.e. at a depth range corresponding to the top of the Algeria and Reggane slabs. The Aegean

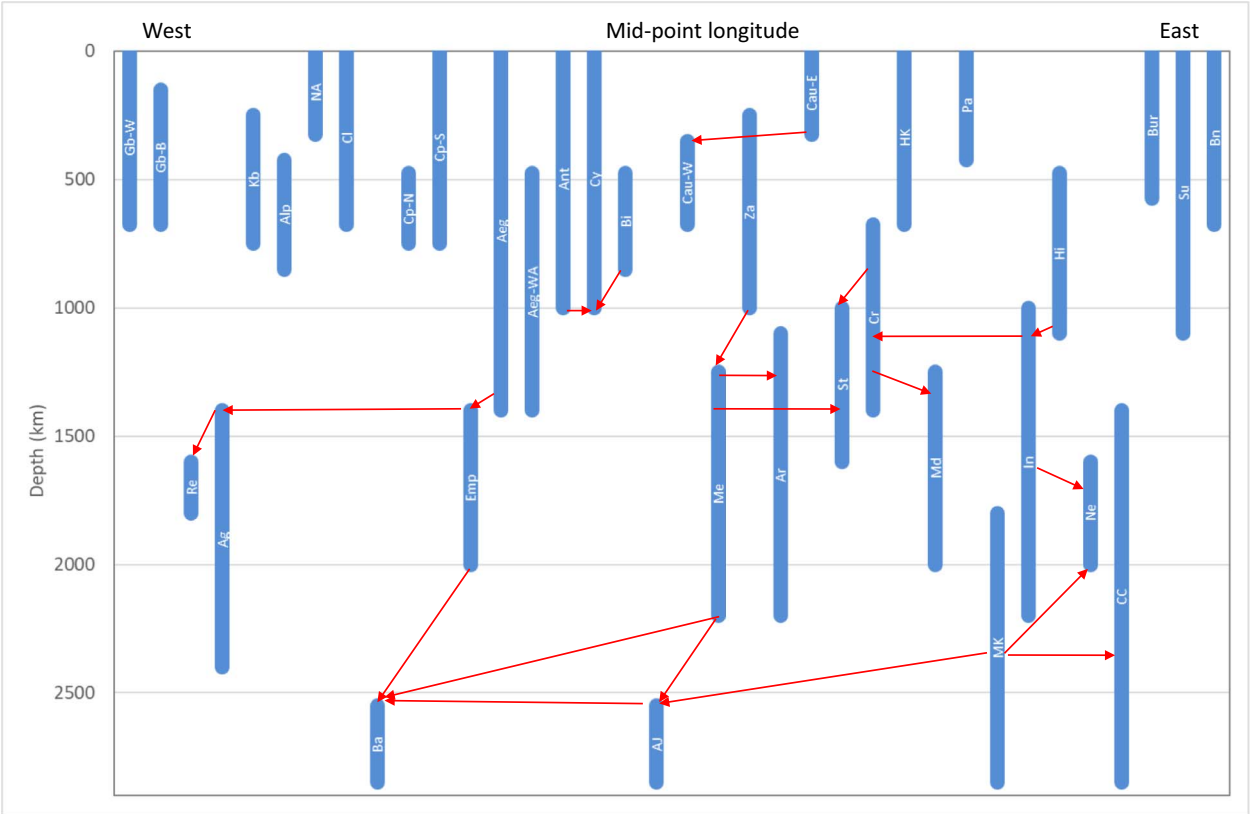

Fig. 1. Interpretation flowchart Tethyan realm. Blue bars indicate depth extent of slabs. Red arrows show the used inter-slab correlations to constrain geological interpretations of slab subduction history.

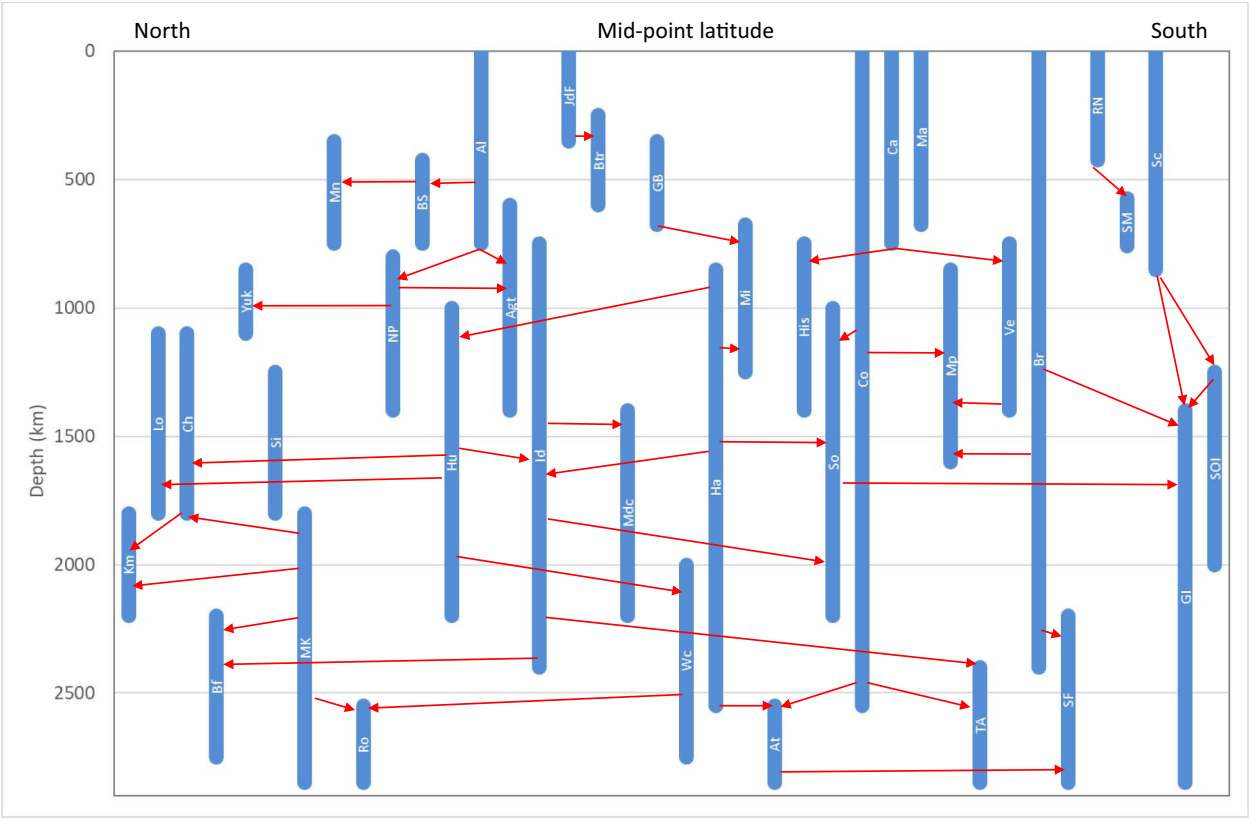

Fig. 2. Interpretation flowchart American realm. Legend same as Fig. 1.

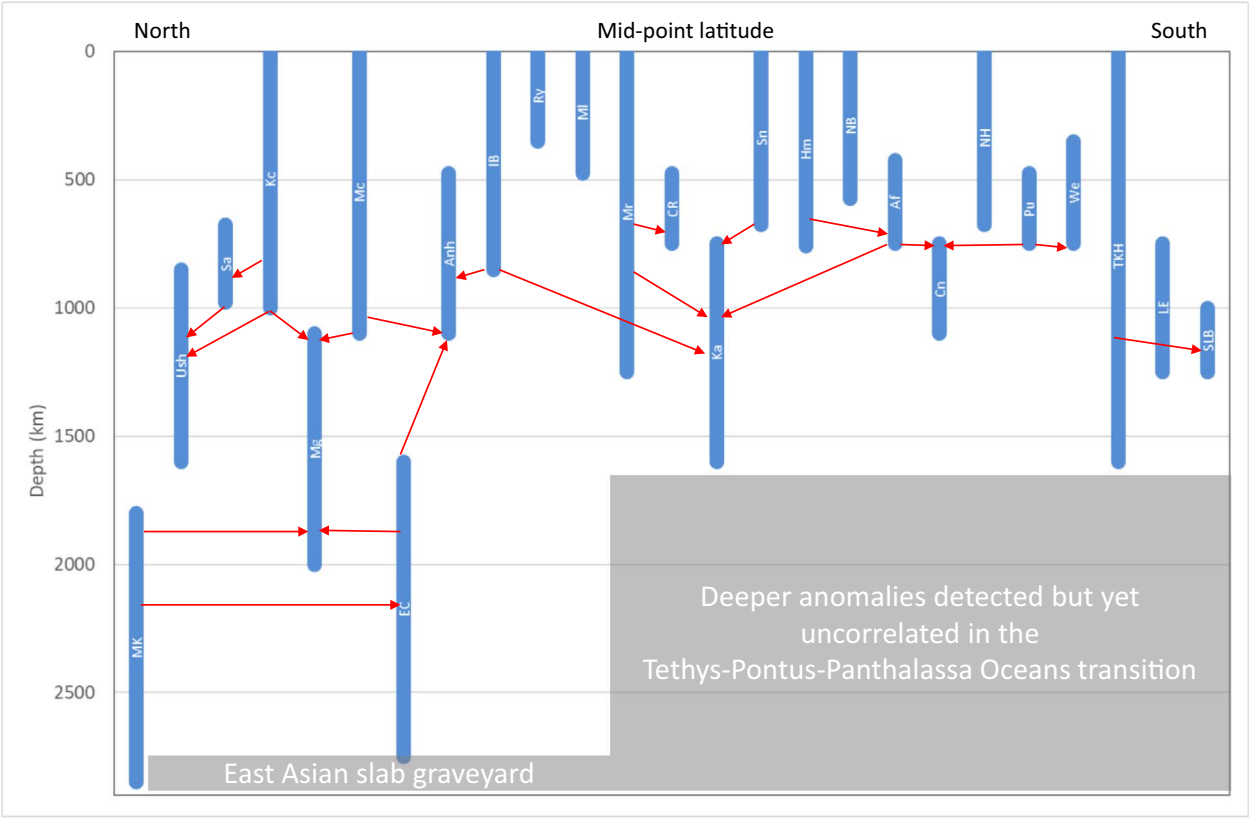

Fig. 3. Interpretation flowchart Australasian realm. Legend same as Fig. 1.

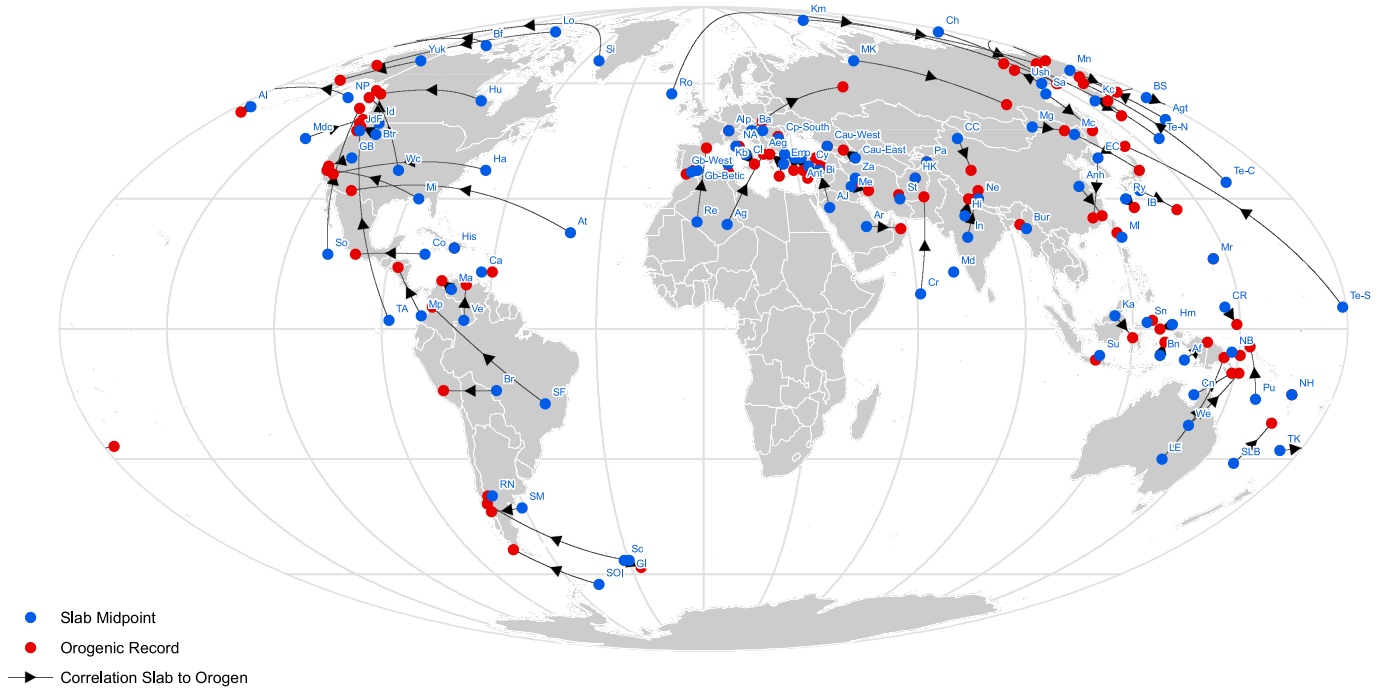

Fig. 4. Midpoints location map. Blue: slab midpoints projected to surface. Red: geological records. Arrows indicate the correlations between slabs and their corresponding geological record and show the displacement of the geological records over time relative to the relatively fixed locations of sinking slabs.

orogen in the overriding plate suggests that the slab has continuously subducted since 120–100 Ma. Immediately below the Aegean slab lies the NW-SE trending Emporios slab (Section 3.32) between ~1300 and 2100 km, i.e. in the same depth interval as the Algeria slab suggesting that the Algeria and Emporios slabs subducted simultaneously along two adjacent subduction zones. The geological record of the Eastern Mediterranean region shows a double Jurassic ophiolite belt – the West and East Vardar ophiolite belts – with ~170 Ma metamorphic sole and supra-subduction zone ophiolitic crustal ages, one emplaced north and eastwards onto Eurasian crust, and one emplaced westwards onto continental crust of Adria, a microcontinental fragment that existed north of Africa surrounded by Alpine and Neotethyan oceanic basins. The ages of obduction are 130–120 Ma. The correspondence between two adjacent slabs with similar depth ranges and two records of subduction with similar ages then leads to the correlation of the Algeria slab to the formation (onset of subduction) and emplacement (end of subduction) of the West Vardar ophiolite belt, and the Emporios slab correlated to the East Vardar ophiolite belt. The Reggane slab to the west of the Algeria slab is then best correlated to a subduction record to the west, but in the vicinity of Adria. There, plate kinematic reconstruction of the Central Atlantic Ocean and Bay of Biscay, and paleomagnetic data from Iberia predict up to ~500 km convergence across the Pyrenees starting ~125 Ma and that ending around ~110 Ma, which is followed by a phase of high-temperature metamorphism and associated volcanism around 100 Ma, which is then interpreted to reflect the timing of break-off of the Reggane slab. With these correlations, *all* geological records of subduction of the (southern) Mediterranean region are correlated to slabs, and *all* slab anomalies in the upper and lower mantle below the southern Mediterranean and North Africa are then correlated to geological records of subduction.

3. Atlas of the underworld

In the Atlas below, we describe the geological evidence on which we base the duration of subduction for each slab. We provide a location, images from the tomographic models UU-P07 and S40RTS and SL2013sv tomographic models in map-view and cross-section, and the location of the correlated geological record. In cross-sections, we plot SL2013sv in the upper mantle and S40RTS in the lower mantle. For every anomaly, we provide 6 cross-sections centred on the midpoint of the anomaly in the online version of the Atlas at www.atlas-of-the-underworld.org, as well as spike resolution tests (Spakman and Nolet, 1988; Rawlinson and Spakman, 2016) for each anomaly in model UU-P07. Depths and interpreted subduction ages of all slabs are summarized in Table 1.

3.1. Aegean - Aeg

The Aegean anomaly (Fig. 5) was previously called 'Aegean Tethys' by van der Meer et al. (2010) and is located below south-east Europe from the deep lower mantle up to the surface at the Hellenic subduction zone. It was one of the first slabs imaged (Spakman, 1986a; Spakman et al., 1988, 1993) and is widely interpreted as a slab that represents north-dipping African lithosphere (e.g. Spakman et al., 1988; De Jonge et al., 1994; Piromallo and Morelli, 1997, 2003; Bijwaard et al., 1998; de Boorder et al., 1998; Faccenna et al., 2003; van Hinsbergen et al., 2005, 2010; Hafkenscheid et al., 2006; Chang et al., 2010; Biryol et al., 2011). Van der Voo et al. (1999b) identified this slab as the II anomaly, and Hafkenscheid et al. (2006) called it the '*Gr*' anomaly, with both papers identifying that the slab deeply penetrates the lower mantle. Where Faccenna et al. (2003) initially interpreted the mantle below the Aegean slab to host a single slab that folded and overturned in the lower mantle, van Hinsbergen et al. (2005) suggested that there are actually two slabs below the Aegean: A deep anomaly between ~2000 and 1500 km, and an anomaly from 1500 km to the surface, associated with continuous northward subduction of oceanic and continental lithosphere, upper crust which accreted to form the Aegean mountain belt on basis of the geological record of the Aegean region, where three separate subduction records are found: A Jurassic – Early Cretaceous record emplaced ophiolites westward and northeastward suggesting two oppositely dipping subduction zones of this age. The northeastern one we associate with the deeper Aegean slab (see 'East-Vardar slab, Section 3.33) and the western with the Algeria slab to the west (Section 3.4). van der Meer et al. (2010) included the Emporios and Aegean

Table 1
Midpoint coordinates, depth, and ages of all slabs and associated geological records used in the Atlas of the Underworld.

Slab name	Abbreviation	Slab midpoint location			Geological record		Slab depth (km)				Slab age (Ma)				Average sinking rate (mm/yr)			
							Base		Top		Base		Top		Base		Top	
		Depth	Lon	Lat	Lon	Lat	Depth	Error	Depth	Error	Max	Min	Min	Max	Rate	Error	Rate	Error
Aegean	Aeg	700	27.0	41.0	24.0	35.5	1400	100	0	0	120	100	0	0	13	1	28	3
Aeg-WestAnatolia	Aeg-WA	938	30.0	40.0	29.0	37.0	1400	100	475	100	120	100	15	15	13	1	32	7
Agattu	Agt	1000	170.0	50.0	169.0	62.0	1400	100	600	50	90	85	50	45	16	1	13	1
Aleutian	Al	375	−175.0	53.5	−175.0	52.0	750	100	0	0	50	46	0	0	16	2	66	7
Algeria	Ag	1900	7.0	24.0	20.0	41.0	2400	200	1400	100	180	170	140	120	14	1	11	1
AlJawf	AJ	2700	38.0	28.0	37.0	40.0	2850	200	2550	200	245	235	205	195	12	1	13	1
Alps	Alp	638	9.0	47.0	9.0	47.0	850	100	425	50	95	75	40	20	10	2	14	5
Anhui	Anh	788	117.0	33.0	119.0	26.0	1100	100	475	50	108	106	90	52	10	1	7	2
Antalya	Ant	500	32.0	40.0	32.0	37.0	1000	100	0	0	100	95	0	0	10	1	1	0
Arabia	Ar	1650	48.0	23.5	58.0	23.0	2200	200	1100	100	105	85	75	65	23	3	16	2
Arafura	Af	588	135.0	−7.0	141.0	−3.0	750	100	425	50	50	45	25	20	16	2	19	3
Atlantis	At	2700	−39.0	22.0	−109.0	32.0	2850	200	2550	200	290	280	230	210	10	1	12	1
Balkan	Ba	2700	17.0	47.0	59.0	59.0	2850	200	2550	200	280	260	220	200	11	1	12	1
Banda	Bn	338	128.0	−6.0	129.0	−3.0	675	50	0	0	16	8	0	0	56	19	74	7
Beaufort	Bf	2475	−128.0	72.0	148.0	66.0	2750	200	2200	200	257	229	193	193	11	1	11	1
BeringSea	BS	588	178.0	56.0	180.0	54.0	750	100	425	50	34	30	25	20	23	3	19	3
Bitlis	Bi	663	37.0	37.0	38.0	38.0	850	100	475	50	70	65	13	10	13	2	41	7
Bitterroot	Btr	425	−115.0	46.0	−123.0	48.0	600	50	250	50	67	65	47	45	9	1	5	1
Brasilia	Br	1200	−59.0	−14.0	−74.0	−14.0	2400	200	0	0	200	173	0	0	13	1	98	10
Burma	Bur	288	95.0	23.0	93.5	24.0	575	50	0	0	40	30	0	0	16	3	11	1
Calabria	Cl	338	14.0	41.0	16.5	38.5	675	50	0	0	85	45	0	0	10	3	52	5
Caribbean	Ca	375	−63.0	13.0	−60.0	13.0	750	100	0	0	55	45	0	0	15	3	15	2
Carlsberg	Cr	1038	61.0	8.0	67.5	30.5	1400	100	675	50	81	65	55	45	19	3	14	2
CarolineRidge	CR	613	146.0	5.0	149.0	1.0	750	100	475	50	26	25	6	5	30	4	95	14
Carpathians-north	Cp-N	613	21.0	47.0	21.5	49.5	750	100	475	50	40	30	12	10	21	4	43	6
Carpathians-south	Cp-S	375	26.0	45.0	26.0	45.5	750	100	0	0	40	30	0	0	21	4	3	0
Carpentaria	Cn	925	140.0	−15.0	149.0	−10.0	1100	100	750	100	83	50	45	20	17	4	23	9
Caucasus-east	Cau-E	163	50.0	40.0	47.0	42.0	325	50	0	0	35	25	0	0	11	2	23	2
Caucasus-west	Cau-W	513	42.0	43.0	42.0	43.0	675	50	350	50	35	25	5	5	23	4	70	10
CentralChina	CC	2125	88.0	45.0	86.0	37.0	2850	200	1400	100	255	245	150	130	11	1	10	1
Chukchi	Ch	1450	170.0	77.0	152.5	60.0	1800	100	1100	100	174	164	129	101	11	1	10	1
Cocos	Co	1275	−80.0	17.0	−100.0	17.0	2550	200	0	0	170	160	0	0	15	1	83	8
Cyprus	Cy	500	34.0	38.0	33.0	35.0	1000	100	0	0	66	65	0	0	15	2	11	1
EastChina	EC	2175	130.0	40.0	116.0	25.5	2750	200	1600	100	253	243	155	118	11	1	12	2
Emporios	EVd	1700	26.0	38.5	22.0	41.0	2000	200	1400	100	170	160	130	120	12	1	11	1
GeorgiaIslands	GI	2125	−30.0	−56.0	−72.0	−41.0	2850	200	1400	200	295	285	185	175	10	1	8	1
Gibraltar-Betic	Gb-B	413	−2.0	37.0	−3.0	37.0	675	50	150	50	85	45	7	1	10	3	40	37
Gibraltar-West	Gb-W	338	−4.0	36.5	−5.5	36.0	675	50	0	0	85	45	0	0	10	3	17	2
GreatBasin	GB	513	−116.0	40.0	−121.5	38.0	675	50	350	50	40	30	20	10	19	3	23	8
Halmahera	Hm	380	131.0	1.0	127.5	0.0	760	100	0	0	16	15	0	0	51	7	74	7
Hatteras	Ha	1700	−70.0	37.0	−118.0	36.0	2550	200	850	100	200	155	59	50	14	2	16	2
Himalayas	Hi	788	78.0	26.0	81.0	30.0	1100	100	475	50	50	35	25	15	26	5	24	6
HinduKush	HK	338	67.0	35.0	67.0	35.0	675	50	0	0	50	30	0	0	17	4	34	3
Hispaniola	His	1075	−72.0	18.5	−72.0	18.5	1400	100	750	100	135	125	45	40	11	1	18	3
Hudson	Hu	1600	−88.0	55.0	−132.0	57.0	2200	200	1000	100	160	140	72	50	15	2	16	3
Idaho	Id	1575	−118.0	49.0	−136.0	58.0	2400	200	750	100	204	203	85	78	12	1	9	1
India	In	1600	77.0	21.0	83.0	30.0	2200	200	1000	100	140	120	50	35	17	2	24	5
Izu-Bonin	IB	425	135.0	32.0	142.5	27.5	850	100	0	0	52	51	0	0	17	2	56	6
JuandeFuca	JdF	175	−122.0	47.0	−123.0	47.0	350	50	0	0	19	17	0	0	19	3	9	1
Kabylides	Kb	500	8.0	38.5	8.0	36.5	750	100	250	50	85	45	15	12	12	4	19	4

(*continued on next page*)

Table 1 (*continued*)

Slab name	Abbreviation	Slab midpoint location			Geological record		Slab depth (km)				Slab age (Ma)				Average sinking rate (mm/yr)			
							Base		Top		Base		Top		Base		Top	
		Depth	Lon	Lat	Lon	Lat	Depth	Error	Depth	Error	Max	Min	Min	Max	Rate	Error	Rate	Error
Kalimantan	Ka	1175	115.0	3.0	120.0	−2.0	1600	100	750	100	70	65	20	20	24	2	38	5
Kamchatka-Kuriles	Kc	500	155.0	55.0	156.0	51.0	1000	100	0	0	52	41	0	0	21	3	83	8
Komsomolets	Km	2000	99.0	82.0	164.0	66.0	2200	200	1800	100	170	150	130	110	14	2	15	2
LakeEyre	LE	1000	140.0	−30.0	146.0	−6.5	1250	100	750	100	75	65	52	49	18	2	15	2
Lougheed	Lo	1450	−107.0	77.0	−159.0	65.5	1800	100	1100	100	170	150	130	110	11	1	9	1
Maldives	Md	1625	71.0	13.0			2000	200	1250	100								
Malpelo	Mp	1225	−79.0	3.0	−87.0	14.0	1600	100	850	100	172	168	101	94	9	1	9	1
Manchuria	Mc	550	130.0	46.0	140.0	37.0	1100	100	0	0	77	50	0	0	17	4	89	9
Manila	Ml	238	122.0	21.0	121.0	22.0	475	50	0	0	15	10	0	0	38	9	43	4
Maracaibo	Ma	338	−71.0	9.0	−74.0	11.0	675	50	0	0	60	55	0	0	12	1	20	2
Mariana	Mr	625	146.0	16.0	146.0	16.0	1250	100	0	0	52	51	0	0	24	2	80	8
Mayn	Mn	550	172.0	64.0	170.5	57.5	750	100	350	50	35	25	20	10	25	5	23	8
Mendocino	Mdc	1800	−138.0	45.0	−125.5	50.0	2200	200	1400	100	202	201	160	125	11	1	10	1
Mesopotamia	Me	1725	46.0	33.0	51.0	32.0	2200	200	1250	100	155	145	70	60	15	1	19	2
Mississippi	Mi	963	−87.0	30.0	−121.0	37.0	1250	100	675	50	85	65	40	40	17	3	17	1
Mongolia	Mg	1550	118.0	48.0	128.0	47.0	2000	200	1100	100	155	110	94	50	15	3	15	5
Mongol-Kazakh	MO	2325	76.0	67.0	118.0	54.0	2850	200	1800	100	240	230	150	130	12	1	13	1
Nepal	Ne	1800	84.0	30.0	85.0	32.0	2000	200	1600	100	210	170	110	100	11	2	15	1
NewBritain	NB	288	148.0	−5.2	150.5	−6.0	575	100	0	0	15	5	0	0	58	30	107	11
NewHebrides	NH	338	168.0	−15.0	168.0	−15.0	675	50	0	0	15	10	0	0	54	12	111	11
NorthAppenines	NA	163	11.0	43.0	12.0	43.0	325	50	0	0	35	30	0	0	10	2	7	1
NorthPacific	NP	1100	−143.0	56.0	160.0	55.0	1400	100	800	100	80	66	42	38	19	2	20	3
Pamir	Pa	213	73.0	39.0	73.0	39.0	425	50	0	0	37	23	0	0	14	4	19	2
Papua	Pu	613	158.0	−16.0	153.0	−4.0	750	100	475	50	90	45	26	20	11	4	21	3
Reggane	Re	1700	−2.0	24.5	1.0	42.5	1800	100	1600	100	125	121	110	100	15	1	15	1
RioNegro	RN	213	−69.0	−39.0	−70.5	−39.0	425	50	0	0	23	15	0	0	22	5	95	9
Rockall	Ro	2700	−13.0	57.0	153.0	60.0	2850	200	2550	200	237	201	170	150	13	1	16	2
Ryukyu	Ry	175	129.0	30.0	130.0	28.0	350	50	0	0	22	21	0	0	17	2	74	7
Sakhalin	Sa	828	140.0	57.0	138.0	47.0	980	100	675	50	101	94	66	62	10	1	11	1
Sangihe	Sn	338	124.0	1.5	125.5	2.0	675	50	0	0	30	25	0	0	25	3	51	5
SanMatias	SM	668	−61.0	−42.0	−72.0	−43.0	760	100	575	100	73	63	49	30	11	2	15	4
SaoFrancisco	SF	2525	−45.5	−17.0	−76.0	5.0	2850	200	2200	200	245	235	225	215	12	1	10	1
Scotia	Sc	425	−32.0	−56.0	−26.0	−58.0	850	200	0	0	80	55	0	0	13	4	43	4
Sisimut	Si	1525	−53.0	67.0	173.0	67.0	1800	100	1250	100	170	150	130	110	11	1	10	1
Sistan	St	1300	60.0	30.0	60.0	31.0	1600	100	1000	100	100	90	59	46	17	1	19	3
Socorro	So	1600	−108.0	17.0	−132.0	53.0	2200	200	1000	100	208	163	55	50	12	2	19	2
SouthLoyaltyBasin	SLB	1125	163.0	−31.0	166.0	−21.5	1250	100	1000	100	60	56	45	30	22	2	27	6
SouthOrkneyIslands	SOI	1625	−48.0	−63.0	−73.0	−53.0	2000	200	1250	100	190	175	103	94	11	1	13	1
Sunda	Su	550	111.0	−6.0	110.0	−7.0	1100	100	0	0	50	45	0	0	23	2	70	7
Telkhinia-Central	Te-C	2525	164.0	34.0	164.0	60.0	2850	200	2200	100	Triassic	Triassic	Lower_Cretaceous	Lower_Cretaceous				
Telkhinia-North	Te-N	2000	158.0	45.0	157.0	64.0	2400	200	1600	100	Triassic	Triassic	Lower_Cretaceous	Lower_Cretaceous				
Telkhinia-South	Te-S	2000	179.0	5.0	143.0	43.0	2400	200	1600	100	Triassic	Triassic	Lower_Cretaceous	Lower_Cretaceous				
Tonga–Kermadec–Hikurangi	TKH	800	174.0	−28.0	−177.0	−27.0	1600	100	0	0	85	30	0	0	28	13	63	6
TransAmericas	TA	2625	−88.0	2.0	−125.0	49.0	2850	200	2400	200	233	220	178	166	13	1	14	1
Ushky	Ush	1225	146.0	60.0	146.0	64.0	1600	100	850	100	109	108	68	67	15	1	13	1
Venezuela	Ve	1075	−67.0	2.0	−67.0	10.0	1400	100	750	100	135	130	70	60	11	1	12	2
Welford	We	550	142.0	−22.0	151.0	−10.0	750	100	350	50	26	20	10	5	33	6	47	17
Wichita	Wc	2375	−98.0	37.0	−134.5	56.0	2750	200	2000	200	233	220	178	166	12	1	12	1
Yukon	Yuk	975	−143.0	67.0	−160.0	61.0	1100	100	850	100	84	72	68	61	14	2	13	2
Zagros	Za	625	48.0	35.0	48.0	34.0	1000	100	250	50	70	60	10	1	15	2	48	44

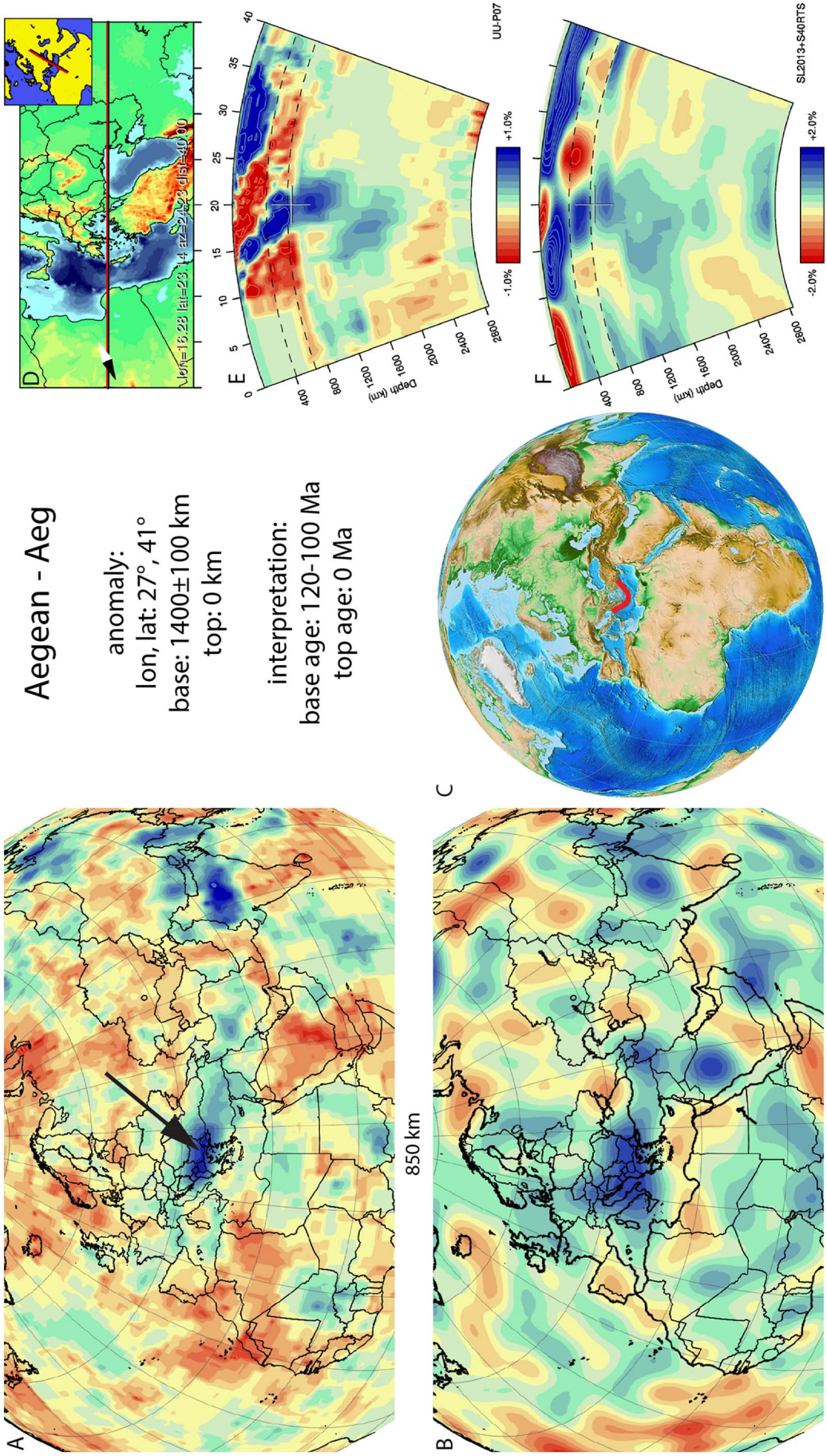

Fig. 5. Aegean anomaly. (Horizontal) [vertical] cross sections through (A)[E] the UUP07 P-wave) and (B)[F] the combined SL2013 and S40RTS S-wave tomographic models; C) red line marks the location of the modern geological record that we interpret to have formed during the subduction of the slab; D) location map of vertical cross-sections E and F. Relative amplitude strength, vertical, lateral extent and dip trend are very similar between tomographic models.

slabs both in the Aegean Tethys slab and assigned an age range of mid-Jurassic to Present. Because the subduction of both slabs can be clearly separated in the geological record, we separate these into two separate lithospheric bodies. For the Aegean slab we avoid the addition "Tethys" because a considerable part of the subducted lithosphere is of continental origin rather than the oceanic nature of the Tethys (van Hinsbergen et al., 2005, 2010).

The onset of northward subduction of the Aegean slab must have started after the emplacement of the East Vardar ophiolites in the early Cretaceous (~130–120 Ma (Schmid et al., 2008)) (See Emporios slab, Section 3.33), and before the onset of arc volcanism in the Sredna-Gorie belt of southern Bulgaria starting around 92 Ma (Stoykov et al., 2004; von Quadt et al., 2005; Zimmerman et al., 2007), and is generally considered to occur around ~110 ± 10 Ma (e.g., Faccenna et al., 2003; van Hinsbergen et al., 2005, 2010; Schmid et al., 2008; Jolivet and Brun, 2010). Subduction of the Aegean slab is still continuous at the Hellenic trench, and seems in the upper mantle laterally disconnected to slabs under western Anatolia (de Boorder et al., 1998; van Hinsbergen et al., 2010; Biryol et al., 2011) Fig. 6). Based on a kinematic reconstruction of western Turkey, the timing of break-off of the Aegean slab below Western Anatolia was estimated at ~15 Ma (van Hinsbergen, 2010; van Hinsbergen et al., 2010).

3.2. Agattu - Agt

The Agattu anomaly (Fig. 6) is a detached slab located below the northernmost Pacific Ocean, in the upper part of the upper mantle and uppermost part of the lower mantle, predominantly south and west of the Aleutian trench. At its deepest it is W-E striking and south dipping, changing to a NW-SE orientation in the uppermost lower mantle. At its shallowest it is located south of the Aleutian slab (Section 3.3). van der Meer et al. (2010) interpreted it as a slab representing the westernmost part of the North Pacific slab (Section 3.68). The tectonic model of Shapiro and Solov'ev (2009) now allow us to refine this interpretation, and define the Agattu slab separately. The Agattu slab is detached and its top is located at a similar depth as the base of the actively subducting Aleutian slab, which started to subduct around 56–46 Ma (Section 3.3). We hence searched for geological records in the NW Pacific realm of subduction that ceased in Eocene time. At a latitude consistent with this intra-oceanic location, Levashova et al. (2000) and Shapiro and Solov'ev (2009) used paleomagnetic data to reconstruct the Achaivayam–Valaginsky terrane. This terrane comprises Upper Cretaceous and Lower Paleocene volcanic and sedimentary rocks of diverse but mostly submarine facies, with older Mesozoic volcano-sedimentary blocks and ophiolite fragments. The arc originated at about 90–85 Ma (Coniacian–Santonian) as an island arc built upon oceanic crust (Bogdanov et al., 1987; Sokolov, 1992, as cited in Shapiro and Solov'ev, 2009, subducting to the southeast and culminating in ophiolite emplacement onto Kamchatka, Sakhalin, and Hokkaido around 50–45 Ma (e.g., Nokleberg et al., 2000). This southeastward subduction zone is not portrayed in most Pacific plate models (e.g., Seton et al., 2015; Müller et al., 2016; Torsvik et al., 2017) who do not discuss and incorporate the geological record of the northwest Pacific region. Paleomagnetic data from the Cretaceous-Paleocene ophiolites and arc rocks of Kamchatka indicate about 2000 km northward transport of the arc terrane from its initial paleolatitude to its modern position at the Eurasian margin between the Campanian (~75 Ma) and the Middle Eocene (50–45 Ma) (Levashova, 1999; Kovalenko, 2003, as cited in Shapiro and Solov'ev, 2009 suggesting north(west)ward roll-back of the slab upon Pacific plate advance. The slab geometry suggests that it was partly formed during NW ward transport towards the Eurasian margin. We therefore interpret the top of the slab to have subducted sometime between 50 and 45 Ma shortly following ophiolite and arc obduction onto the continental margin.

3.3. Aleutian - Al

The Aleutian anomaly (Fig. 7) is located in the upper mantle below the southern Bering Sea and Alaska and connects to the surface in the Aleutian subduction zone. It was previously identified in the upper mantle (Gorbatov et al., 2000; Qi et al., 2007; Koulakov et al., 2011; Martin-Short et al., 2016). In the UU-P07 model the Aleutian slab is continuous and penetrates the top of the lower mantle below the southern Bering Sea. van der Meer et al. (2010) initially assumed an inferred onset of magmatism in the Kluane arc at the southern margin of Alaska in the late Cretaceous to Eocene (Nokleberg et al., 2000), as a base age of the slab. We now correlate the Kluane Arc to a more easterly, deeper slab (Yukon slab, Section 3.93). Instead, we use the onset of subduction at the Aleutian trench as age for the base of the slab. In the tectonic reconstruction of Shapiro and Solov'ev (2009), 56–54 Ma was inferred as onset of subduction below the Aleutians, based on a change in plate motion of the Pacific plate (Creager and Scholl, 1973; Scholl et al., 1989; Geist et al., 1994). $^{40}Ar/^{39}Ar$ datings of volcanic and plutonic rocks from several islands along the Aleutian arc shows that volcanism was underway by 46 Ma (Jicha et al., 2006; Chekhovich et al., 2014, providing a minimum age for the onset of subduction. Chekhovich et al. (2014) estimated the time of origination of the Aleutian subduction zone is estimated at to be 47 ± (2–3) Ma. We therefore adopt a 50–46 Ma age range for the onset of subduction of the Aleutian slab.

3.4. Algeria - Ag

The Algeria anomaly (Fig. 8) is a detached slab located below NW Africa and the Mediterranean from the deep mantle up to mid-mantle and was first described by van der Meer et al. (2010). The neighbouring base of the Emporios slab (Section 3.33) and the N–S trend of the Algeria anomaly is used to infer that it is the best candidate to represent eastward subducted lithosphere below the West Vardar ophiolites sensu Schmid et al. (2008), found from the Pannonian Basin to southern Greece over a reconstructed distance (e.g., Maffione et al., 2015a) similar to the N–S length of the Algeria slab. The slab is interpreted to represent oceanic lithosphere that was attached to Adria and that subducted below these ophiolites. This lithosphere was referred to as the Meliata-Maliac ocean by Stampfli and Borel (2004). The onset of subduction below the West-Vardar ophiolites likely shortly predated the cooling of metamorphic soles below the west-Vardar ophiolites of Greece, Albania and the Dinarides, dated at 174–157 Ma, by several million years (Dimo-Lahitte et al., 2001; Liati et al., 2004; Karamata, 2006; Šoštarić et al., 2014): we consequently interpret the Algeria anomaly as a slab with a 175 ± 5 Ma age for the base. Obduction of the ophiolites onto eastern Adria, currently in the Dinarides-Hellenides was shown by sedimentary overlap assemblages in the Dinarides and Hellenides to have finalized in the early Cretaceous, around 130 ± 10 Ma (Schmid et al., 2008; Scherreiks et al., 2014; Tremblay et al., 2015; Maffione et al., 2015a), which we take as the age for the top of the slab.

3.5. Al Jawf - AJ

A NW-SE elongated anomaly is imaged overlying the core-mantle boundary below the Red Sea and most of Arabia, which we here define for the first time as the Al Jawf anomaly (Fig. 9). Resolution tests show that the anomaly is poorly resolved, and our interpretation is therefore tentative. In the west, the body reached shallower depths, rising up to ~2400 km depth into the lower mantle. Based on correlation with the shallower Emporios slab (Section 3.33), the Mesopotamia slab (Section 3.64) towards the North, and the Central China slab (Section 3.30) and the Mongol-Kazakh slab (Section 3.67) at similar depths to the NE, we infer the Al Jawf slab likely formed by subduction to the south of Laurasia in pre-middle Jurassic time. We consequently interpret this

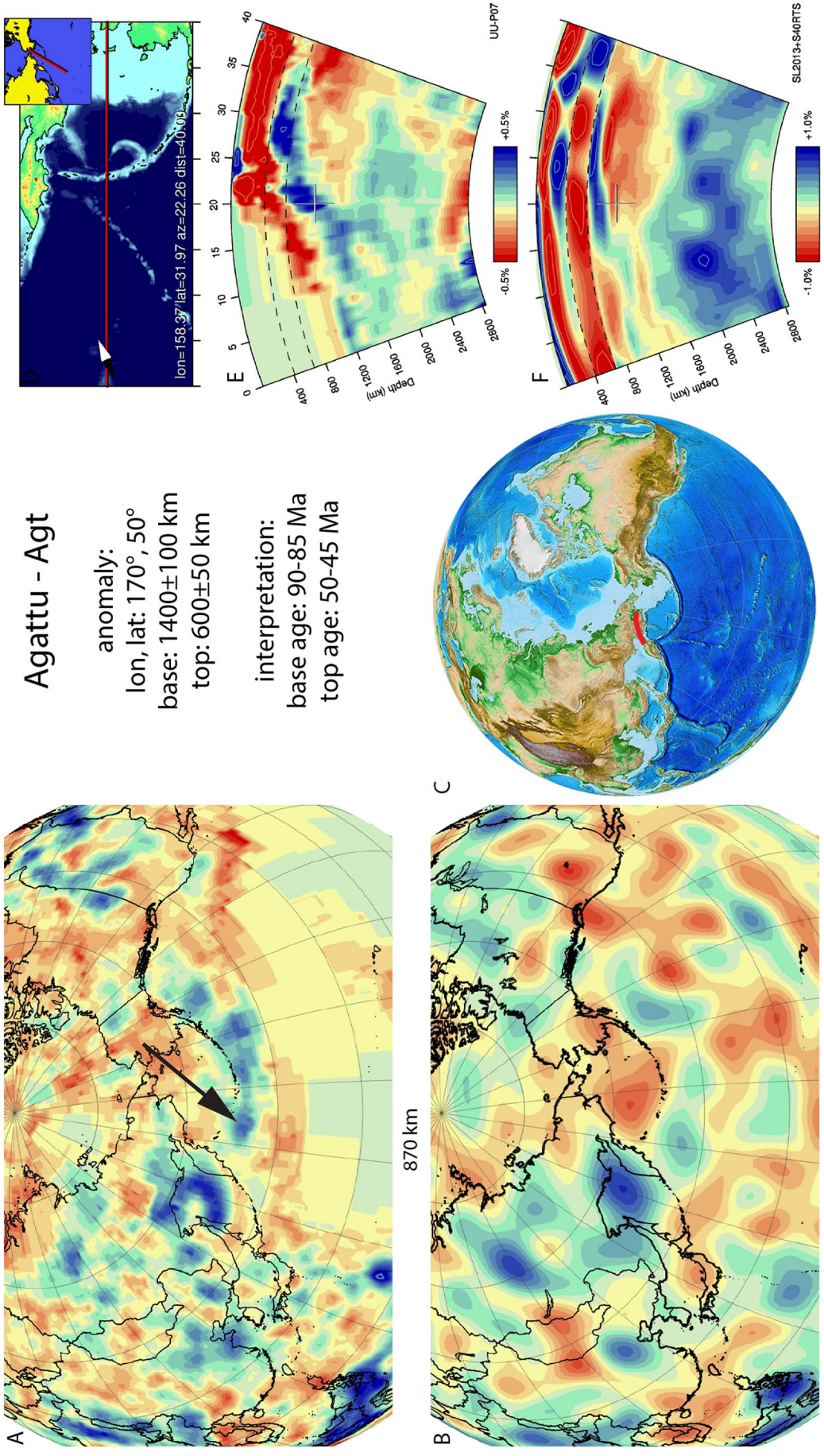

Fig. 6. Agattu anomaly. Legend same as Fig. 5. Relative amplitude strength, and lateral extent are fairly similar between tomographic models. Vertical extent and dip trend differ.

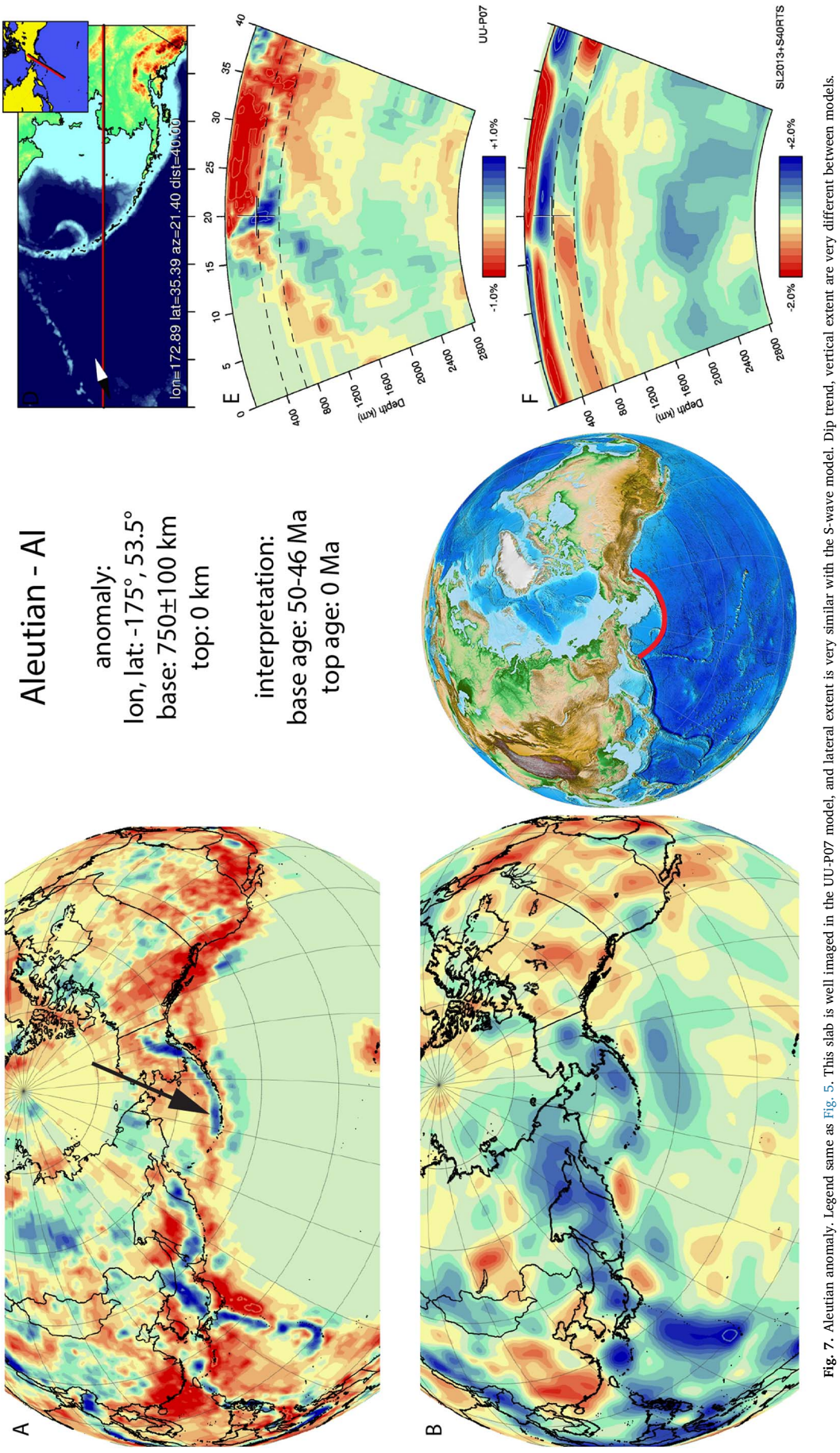

Fig. 7. Aleutian anomaly. Legend same as Fig. 5. This slab is well imaged in the UU-P07 model, and lateral extent is very similar with the S-wave model. Dip trend, vertical extent are very different between models.

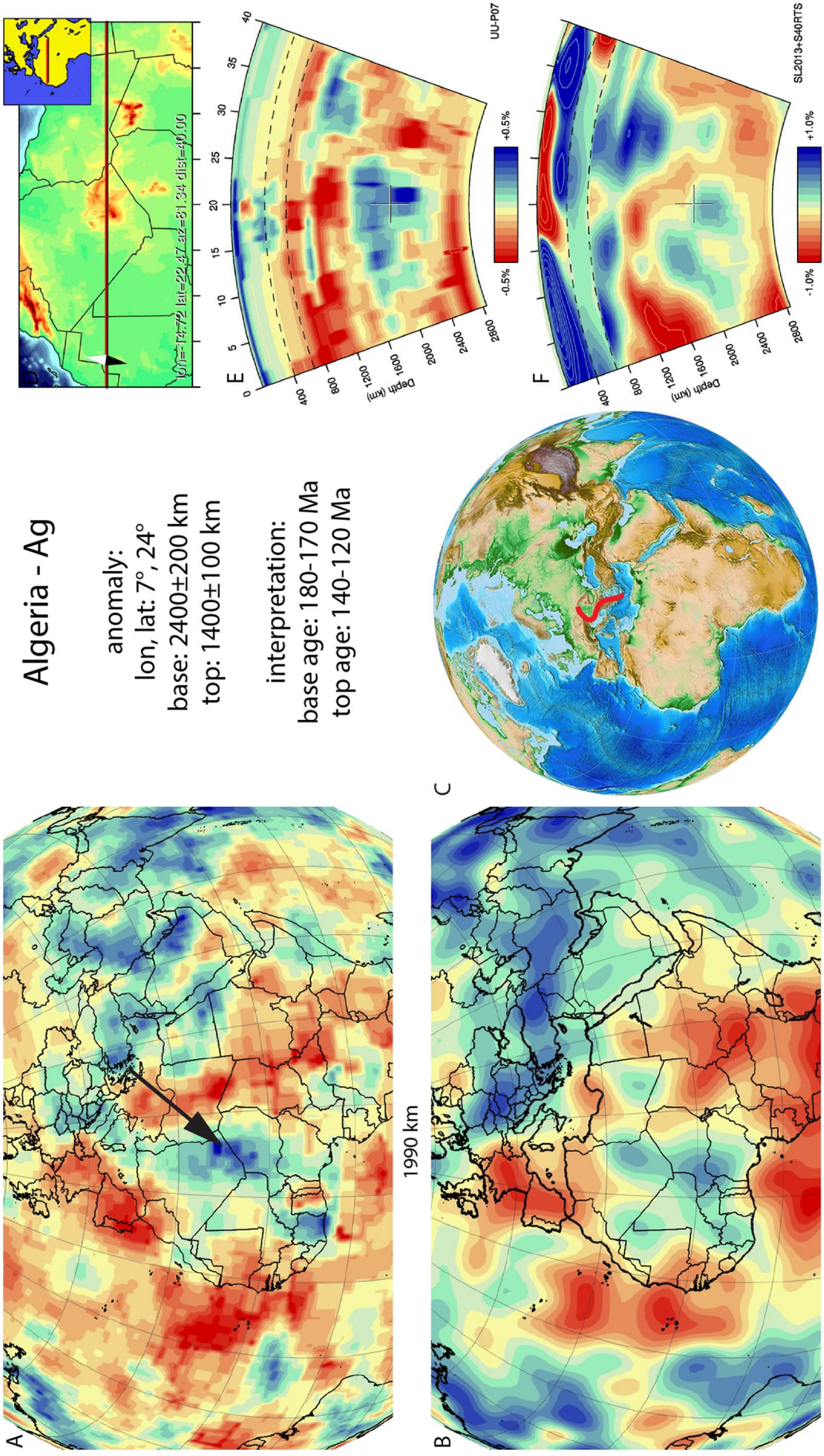

Fig. 8. Algeria anomaly. Legend same as Fig. 5. Lateral location is similar between tomographic models. Relative amplitude strength is weaker in the used S-wave models. Lateral and vertical extent differs between tomographic models. Dip trends are not imaged.

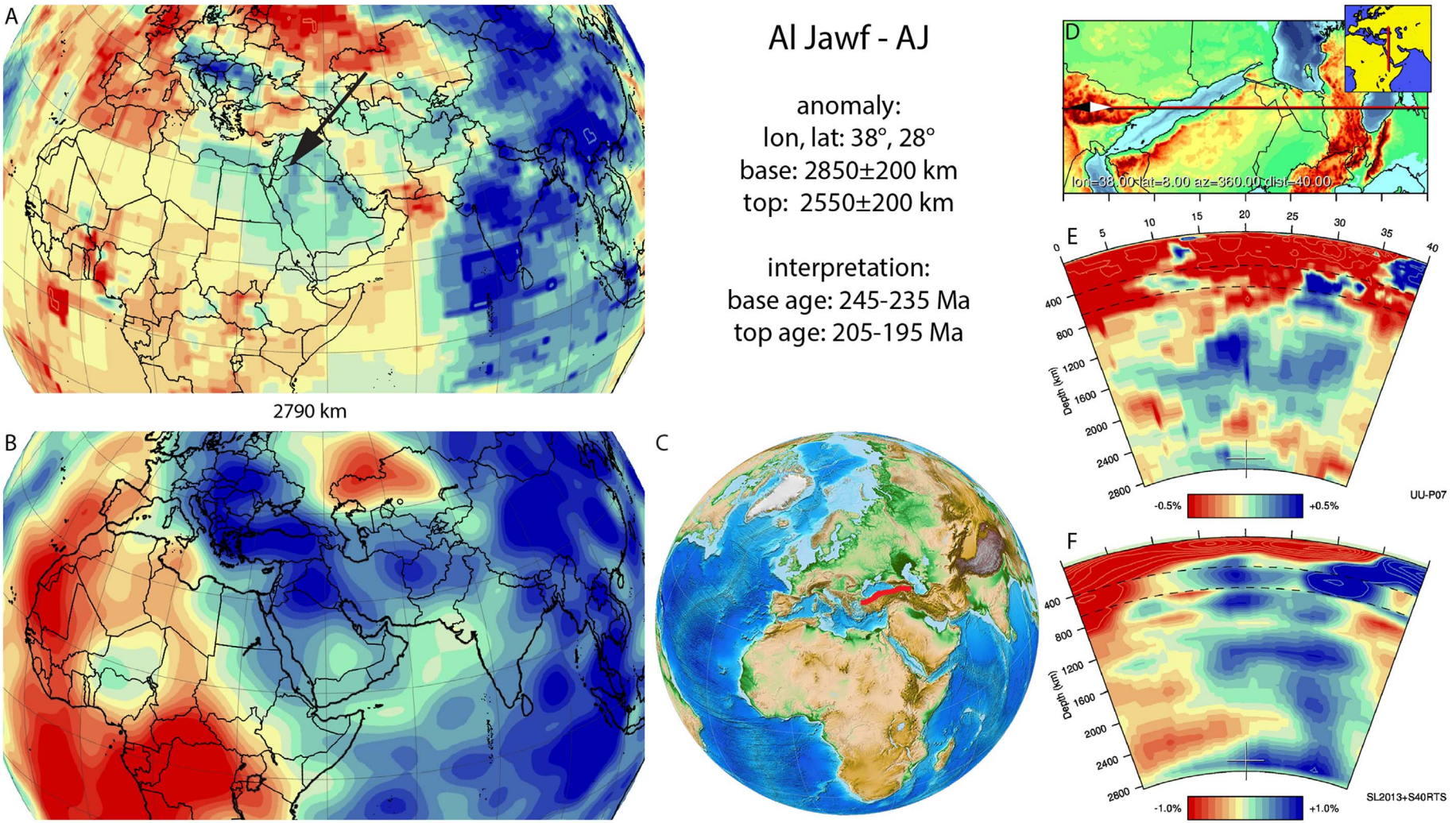

Fig. 9. Al Jawf anomaly. Legend same as Fig. 5. Positive anomalies are identified in the same location in both tomographic models with a similar vertical extent, flat on top of the CMB. Relative amplitude strength, lateral extent differ between tomographic models. In the S-wave model this anomaly is much larger and merges with the Balkan anomaly to the NW.

anomaly as Paleotethys lithosphere that subducted during the opening of the Neotethys between the Gondwana-derived 'Cimmerian' continental fragments and Arabia-Africa. Neotethys opening and Paleotethys subduction is not the same age in the Tethyan realm. Subduction between the Cimmerian continents of Iran and Arabia is paleomagnetically and stratigraphically constrained to occur between the Late Permian and the Early Triassic collision of the Iranian Cimmerian continents with Eurasia, 230 ± 10 Ma (Stampfli and Borel, 2002; Muttoni et al., 2009). Closure of the Paleotethys in the Eastern Mediterranean region was younger, and may either have occurred by northward (Okay and Nikishin, 2015), or, as more widely accepted, southward subduction (Sengör and Yilmaz, 1981; Dokuz et al., 2017) below the Sakarya continental fragment. A record of subduction is reflected by the Karakaya mélange complex in northern Turkey. This complex contains Devonian radiolarian cherts, showing that Paleozoic oceanic crust was consumed (Okay et al., 2011). $^{40}Ar/^{39}Ar$ ages of eclogite blocks in the Karakaya subduction mélange of 215–203 Ma (Okay and Monié, 1997; Okay et al., 2002) show that subduction was active until the latest Triassic. This mélange is unconformably overlain by Lower Jurassic limestones which may mark the end of subduction around ~200 Ma (see Sayıt and Göncüoglu, 2013 for a review). In addition, Middle Jurassic, ~170 Ma old lavas in the Pontides were interpreted to reflect Paleotethys slab break-off (Dokuz et al., 2017) and we adopt a 200–170 Ma age for the top of the Al Jawf slab. Since there was minimal convergence between Gondwana and Laurasia in the Triassic, the closure of the Paleotethys was almost entirely accommodated by contemporaneous opening of the Neotethys (Gutiérrez-Alonso et al., 2008). The oldest radiolarian cherts obtained from mélanges that formed during subduction of the Neotethys in Turkey along the Izmir-Ankara suture zone are Ladinian-Carnian in age (242–228 Ma) (Tekin et al., 2002; Tekin and Göncüoğlu, 2007) provide a minimum age for opening of the Neotethys and thus for the onset of subduction of the Paleotethys. Because shallower slabs in the mantle in the region of the Al Jawf slab were all correlated to Jurassic and younger geological records, we correlate the Al Jawf slab to the youngest, Triassic-Jurassic record of Paleotethys subduction in the eastern Mediterranean region and therefore adopt a minimum age of 240 Ma for the base of the western end of the Al Jawf anomaly, and a 200 Ma age for the top. The S-wave tomographic images suggest that to the east, there may be more lithosphere present that may be the relics of the Permo-Triassic slabs of the Paleotethys that formed east of the Al Jawf slab, but in the UU-P07 model, we find no sufficient resolution to independently confirm this.

3.6. Alps - Alp

The Alps anomaly (Fig. 10) was first detected by Spakman (1986b), Kissling (1993) and Kissling and Spakman (1996) and was interpreted by Spakman and Wortel (2004) as the remnant of the Piemonte-Ligurian ocean that subducted in the Alps. The Alps anomaly is interpreted as a curved body of detached lithosphere that follows the oroclinal shape of the western Alps, and lies on the 660 km discontinuity, with its base penetrating the upper part of the lower mantle, reaching ~800 km depth (Fig. 11). The Alps slab is disconnected from shallower anomalies below the western and eastern Alps that are imaged to < 200 km depth (Lippitsch et al., 2003; Kissling, 2008) and that are interpreted as European continental lithosphere in the west, and Adriatic continental lithosphere in the east that subducted in the last 20 Ma (e.g., Schmid et al., 2004; Handy et al., 2010, 2014). The Alps slab likely represents oceanic lithosphere of the Piemonte-Ligurian and Valais oceans and continental lithosphere of the intervening Briançonnais microcontinent (Handy et al., 2014) that subducted in the Alps. The oldest definitive record of subduction, with a southward vergence, in the geological record of the western Alps is the HP-LT metamorphism of the Sesia zone, with an age around 75–65 Ma (Handy et al., 2010) and references therein). Subduction must have started prior to this time, and may have initiated due to a change in relative Africa-Europe convergence from E–W to N–S around 85 Ma (Handy et al., 2014), which we adopt as the age of the base of the Alps slab, with a somewhat arbitrary but conservative uncertainty estimate of ± 10 Ma. Break-off of the Alps slap was interpreted to be reflected by a series of granitoid intrusions of 33 ± 8 Ma (von Blanckenburg and Davies, 1995). In more recent years also rapid uplift and exhumation in the Alps in the Early Oligocene was interpreted to possibly reflect a phase of slab break-off (Jourdan et al., 2013). In any case, breakoff of the Alps slab in the eastern Alps must have occurred prior to the onset of northward underthrusting of Adriatic lithosphere, which according to geological interpretations of the southern Alps occurred since ~20 Ma (Ustaszewski et al., 2008). Following these constraints, we conservatively adopt an age for the top of the Alps slab of 30 ± 10 Ma.

3.7. Anhui - Anh

The Anhui anomaly (Fig. 11) is located in the upper part of the lower mantle and lower part of upper mantle below southeastern China. It has previously been imaged by Wei et al. (2012), who suggested it may represent Pacific or Izanagi lithosphere that detached from the present Pacific slab. Its shape is irregular at the base and forms a broad anomaly at 810 km depth. At shallower depths it thins and is not imaged above the 440-km discontinuity. Towards the north, the Manchuria slab (Section 3.54) shares similar flat-slab characteristics, although the Anhui anomaly is located somewhat deeper in the mantle. We interpret this anomaly as the Anhui slab with the subduction history below the South China block postdating the subduction of the East China slab (Section 3.30).

Following the formation of a slab window and tectonic inversion as a result of ridge subduction and/or collision with the West Philippine block (Li et al., 2014a), subduction below South China recommenced with arc magmatism and crustal extension (107–86 Ma). The exact end of that phase of subduction is unclear. Generally, Cretaceous magmatism migrated progressively eastward towards the Taiwan area and is reported to have ceased at 90–86 Ma (Li et al., 2014a, 2014c). Subsequent transpression is associated with the ESE-ward retreat of the Pacific subduction zone (Li et al., 2014a), which, however, corresponds to the Izu-Bonin subduction zone that started at ~52 Ma (see Section 3.44). This leaves a ~30 Myr subduction gap in the region (see also Hall, 2002; Li et al., 2012), here interpreted as the waning of the Anhui slab subduction. Future research may require revising our interpretation of the Anhui slab.

3.8. Antalya - Ant

The Antalya anomaly (Fig. 12) is interpreted as a N–S striking, eastward dipping slab below the Bay of Antalya and the western Taurides of southern Turkey. It was first shown by De Boorder et al. (1998), and later, in more detail, by Biryol et al. (2011). Seismic tomographic images clearly show that the Antalya slab is disconnected from the Aegean-west-Anatolian slab (Section 3.1) (van Hinsbergen et al., 2010; Biryol et al., 2011) along a NE-SW trending zone that was interpreted as a subduction transform edge propagator (STEP) fault (Govers and Wortel, 2005). Below 300–400 km depth, the Antalya slab becomes tomographically indistinguishable from the Cyprus slab (Section 3.30), which plunges down into the top of the lower mantle.

Subduction in southern Anatolia occurred below oceanic lithosphere, preserved in a wide belt of ophiolites. Metamorphic sole cooling ages of these ophiolites, widely regarded as forming within several million years after subduction initiation (Hacker, 1990; Wakabayashi and Dilek, 2000; van Hinsbergen et al., 2015), are ~92 ± 3 Ma (Çelik et al., 2006), suggesting subduction initiation several million years earlier, ~95–100 Ma, which we adopt for the age of the base of the Antalya and Cyprus slabs.

Even though the Antalya slab is associated with a Benioff zone (Kalyoncuoğlu et al., 2011), it is not evident if and where the Antalya

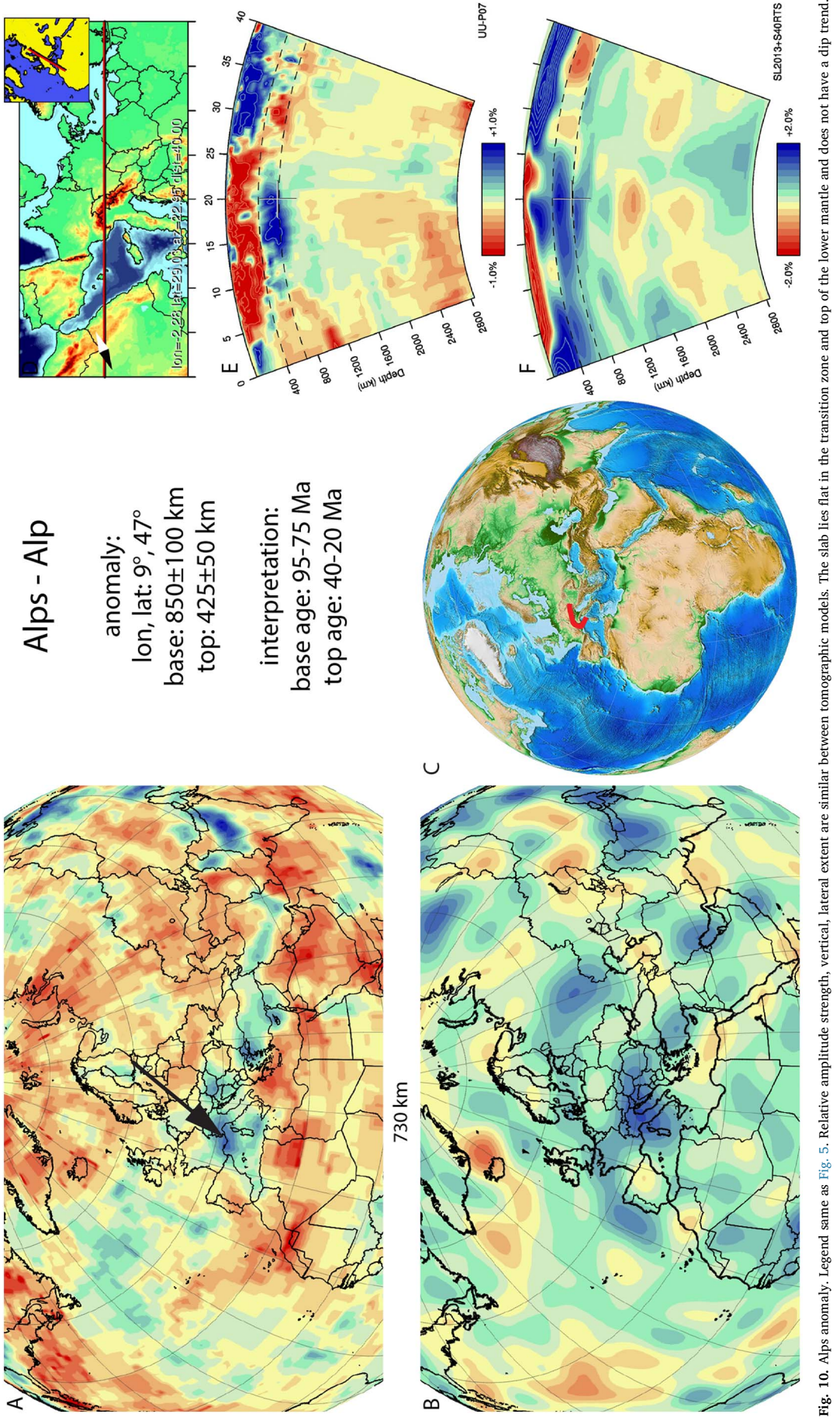

Fig. 10. Alps anomaly. Legend same as Fig. 5. Relative amplitude strength, vertical, lateral extent are similar between tomographic models. The slab lies flat in the transition zone and top of the lower mantle and does not have a dip trend.

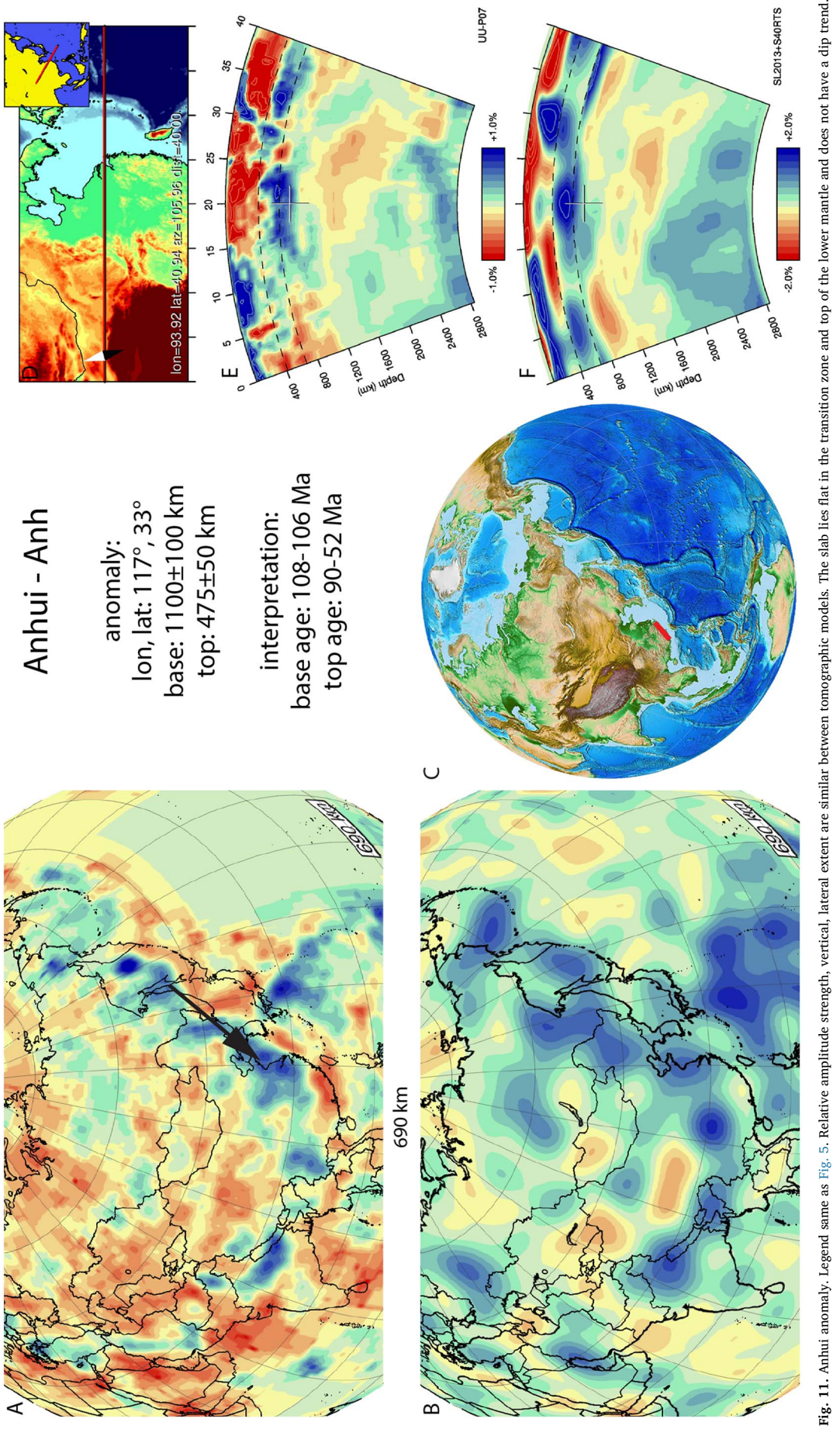

Fig. 11. Anhui anomaly. Legend same as Fig. 5. Relative amplitude strength, vertical, lateral extent are similar between tomographic models. The slab lies flat in the transition zone and top of the lower mantle and does not have a dip trend.

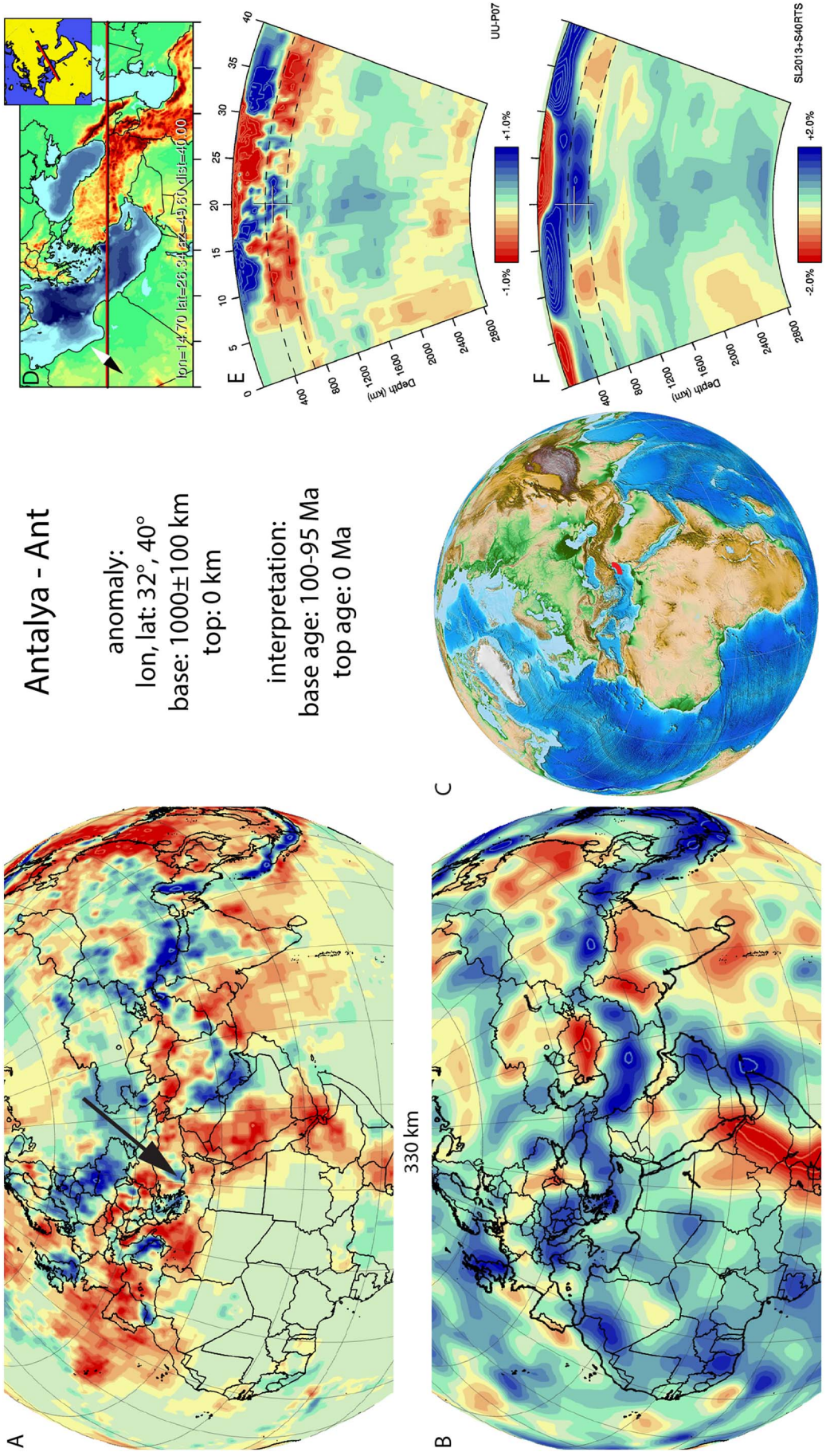

Fig. 12. Antalya anomaly. Legend same as Fig. 5. This slab is well imaged in the UU-P07 model. Dip trend, vertical and lateral extent are very different between tomographic models.

slab is connected to a subduction thrust at the surface. Biryol et al. (2011) and Schildgen et al. (2012) interpreted the Antalya slab to be a part of the Cyprus slab that tore off and rotated into a N–S orientation. Recently, however, Koç et al. (2016) argued that subduction of the Antalya slab accommodated E–W shortening in the heart of the Isparta triangle until at least Pliocene time, and created E–W overriding plate extension in southern Turkey since at least middle Miocene time. Based on a paleomagnetic study of a Central Anatolian volcanic arc, Lefebvre et al. (2013) showed that a N–S trending subduction zone must have already existed since late Cretaceous time and Advokaat et al. (2014a) and van Hinsbergen et al. (2016) argued that African plate subduction in Anatolia was accommodated along discrete E–W and N–S trending segments since the onset of subduction. The Antalya and Cyprus slabs may thus have been two independent slabs since the onset of subduction, but their close vicinity makes them tomographically indistinguishable at depth.

3.9. Arabia - Ar

The Arabia anomaly belt (Fig. 13) is located in the mid-mantle from the northern part of the Red Sea to the southeast below the southeastern coast of Saudi Arabia. The Arabia anomaly belt was previously identified by Hafkenscheid et al. (2006) and identified as the Eg and SA slabs. They are located south of and at a depth interval overlapping with, and hence probably subducted in part simultaneously with and south of the Mesopotamia slab (Section 3.60) to the NE that subducted along the Eurasian margin between 150 and 65 Ma. The Arabia anomalies thus likely represent Neotethyan lithosphere that subducted intra-oceanically. Intra-oceanic subduction within the Neotethys between Arabia and Eurasia is a well-known event in the Late Cretaceous, and culminated in the obduction of ophiolites over the Arabian margin (the Semail ophiolite of Oman, and the Baer Bassit and Hatay ophiolites of Syria and SE Turkey, respectively, and likely the Troodos ophiolite of Cyprus, in the Late Cretaceous (70 ± 5 Ma; Koop and Stoneley, 1982; Al-Riyami et al., 2002; Dilek and Furnes, 2009; Homke et al., 2009; Searle and Cox, 2009; Agard et al., 2011; Maffione et al., 2017). These foreland basin deposits and overlap assemblages provide the likely age for break-off of the Arabia slab. The minimum age of onset of subduction below the Arabian ophiolites is provided by the age of their metamorphic soles (95 ± 5 Ma: Hacker, 1994; Hacker et al., 1996; Al-Riyami et al., 2002; Warren et al., 2003; Agard et al., 2007).

3.10. Arafura - Af

The Arafura anomaly (Fig. 14) corresponds to anomaly A6 of (Hall and Spakman, 2002, 2004). It is interpreted as a NNW-SSE trending slab, flat-lying at the top of the lower mantle and the base of the upper mantle from north of the Bird's Head, beneath the Arafura Sea, to the Gulf of Carpentaria. Towards the north, the Arafura slab is in the vicinity of the base of the Halmahera slab that started subduction around 15 Ma (Section 3.36), suggesting that the Arafura slab should be correlated to a subduction zone that terminated east of Halmahera in mid-Late Cenozoic time. Hall and Spakman (2002, 2004) interpreted the slab as the result of northward subduction underneath the Philippines-Halmahera arc between 45 and 25 Ma. The geological record of this Paleogene subduction zone is, according to the reconstruction of Hall (2002), now found on the eastern Philippines. Wu et al. (2016) interpreted the anomaly to be an East Asian Sea south slab, being the result of southward subduction underneath the Solomon Sea between 50 and 20 Ma. Both interpretations are consistent with the modern position of the slab and we therefore adopt 50–45 Ma and 25–20 Ma as age ranges for the base and top of the Arafura slab.

3.11. Atlantis - At

The Atlantis anomaly (Fig. 15) is located below the central Atlantic Ocean, covers the core-mantle boundary, and was first identified in van der Meer et al. (2010). The Cocos and Hatteras slabs (Sections 3.29, 3.37) shallower in the mantle to the west leads us to interpret the Atlantis anomaly as a slab with a pre-Jurassic subduction age. Several correlations to the geological record were discussed in van der Meer et al. (2010), with a preferred interpretation that the Atlantis slab represents Panthalassa oceanic lithosphere that subducted along the western margin of Laurasia until the middle Triassic. Recently Hadlari et al. (2017) with a synthesis of U-Pb detrital zircon data corroborated a Triassic subduction zone and continental magmatic arc system along western Laurentia. The disconnection of the Atlantis and Cocos and Hatteras slabs results from a pause in subduction along western Laurentia illustrated by a gap in magmatism at the western continental margin of Laurentia during the mid-Late Triassic (Ward, 1995; Nokleberg et al., 2000; Barboza-Gudiño et al., 2008; DeCelles et al., 2009).

3.12. Balkan - Ba

The Balkan anomaly (Fig. 16) is located below south-eastern Europe and overlies the core-mantle boundary. It was first identified in van der Meer et al. (2010). The Emporios slab (Section 3.32), Mesopotamia slab (Section 3.60) to the northeast, both higher in the mantle and correlated to geological records of Jurassic and younger subduction, were used to infer to interpret the anomaly as the Balkan slab representing lithosphere that subducted prior to the Jurassic age. The Mongol-Okhotsk subduction in the east constrains the Siberia block to a Triassic to Jurassic position northeast of the Balkan slab. The Balkan slab therefore is likely the result of subduction to the west of Siberia. The Al Jawf slab (Section 3.5), interpreted as subducted Paleotethyan lithosphere, suggests a subduction location of the Balkan slab northwest of southern Laurasia. van der Meer et al. (2010) considered the Solonker Ocean that subducted between the North China block and Amuria until Triassic time (Xiao et al., 2010), and the Uralian ocean that intervened Siberia and Baltica as potential sources of this slab. The position of this slab in the light of global plate reconstructions makes a correlation to the Uralian Ocean more likely. The collision between Siberia and Baltica occurred in the Late Permian (~280–250 Ma) (Cocks and Torsvik, 2007, 2011; Torsvik et al., 2012), which we adopt as the age for the top of the Balkan slab.

In the S40RTS model the Balkan slab is part of a much larger NW-SE trending anomaly of > 4000 km, from the North Sea to Anatolia, where it connects to the Al Jawf slab. This large extent may represent a a more complete record of the Permian Uralian Ocean, but in the UUP07 model only the Balkan slab (< 2000 km) is detected.

3.13. Banda - Bn

The Banda anomaly (Fig. 17) is interpreted as an amphitheatre-shaped, south-, west-, and north-dipping slab that underlies the Banda Sea in southeast Indonesia and that is still, connected to the surface in the north, east, and south. It was first shown in Fukao et al. (1992), Puspito et al. (1993), Widiyantoro and van der Hilst (1996), and Rangin et al. (1999) and topic of reconstruction in Hafkenscheid et al. (2001), Wu et al. (2016), and particularly in Spakman and Hall (2010). The deepest part of the Banda slab reaches the 660 km discontinuity. Spakman and Hall (2010) showed kinematic reconstructions suggesting that subduction of the proto-Banda embayment of the Australian continent formed the Banda slab that started around ~15 Ma by eastward rollback. This was partly associated with delamination of the mantle lithosphere of the Western Sula Spur directly north of the subducting embayment and with ultra-high temperature metamorphism in crustal rocks now found on the island of Seram. This metamorphism was recently dated at 16 Ma (Pownall et al., 2014), suggesting a somewhat earlier initiation of subduction of the Banda embayment. A recent reconstruction of the fold-thrust belt of Timor, in the south of the Banda

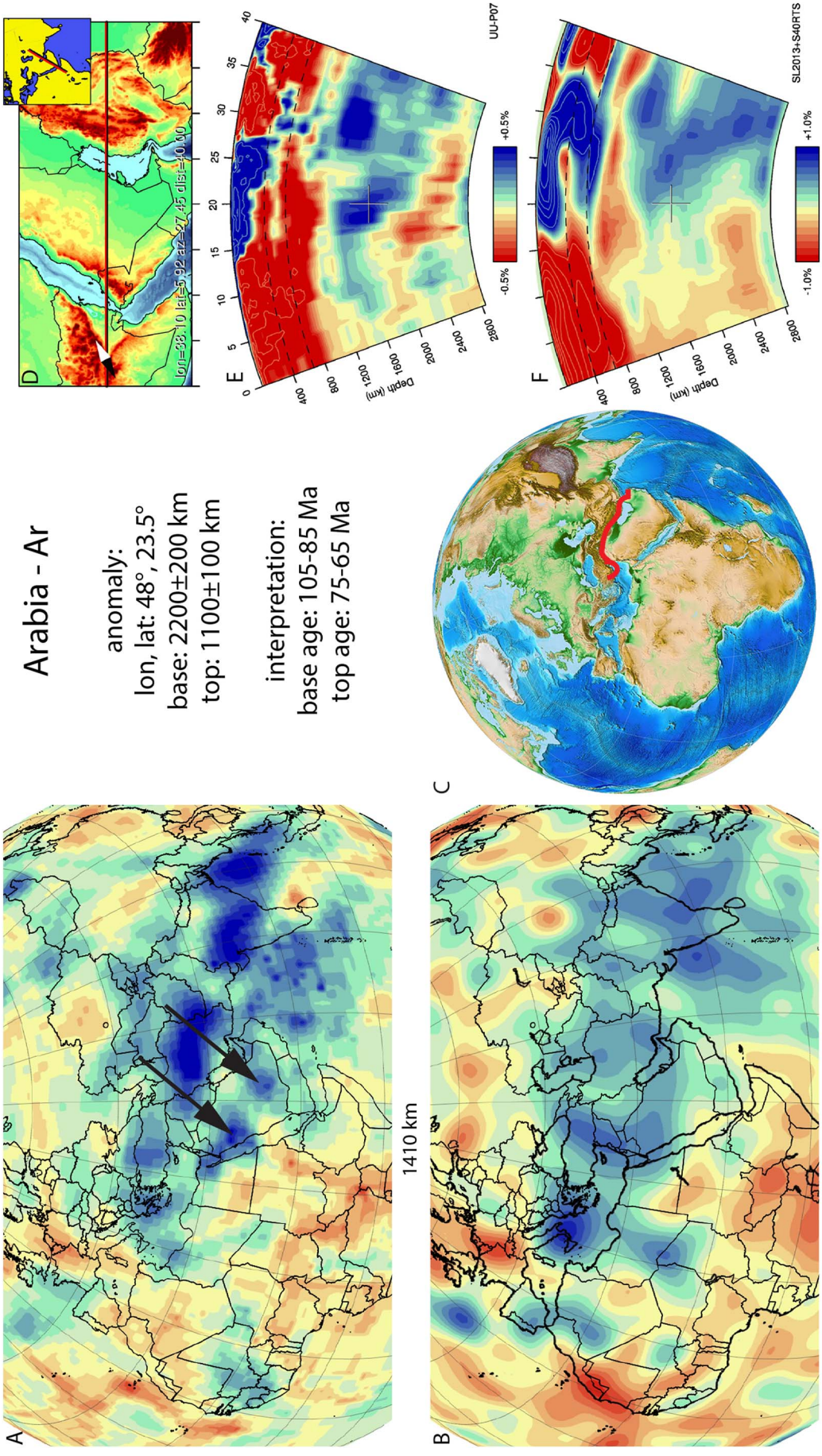

Fig. 13. Arabia anomalies, legend same as Fig. 5. Relative amplitude strength and dip trend is similar between tomographic models. Lateral and vertical extent differ.

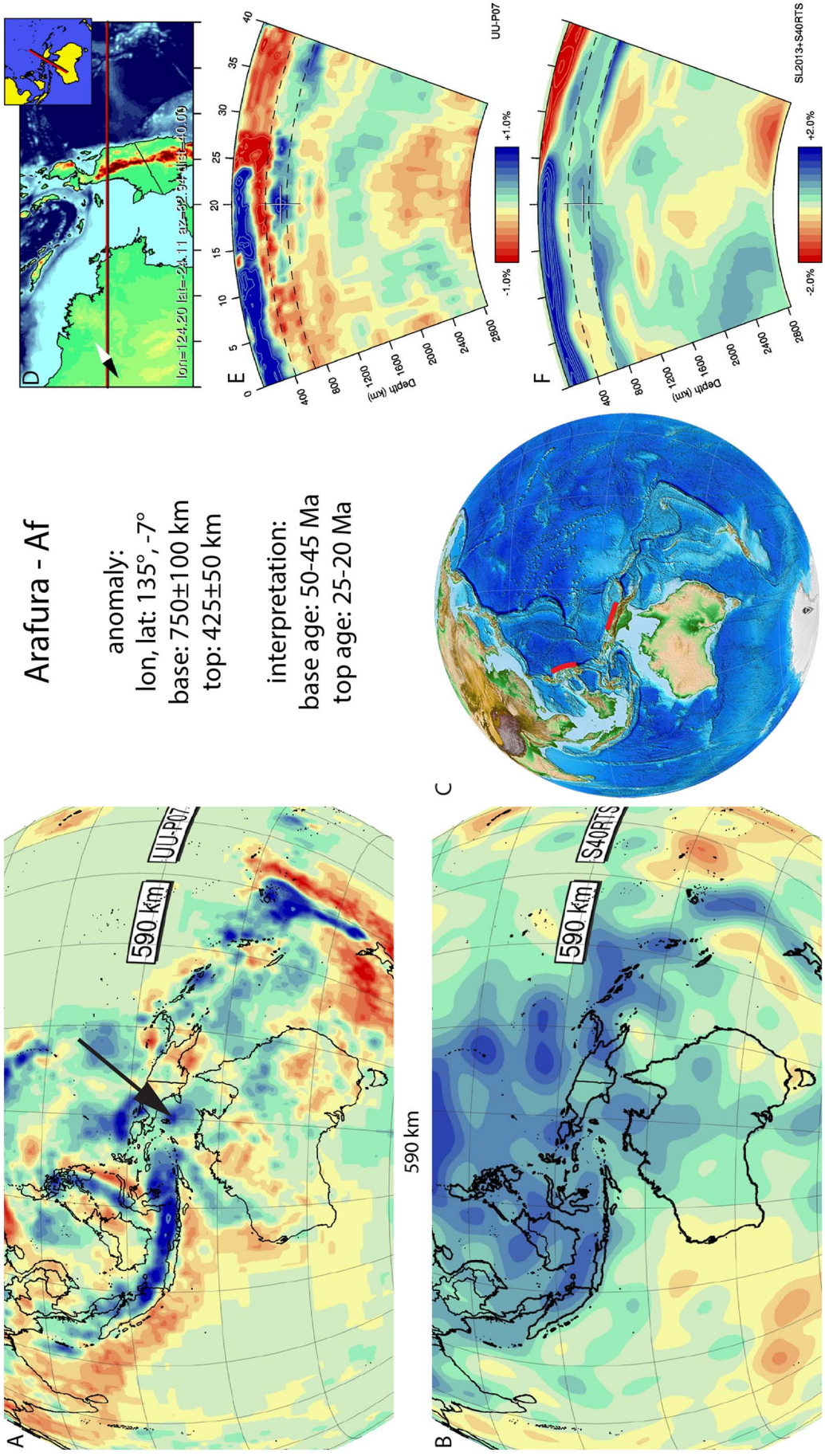

Fig. 14. Arafura anomaly. Legend same as Fig. 5. Vertical and lateral location and dip trend are very similar between tomographic models. Relative amplitude strength is weaker in the used S-wave models.

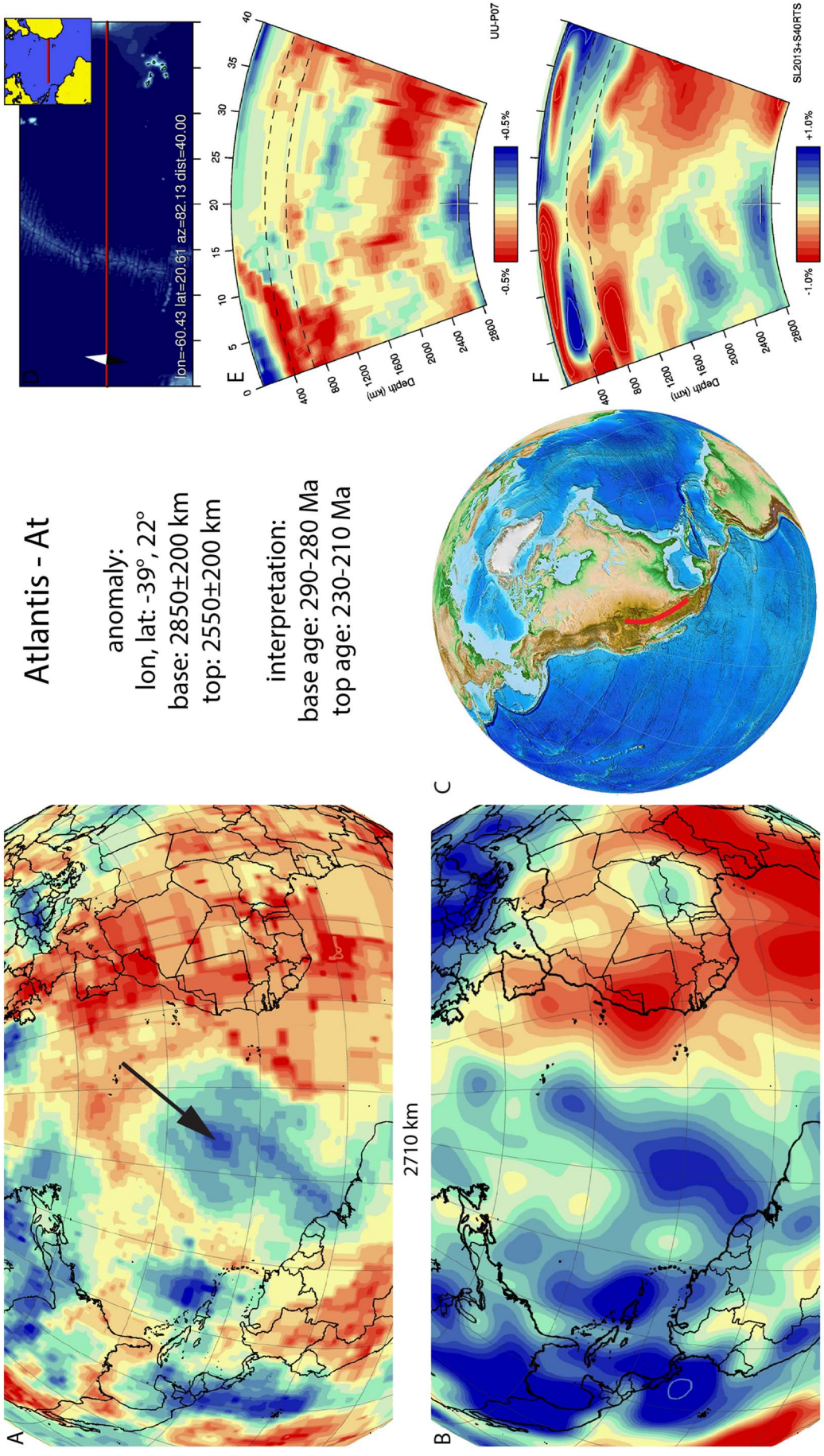

Fig. 15. Atlantis anomaly. Legend same as Fig. 5. Positive anomalies are identified in the same location in both tomographic models with a similar Relative amplitude strength, vertical and lateral extent, flat on top of the CMB.

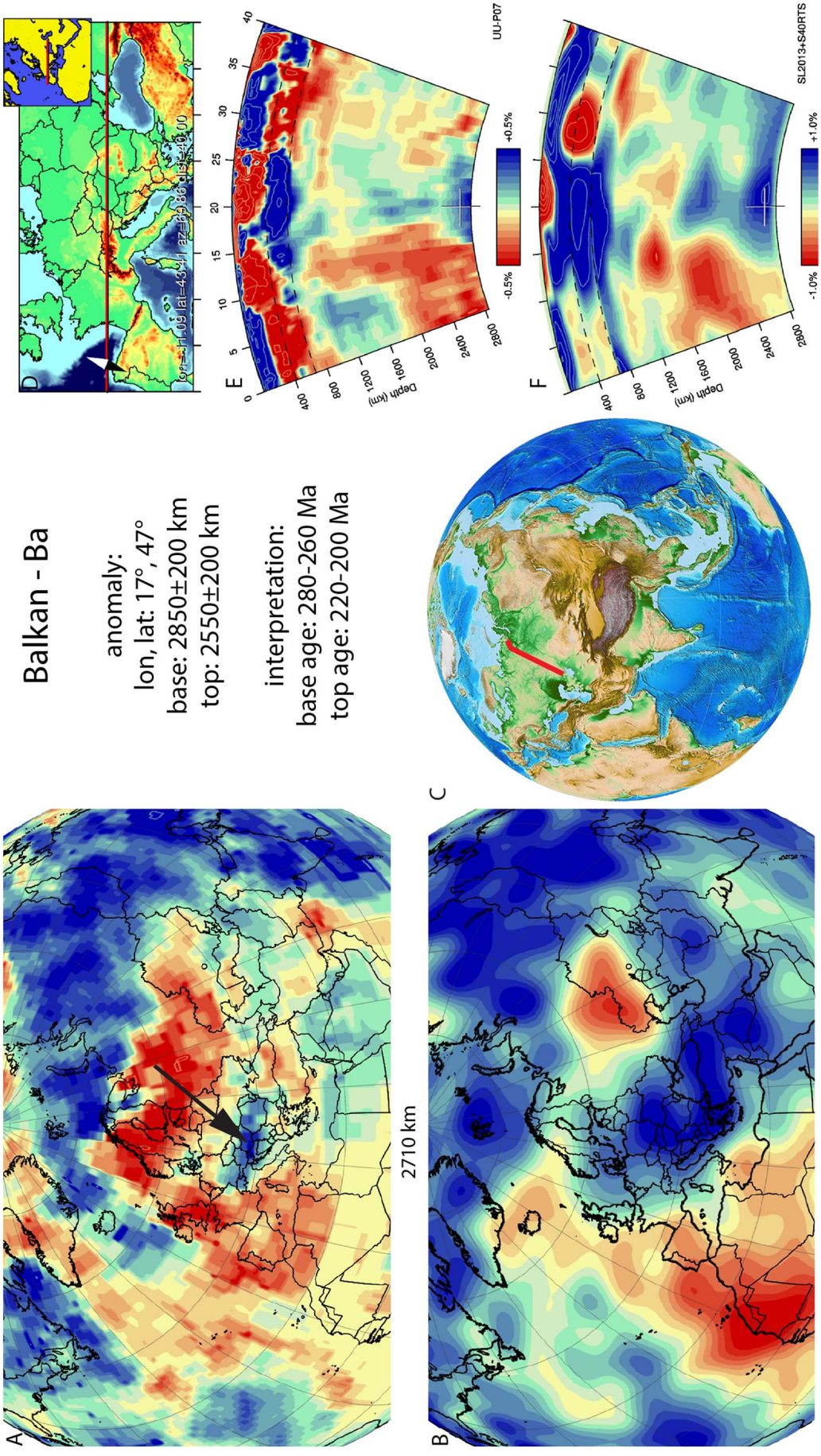

Fig. 16. Balkan anomaly. Legend same as Fig. 5. Positive anomalies are identified in the same location in both tomographic models with a similar vertical extent, flat on top of the CMB. Relative amplitude strength, lateral extent differ between tomographic models. In the S-wave model this anomaly is much larger and merges with the Al Jawf anomaly to the SE.

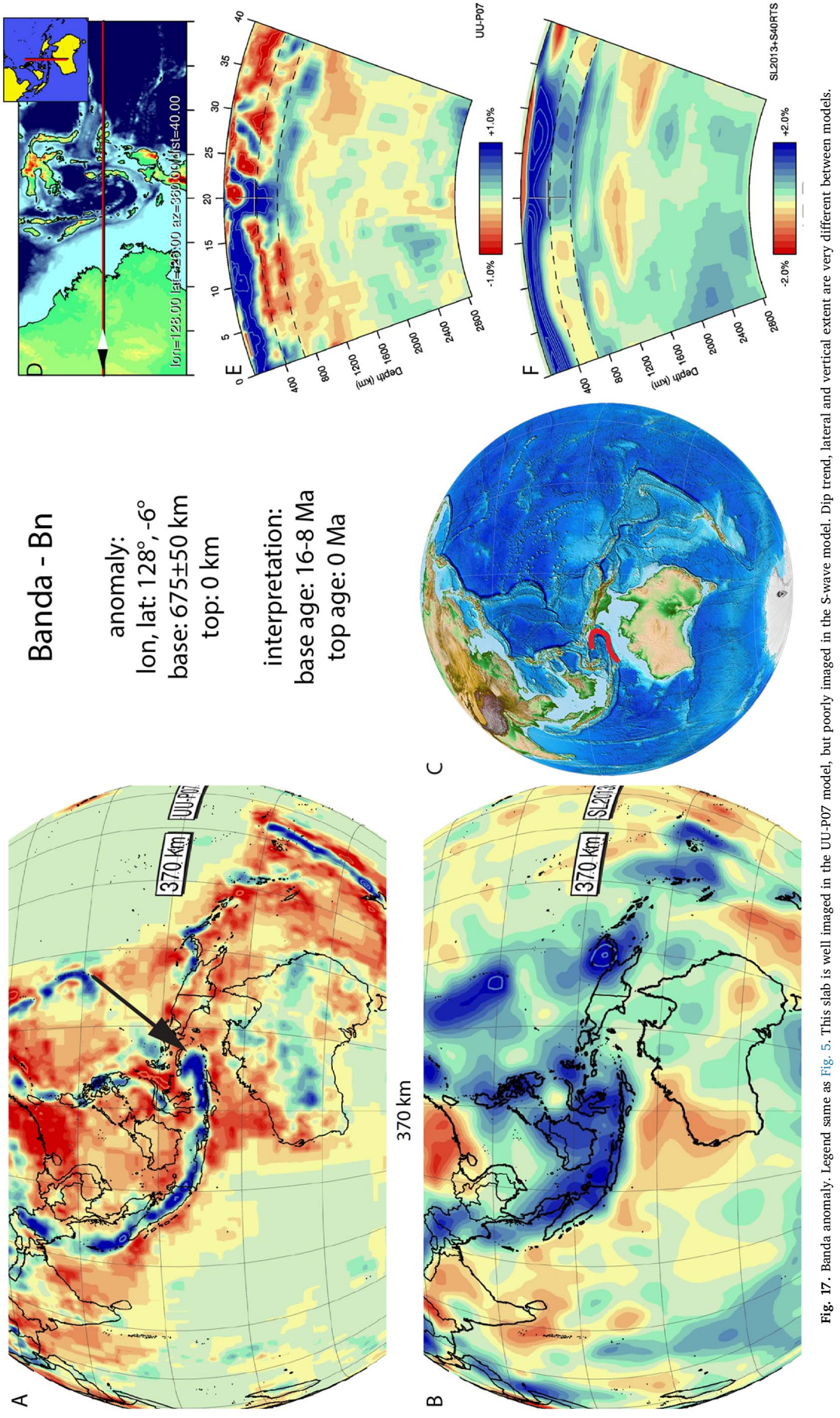

Fig. 17. Banda anomaly. Legend same as Fig. 5. This slab is well imaged in the UU-P07 model, but poorly imaged in the S-wave model. Dip trend, lateral and vertical extent are very different between models.

embayment, shows that at least the last 8 Myr of subduction consumed ~350 km of (continental) lithosphere (Tate et al., 2014, 2015, 2017). The lithosphere now lying between 650 and 500 km depth thus must have subducted prior to ~8 Ma and after 16 Ma. We thus use a 12 ± 4 Ma as estimate for the start of its subduction.

3.14. Beaufort - Bf

The Beaufort anomaly (Fig. 18) is located below North Alaska and the Beaufort Sea within the deep mantle. It was first identified in van der Meer et al. (2010) and subsequently Shephard et al. (2014) interpreted its dynamic evolution based on modelling. The base of the Mongol-Kazakh slab (Section 3.63), as well as the base of the Idaho slab (Section 3.42) to the south at similar depth, led us to interpret the anomaly as the Beaufort slab representing lithosphere that likely subducted during the Early or Middle Mesozoic in the Arctic. Nokleberg et al. (2000) reconstructed subduction of Arctic/Panthalassa lithosphere at the Alazeya arc and forming the Aluchin subduction zone terrane, during the Late Triassic-Jurassic, and was chosen by van der Meer et al. (2010) as most likely correlation for this slab, with the time of subduction of 230–144 Ma. Shephard et al. (2014) preferred a tectonic model suggested that the source of the Alazeya arc was subducting Panthalassa lithosphere between 230 and 193 Ma, followed by a subduction polarity reversal in the reconstruction of Nokleberg et al. (2000). A more recent geological and geochronological study of Sokolov et al. (2009) described the Alazeya arc and several of its terranes (Yarakvaam, Vurguveem, and Aluchin ophiolites) in more detail and found ages of amphibolites associated with ophiolites (239.1 ± 8 Ma) or in tectonic blocks in sub-ophiolitic melanges (229–257 Ma). Sokolov et al. (2009) interpreted this to reflect the age range of the entire subduction history below the Aluchin ophiolite. Amphibolites associated with ophiolites are, however, frequently related to the early stages of subduction (metamorphic soles), after which temperatures in the subduction zones decrease and blueschists are formed instead. Sokolov et al. (2009) does not describe the structural context of these amphibolites within the ophiolite structure in detail, but we conservatively estimate the 257–229 Ma age range to reflect the age of the base of the Beaufort slab, reasonably in line with the estimates of Nokleberg et al. (2000), and adopt the 193 Ma age preferred by Shephard et al. (2014) as the end of subduction.

3.15. Bering Sea - BS

The Bering Sea anomaly (Fig. 19) is located below the Bering Sea, is detached, and is flat-lying at the 660-km discontinuity. Towards the south it is close to, but separated from the Aleutian slab (Section 3.3). Towards the west, it is close to but separated from the Agattu slab. Towards the north, it connects to the N–S trending Mayn slab (Section 3.59). Gorbatov et al. (2000) suggested that the separation between the Aleutian slab and the Bering Sea anomaly would have been caused by the Kula-Pacific ridge subduction and estimated a ~48 Ma age for break-off. There is no clear reason, however, why the Kula lithosphere would become located farther north than the Pacific lithosphere to explain the separation between the Bering Sea and Aleutian slabs. The Bering Sea contains, moreover, evidence for a short-lived Cenozoic intra-oceanic subduction zone to the north of the Aleutian trench. This subduction formed the volcanic arc of the Bowers Ridge which is clearly visible in the bathymetry of the western Bering Sea. Nokleberg et al. (2000). The presence of a trench filled with as much as 12 km of Cenozoic sedimentary rocks at the base of the north and east slopes of the Bowers Ridge suggests that the unit formed in a Cenozoic arc-trench system that faced northeast (Nokleberg et al., 2000). We do not see any other slab that could represent the Bowers Ridge subduction other than the Bering Sea slab. Recently Wanke et al. (2012) dated volcanic rocks of the Bowers Ridge at Oligocene-Miocene (32.3 ± 2 to 22.7 ± 2.7 Ma), which we adopt as the age range of the subduction of the Bering Sea slab. The size of the Bering Sea slab however seems to be bigger than the Bowers basin, which may suggest that the close vicinity of other slabs may lead to blurring of the tomographic image increasing its apparent size.

3.16. Bitlis - Bi

The Bitlis anomaly (Fig. 20) is a detached and is located below southeast Anatolia in the upper mantle and uppermost lower mantle. It was identified by Zor (2008), as the western Lh1 anomaly, which forms in his model a narrow band just south of the modern Bitlis suture. Other tomographic models published in Faccenna et al. (2006), Hafkenscheid et al. (2006), Lei and Zhao (2007), Biryol et al. (2011), and Skolbeltsyn et al. (2014), or the UUP07 model (Fig. 21) do not show such detail, but consistently show an anomaly lying on the 660 km discontinuity, interpreted by these authors as detached lithosphere (Bitlis slab). Our model, as well as Hafkenscheid et al. (2006), suggests that the Bitlis slab penetrates the 660 km discontinuity. We interpret the Bitlis slab depth between 440 and 920 km depth. Break-off of the Bitlis slab is widely interpreted to have occurred at 13–10 Ma ago, which corresponds to the end of deep-marine sediment deposition in the suture zone, a rapid phase of erosional denudation of the Bitlis massif, and a volcanic flare-up in eastern Anatolia (Keskin, 2003; Sengör et al., 2003; Faccenna et al., 2006; Hüsing et al., 2009; Okay et al., 2010). The onset of subduction of the Bitlis slab is more difficult to assess. In late Cretaceous time, ophiolites were obducted onto northwestern Anatolia in southeastern Turkey, Syria, and further west in Cyprus and southern Anatolia. These ophiolites formed since ~95 Ma as reflected by crustal crystallization ages and cooling ages of metamorphic soles, and uppermost Cretaceous, ~70–65 Ma sediments unconformably cover the obduction thrust (Al-Riyami et al., 2002; Kaymakci et al., 2010; Karaoğlan et al., 2012, 2014). We interpreted this obduction to reflect the end of subduction of the western part of the Arabia slabs (Section 3.10) with a top at ~1100 ± 100 km, to the south of the Bitlis slab. Moix et al. (2008) and Maffione et al. (2017) suggested that obduction of these ophiolites followed upon westward radial roll-back of an east-dipping subduction zone into the eastern Mediterranean region, which would have been accompanied by the opening of a back-arc until ophiolite obduction. The Bitlis slab probably represents lithosphere of this back-arc, with subduction starting at or after ~70–65 Ma, which we adopt for the age of the base of the Bitlis slab.

3.17. Bitterroot - Btr

The Bitterroot anomaly (Fig. 21) is detached and located in the upper mantle below western North America, and is hook-shaped at a depth of ~200 km. In tomographic studies it has been imaged to depths of 230–600 km (Schmandt and Humphreys, 2011). Its distal position relative to the trench has recently been interpreted as the result of flat-slab subduction, which may be correlated to the geological record that shows the accretion of the Siletzia micro-continent to North America starting at ~60 Ma (Schmandt and Humphreys, 2011). Following this accretion, regular subduction at the Cascadia subduction zone (see Juan de Fuca slab, Section 3.45) led to arc volcanism in Oregon and Washington beginning ca. 45–40 Ma (Schmandt and Humphreys, 2011; Wells and McCaffrey, 2013). The volcanic arc associated with the Bitterroot subduction we interpret to be the Challis-Absaroka arc, extending nearly 1000 km into the present-day Laurentian continental interior and located above the Bitteroot anomaly. The age of this arc is ~55–45 Ma (Humphreys, 2009). Recently the volcanics were dated by U-Pb geochronology by (Gaschnig et al., 2017) and we interpret the Bitterroot peraluminios suite (66–53 Ma) and Challis intrusives (~50–46 Ma) to have resulted from subduction of the slab. We therefore adopt 66 Ma as start of subduction and 46 Ma as end of subduction leading to the formation of the Bitterroot slab.

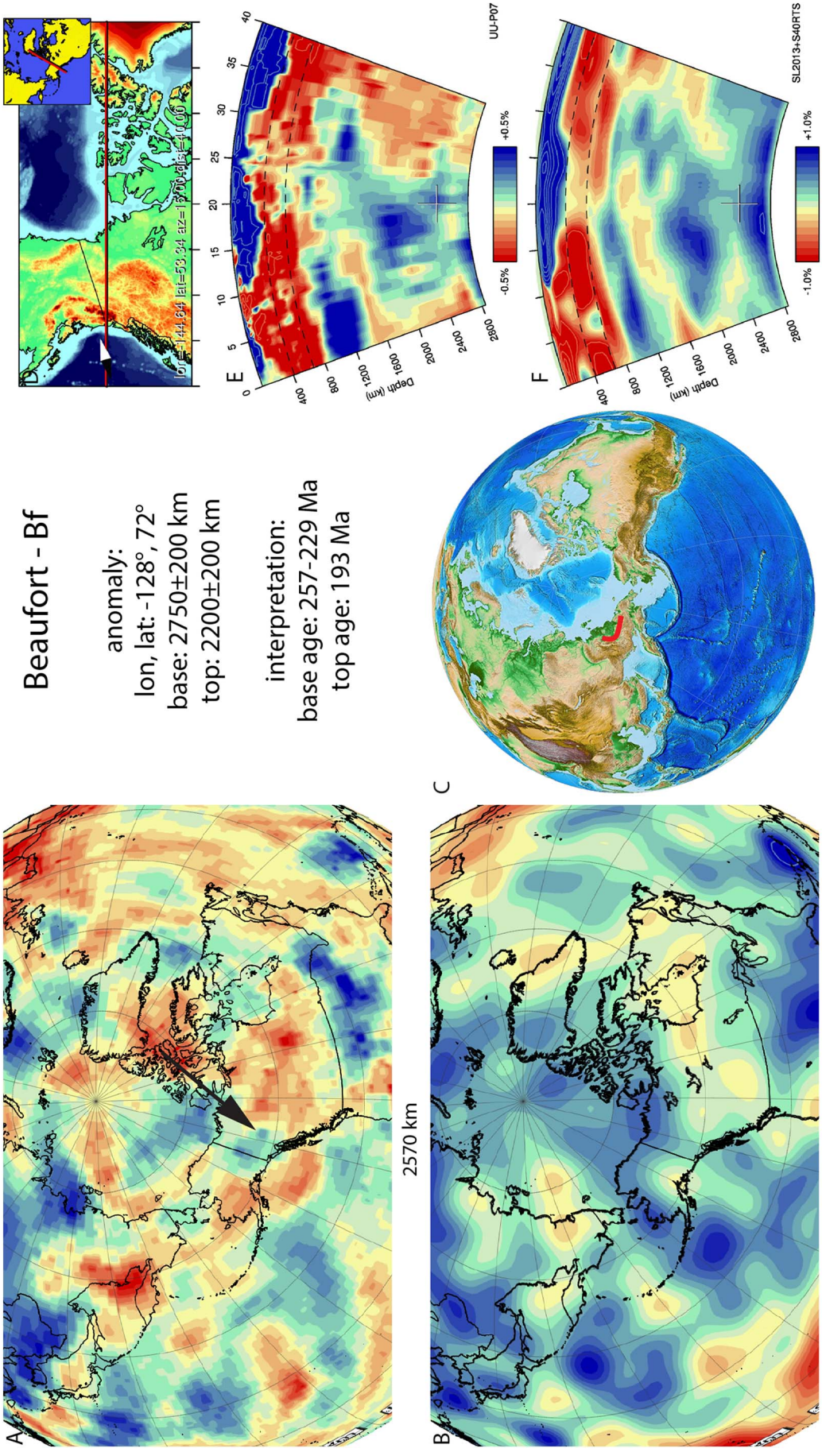

Fig. 18. Beaufort anomaly. Legend same as Fig. 5. Positive anomalies are identified in the same location in both tomographic models with a similar Relative amplitude strength, however vertical and lateral extent differ.

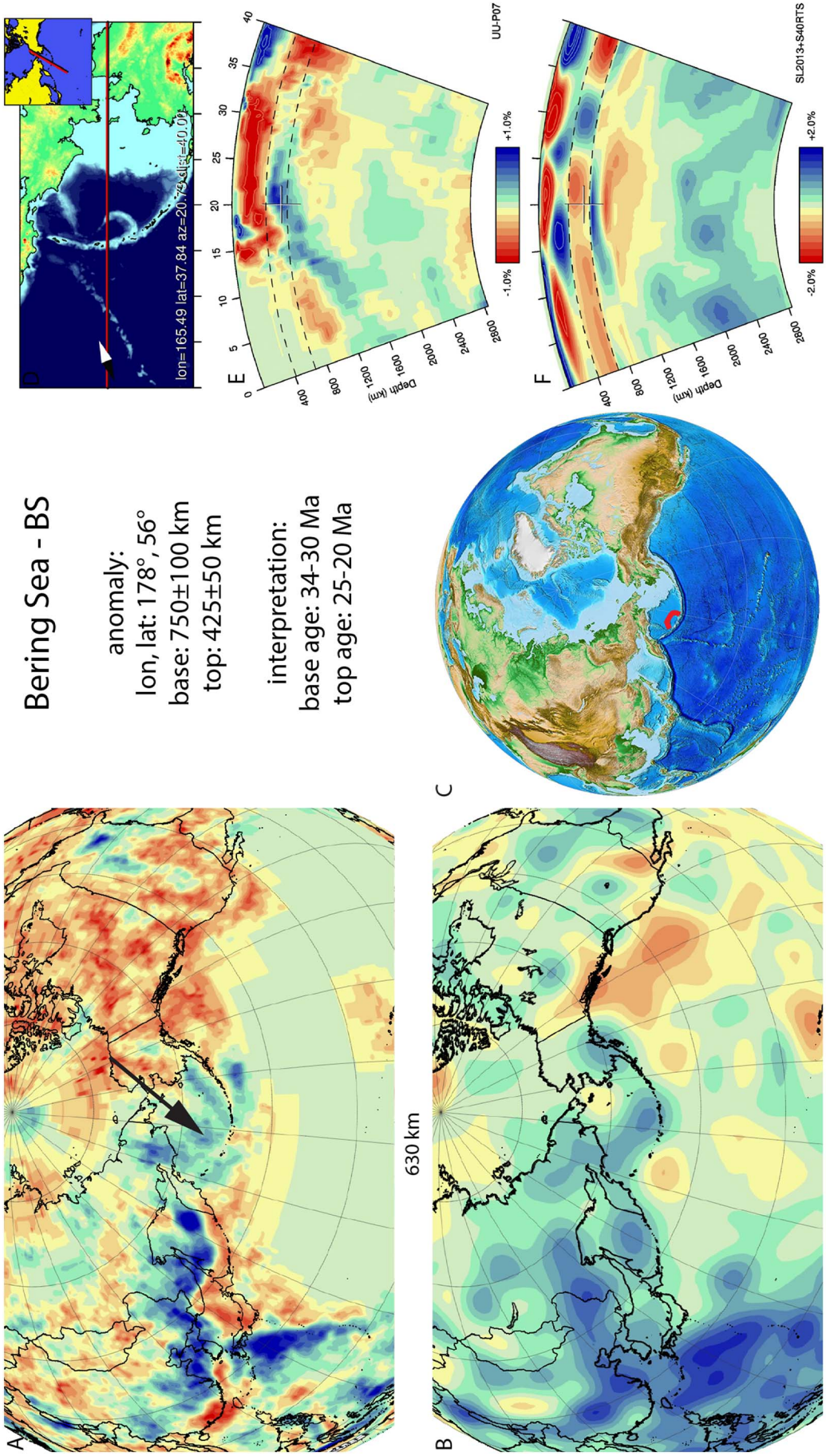

Fig. 19. Bering Sea anomaly. Legend same as Fig. 5. This slab is well imaged in the UU-P07 model, and lateral extent is very similar with the S-wave model. Vertical extent is different between models.

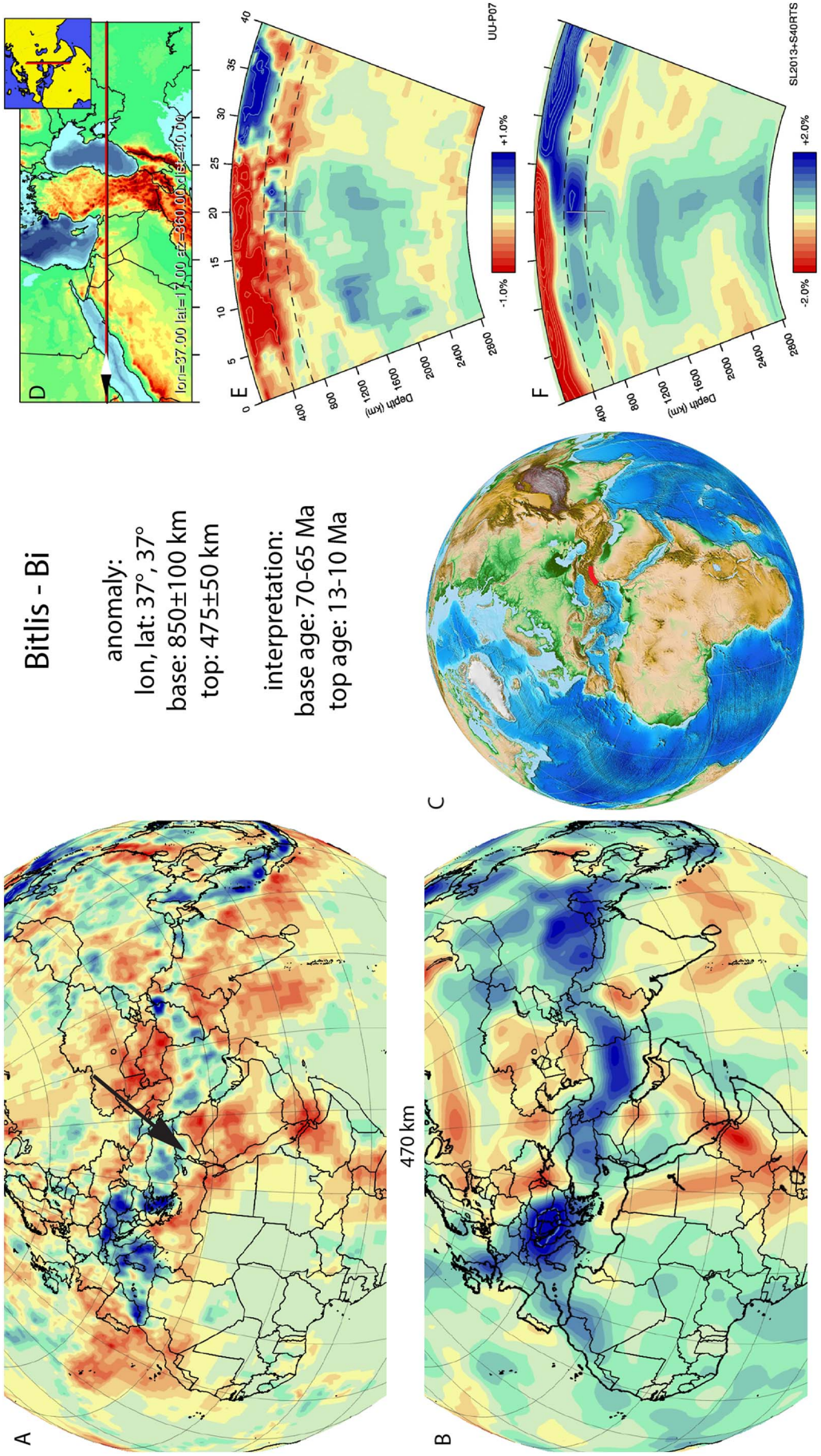

Fig. 20. Bitlis anomaly. Legend same as Fig. 5. Positive anomalies are identified in the same location in both tomographic models with a similar Relative amplitude strength, however vertical and lateral extent differ.

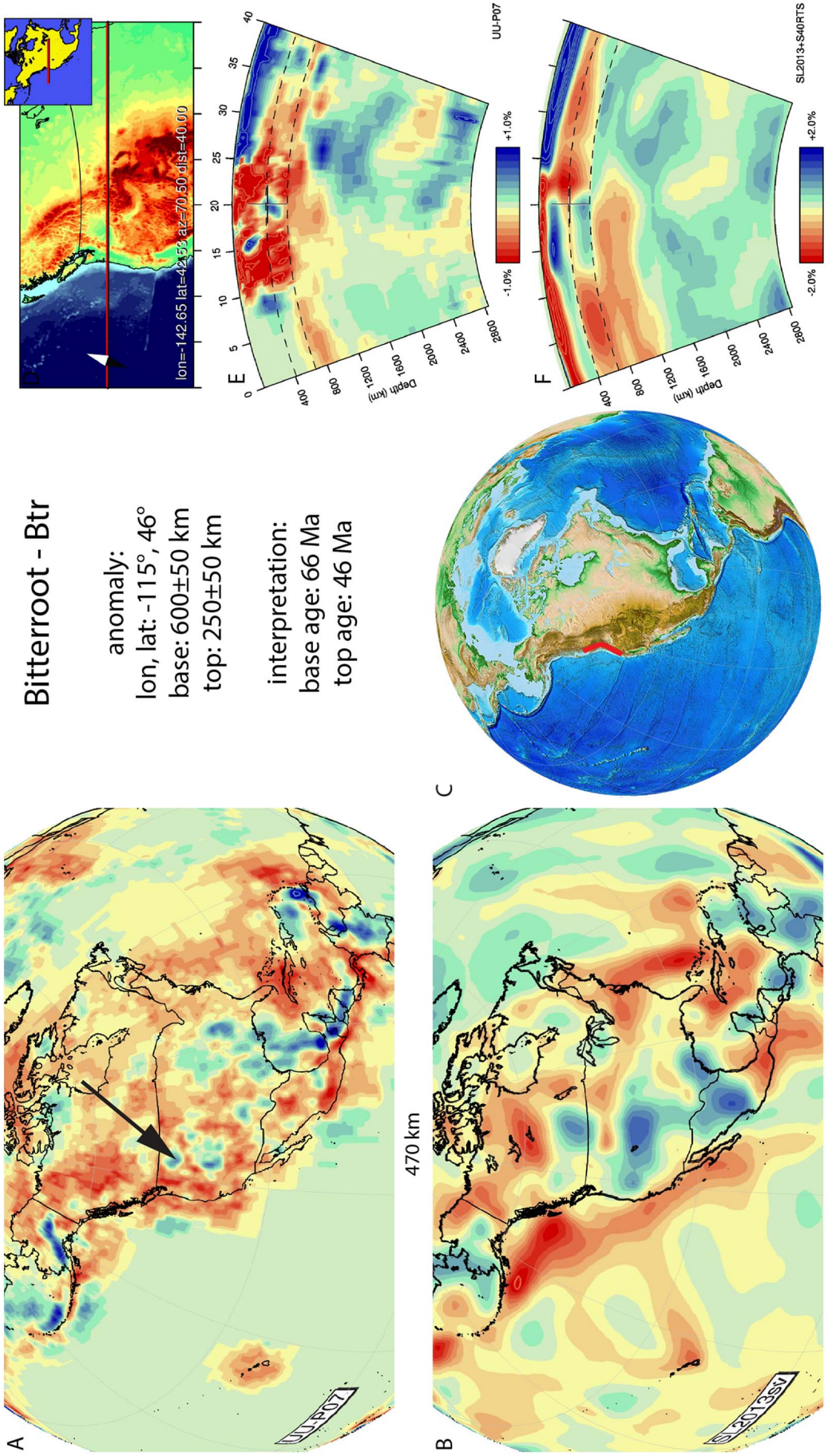

Fig. 21. Bitterroot anomaly. Legend same as Fig. 5. Positive anomalies are identified in similar location in both tomographic models with a similar Relative amplitude strength, however vertical and lateral extent differ.

3.18. Brasilia - Br

The Brasilia anomaly (Fig. 22) is located below central South America from the deep lower mantle to the Andean trench. It is N–S to NW–SE trending. Above 1175 km it connects to shallower slabs, including the Venezuela slab (Section 3.90) and the Malpelo slab (Section 3.53) to the north. We interpret the anomaly as a slab that resulted from Mesozoic-Present Farallon-Nazca lithosphere subduction at the South American continental margin. The start of arc magmatism in Peru has been recently documented to have ages ranging from ~200 Ma (Demouy et al., 2012), 180–145 Ma (Villagomez et al., 2011) to 173 Ma (Boekhout et al., 2012), which we take as the minimum age range for the start of subduction. These studies find a gap in magmatism between 145 and 110 Ma (Villagomez et al., 2011; Boekhout et al., 2012; Demouy et al., 2012), followed by volcanism into the Cenozoic (Demouy et al., 2012; Jones et al., 2014). In the tomographic model UUP07 there is not a noticeable gap visible in the slab, however the anomaly considerably weakens at 2100 km. In S40RTS, the anomaly appears to have a slab window at some locations at 2200 km, but the anomaly appears to be otherwise contiguous in the south. We do not find evidence from the tomographic models to spatially separate a deeper Jurassic slab from a Cretaceous-Cenozoic slab and therefore treat the Brasilia slab as one single slab that subducted since at least 200–173 Ma. The SL2013 model does show a significant positive anomaly on top of the transition zone, up to 2000 km east of the trench (Fig. 22F). Another flat-lyuing anomaly in the transition zone and shallow lower mantle is visible in the tomographic model of Li et al. (2008) and modelled by Faccenna et al., 2017. In their interpretation it has from subduction possibly as old as 100 Ma. These shallower anomalies are not expressed in the UU-P07 model and we therefore suggest that the tomographic imaging of these anomalies and subduction evolution at depth require further investigation.

3.19. Burma - Bur

A N–S striking, steeply east-dipping anomaly has been described below the West Burma block (Fig. 23) by Huang and Zhao (2006), Li et al. (2008), Zhao and Ohtani (2009), Pesicek et al. (2010), Replumaz et al. (2010a), and Koulakov (2011). This was interpreted as a slab that is disconnected in the upper few hundred kilometres of the mantle from the Sunda slab below Sumatra (Section 3.85) through a slab window below the Andaman Islands. The deepest parts of the Burma slab reach ~710 km depth (Fig. 24). The eastward dip of the Burma slab led Li et al. (2008) to interpret the Burma slab as Indian plate lithosphere that subducted below the Burma block. The Burma block in Neogene time has acted as a forearc sliver that moved northward relative to the adjacent Indochina block, bounded in the west by a fold-thrust system (along which the Burma slab subducted), and in the east by a transform fault zone (Morley, 2002; Bertrand and Rangin, 2003; Maurin and Rangin, 2009). The West Burma block contains Paleozoic and older metasediments which tectonically overlies an ophiolite with upper Cretaceous oceanic crust that in turn was obducted onto India (Acharya and Mitra, 1986). The ophiolite overlies a foreland basin with Cretaceous to Upper Eocene to Lower Oligocene clastic sediments, and is unconformably covered by shallow marine to fluvial Upper Eocene sediments (Ghose et al., 2010), constraining the final obduction onto India to the Late Eocene-Early Oligocene, ~35 ± 5 Ma. By that time, northeastern India was in a position adjacent to, and underwent highly oblique convergence with the West Burma block. A kinematic restoration of the oblique Burma subduction zone of van Hinsbergen et al. (2011a) suggests that ~600–700 km of E–W convergence occurred between India and the Burma Block since ~30–40 Ma, alongside ~1100 km of northward motion of the Burma block relative to Indochina. This 600–700 km corresponds to the length of the Burma slab and we consequently interpret the base of this slab to have started subduction around 35 ± 5 Ma.

3.20. Calabria - Cl

The Calabria slab (Fig. 24) was first documented by Spakman (1986a) and Spakman et al. (1993), and has since been a prominent feature in tomographic models (e.g. Piromallo and Morelli, 1997, 2003; Spakman and Wortel, 2004; Chang et al., 2010). The Calabria slab is lying flat at the base of the upper mantle and that has not penetrated the lower mantle yet. It is still subducting along the Calabrian subduction zone. Estimates for the onset of northward subduction in the western Mediterranean vary from ~80 to 35 Ma (Rosenbaum et al., 2002b; Faccenna et al., 2004). A recent kinematic reconstruction of the western Mediterranean region of van Hinsbergen et al. (2014) showed that Africa-Iberia convergence, as estimated from the Atlantic ocean spreading reconstructions and corrected for intra-Iberian and intra-African shortening, started around 85 Ma, and was very slow until 45 Ma (< 100 km), after which subduction accelerated. This led to inception of arc volcanism in Sardinia and in the Provence around 38 Ma (Lustrino et al., 2009), and was followed by the inception of roll-back and back-arc extension around 30 Ma (Faccenna et al., 2001, 2004; Rosenbaum et al., 2002b; Rosenbaum and Lister, 2004; van Hinsbergen et al., 2014). Because it is uncertain when the slow convergence culminated in the inception of Calabrian subduction, we adopt a wide time range for the base of the Calabrian slab of 65 ± 20 Ma.

3.21. Caribbean - Ca

The Caribbean anomaly (Fig. 25) is located in the upper mantle below the eastern Caribbean Sea rising to the surface at the Lesser Antilles subduction zone where Central Atlantic oceanic lithosphere subducts westward. The anomaly is interpreted as a slab dipping steeply westwards from the surface to a depth of 600 km, changing to a subhorizontal position below this depth (van der Hilst and Spakman, 1989; van Benthem et al., 2013). The base of the slab is at least 45 Ma old, as shown by the ages of onset of the Lesser Antilles arc (Burke, 1988), and the Paleocene Grenada and Tobago basins may have formed shortly after initiation of subduction along the Lesser Antilles subduction zone (Boschman et al., 2014). The Lesser Antilles subduction zone likely formed by inversion of a STEP fault that accommodated the northward retreat of the Hispaniola slab (Section 3.41) after that slab decoupled from the Venezuela slab (Section 3.90) (see also van Benthem et al., 2013). This may explain why the Caribbean slab is not physically connected – at least in its central portion – to these two deeper slabs (Boschman et al., 2014). Based on the reconstruction of Boschman et al. (2014) and the onset age of the Lesser Antilles arc, we adopt a 50 ± 5 Ma age for the base of the slab.

3.22. Carlsberg - Cr

The Carlsberg anomaly (Fig. 26) is detached and NNE-SSW trending below the northwestern Indian Ocean and was identified by Gaina et al. (2015) in the top of the lower mantle between 800 and 1400 km depth. The location and depth of the top suggest that the slab should be correlated to a geological record of past subduction in Late Mesozoic or Early Cenozoic time to the southwest of the Himalaya. Gaina et al. (2015) interpreted the anomaly as the Carlsberg slab that subducted as a result of highly oblique subduction of Indian lithosphere below oceanic lithosphere of the African (Arabian) plate in the Late Cretaceous to Paleocene. Initiation and arrest of its subduction is reflected in the geological record by formation and obduction of the Bela and Muslim Bagh ophiolites in Pakistan and the Kabul-Altimur ophiolites on the Kabul block in Afghanistan (Gnos et al., 1997; Gaina et al., 2015). The oldest radiometric age of supra-subduction ophiolites in western Pakistan that were interpreted to have formed above this subduction zone is an 80.2 ± 1.5 Ma U/Pb age from a plagiogranite dyke (Kakar et al., 2012), whereas metamorphic soles below these ophiolites have 65–70 Ma ages (Mahmood et al., 1995; Gnos et al., 1998). We follow

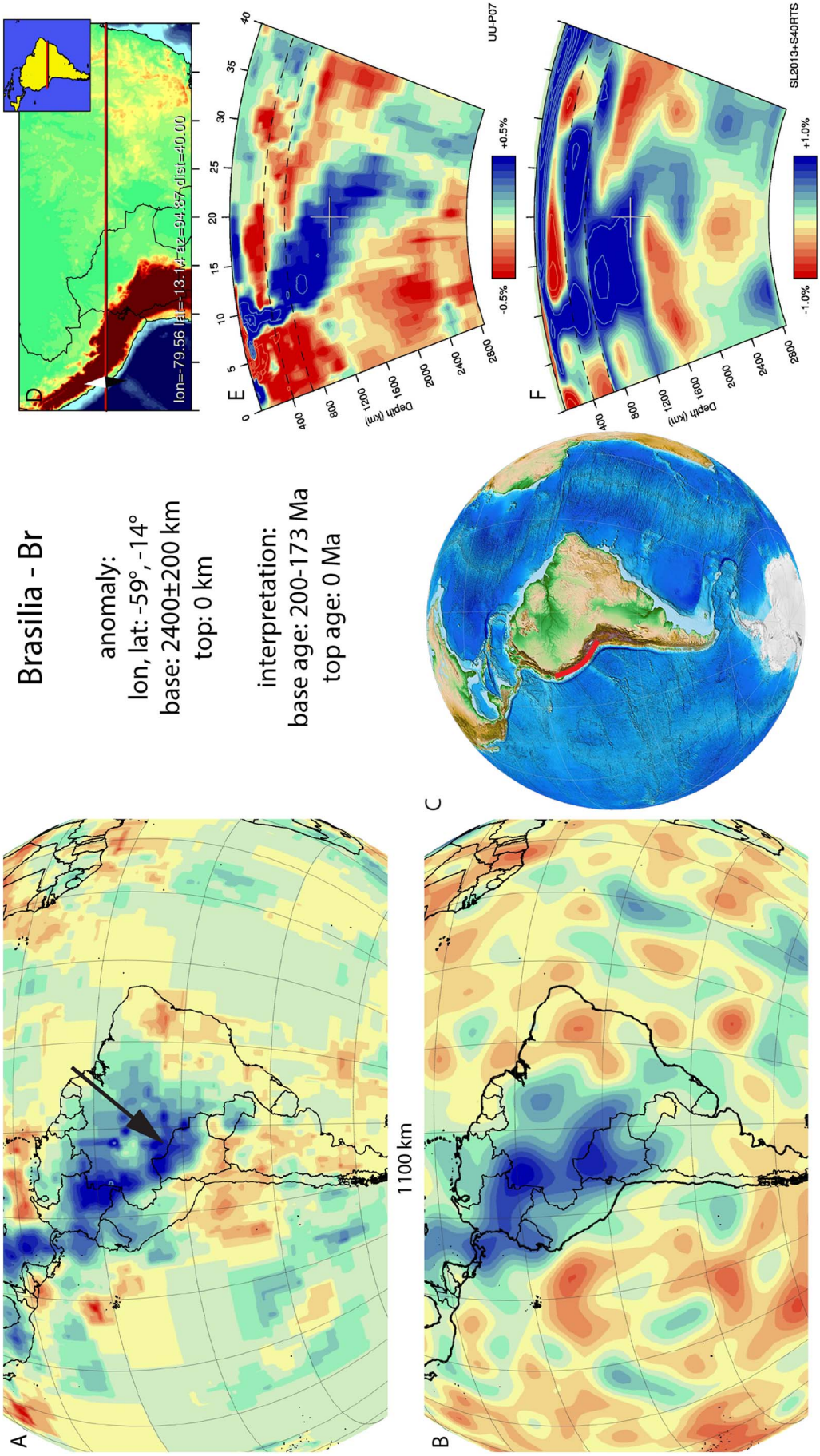

Fig. 22. Brasilia anomaly. Legend same as Fig. 5. Relative amplitude strength, vertical, lateral extent and dip trend are very similar between tomographic models.

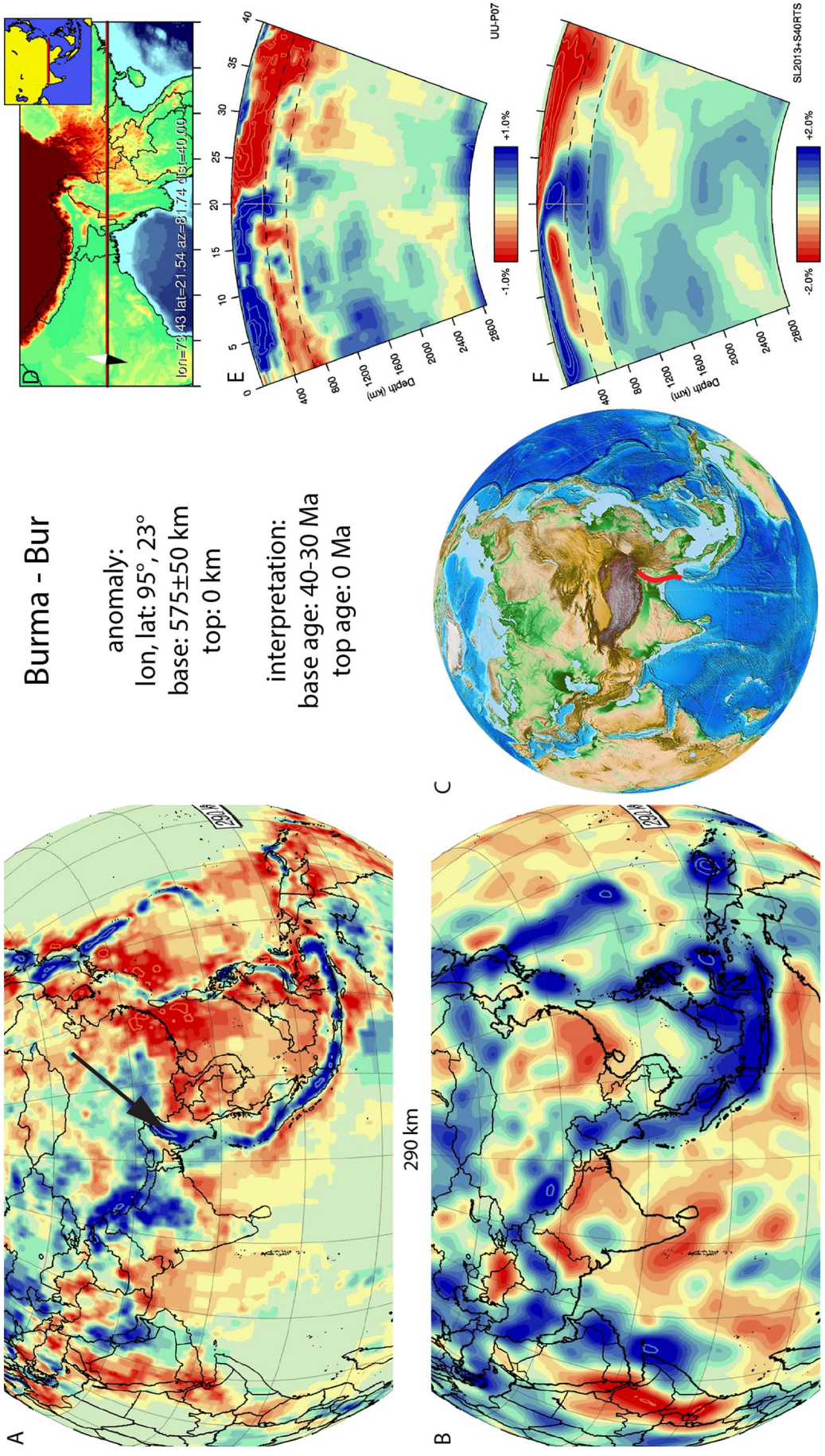

Fig. 23. Burma anomaly. Legend same as Fig. 5. Relative amplitude strength and dip trend are similar between tomographic models. Vertical and lateral extent differ.

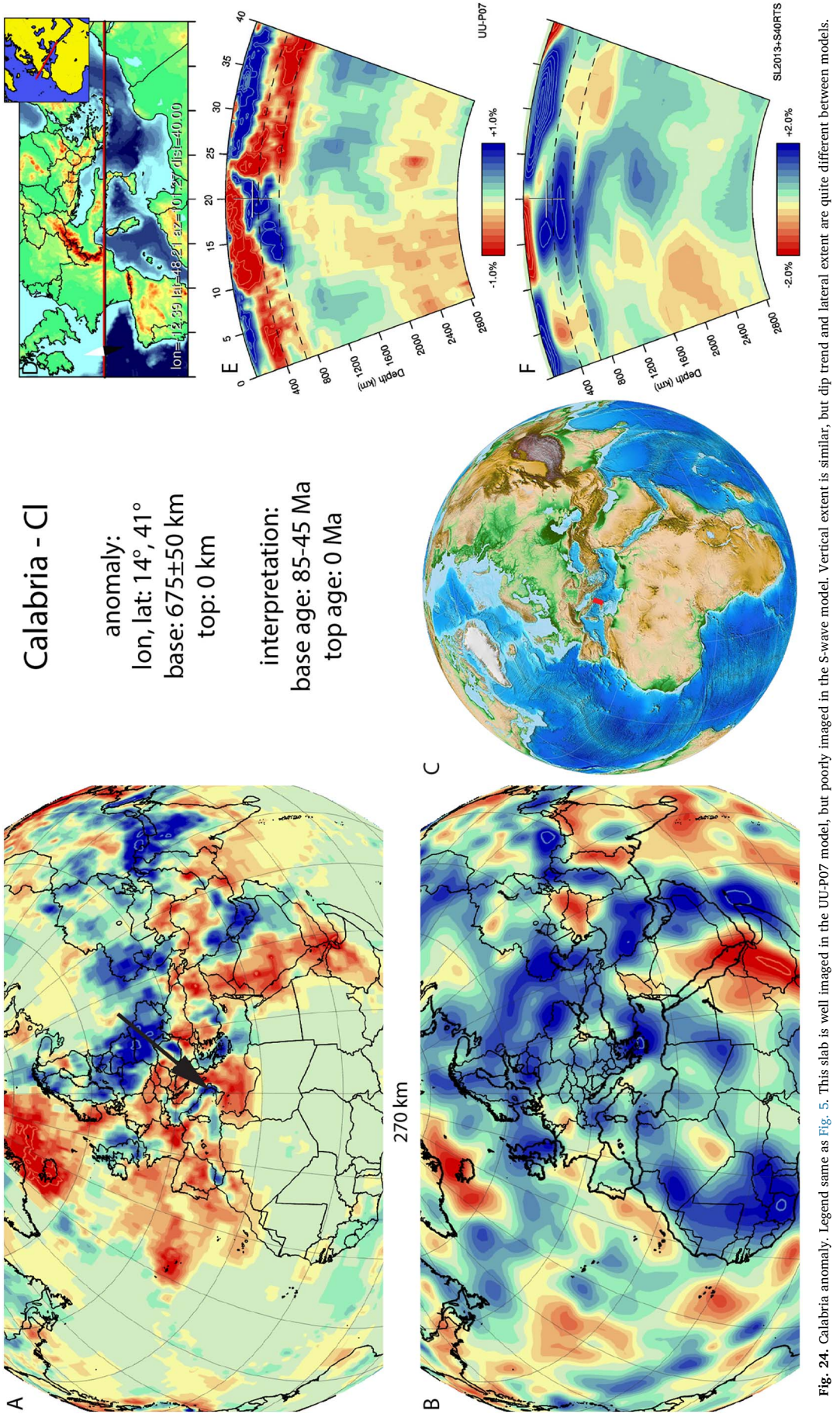

Fig. 24. Calabria anomaly. Legend same as Fig. 5. This slab is well imaged in the UU-P07 model, but poorly imaged in the S-wave model. Vertical extent is similar, but dip trend and lateral extent are quite different between models.

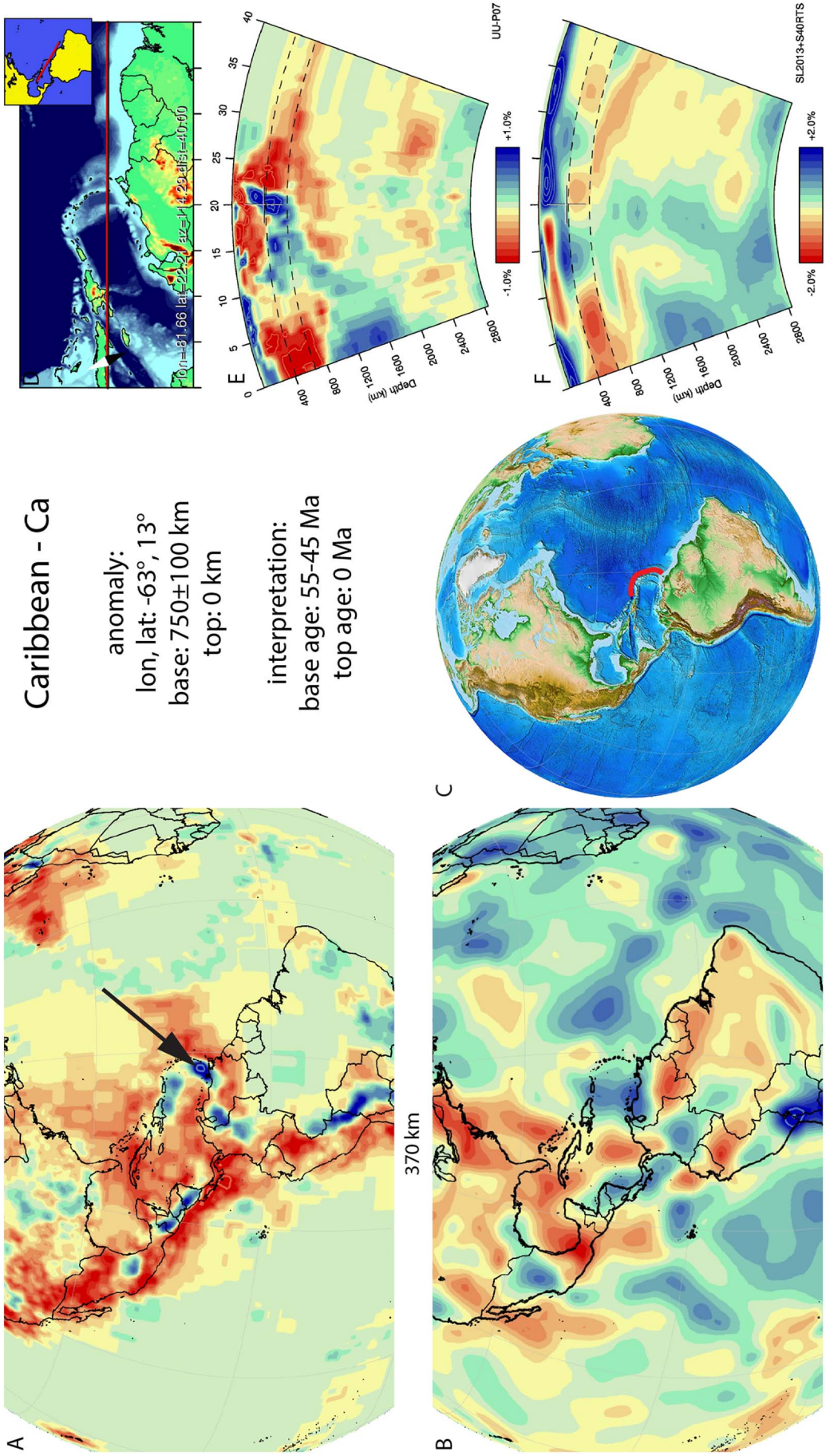

Fig. 25. Caribbean anomaly. Legend same as Fig. 5. This slab is well imaged in the UU-P07 model, but poorly imaged in the S-wave model. Dip trend, lateral and vertical extent are quite different between models.

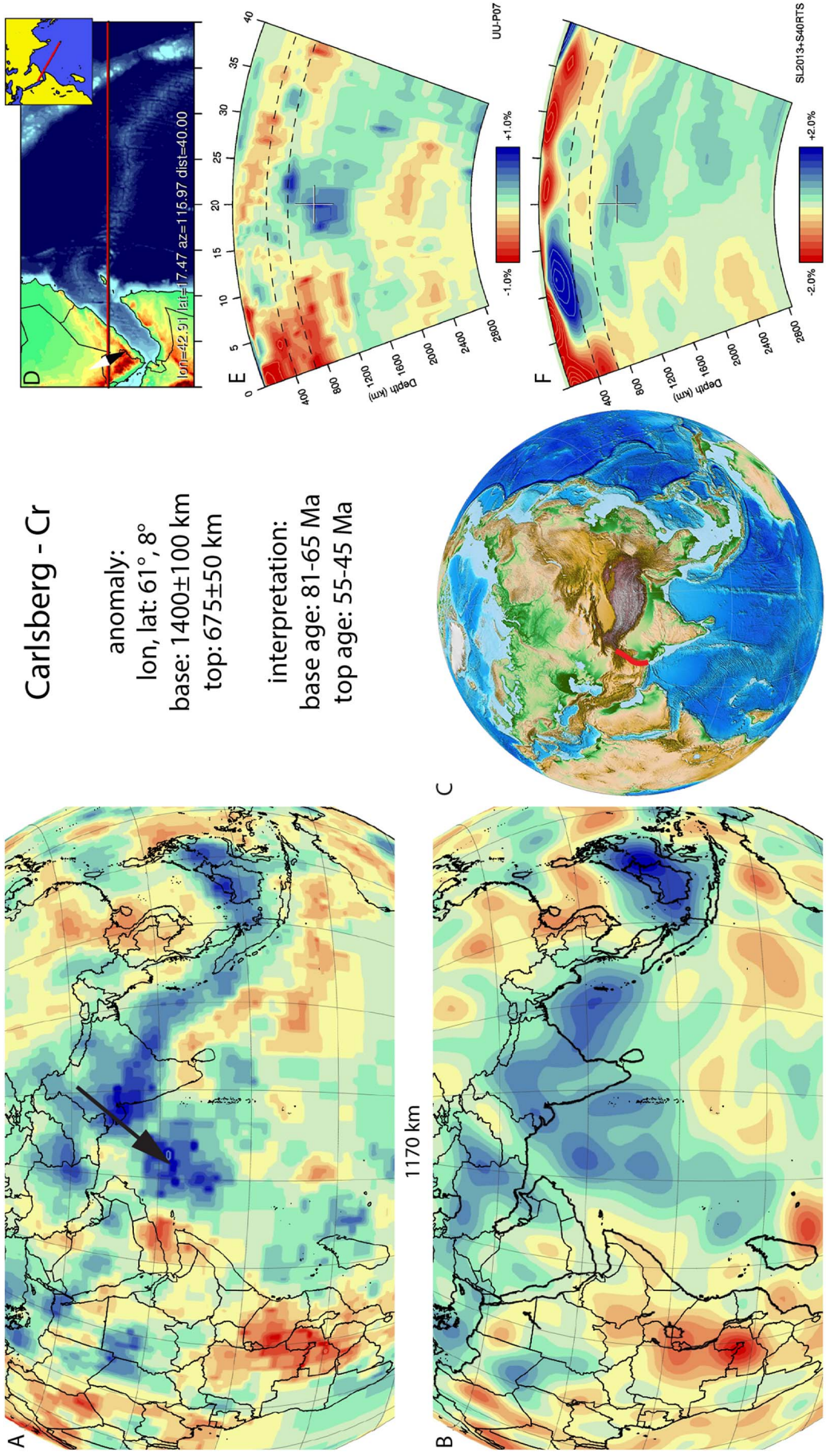

Fig. 26. Carlsberg anomaly. Legend same as Fig. 5. Vertical, lateral extent and dip trend are very similar between tomographic models. Relative amplitude strength is weaker in the S-wave model.

the interpretation of the Carlsberg slab of Gaina et al. (2015) and adopt a 73 ± 8 Ma age range for the subduction of its base. The end of subduction is reflected by Eocene foreland basin deposits on the Indian and Arabian margin and overlap assemblages sealing the obduction thrust of ~55–45 Ma (Gnos et al., 1997; Khan and Clyde, 2013; Gaina et al., 2015).

3.23. Caroline ridge - CR

The Caroline Ridge anomaly (Fig. 27) was identified by Hall and Spakman (2002, 2004) and is draped on the 660 km discontinuity below the Caroline Ridge, north of Papua New Guinea. It lies south of the Mariana slab (Section 3.57), but according to the reconstruction of Hall (2002) is not directly related to it. (Hall, 2002) reconstructed an intra-oceanic subduction zone that accommodated Pacific plate subduction at the location of the Caroline Ridge anomaly initiating at ~25 Ma along a transform fault that accommodated clockwise rotation of an intra-oceanic subduction zone that rolled back southward towards Papua New Guinea, opening the Caroline Sea plate lithosphere in its back-arc position. This subduction zone came to an arrest at ~5 Ma according to Hall (2002). Wu et al. (2016) named this anomaly the New Guinea Offshore slab and suggested an age range of 25–10 Ma. We use the largest age range of these interpretations and adopt 25 and 5 Ma as the ages for onset and end of subduction of the Caroline Sea plate forming the Caroline Ridge slab.

3.24. Carpathians - Cp

The Carpathian anomaly (Fig. 28) is found draped on the 660 km discontinuity below the Carpathian oroclinal fold-thrust belt and its back-arc region, the Pannonian basin. It has been long known and is imaged in numerous tomographic models (Spakman, 1991; Spakman et al., 1993; Bijwaard et al., 1998; Wortel and Spakman, 2000; Piromallo and Morelli, 2003; Ren et al., 2012; Zhu et al., 2012). Apart from the southeastern corner of the Carpathian orocline – the Vrancea area, where a slab and associated Benioff zone are still imaged to be connected to the European lithosphere – the Carpathian anomaly is disconnected from the surface.

The anomaly is interpreted as the Carpathian slab that resulted from westward subduction of Eurasian lithosphere below several terranes (Tisza-Datca and AlCaPa blocks) that became separated from Eurasia during Jurassic opening of the Piemonte-Ligurian Ocean (Schmid et al., 2008; Vissers et al., 2013) and that were deformed in a Cretaceous orogenesis unrelated to, and prior to the westward Carpathian subduction history (Csontos and Voros, 2004; Schmid et al., 2008). This westward subduction led to the formation of a thin-skinned fold-thrust belt – the outer Carpathians. The onset of this deformation occurred around 35 ± 5 Ma (Matenco and Bertotti, 2000; Matenco et al., 2003; Gągała et al., 2012; Handy et al., 2014), and became associated with back-arc extension since ~20 Ma, opening the Pannonian basin (Horvath et al., 2006; Matenco and Radivojević, 2012), followed by arrest of shortening and unconformable covering of the frontal thrust system around 10–12 Ma in the northeastern Carpathians (Matenco and Bertotti, 2000; Gągała et al., 2012). We adopt the 11 ± 1 Ma as the age of break-off of the Carpathian slab. Finally, we note that the northern part of Carpathians hosted by the AlCaPa terrane, north of the Periadriatic-Ballaton fault, underwent several hundreds of kilometres more subduction and extension in the Miocene than the area hosted by the Tisza-Datca terranes to the south (Ustaszewski et al., 2008). This suggests that the Carpathian anomaly is in fact composed of two slabs, separated by a transform fault, whereby the southern slab may still be connected to the surface in the Vrancea area (Fig. 30). Our tomographic image, as well as that of Ren et al. (2012) appears to show such a disconnection between the two bodies below the Ballaton line.

3.25. Carpentaria - Cn

The Carpentaria anomaly (Fig. 29) corresponds to anomaly A8 of Hall and Spakman (2002, 2004). It lies in the upper part of the lower mantle below the Gulf of Carpentaria below northern Australia and Papua New Guinea. It is located deeper in the mantle than the Arafura and Papua slabs that lie to the west and east respectively, and which likely subducted since ~45 Ma (Sections 3.70 and 3.10, respectively). This led Hall and Spakman (2002, 2004) to interpret the Carpentaria anomaly as a slab with a pre-middle Eocene age of subduction. They consequently suggested that the Carpentaria slab may represent Australian plate lithosphere that subducted westward prior to the polarity switch associated with the onset of subduction of below the Melanesian arc around 45 Ma (see also Gurnis et al., 2000). Hall and Spakman (2002, 2004) suggested a Cretaceous age for the onset of subduction. Based on plate reconstructions of the SW Pacific and southern Pacific ocean basins, Seton et al. (2012) showed that convergence between the Pacific and SW Pacific basins must have occurred since at least 83 Ma, which we adopt as the minimum age for the onset of the Carpentaria slab. Wu et al. (2016) interpreted the anomaly to be an East Asian Sea south slab, being the result of southward subduction underneath Papua New Guinea and Solomon Sea between 50 and 20 Ma. We therefore use an age range of 83–50 and 45–20 Ma for the base and top of the slabs.

3.26. Caucasus - Cau

Tomographic images and earthquake locations have shown a complex mantle structure below the Caucasus (Fig. 30). The Eastern Caucasus is underlain by a northward dipping zone of seismicity with earthquakes reaching > 150 km depth, which was interpreted to bound a 130–280 km long, northward dipping slab (Maggi and Priestley, 2005; Skolbeltsyn et al., 2014; Mumladze et al., 2015) (Fig. 33). The western Caucasus, however, does not display seismicity deeper than 50 km (Mumladze et al., 2015). Instead, seismic tomographic images show an anomaly between ~650 and 350 km depth that may represent a body of lithosphere that delaminated from the base of the western Caucasus. This was first noted in Brunet et al. (2000b), and shown for the first time in Hafkenscheid et al. (2006). Subsequently, seismic tomographic images of Zor (2008) and Koulakov et al. (2012) confirmed the location and size of this body.

The onset of shortening and uplift in the Caucasus, as a proxy for the age of subduction of the base of the Caucasus anomalies, may be estimated by a first phase of denudation in Oligocene that is detected by low-temperature thermochronology (Vincent et al., 2007, 2010; Cowgill et al., 2016), at 30 ± 5 Ma, whereby Vincent et al. (2017) showed that the older end of this age range is probably most realistic. Break-off of the anomaly below the western Caucasus may coincide with the rapid phase of uplift and crustal shortening that started around 5 Ma (Forte et al., 2010, 2014; Avdeev and Niemi, 2011). Because the slab is much narrower than the elongated E–W subduction zone that existed until at least Early Cenozoic time along the southern Pontides of Turkey (e.g., Meijers et al., 2010), we consider it unlikely that the narrow western Caucasus slab is related to this subduction zone. We have not interpreted a slab of this Pontide subduction zone, but suspect that it is located within the wide anomaly below Turkey of which the southern parts are interpreted as the Cyprus (Section 3.33), Bitlis (Section 3.17), and Antalya slabs (Section 3.9).

3.27. Central China - CC

The Central China anomaly (Fig. 31) is located in the lower mantle from the core-mantle boundary upwards to a depth of ~1500 km. It was first defined by van der Meer et al. (2010), who separated the slab from the Mongol-Kazakh slab (Section 3.67) as defined by Van der Voo et al. (1999a). van der Meer et al. (2010) interpreted the Central China slab as representing Paleotethyan lithosphere that subducted between

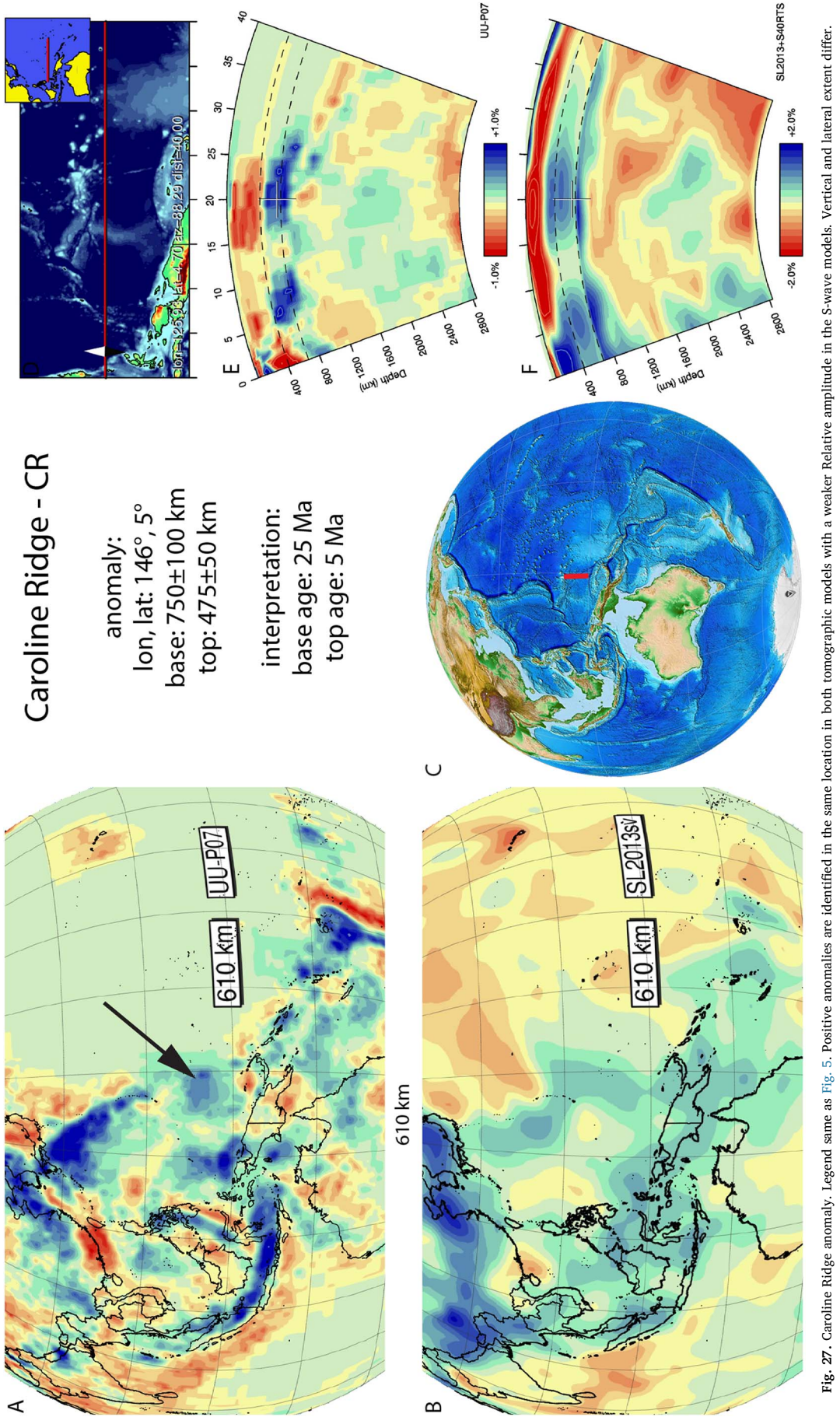

Fig. 27. Caroline Ridge anomaly. Legend same as Fig. 5. Positive anomalies are identified in the same location in both tomographic models with a weaker Relative amplitude in the S-wave models. Vertical and lateral extent differ.

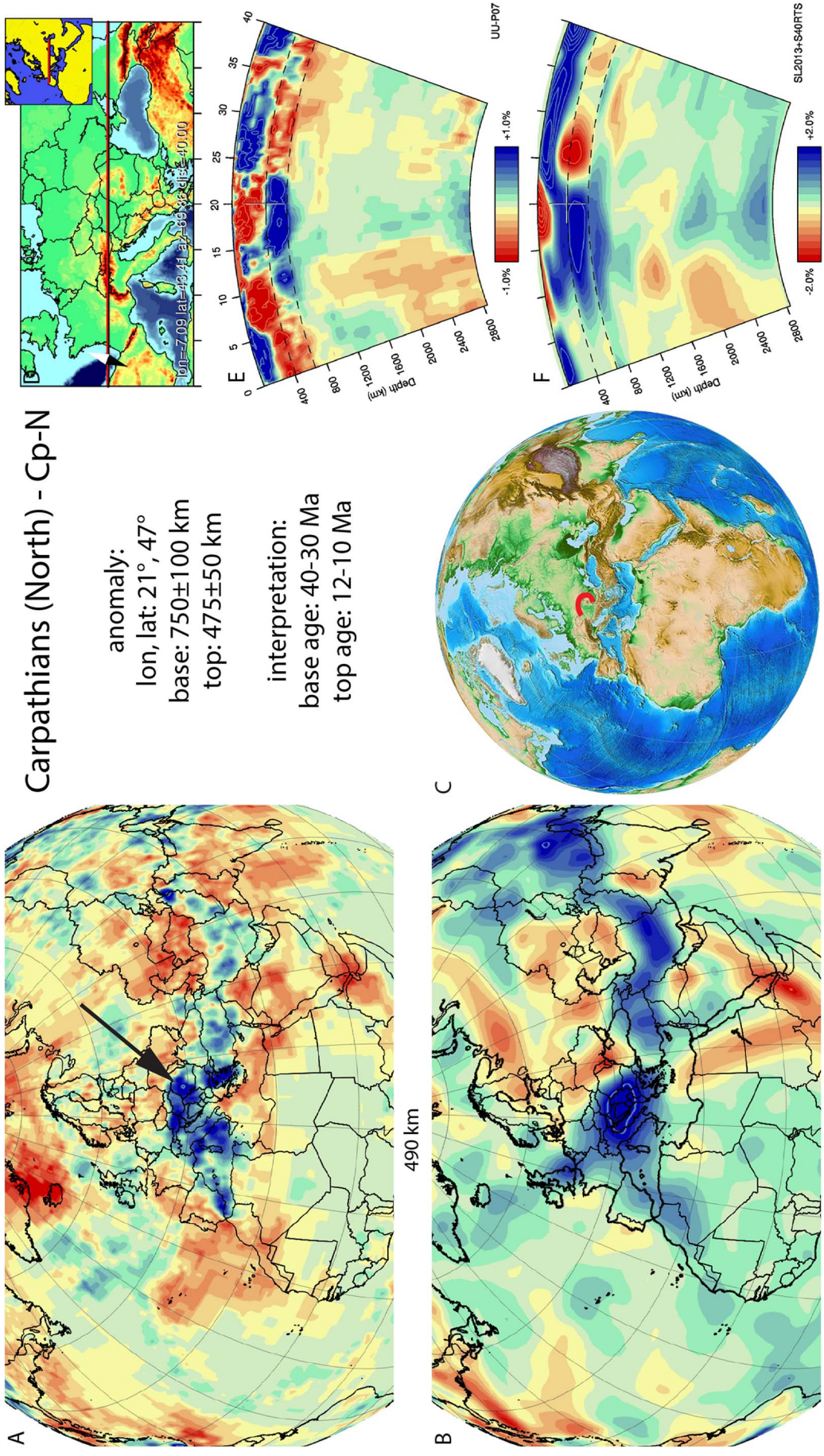

Fig. 28. Carpathian (north) anomaly. Legend same as Fig. 5. This detached part of the slab is well imaged in the UU-P07 model, but less well delineated in the S-wave model. Relative amplitude strength and lateral extent are similar between models. There is no dip trend visible, and the slab appears to flat-lying on top of the transition zone.

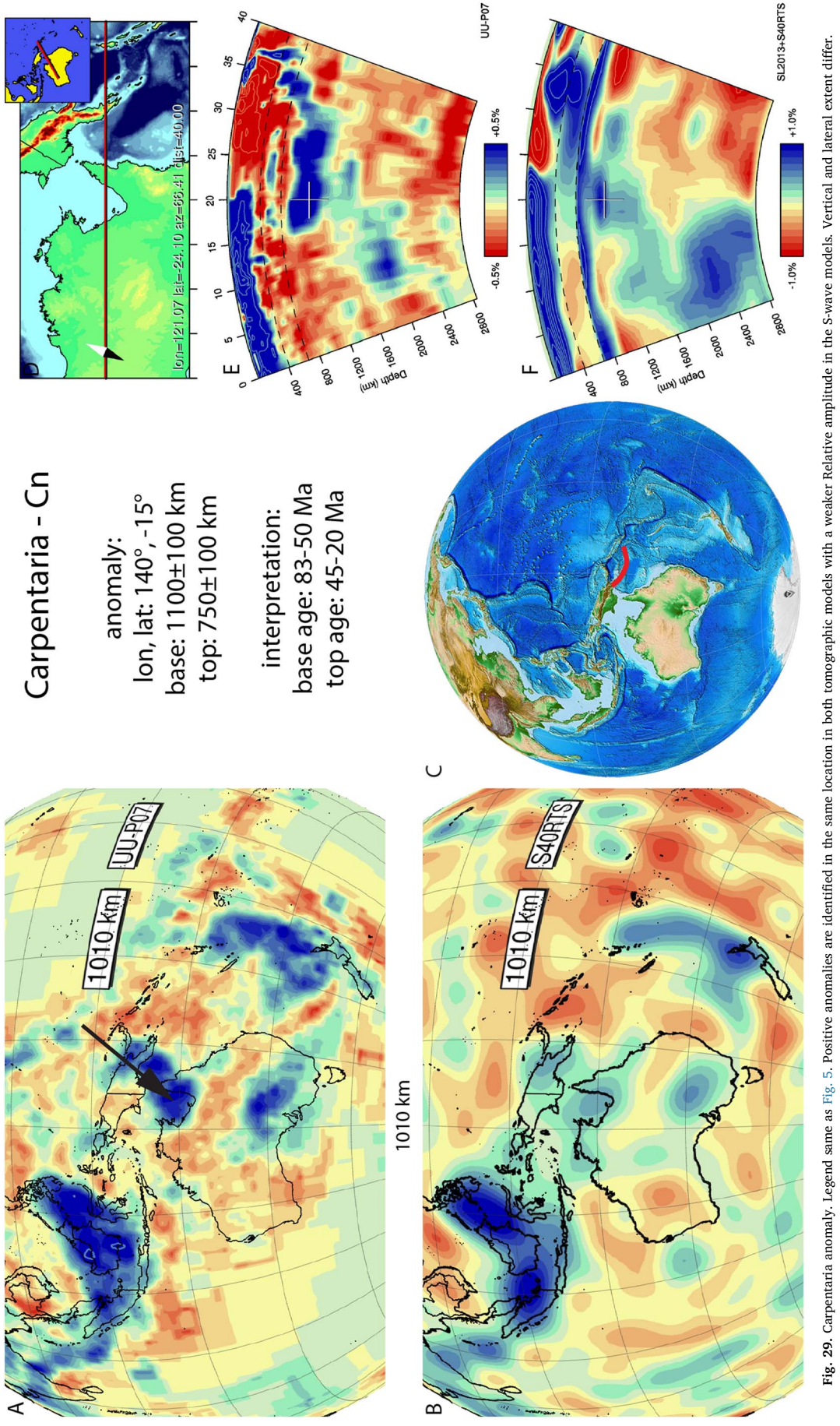

Fig. 29. Carpentaria anomaly. Legend same as Fig. 5. Positive anomalies are identified in the same location in both tomographic models with a weaker Relative amplitude in the S-wave models. Vertical and lateral extent differ.

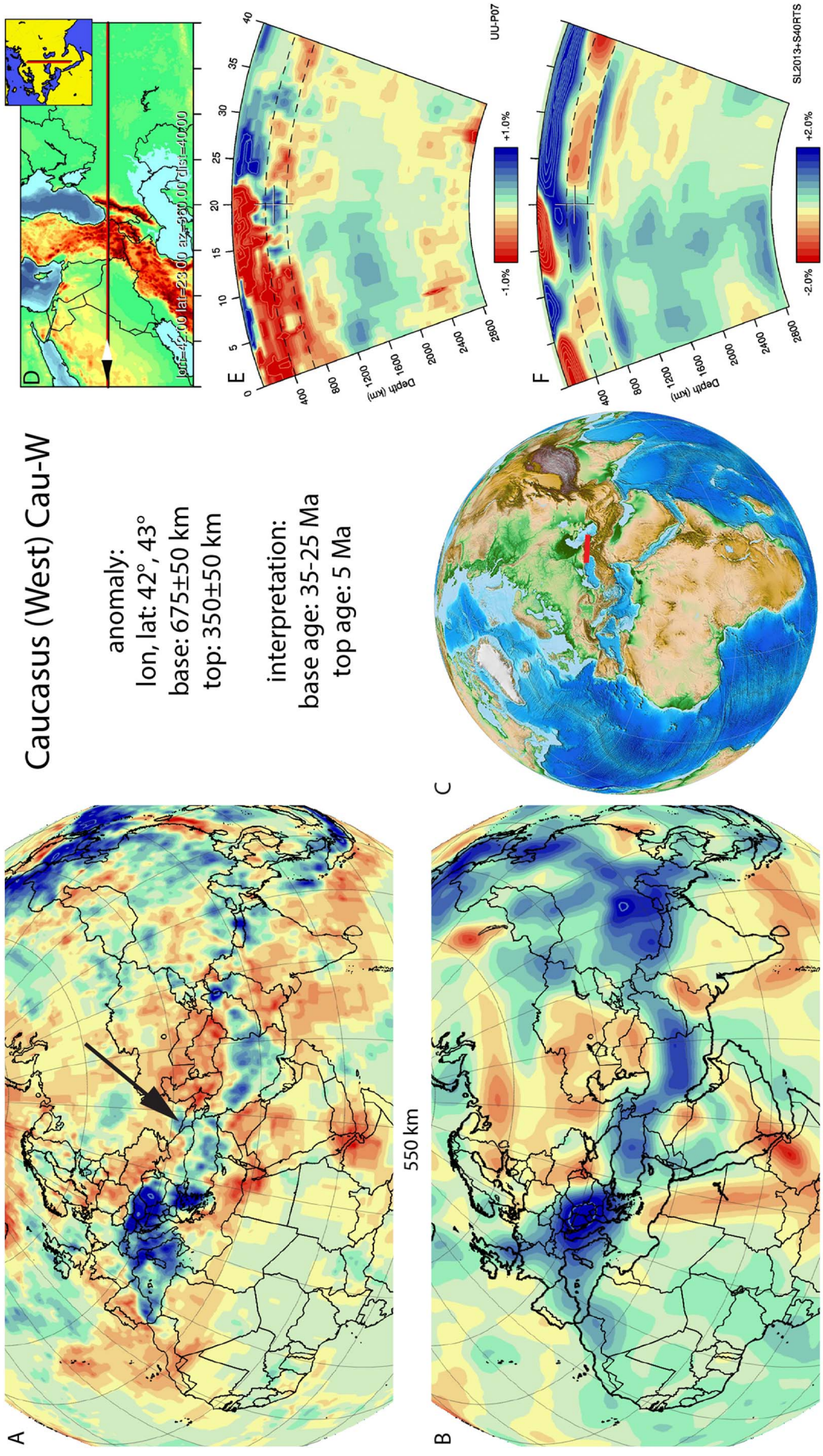

Fig. 30. Caucasus West anomaly. Legend same as Fig. 5. Relative amplitude strength, vertical and dip trend are similar between tomographic models. Lateral extent differs.

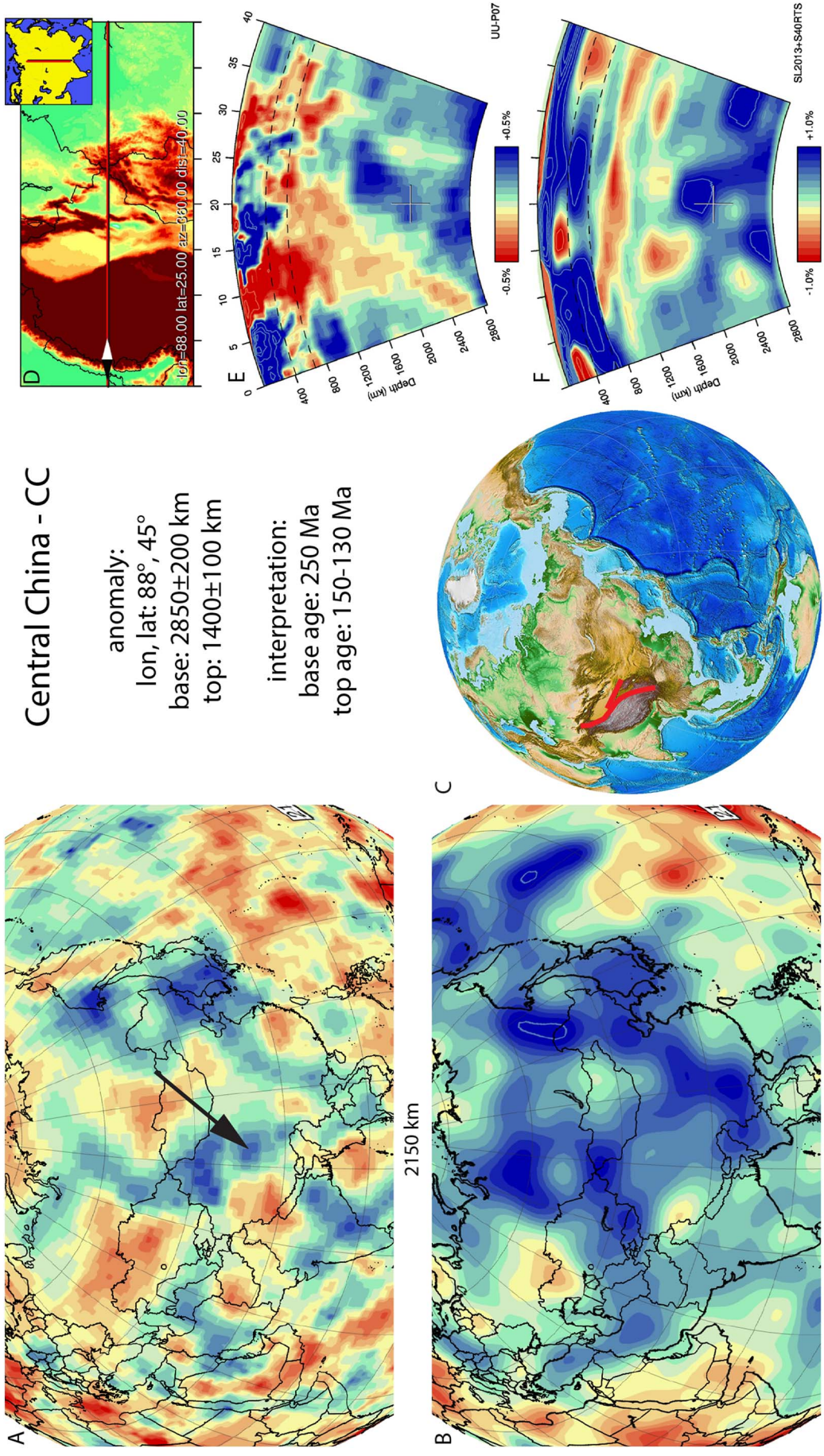

Fig. 31. Central China anomaly. Legend same as Fig. 5. Positive anomalies are identified in the same location in both tomographic models with an overall stronger Relative amplitude in the S-wave models. Vertical and lateral extent differ.

North China, northeast Tibet and Eurasia following interpretations of Stampfli and Borel (2004), assigning a Permian to Early Cretaceous age to this slab. Recently, however, Van der Voo et al. (2015) proposed that the Mongol-Okhotsk subduction zone started as a westward dipping subduction zone below Siberia in the north and Amuria in the south, whereby the northern, currently WNE–WSW trending margin of Amuria along the Mongol-Okhotsk suture was oriented N–S until Triassic time and rotated counterclockwise towards its current orientation throughout the Late Triassic and Jurassic, culminating in an orocline around the western termination of the Mongol-Okhotsk suture in western Mongolia. In that interpretation, the Central China slab subducted since at least Triassic times until the latest Jurassic below Amuria, and form the southward continuation of the Mongol-Kazakh slab. The paleomagnetic data summarized in Van der Voo et al. (2015) in addition imply that the North China block moved 1000's of km northward relative to Siberia-Kazakhstan until the latest Jurassic-earliest Cretaceous, requiring that the North China-Kazakhstan plate boundary should accommodate significant (oblique) convergence. Although the location of such a plate boundary remains enigmatic, a 'Paleotethyan' origin as implied in Stampfli and Borel (2004) is not excluded. If related to the advance of NE Tibet to Eurasia, the Central China slab subducted since at least Triassic and probably earlier time, and ended around the Jurassic-Cretaceous boundary 140 ± 10 Ma. An alternative interpretation would be that the Central China slab resulted from subduction along the Songpan Ganzi suture between the Qiangtang and Kunlun terranes. This subduction also started prior to the Triassic, and ended in Late Triassic or Early Jurassic time, ~200 Ma ago (e.g., Pullen and Kapp, 2014). In the recent reconstruction of Van der Voo et al. (2015) the reconstructed position of the Songpan-Ganzi suture would however be ~15° south of the slab and is therefore considered an unlikely candidate associated with the subduction of the slab.

3.28. Chukchi - Ch

The W-E trending Chukchi anomaly (Fig. 32) is located below North Siberia and the Chukchi Sea (Arctic Ocean) within the mid-mantle. At its base, at equivalent latitudes it is located in between the top of the Mongol-Kazakh slab (Section 3.63) towards the west and the Hudson slab (Section 3.41) towards the east. It was first identified in van der Meer et al. (2010), who interpreted it as the Chukchi slab representing paleo-Arctic lithosphere, subducted below the Upper Jurassic to Lower Cretaceous Koyukuk arc in a (near-) continental margin position. However, in the subsequent interpretation van der Meer et al. (2012), we considered it more likely that the Chukchi slab resulted from northward Panthalassa Ocean subduction. This subduction may correlate with the Kony-Murgal arc Nokleberg et al. (2000), in which the age of was poorly constrained between Triassic and Early Cretaceous. Sokolov (2010) pointed out that the Middle Jurassic of the Kony-Murgal arc is characterised by structural rearrangements and deformation coinciding in time with the onset of the formation of the system of Pacific plates controlling the present-day appearance of the Pacific Ocean. This results in the start of the Late Jurassic–Early Cretaceous Uda–Murgal arc in the region of the Chukchi slab. Noteworthy is that the slab at its eastern extent has a N–S trend both in the UUP07 and S40RTS model, suggesting a change in subduction zone orientation. This change would fit with the eastward extent of the Uda-Murgal arc into the Pekulney and Oloy arcs during the Late Jurassic -Early Cretaceous (Nokleberg et al., 2000) and subsequently modelled by Shephard et al. (2013) between 160 and 108 Ma. According to Sokolov et al. (2009), the accretionary prism (Beregovoi terrane) started forming in the Middle Jurassic, and the volcanic arc (central Taigonos terrane) ended in the Barremian-Albian. We therefore adopt a 174.1–163.5 Ma for the start of subduction and an end of 129.4–100.5 Ma for the end of subduction.

3.29. Cocos - Co

The Cocos anomaly (Fig. 33) is part of the set of anomalies commonly, and in our previous compilation in van der Meer et al. (2010), referred to as the Farallon slab, as originally defined by Grand et al. (1997) and also imaged by e.g. Bijwaard et al. (1998), Fukao and Obayashi (2013) and Sigloch and Mihalynuk (2013). The anomaly is interpreted as the Cocos slab and is NW-SE trending, and dips from the Central American trench, where it connects to the subducting Cocos plate, down to the lower mantle below the northern Caribbean region and eastern North America. Rogers et al. (2002) showed tomographic images of the Cocos slab below Central America and suggested that it may have detached in recent times at a depth of ~200–300 km, but our tomographic model UU-P07 does not reveal this gap. Recently detached or not, the Cocos slab is the longest contiguous anomaly in our database. It can be distinguished from the Hatteras slab (Section 3.37), although it may connect with this slab at mid-mantle depths, where it locally assumes a N–S strike. Above 1100 km depth the NW-SE strike reappears, all the way up towards the Central American trench.

The location of the deepest part of the anomaly corresponds to the slabs that (Sigloch and Mihalynuk, 2013) interpreted as resulting from Franciscan intra-oceanic subduction, forming their SF1 slab, which resides at shallower depth. We adopt their interpretation, and extend the SF1 slab into the deepest mantle. The Cocos slab is the only still-subducting segment of the once vast Farallon oceanic plate and is currently subducting the Cocos plate below Mexico. Correlating the Cocos slab to the Franciscan melange predicts that North America moved northward relative to the Cocos slab during its subduction, which may be tested in future studies. Although there is debate when the 'Franciscan' phase of subduction initiated, most agree that subduction was underway by 170–160 Ma, the time of formation of high temperature – high-pressure metamorphic rocks in the structurally higher levels of the Franciscan complex (Anczkiewicz et al., 2004; Wakabayashi and Dumitru, 2007; Hoisch et al., 2014; Wakabayashi, 2015), which we adopt as the minimum age of the start of subduction of the Cocos slab.

3.30. Cyprus - Cy

The Cyprus anomaly (Fig. 34) was imaged by Faccenna et al. (2006) and Biryol et al. (2011) and is interpreted as a north-dipping slab that may or may not be still attached to the African lithosphere to the south of the island of Cyprus. In the upper several hundred kilometres of the mantle, it is clearly disconnected from the Antalya slab (Section 3.8), but in the lower part of the upper mantle, the two slabs become indistinguishable (Biryol et al., 2011). We do therefore not add a separate estimate for the age of the base of the Cyprus slab, but apply the estimate for the base of the Antalya slab of 95 ± 5 Ma. The Cyprus slab consequently likely contains oceanic lithosphere of the Izmir-Ankara ocean, continental lithosphere of the Taurides, and oceanic lithosphere that subducted after the Late Cretaceous-Eocene accretion of the Taurides. This oceanic lithosphere must have connected to the Troodos ophiolite on Cyprus that emplaced in the late Cretaceous onto continental rocks exposed in the Kyrenia range following roll-back of an original East-dipping subduction zone into the SE Mediterranean region (Moix et al., 2008; Maffione et al., 2017), whereby the Cyprus (Troodos) and Syria (Baer Bassit) ophiolites underwent large counterclockwise rotations (Morris et al., 2002). The age of obduction is best constrained by Maastrichtian sediments that unconformably cover the contact of the ophiolite with its underlying melange that contains Triassic passive margin carbonates (Swarbrick and Naylor, 1980; Bailey et al., 2000). Similar to the Bitlis slab (Section 3.16), we suggest that the much of the Cyprus slab consists of this back-arc that formed during late Cretaceous roll-back.

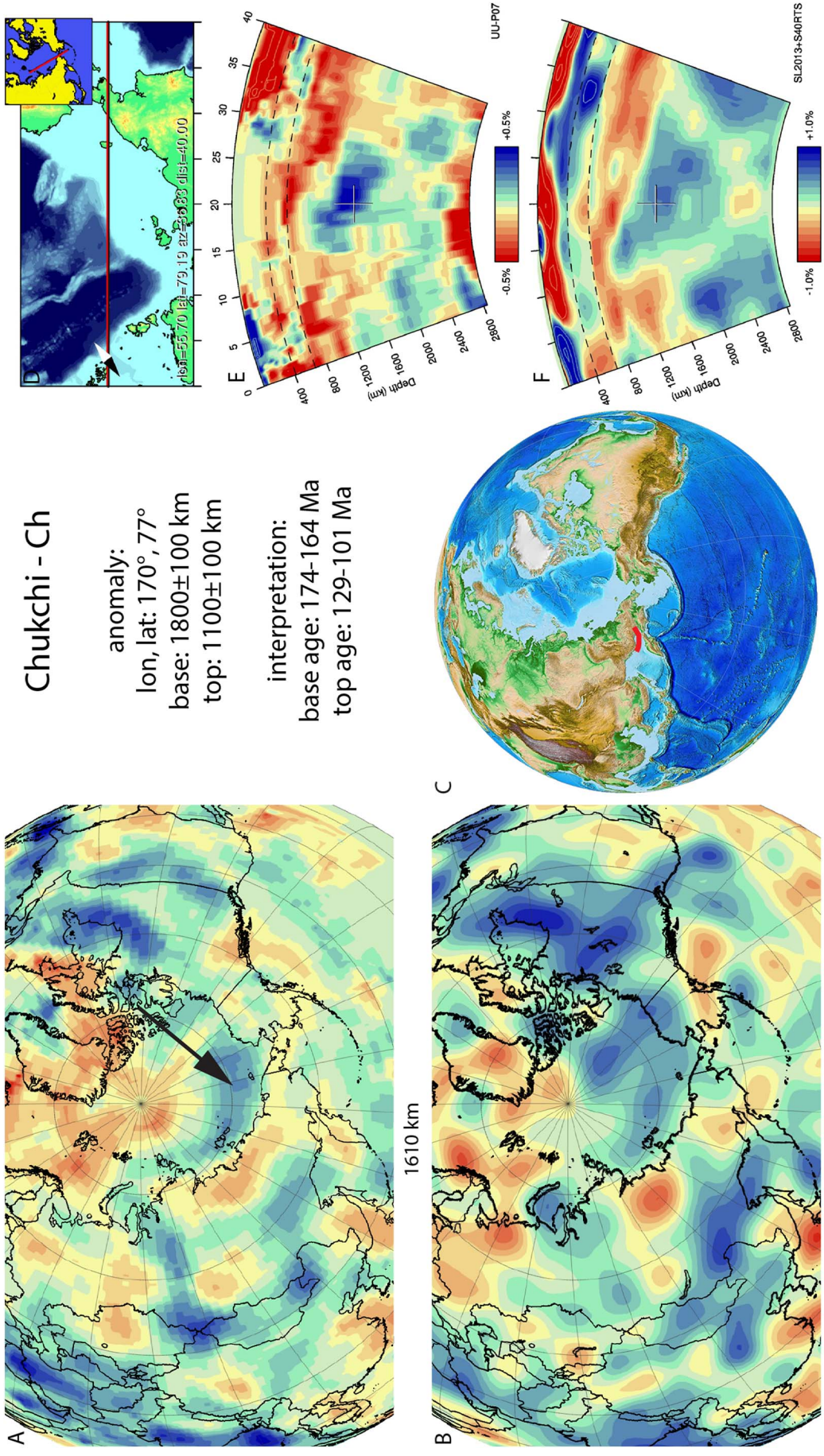

Fig. 32. Chukchi anomaly. Legend same as Fig. 5. Positive anomalies are identified in the same location in both tomographic models with similar dip trend, lateral and vertical extent and Relative amplitude strength.

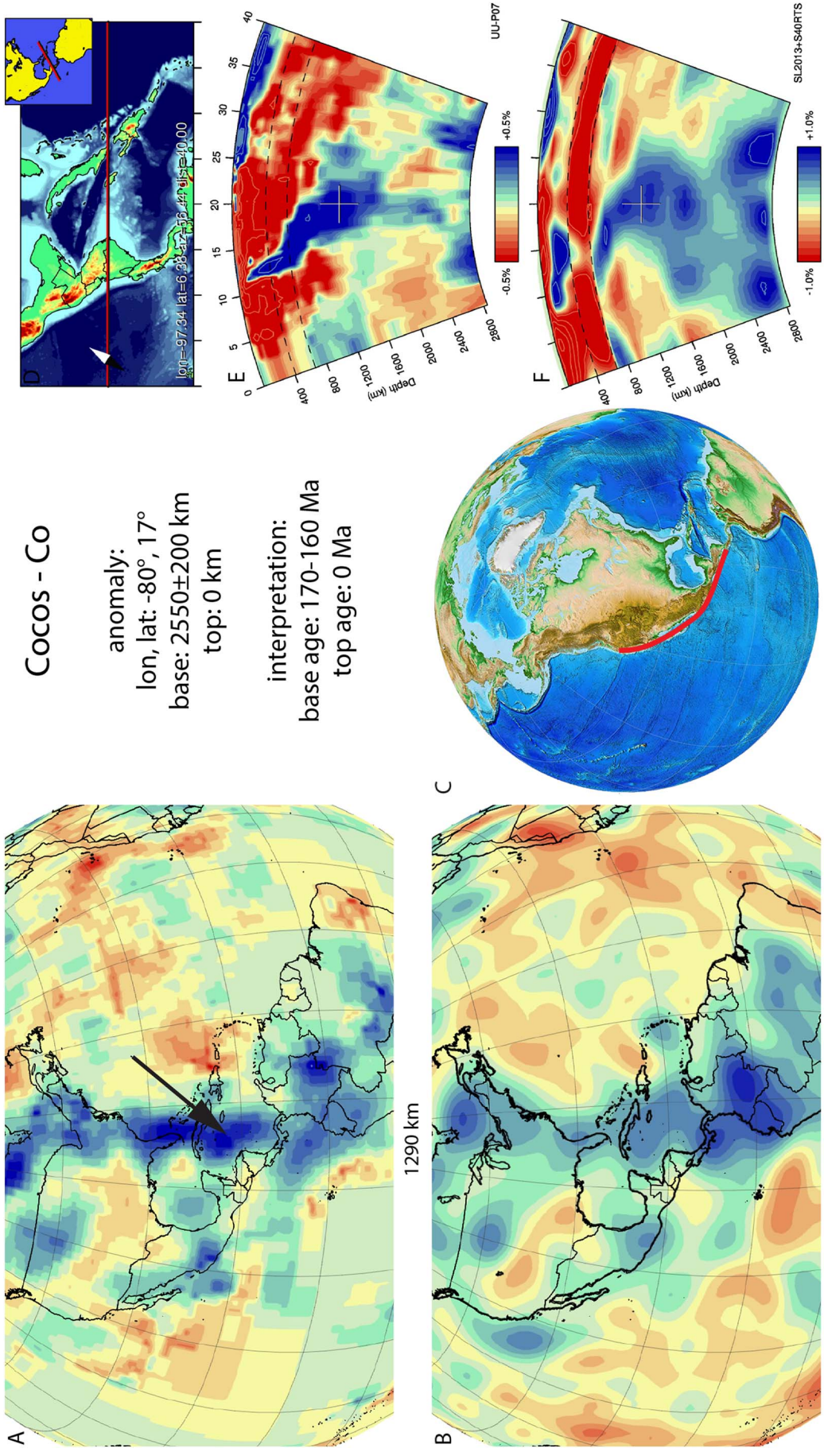

Fig. 33. Cocos anomaly. Legend same as Fig. 5. Vertical, lateral extent and dip trend are similar between tomographic models. Relative amplitude strength is weaker in the S-wave model. The continuation in the transition zone is less well resolved in the SL2013 model.

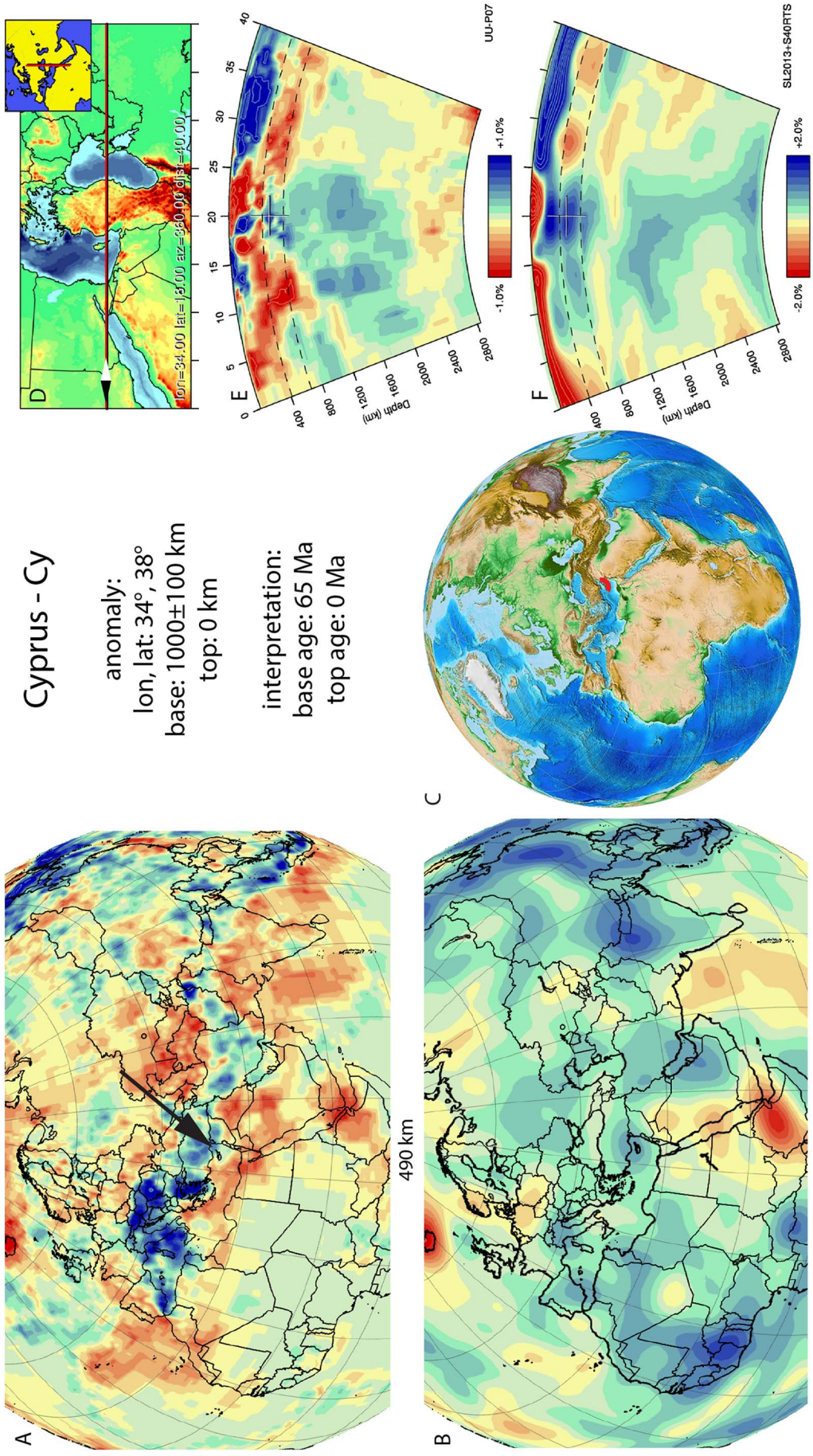

Fig. 34. Cyprus anomaly. Legend same as Fig. 5. Relative amplitude strength, vertical and lateral extent are similar between tomographic models. Dip trend is better visible in the UU-P07 model.

3.31. East China - EC

The East China anomaly (Fig. 35) is located below eastern Asia from the core mantle boundary up into the deep mantle (~2000 km depth) and east of the Mongol-Kazakh slab (Section 3.63). At its shallowest point (~1700 km), it connects to Mongolia slab (Section 3.62) to the NW. Due to the thickness of the anomaly slab (> 1000 km) we tentatively suggest it may comprise multiple SW-NE trending slabs. Van der Voo et al. (1999a) identified this anomaly as a Pacific slab, which formed due to westward subduction of paleo-Pacific (Panthalassa) lithosphere at the east-Asian margin during Mongol-Okhotsk subduction. This suggests that we best correlation the East China slab to a Triassic-Jurassic geological record east of Mongolia. Previously, we correlated the anomaly with the Triassic to Late Jurassic evolution of the Korean peninsula, the North China block, and Japan (van der Meer et al., 2010). Li and Li (2007) described how subduction that started in the Triassic culminated during the Early Jurassic in a flat slab below the South China craton. Foundering of this slab took place between 180 and 155 Ma. However, Li et al. (2014a) showed that magmatism in South China occurred over a zone of ~600 km wide between 145 and 118 Ma, which they inferred to be caused by the migration of a subducting ridge. This ridge subduction may be used as timing of slab break-off which we adopt here, although future study into the kinematic history of the Panthalassa-North China subduction history may require altering this interpretation.

3.32. Emporios - Emp

The Emporios anomaly (Fig. 36) is located in the lower mantle slightly south of, and immediately below the Aegean slab, between 1500 and 2000 km. The name derives from a village on the island of Chios, Greece, which is located above the midpoint of the slab. Previously, van der Meer et al. (2010) followed the interpretation of van Hinsbergen et al. (2005) that the Emporios slab represents Jurassic to Early Cretaceous intra-oceanic (north)eastward dipping subduction within the western part of the Neotethys culminating in ophiolite obduction of the Hellenic and Albanides ophiolites (e.g. Othris, Pindos and Mirdita ophiolites) in the Early Cretaceous (~130 Ma ago) – now known as the 'west-Vardar ophiolites' of Schmid et al. (2008). Stampfli and Borel (2004) and Schmid et al. (2008), and more recently Jahn-Awe et al. (2010) and Natal'in et al. (2012), however, pointed out that two Jurassic-Early Cretaceous intra-oceanic subduction zones existed in the Vardar ocean, not only emplacing the west-Vardar, but also the East-Vardar ophiolites. The latter were thrusted onto the fringes of the Moesian platform (i.e. onto the circum-Rhodope units and Biga peninsula) It is more likely that the slab present below, and slightly south of the Aegean slab is associated with southward subduction below the east Vardar ophiolites instead. The age of onset of subduction is similar to that previously inferred, and is occurred ~170 Ma ago as shown by the oldest ages of the supra-subduction zone ophiolitic crust of the northeast Aegean ophiolites (e.g., Guevgueli, Samothraki, and Sithonia ophiolites (Magganas et al., 1991; Robertson, 2002; Koglin et al., 2009). The age of the top of the slab is likely somewhat older than the age of the base of the Aegean slab, for which we inferred an age of 110 ± 10 Ma (Section 3.1). The west-Vardar slab should be found farther to the west (here interpreted as the Algeria slab, Section 3.4).

3.33. Georgia Islands - GI

The Georgia Island anomaly (Fig. 37) is located below the southern Atlantic and Antarctic Oceans from the core-mantle boundary up into the mid-mantle, separated from the shallower Scotia slab (Section 3.79). It is interpreted as a slab that appears to be flattened on the core-mantle boundary and has a W-E trend at shallower depths. It was first identified by van der Meer et al. (2010), who inferred an Early-Middle Mesozoic age of subduction. On trend with other deep slabs (i.e. Cocos (Section 3.29) and Brasilia (Section 3.18) that subducted below the Americas in the Mesozoic, the Georgia Islands slab probably subducted farther south along the southwestern Gondwana margin. The magmatic arc history of southern South America shows a gap in magmatism between the Early Triassic and the Jurassic, after which subduction reinitiated (Martin, 2007). The Jurassic and younger subduction history we associate with the more westerly located South Orkney Island slab in the mid-mantle (Section 3.84).

Pre-Jurassic subduction in southern South America started at least in Carboniferous time (Pankhurst et al., 2006), although the anomaly that is still visible at the core-mantle boundary may represent lithosphere that subducted well thereafter at this trench. This subduction is associated with a continuous volcanic arc peaking in activity during the Late Permian (280–270 Ma) and remaining active until the Early Triassic (~245 Ma) (Pankhurst et al., 2006; Ramos, 2008). This episode of subduction culminated in the Gondwanide orogeny of the Triassic (~250–215 Ma), followed by regional extension (Pankhurst et al., 2006; Cawood and Buchan, 2007; Elliot and Fanning, 2008; Ramos, 2008; Tankard et al., 2009). The timing of slab detachment is highly uncertain, and may be inferred from the tectonic model of Dalziel et al. (2013) who interpreted the following sequence of events. Prior to 270 Ma a mantle plume impinged under the subducting slab, underplating it and causing the subducting slab to flatten. This induced the Gondwanide deformation and reduced arc volcanism during the 270–240 Ma period. Normal oceanic subduction and arc volcanism returned after the period of Gondwanide deformation. At approximately 200 Myr, a new mantle plume impinged beneath the subducted slab below Patagonia and southern Africa, eventually resulting in the Karoo-Ferrar Large Igneous Province at 182 Ma, and break-up and detachment of the Gondwana Island slab. We assume this 200–180 Ma age as the age of break-off, somewhat younger than in our previous interpretation of van der Meer et al. (2010).

3.34. Gibraltar - Gb

The Gibraltar anomaly (Fig. 38) is located in the upper mantle below the Alboran Sea. Its base is resting on the 660 km discontinuity, and it is still connected to Atlantic crust in the west, is dipping eastwards and is interpreted as subducted lithosphere. Below southern Iberia, the slab curves into an E–W strike, dipping southwards, and is largely detached. The first tomographic images of subduction remnants in the Gibraltar region imaged the E–W trending, detached portion below southern Iberia Spakman, 1986a; Blanco and Spakman (1993) and interpreted subduction in the Gibraltar region to have occurred southwards. With the advent of more advanced tomographic models it became clear, however, that the Gibraltar slab is curved, and mainly dips eastwards reaching the 660 km discontinuity (Gutscher et al., 2002; Piromallo and Morelli, 2003; Spakman and Wortel, 2004; Bezada et al., 2013; van Hinsbergen et al., 2014; Chertova et al., 2014). Since plate convergence between Iberia and Africa is only 100–250 km (increasing eastwards) since the Cretaceous, the bulk of subduction of the Gibraltar slab must have resulted from roll-back. Assuming that the slab did not stretch significantly, subduction of the Gibraltar slab started below the Balearic islands (Spakman and Wortel, 2004), with plate circuit and geological constraints suggesting an onset of deep underthrusting around 45 Ma following very slow convergence between 85 and 45 Ma (van Hinsbergen et al., 2014), culminating in roll-back since ~27 Ma (Lonergan and White, 1997; Rosenbaum et al., 2002b; Faccenna et al., 2004, 2014). The E–W trending, south-dipping portion of the Gibraltar slab below southern Iberia likely resulted from > 180° counterclockwise rotation during roll-back (Rosenbaum et al., 2002b; Spakman and Wortel, 2004; Chertova et al., 2014; van Hinsbergen et al., 2014) and its detachment likely occurred following the arrest of rapid thrusting in the sub-Betic fold-thrust belt, around 7–8 Ma (Platt et al., 2003; Garcia-Castellanos and Villasenor, 2011).

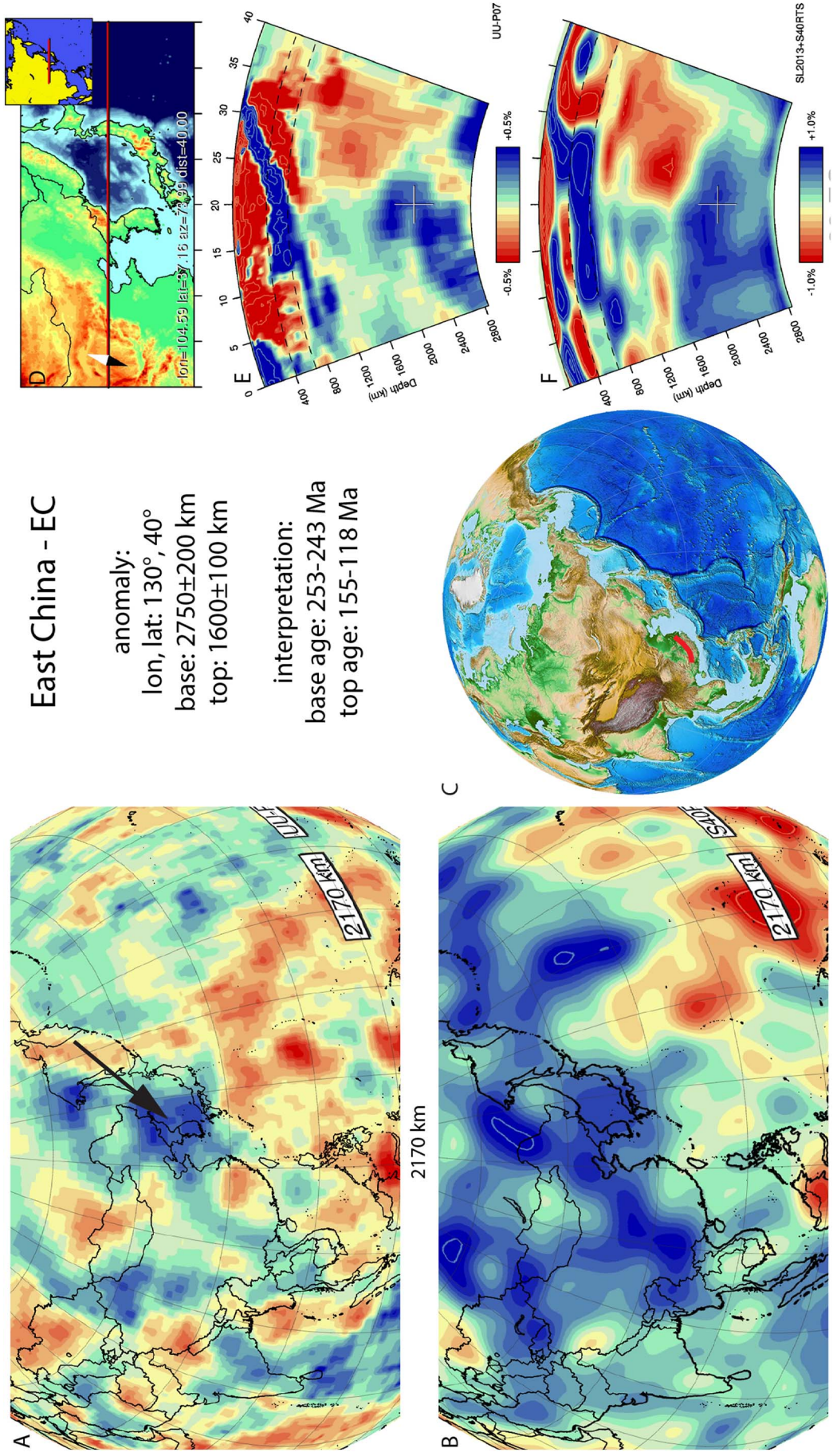

Fig. 35. East China anomaly. Legend same as Fig. 5. Positive anomalies are identified in the same location in both tomographic models with similar, lateral and vertical extent and Relative amplitude strength. Dip trend is not visible. The transition to other anomalies further west is quite different between tomographic models, and these anomalies are stronger in the S40RTS model.

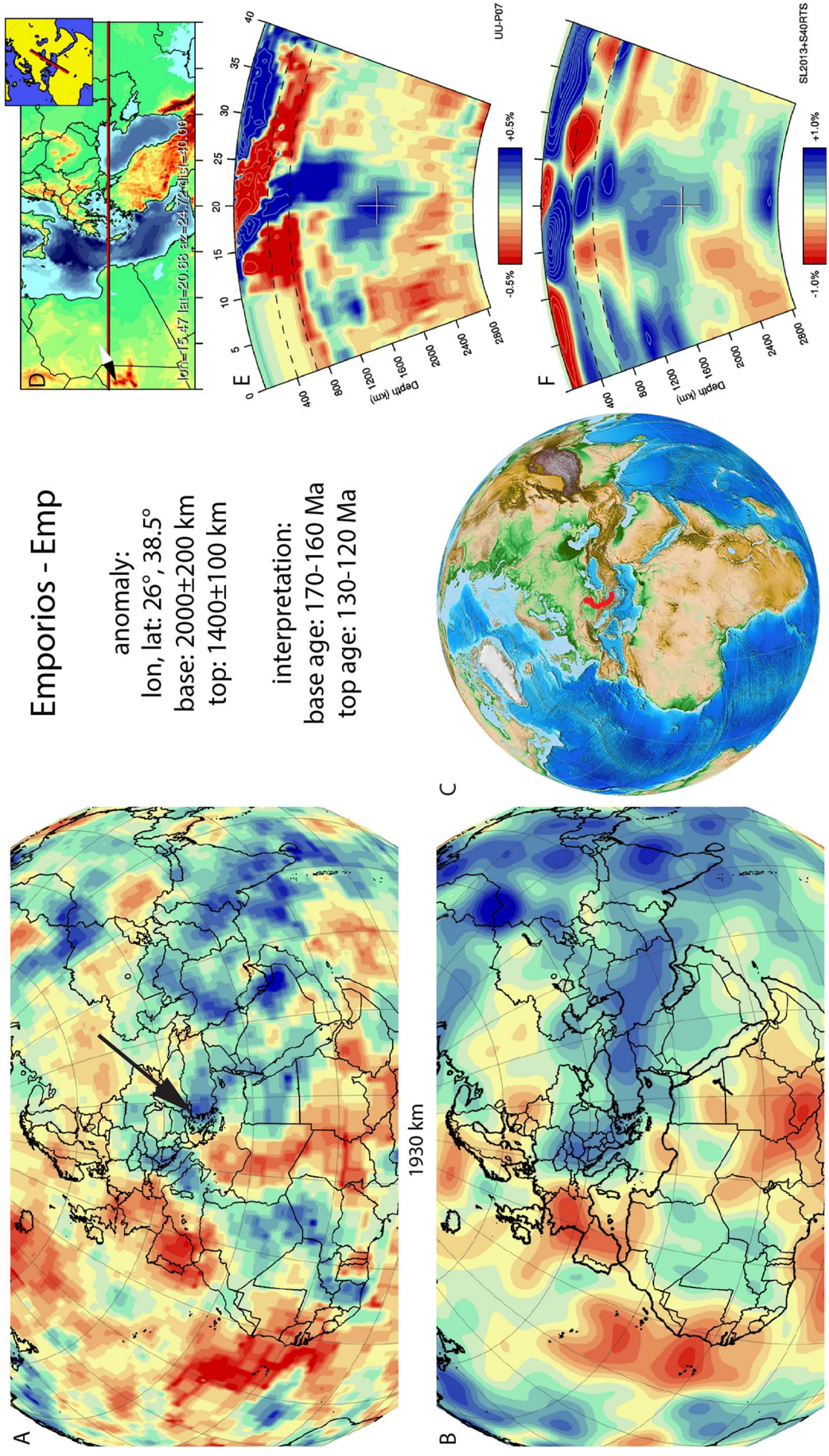

Fig. 36. Emporios anomaly. Legend same as Fig. 5. Relative amplitude strength, vertical, and dip trend are very similar between tomographic models. Lateral extent differs.

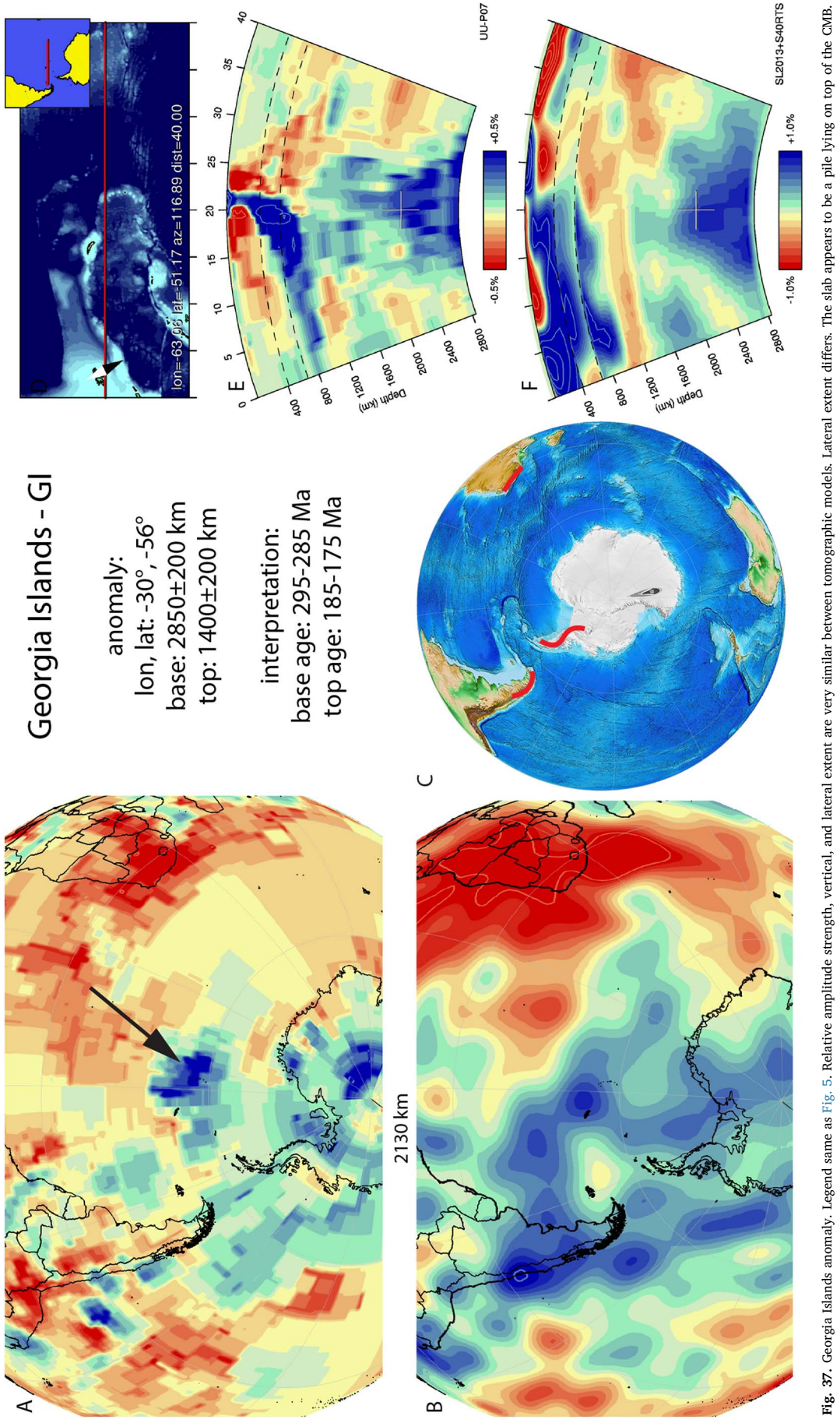

Fig. 37. Georgia Islands anomaly. Legend same as Fig. 5. Relative amplitude strength, vertical, and lateral extent are very similar between tomographic models. Lateral extent differs. The slab appears to be a pile lying on top of the CMB.

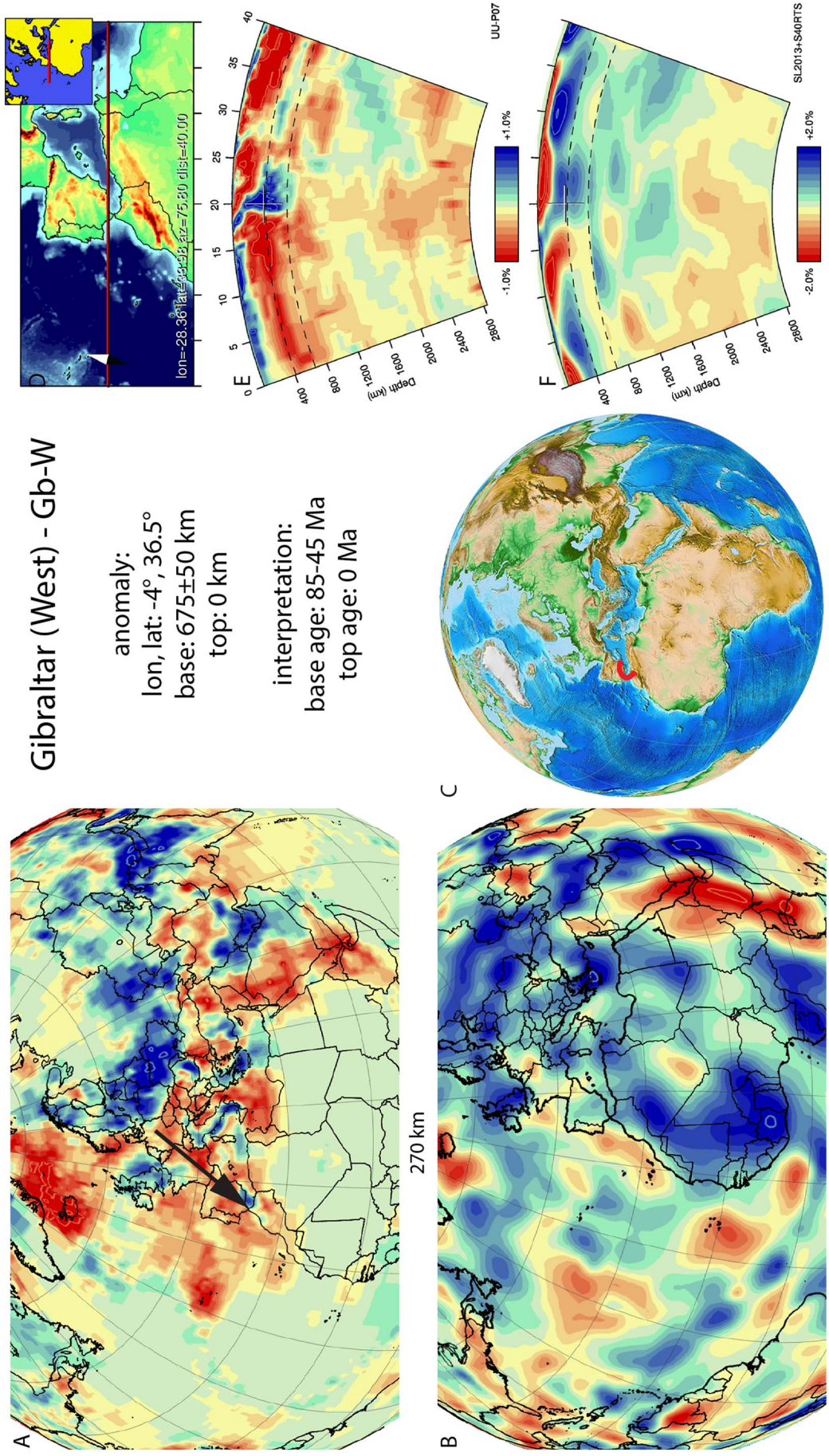

Fig. 38. Gibraltar-West anomaly. Legend same as Fig. 5. Relative amplitude strength, vertical, and dip trend are very similar between tomographic models. Lateral extent differs.

3.35. Great Basin - GB

A positive wave speed anomaly below the Great Basin, Nevada (Fig. 39) was originally named the Nevada Cylinder (Roth et al., 2008). The Great Basin anomaly is located in the upper mantle below southwestern North America, and has been imaged at depths of ~100–800 km (West et al., 2009). It has an overall N–S trend and dips to the NE. It has been interpreted as either a lithospheric drip due to gravitational instability (West et al., 2009), a relic of the Laramide flat slab (Schmandt and Humphreys, 2011), perhaps fragmented by fracture zones (Sigloch, 2011), or a putative mantle plume (Obrebski et al., 2010). Based on its elongation and dip, we interpret the anomaly to result from Cenozoic subduction, and follow the interpretation of Liu and Stegman (2011) who consider it subducted Farallon oceanic lithosphere. Based on mantle convection modelling, they argued that its subduction initiated at ~35 Ma, and ended with slab detachment at ~15 Ma. Its subduction may correspond to phase of ignimbritic volcanism in the Great Basin between 31 and 20 Ma (Best and Christansen, 1991; Dickinson, 2006).

3.36. Halmahera - Hm

The Halmahera anomaly (Fig. 40) corresponds to the A4 anomaly of Hall and Spakman (2002, 2004) and was previously imaged by Widiyantoro and van der Hilst (1997), Hall and Spakman (2015), and Wu et al. (2016). It is interpreted as one of the two actively subducting slabs attached to the Molucca Sea basin lithosphere, the other being the Sangihe slab (Section 3.76). It is subducting eastwards below the island of Halmahera and reaches the base of the upper mantle. Wu et al. (2016) separated this slab into three slabs; Molucca Sea East slab in the upper mantle and East Asian Sea west and Ayu Trough Deep in the upper-lower mantle transition zone. In our tomographic model we cannot confidently separate these slabs. Subduction below Halmahera started at 15 Ma in both reconstructions of Hall (2002) and Wu et al. (2016), which we adopt as age for the base of the slab.

3.37. Hatteras - Ha

The Hatteras anomaly (Fig. 41) is part of the set of anomalies commonly, also in our previous compilation in van der Meer et al. (2010), interpreted as the Farallon slab, initially defined by Grand et al. (1997). It is located below eastern North America within the lower mantle. The anomaly is generally interpreted to represent eastward subducted Farallon oceanic lithosphere (Grand et al., 1997; Bunge and Grand, 2000; van der Meer et al., 2010) below the North American continental margin. The Hatteras slab corresponds to the MEZ and in part the SF1 slab of Sigloch and Mihalynuk (2013), who, based on their interpretation of the geological records of the Wrangellia and Stikinia composite terranes of the North American Cordillera, interpreted the slab to be predominantly intra-oceanic, westward subducted Mezcalera Ocean lithosphere (their MEZ slab) and only a small part Farallon-derived (their SF2 slab). Their pre-100 Ma interpretation, however, is based on a true-polar wander corrected paleomagnetic reference frame without longitude control under the assumption that Africa was longitudinally fixed (Torsvik et al., 2008a, 2008b). van der Meer et al. (2010) showed that such an assumption leads to major mis-locations of reconstructed subduction zones relative to their corresponding slabs, particularly for the still-subducting Aegean slab, of 1000–2000 km. A much better match between slabs and subduction zones arises with a westward longitude shift, which places the location of the Hatteras slab much closer to the west-North American margin, making a Mezcalera origin unlikely. In addition, Liu (2014) found that westward subduction of Mezcalera oceanic lithosphere would not be able to generate sufficient volume for the slab. One of the arguments supporting that part of the Hatteras slab resulted from intra-oceanic subduction is the mismatch between the reconstructed location and shape of the North American continental margin and the outline of the slab (Sigloch and Mihalynuk, 2013). This occurs mostly towards the south, an area where Sigloch and Mihalynuk (2013) have interpreted the Franciscan intra-oceanic subduction zone, forming the deeper parts of the Cocos slab (their SF1 slab, see Section 3.29). By extending the Cocos slab and preceding Franciscan intra-oceanic subduction into the deepest parts of the mantle, this would resolve most of the mismatch. The Hatteras slab would then represent (predominant) subduction at the continental margin.

Debate exists on the age of onset of continental margin subduction, with estimates varying from ~100 Myr (Grand et al., 1997), prior to 100 Ma (Liu et al., 2008), or since 150 Ma (Sigloch et al., 2008). In the interpretation of Sigloch and Mihalynuk (2013), the intra-oceanic subduction zone was overridden by the continental margin, followed by initiation of Rocky Mountain deformation, recorded by synorogenic clastic wedge (160–155 Ma), which we adopt as minimum age of start of subduction. Tectonic studies (Ward, 1995; Nokleberg et al., 2000; DeCelles et al., 2009), however, suggested that subduction at the western margin of North America (then part of Laurentia) initiated earlier, from the Early Jurassic onwards. Consequently, van der Meer et al. (2010) interpreted the base of the slab as Early Jurassic. Magmatism in the Sierra Nevada batholith started at ~200 Ma (DeCelles et al., 2009), which we adopt as the maximum age of the base of the Hatteras slab.

Towards the top of the lower mantle, the N–S trending Hatteras slab ceases to exist and is replaced by the NW-SE trending SF3 slab of Sigloch and Mihalynuk (2013). This happened after the South Farallon trench steps westward following accretion of the Shatsky Rise Conjugate plateau, and a slab window formed leading to Sonora volcanism including the Tarahumara ignimbrite province (Sigloch and Mihalynuk, 2013). The volcanic rocks and granitic plutons were dated by González-León et al. (2011). The age of the Tarahumara Formation is between ca. 79 and 59 Ma; the monzonitic to granitic plutons have ages of ca. 71–50 Ma (We have adopted 59–50 Ma as the end of subduction of the Hatteras slab.

3.38. Himalayas - Hi

The Himalayas anomaly (Fig. 42) is located below the northern part of the Indian continent from the upper part of the lower mantle up to the upper mantle. In previous tomographic studies it has been referred to as the IV (Van der Voo et al., 1999b) or Hi anomaly (Hafkenscheid et al., 2006), and it was also imaged by Li et al. (2008), and shown in Replumaz et al. (2004, 2010b, 2010c) and van Hinsbergen et al. (2012). van der Meer et al. (2010) followed the interpretation of Hafkenscheid et al. (2006), who suggested that this lithosphere represents Neotethyan lithosphere that formed as back-arc lithosphere associated with the late Cretaceous Spontang arc. The Himalaya anomaly, however, is the shallowest anomaly associated with convergence between India and Asia, and consequently likely represents the youngest slab, interpreted to reflect either continental crust of Greater India (Replumaz et al., 2010c), or (partly) oceanic crust of Greater India that according to paleomagnetic data formed in Cretaceous time (Greater Indian Basin of van Hinsbergen et al., 2012). Given the northward subduction polarity of India below Asia, the southward dip of the Himalayas slab likely indicates that the slab is overturned (Replumaz et al., 2010c). Although the inferred nature of the lithosphere of the Himalaya slab differs in the scenarios of Replumaz et al. (2010c) and van Hinsbergen et al. (2012, 2017b), the inferred age for top of the slab are similar, 20 ± 5 Ma, after which time India-Asia convergence can be fully accounted for by intra-continental shortening and horizontal underthrusting of Indian lithosphere below the Tibetan Plateau. The age of the base of this slab is difficult to assess. Based on the volume of the Himalaya slab compared to India-Asia convergence rates, Replumaz et al. (2010b) estimated a ~35 Ma age, and consensus exists that the Himalaya slab represents Greater Indian lithosphere, i.e. lithosphere that subducted after the collision of northernmost Indian

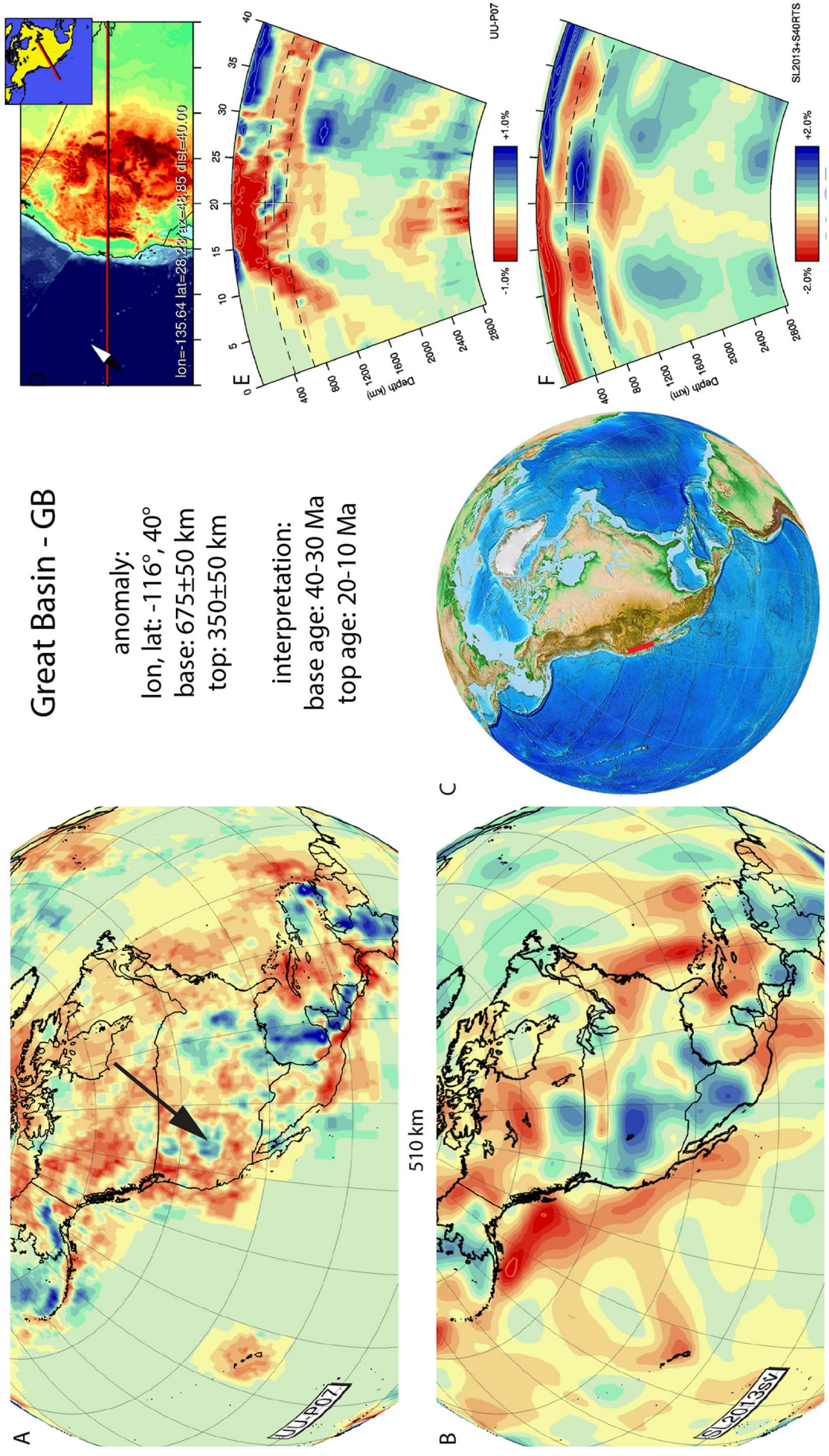

Fig. 39. Great Basin anomaly. Legend same as Fig. 5. Relative amplitude strength, vertical, lateral extent and dip trend are very similar between tomographic models.

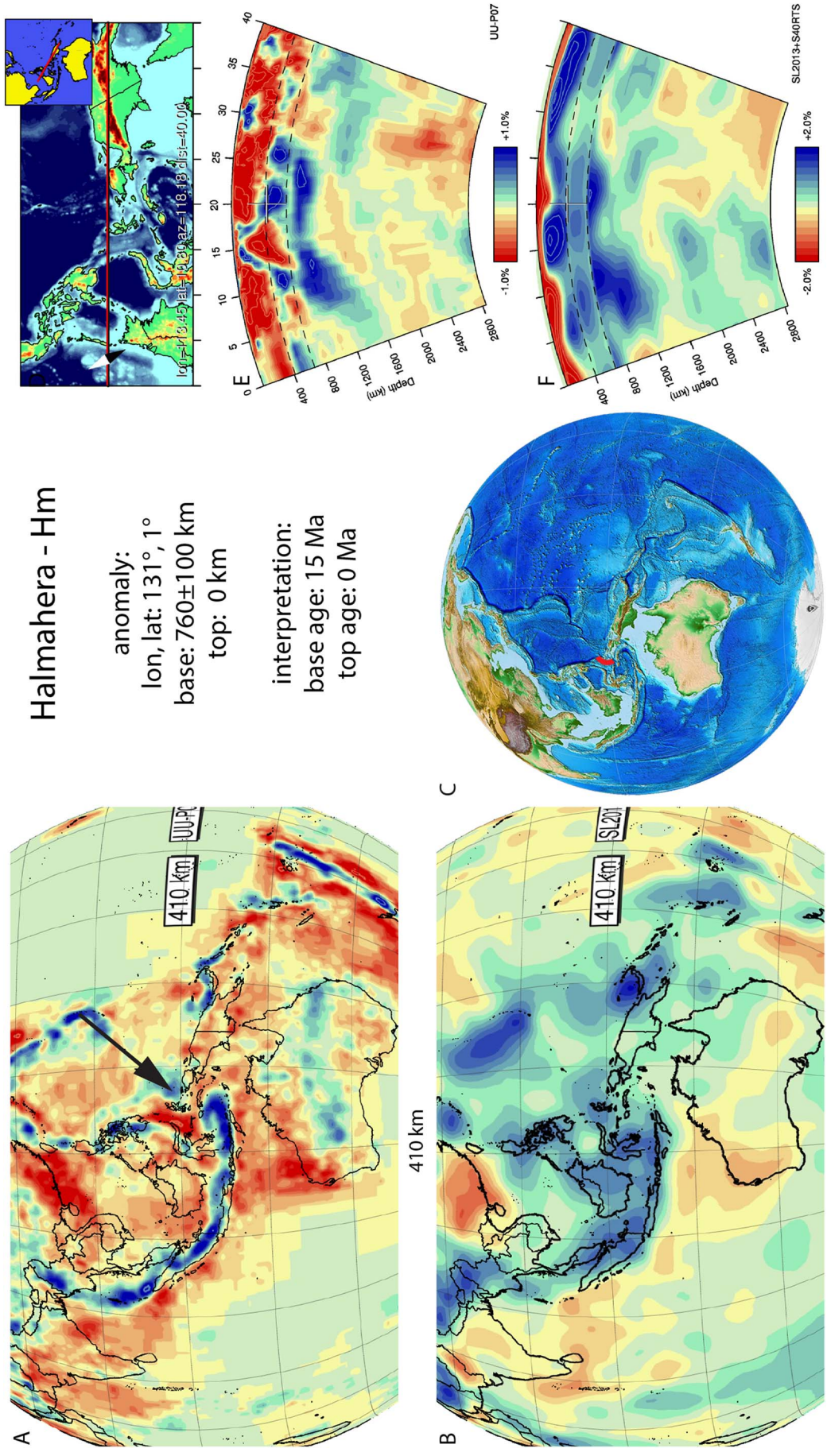

Fig. 40. Halmahera anomaly. Legend same as Fig. 5. This slab is well imaged in the UU-P07 model with clear dip trend, but lateral and vertical extent are less well imaged in the S-wave models.

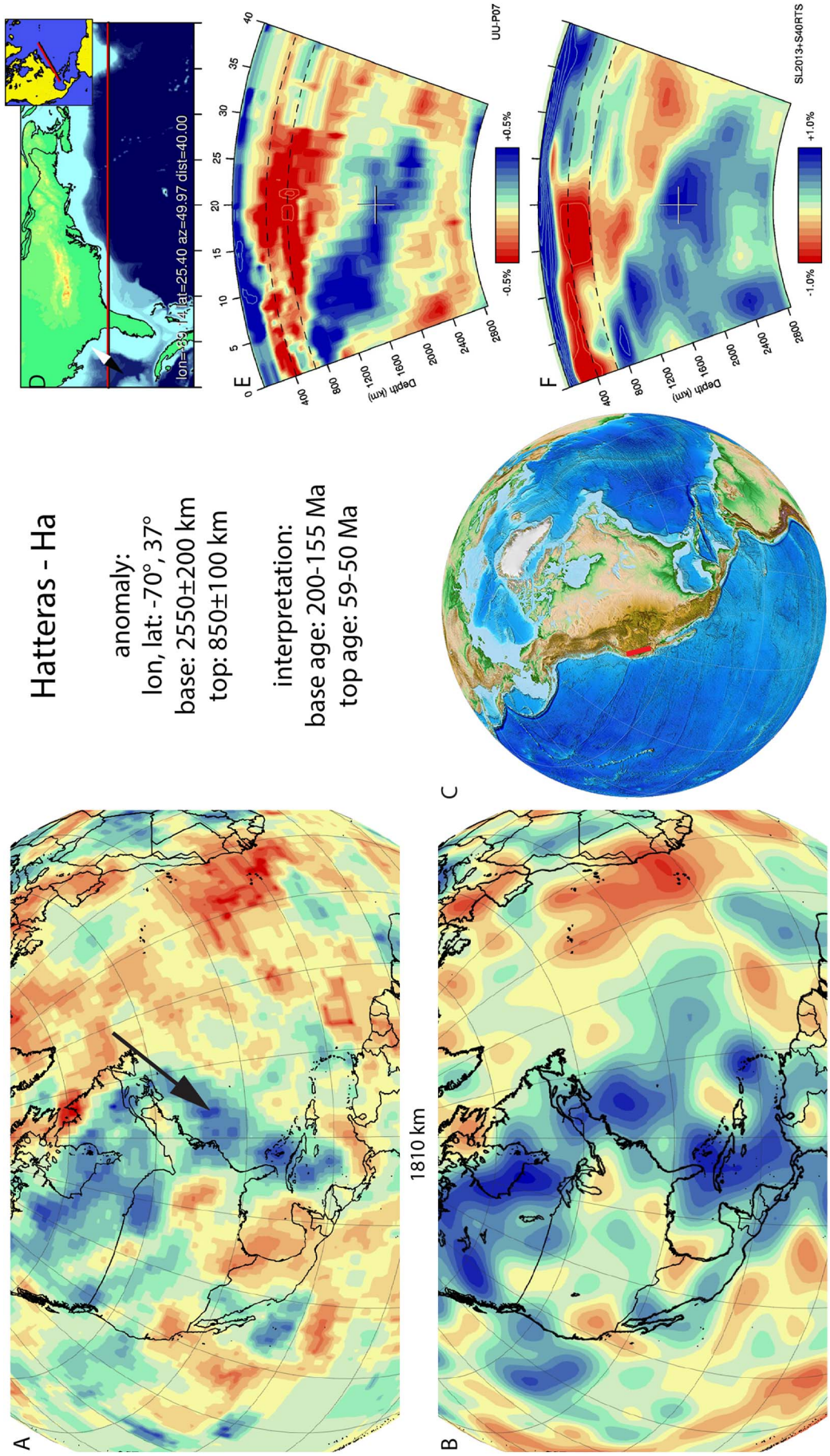

Fig. 41. Hatteras anomaly. Legend same as Fig. 5. Dip trend, Relative amplitude strength, vertical and lateral extent are very similar between tomographic models.

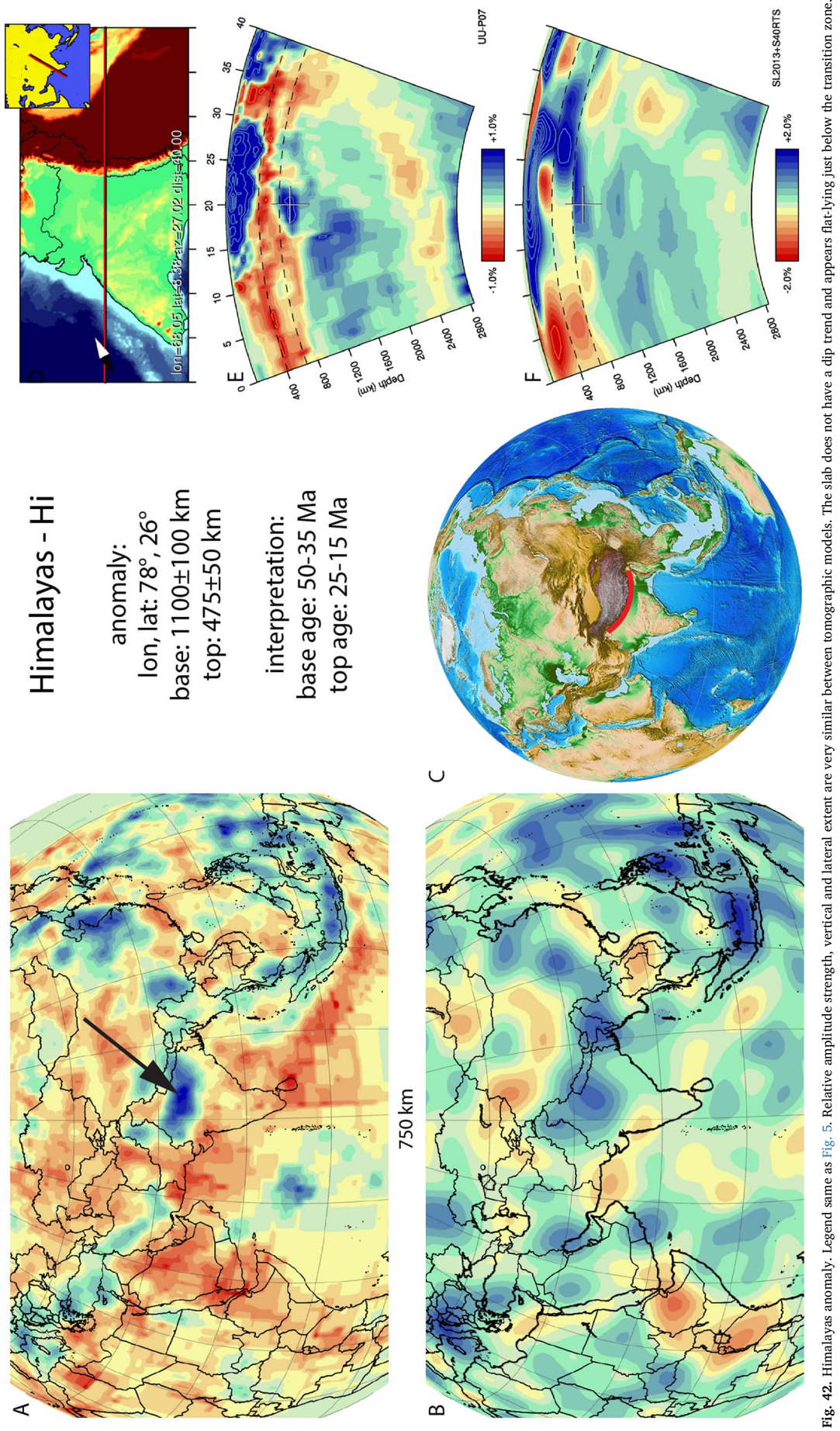

Fig. 42. Himalayas anomaly. Legend same as Fig. 5. Relative amplitude strength, vertical and lateral extent are very similar between tomographic models. The slab does not have a dip trend and appears flat-lying just below the transition zone.

plate continental lithosphere with Asia around 50 Ma. We adopt a 43 ± 8, Ma for the base of the Himalaya slab.

3.39. Hindu Kush - HK

A narrow, E–W trending, steeply north-dipping anomaly was described below the Hindu Kush region of North Pakistan, from deep earthquakes reaching 250 km depth (Pegler and Das, 1998; Pavlis and Das, 2000; Lister et al., 2008; Zhang et al., 2011) and seismic tomography shows it reaches a depth of ~600 km (Van der Voo et al., 1999b; Negredo et al., 2007; Li and van der Hilst, 2010; Replumaz et al., 2010b; Kufner et al., 2014, 2016) (Fig. 43). The Hindu Kush anomaly is typically seen as subducted Indian plate lithosphere attached to continental crust of NW India (Negredo et al., 2007; Lister et al., 2008; Replumaz et al., 2010a; Kufner et al., 2016). This interpretation requires that India has been horizontally underthrust northward below the Sulaiman Lobe of Pakistan, south of the Hindu Kush, over a N–S distance of ~500 km to reach the location where the Hindu Kush slab dips steeply northward. We may thus estimate the minimum age for the moment of subduction of the base of the Hindu Kush slab by reconstructing since when India and Asia have converged 1100 km (500 km northward underthrusting of India plus 600 km of slab length) at the longitude of the Hindu Kush slab, assuming no overriding plate shortening, i.e. 30 Ma according to the reconstruction of van Hinsbergen et al. (2011b). Recently, however, Kufner et al. (2014) suggested that the Hindu Kush slab may correspond to Asian lithosphere instead, since at depth the Hindu Kush slab cannot be distinguished from the Pamir slab (see Section 3.69). Gaina et al. (2015) developed a scenario assuming that the Hindu Kush slab is Asian, showing that it must have subducted between the Helmand Block of Afghanistan and the Tadjik depression. Taking the westward disappearance of the Hindu Kush slab into account, these authors proposed an (unconstrained) counterclockwise rotation of the Helmand block, keeping the Kandahar arc of the Afghan block contiguous with the Kohistan-Gangdese arc of Karakoram-Tibet. This scenario would provide ~600 km of Helmand-Tadjik convergence since ~50 Ma. Although speculative, this age may provide a maximum age for the base of the Hindu Kush slab. We allow a 50–30 Ma age range for the base of the Hindu Kush slab.

3.40. Hispaniola - His

The Hispaniola anomaly (Fig. 44) is detached and located below the island of Hispaniola in the northern Caribbean region, at a depth of 800–1400 km. It was first identified by van Benthem et al. (2013), who interpreted it as the nGAC slab (northern Great Arc of the Caribbean). We name the slab Hispaniola according to its current location. Its detached nature and location in the top of the lower mantle and its position west of the Caribbean slab and east of and above the Cocos slab suggests that it should be correlated to a geological record of past Cretaceous or Paleogene subduction in the northern Caribbean region. van Benthem et al. (2013) interpreted this anomaly to represent lithosphere that subducted below Cuba and Hispaniola in Cretaceous to Eocene time, which decoupled from the Venezuela slab (Section 3.90), or 'sGAC' slab in terminology of van Benthem et al. (2013), upon the Paleogene northward retreat of the Cuba segment relative to South America (see also Pindell and Kennan, 2009; Boschman et al., 2014). Cuba and Hispaniola show a history of subduction of the North American plate, comprising oceanic Proto-Caribbean lithosphere, a microcontinental terrane, and the North American continental margin below the oceanic Caribbean plate represented by ophiolite and arc rocks (García-Casco et al., 2008; Pindell and Kennan, 2009). The oldest record of subduction in Cuba is represented by ~130 ± 5 Ma volcanic arc and high-pressure, low-temperature metamorphic rocks (García-Casco et al., 2006; Stanek et al., 2009), and subduction terminated between 45 and 40 Ma shown by the youngest foreland basin deposits and oldest overlap assemblages (Iturralde-Vinent et al., 2008).

3.41. Hudson - Hu

The Hudson anomaly (Fig. 45) is part of the set of anomalies commonly, also in our previous compilation in van der Meer et al. (2010), referred to as the Farallon slab, initially defined by Grand et al. (1997). It is located below northern North America within the lower mantle. The NW-SE trending Hudson anomaly is interpreted as the northernmost slab of the family of Farallon slabs and is entirely contained in the lower mantle. At its eastern end it connects to the northern part of the N–S trending Hatteras slab (Section 3.37).

Sigloch and Mihalynuk (2013) referred to the Hudson slab as the ANG slab, and inferred that it formed due to southwestward subduction of Angayucham oceanic lithosphere since 140 Myr based on their interpretation of the amalgamation history of the Wrangellia superterrane of the North American Cordillera. We infer Angayucham subduction led to the formation of the Lougheed slab instead (Section 3.51). Rather, we follow Nokleberg et al. (2000), who suggested that eastward subduction of Farallon/Panthalassa lithosphere occurred at this latitudinal position at the Stikinia arc while it was (close to) being accreted to the continental margin subduction zone (Hatteras slab, Section 3.37). Collision started by 72–69 Myr and was accomplished by 55–50 Myr ago (Sigloch and Mihalynuk, 2013), which we take as age range for the top of the slab.

Johnston and Borel (2007) interpreted a two-stage process, a first involving intra-oceanic subduction and arc formation and accretion forming the Stikinia-Quesnellia superterrane between 230 Ma to 150 Ma within the (eastern) Panthalassa. In a second stage, from 150 Ma to 55 Ma, this arc migrated towards North America, collided, and moved northward parallel to the continental margin. We interpret stage one to have resulted in the Wichita slab (Section 3.91) and correlate their stage two with the Hudson slab.

3.42. Idaho - Id

The Idaho anomaly (Fig. 46) is located below western North America from the deep mantle up to upper part of the lower mantle. It was interpreted as the Idaho slab by van der Meer et al. (2010) and corresponds to the S2 anomaly of Sigloch et al. (2008) and Shephard et al. (2013) and Cascadia Root (CR) anomaly of Sigloch and Mihalynuk (2013). It has been interpreted as Farallon lithosphere that subducted in the Cenozoic Sigloch et al. (2008) and Shephard et al. (2013) or as lithosphere of the Kula plate that subducted in the Cretaceous (Ren et al., 2007; Shephard et al., 2013). Sigloch et al. (2008) suggested that the Idaho slab subducted after, and below the northern extent of the Farallon slab to the NE (defined here as the Hudson slab, Section 3.41) after the Hudson slab broke off in the late Cretaceous. van der Meer et al. (2010) argued that such an interpretation would require that the Hudson slab remained stagnant in the mantle since the Late Cretaceous, whereas the Idaho slab sank rapidly into the lower mantle, which they considered unlikely. Instead, they followed Nokleberg et al. (2000), who reconstructed northward to eastward subduction of Farallon/Panthalassa lithosphere in the latitude range of the Idaho slab based on paleomagnetic data from the northern parts of the Wrangellia terrane. The Wrangellia terrane comprises of four island arcs, the Devonian Sicker, the late Paleozoic Skolai, the Late Triassic and Early Jurassic Talkeetna-Bonanza, and the Late Jurassic through mid-Cretaceous Gravina arcs (Nokleberg et al., 2000). van der Meer et al. (2010, 2012) interpreted the Idaho slab as Farallon/Panthalassa lithosphere resulting in the Talkeetna-Bonanza and Gravina arcs. U-Pb zircon ages of mid-crustal plutons of he Bonanza arc show that these were emplaced between 203.8 Ma and 164 Ma (Canil et al., 2013; D'Souza et al., 2016). Based on their present-day relative locations between the Mendocino (Section 3.59) and Idaho slabs and arcs, we tentatively suggest that the Idaho slab is correlated with the Bonanza arc. Following one of the

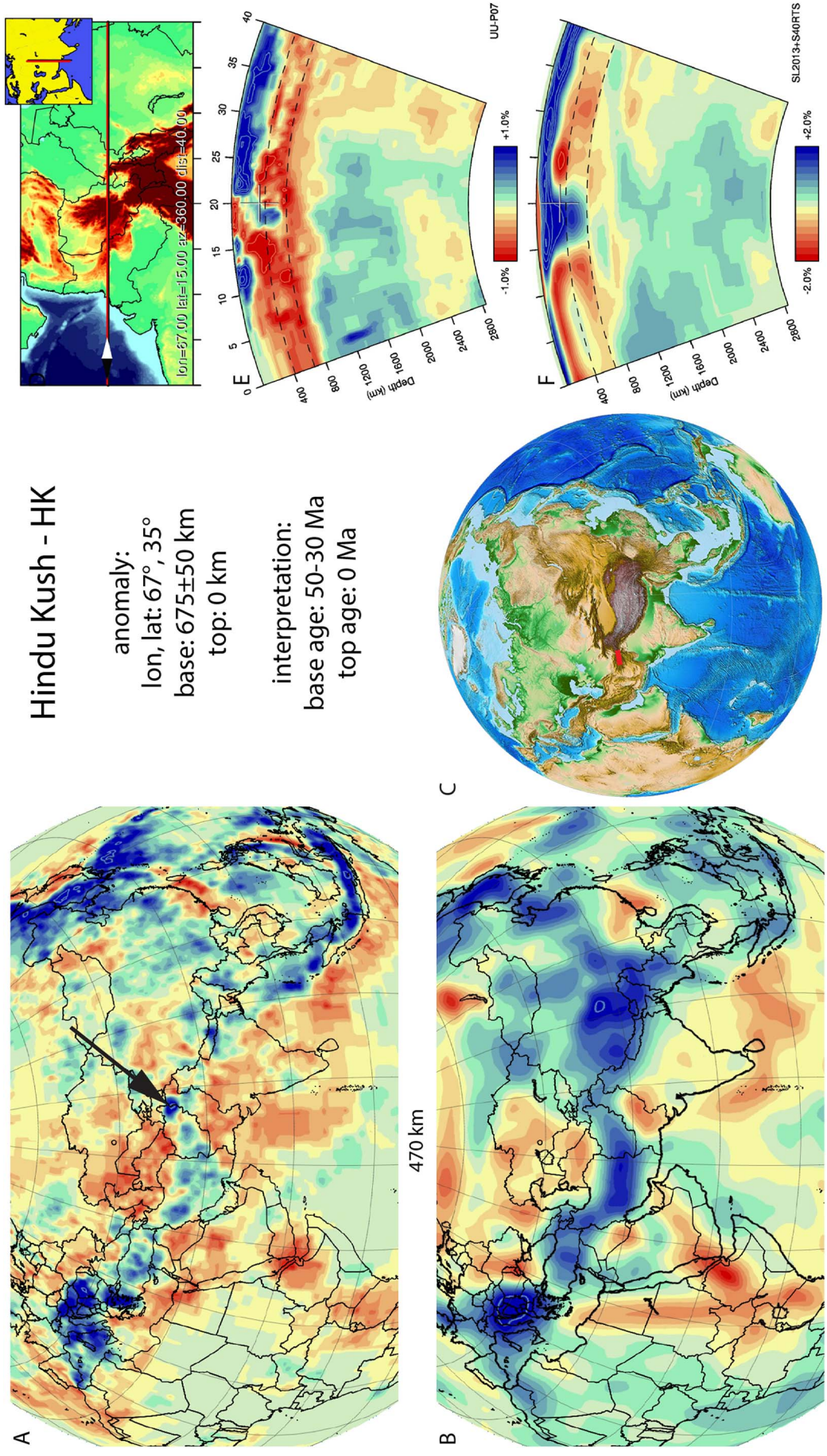

Fig. 43. Hindu Kush anomaly. Legend same as Fig. 5. Positive anomalies are identified in the same location in both tomographic models with similar vertical extent and Relative amplitude strength, but are considerably different extent. Dip trend is visible in UU-P07, but not in SL2013.

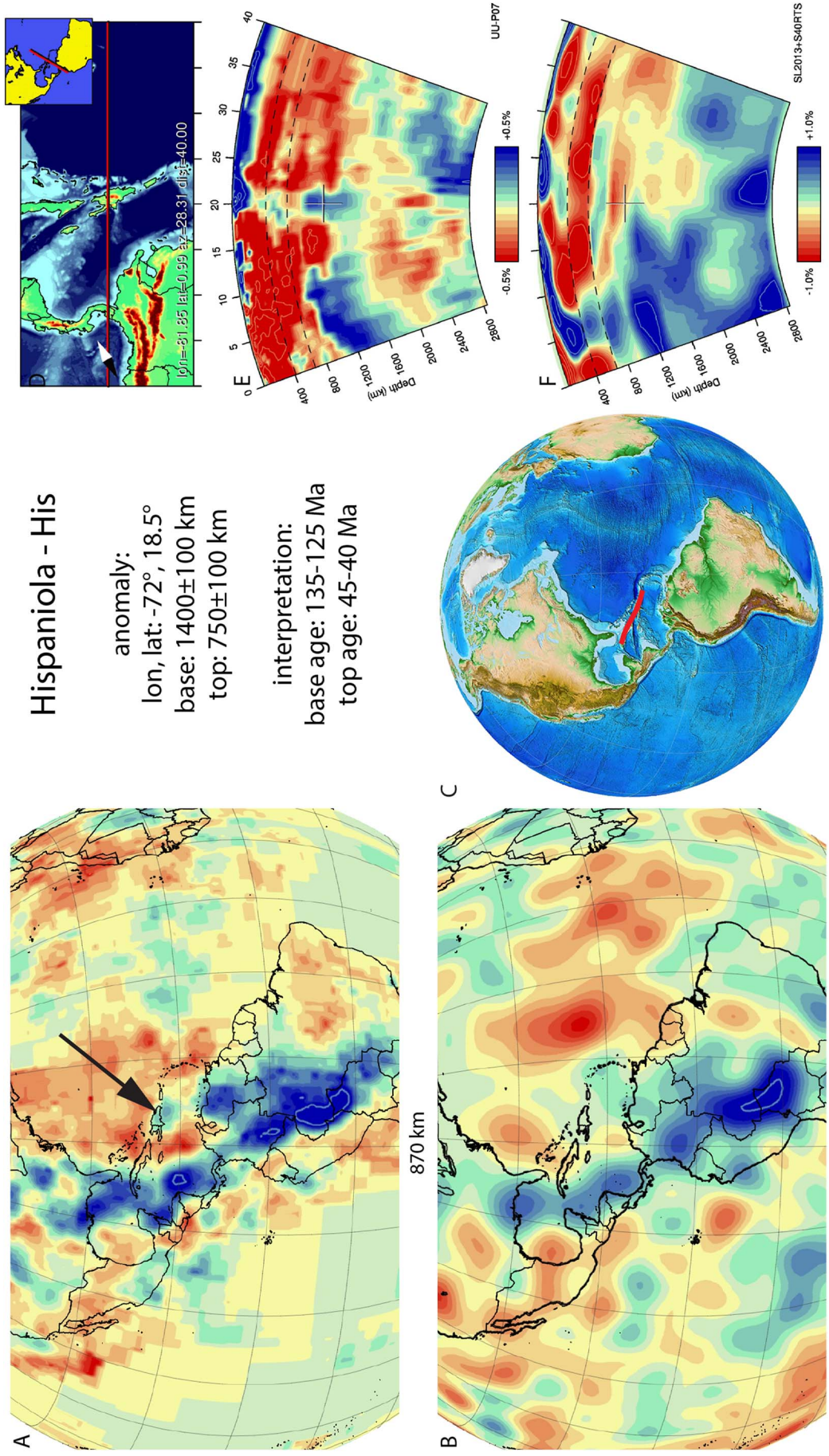

Fig. 44. Hispaniola anomaly. Legend same as Fig. 5. Positive anomalies are identified in the same location in both tomographic models with but are considerably different in lateral and vertical extent and Relative amplitude strength. Dip trend appears to be near-vertical UU-P07.

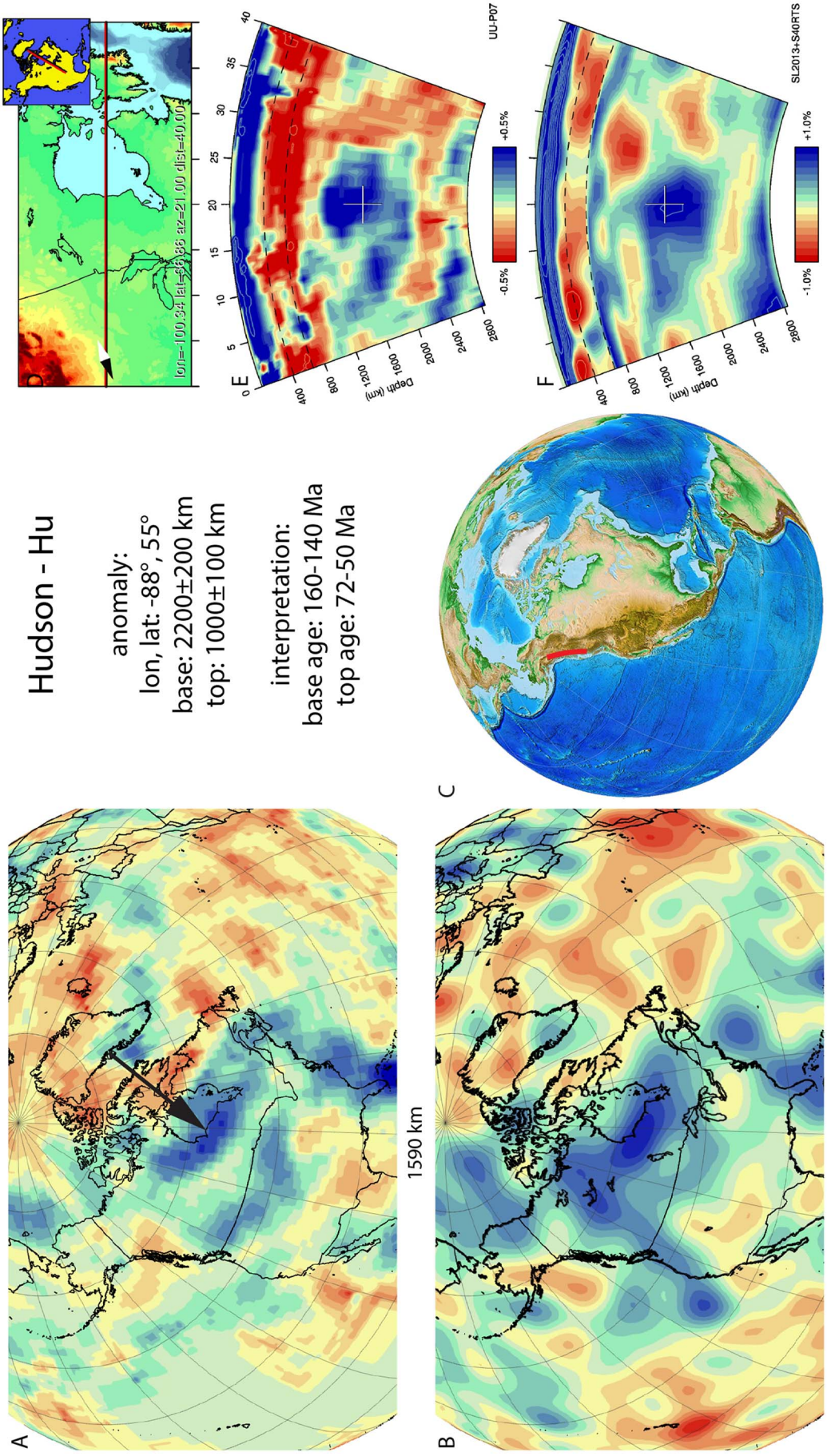

Fig. 45. Hudson anomaly. Legend same as Fig. 5. Relative amplitude strength, vertical and lateral extent are very similar between tomographic models. There is not a dip trend visible.

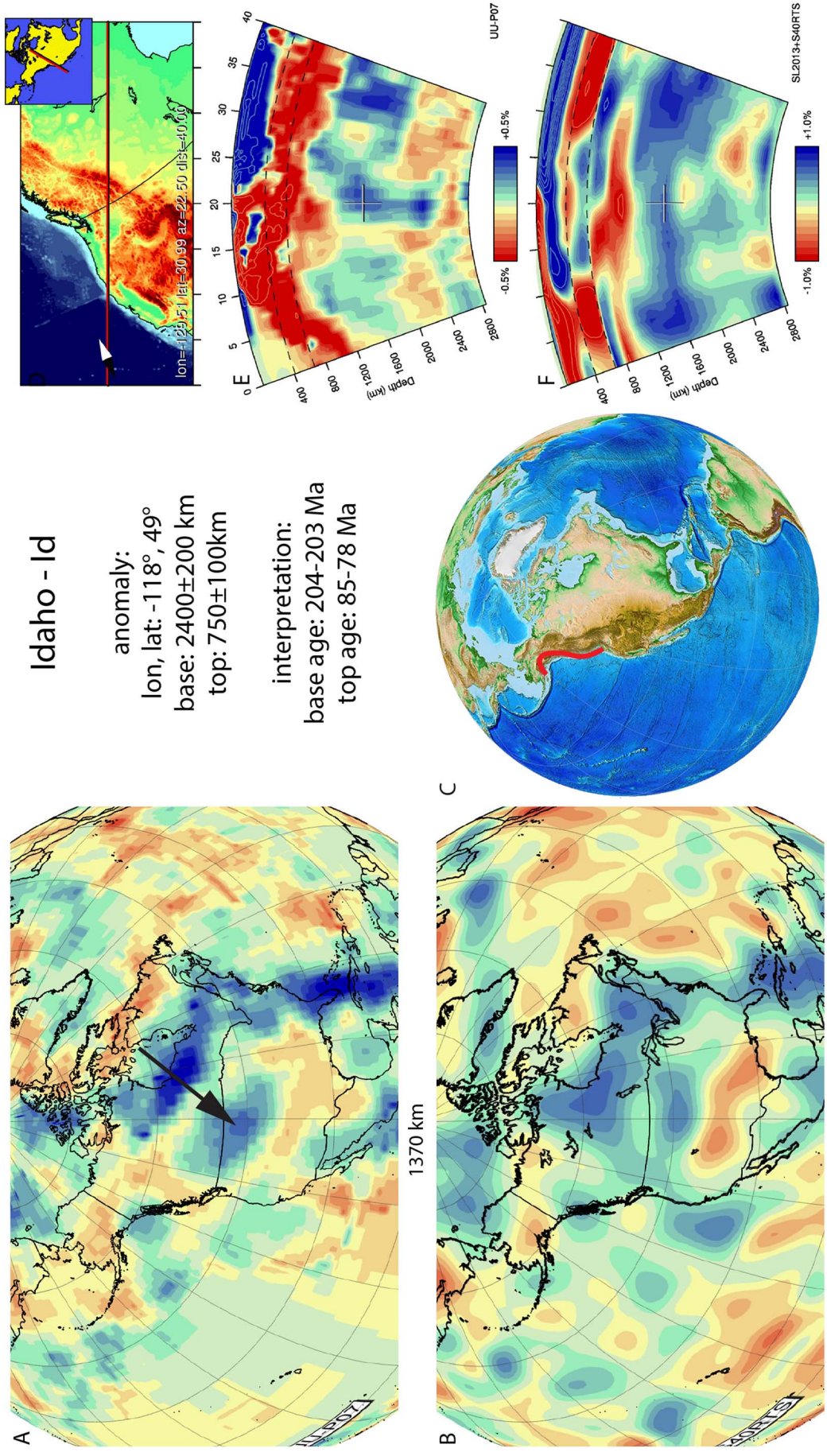

Fig. 46. Idaho anomaly. Legend same as Fig. 5. Positive anomalies are identified in the same location in both tomographic models with a similar lateral and vertical extent and Relative amplitude strength. The slab appears to dipping to near-vertical in UU-P07.

accretion scenarios of Nokleberg et al. (2000), end of subduction and accretion to the continental margin was modelled by Shephard et al. (2013), who modelled accretion to occur at 140 Ma. However, Sigloch and Mihalynuk (2013), suggested that the final terrane accretion occurred later at 55–50 Myr ago. However,this late accretion date is specifically referring to the Siletzia terrane, which may be mostly a large igneous plateau related to the Yellowstone plume (Wells et al., 2014) and therefore not the result of subduction. Gehrels et al. (2009) argued that on the basis of U-Pb and Hf isotope analysis of detrital zircons from strata of the Gravina belt that during the mid-Cretaceous the Gravina belt collapsed and the Alexander-Wrangellia terrane was accreted until 85 Ma to the Stikine and Yukon Tanana terranes at the continental margin. High-flux magmatism continued during this accretionary event at 100–80 Ma, which we associate with the final intra-oceanic arc accretion A dramatic reduction in magmatic flux occurred at ca. 78 Ma, which continued until ca. 55 Ma. We therefore associate a break-off age of 85–78 Ma in our current compilation, defining the top of the Idaho slab.

3.43. India - In

The India anomaly (Fig. 47) is located below India. The India anomaly was classified by Van der Voo et al. (1999b) as the 'II' anomaly, by Replumaz et al. (2010c) as the 'TH' anomaly, and it was also identified by Hafkenscheid et al. (2006), Li et al. (2008), and van Hinsbergen et al. (2012). The India anomaly is widely interpreted to represent Neotethyan oceanic lithosphere that subducted below the southern Tibetan Plateau before the inception of India-Asia collision. Initiation of its subduction probably occurred after the collision of the Lhasa terrane with the Qiangtang terrane of central Tibet, which occurred ~130 Ma–120 Ma ago (Yin and Harrison, 2000; Kapp et al., 2007; Li et al., 2017). Subduction of the India slab generated the long-lived Gangdese volcanic arc on the Lhasa terrane since early Cretaceous time (Ji et al., 2009) and was associated with the formation of supra-subduction zone ophiolites in the Lhasa forearc (Huang et al., 2015; Maffione et al., 2015b). We date the base of the India slab at 130 ± 10 Ma and note that this is a minimum age. The top of the slab coincides in age with that of the base of the Himalaya slab of 43 ± 8 Ma (Section 3.38), the subduction of which accommodated India-Asia convergence after break-off of the India slab.

3.44. Izu-Bonin - IB

The Izu-Bonin anomaly (Fig. 48) is interpreted to reflect Pacific lithosphere that subducted beneath the Philippine Sea Plate. It is well-imaged in seismic tomographic models of van der Hilst et al. (1991), Bijwaard et al. (1998), Gorbatov and Kennett (2003), Widiyantoro et al. (1999), Sugioka et al. (2010), Fukao and Obayashi (2013), and Jaxybulatov et al. (2013) and extends from the present-day Izu-Bonin-Mariana trench to the base of the upper mantle, where it is horizontally overlying the 660 km discontinuity. The Izu-Bonin slab is connected to the Mariana slab (Section 3.57) in the upper 300–400 km of the mantle, but is disconnected through a vertical slab tear at greater depth, allowing for the Mariana slab to penetrate steeply into the lower mantle (Miller et al., 2004, 2005). Previous reconstructions estimated subduction of the Mariana-Izu Bonin subduction zone to have started at 48 Ma (Seno and Maruyama, 1984) to 50 Ma (Wu et al., 2016).

The Mariana-Izu Bonin forearc has been instrumental in the development of models linking geochemical evolution of subduction-related magmas in a forearc position to subduction initiation (Stern and Bloomer, 1992; Dewey and Casey, 2011; Stern et al., 2012). U/Pb and $^{40}Ar/^{39}Ar$ ages of the oldest forearc lavas that are believed to have formed during subduction initiation are consistently 51–52 Ma (Ishizuka et al., 2011; Reagan et al., 2013; Arculus et al., 2015), which we adopt as age for the onset of subduction of the Izu-Bonin slab.

3.45. Juan de Fuca - JdF

The Juan de Fuca anomaly (Fig. 49) is located below western North America, is N–S trending and is interpreted to be the still-subducting slab at the Cascadia subduction zone. In tomographic studies it has been imaged to depths of 250–400 km (Sigloch et al., 2008; Schmandt and Humphreys, 2011; Chu et al., 2012). The Juan de Fuca slab has been interpreted as the result of the reinstatement of normal subduction following the accretion of the Siletzia microcontinent, and a subsequent period of flat-slab subduction (Schmandt and Humphreys, 2011). Above the slab lies the Cascadian arc, where magmatism started at 45–40 Ma (Schmandt and Humphreys, 2011; Wells and McCaffrey, 2013). The slab has been interpreted to be broken up by the Yellowstone plume (Obrebski et al., 2010; Long, 2016). Fragmentation of the slab presumably occurred just prior to the arrival of the plume at the surface, around 19–17 Ma (Obrebski et al., 2010. We adopt this as the age of the base of imaged slab. Some weak positive anomalies are imaged in the UU-P07 model towards the east and northeast, named the F1 and F2 slabs in Obrebski et al., 2010 and Long, 2016, which may represent the remnant slabs of 45–19 Ma subduction, separated from the Juan de Fuca slab by the Yellowstone plume.

3.46. Kabylides - Kb

The Kabylides anomaly (Fig. 50) is located in the upper mantle below the north African margin of Algeria and was first identified by Spakman and Wortel (2004). It dips steeply, resting on the 660 km discontinuity, and is interpreted as a slab that is detached above 200 km depth. The Kabylides anomaly is interpreted to represent part of the African plate that subducted northward below the Baleares margin since ~85–45 Ma (van Hinsbergen et al., 2014) then still contiguous with the Gibraltar slab (Section 3.34). Subsequent roll-back led to southward retreat of the subduction zone, and underthrusting of the North African margin in Miocene time (Michard et al., 2006), followed by slab segmentation and further westward retreat of the Gibraltar slab (Section 34), leaving the Kabylides slab behind which subsequently detached from the north African margin (Spakman and Wortel, 2004; Michard et al., 2006; Chertova et al., 2014; van Hinsbergen et al., 2014). The age of slab break-off is estimated at 15–12 Ma, inferred from the end of African underthrusting below the leading edge of the European plate exposed in the Kabylides massifs, as well as break-off induced magmatism (Coulon et al., 2002; Michard et al., 2006).

3.47. Kalimantan - Ka

The Kalimantan anomaly (Fig. 51) is located below southeast Asia from the middle to the upper part of the lower mantle (Widiyantoro and van der Hilst, 1996, 1997; Rangin et al., 1999; Replumaz et al., 2004; Hall et al., 2008; Zahirovic et al., 2012; Fukao and Obayashi, 2013). It is frequently interpreted as one single slab together with the Sunda slab (Section 3.86). However, the Kalimantan anomaly is not present in the western part of the Sunda slab, where the Sunda slab does not penetrate the upper-lower mantle boundary (Hall and Spakman, 2015), and its tip lies just to the south of the Kalimantan anomaly. In addition, the Kalimantan slab is striking NE-SW, whereas the Sunda slab strikes WNW-ESE. This suggests that the Kalimantan anomaly results from a history of subduction north of, and starting earlier than the Sunda slab. Slabs to the east of the Kalimantan anomaly that started to subduct around 55–45 Ma, e.g., Izu-Bonin (Section 3.45), Mariana (Section 3.57), Arafura (Section 3.10), or Caroline Ridge (Section 3.23) still reside in the upper mantle or penetrated into the top of the lower mantle. The base of the Kalimantan anomaly is thus likely of Late Cretaceous or Paleogene subduction age. Hall (2012) concluded that westward subduction below west Sulawesi, Sumba, and Borneo (i.e. Kalimantan) started ~70–65 Ma, and ended 50–45 Ma, at which time subduction of the Sunda slab started to the south and west (Section 3.85). In addition,

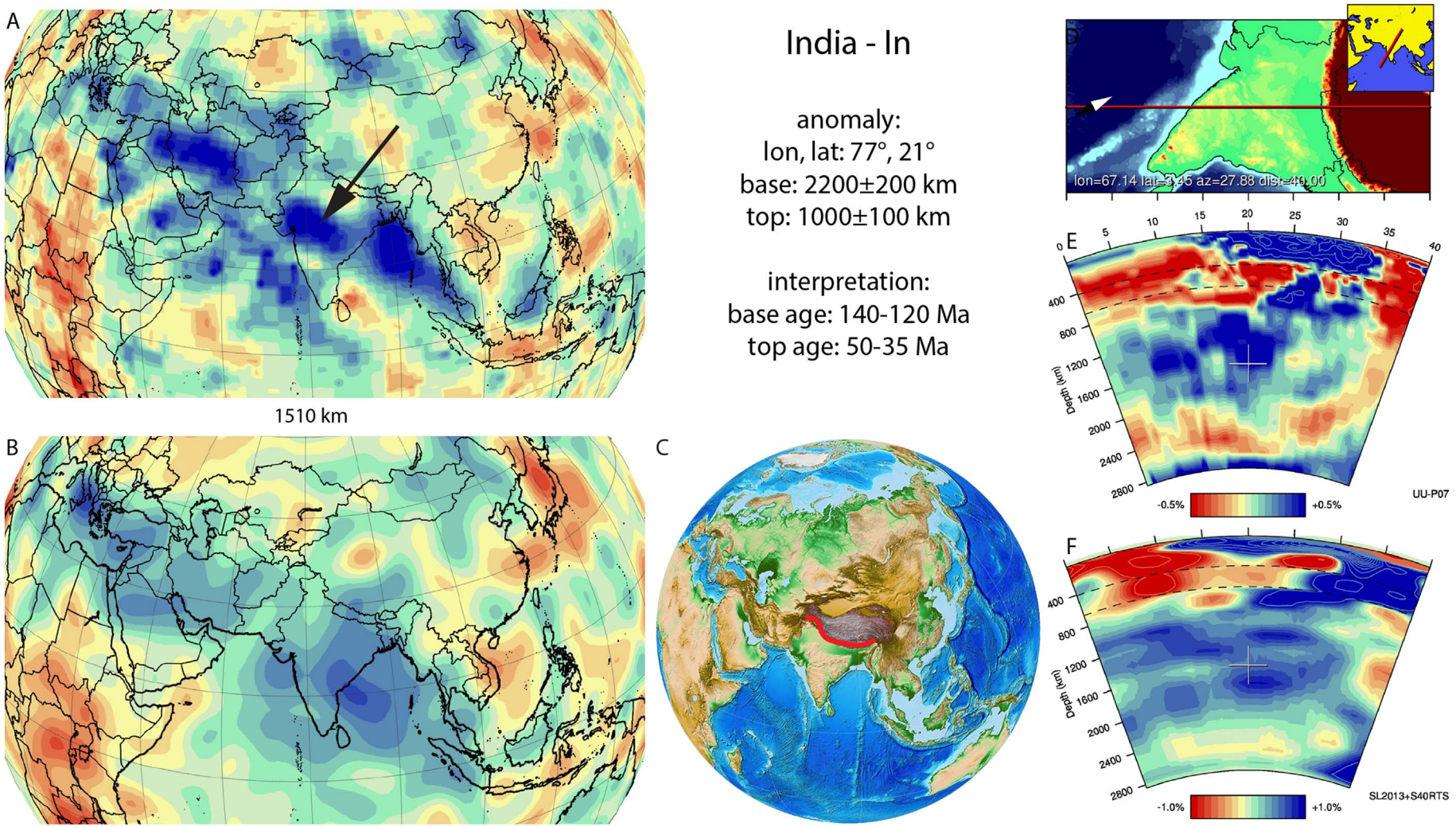

Fig. 47. India anomaly. Legend same as Fig. 5. Positive anomalies are identified in the same location in both tomographic models with a similar vertical extent and Relative amplitude strength. Lateral extent differs. The slab does not have identifiable dip.

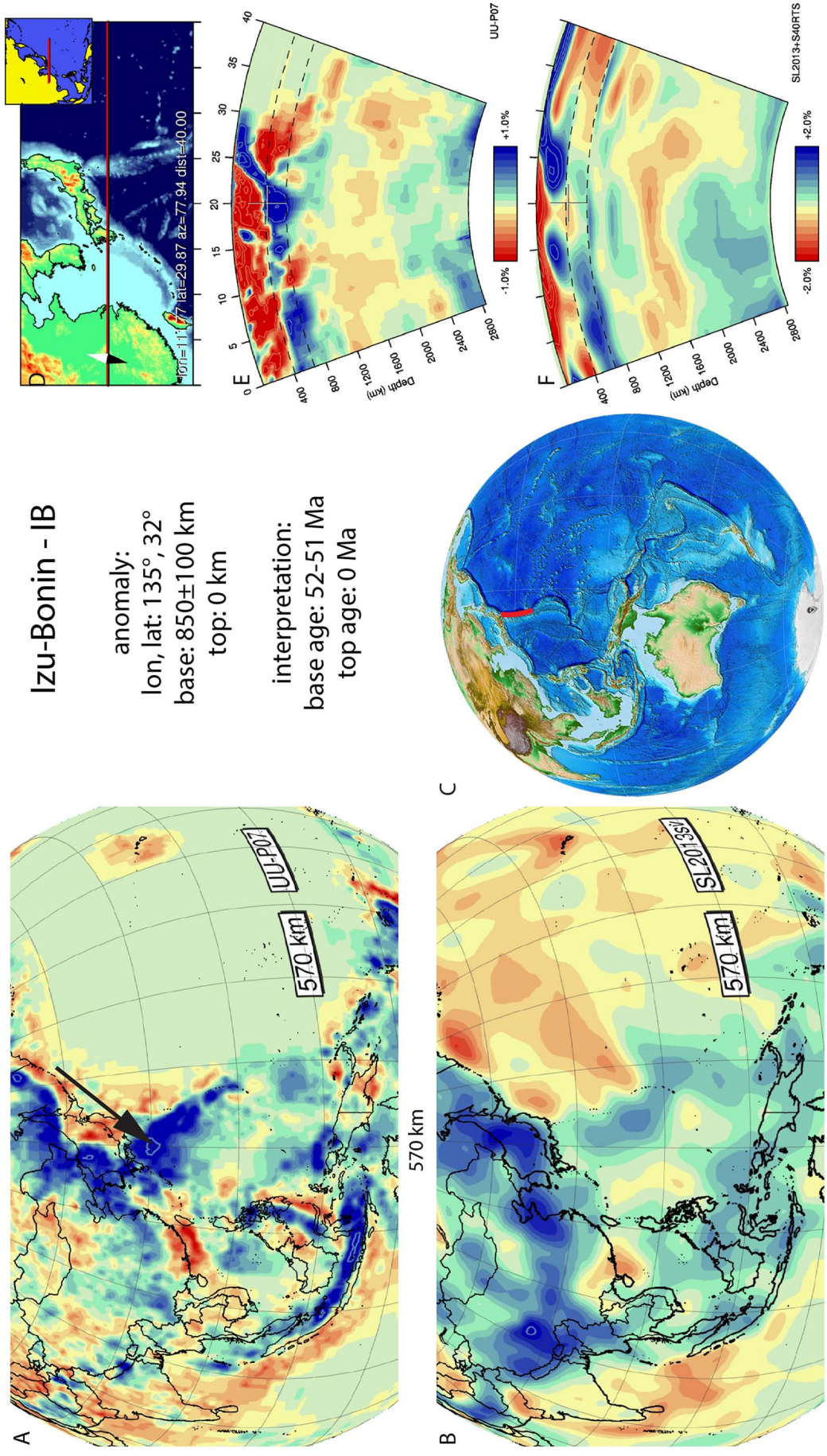

Fig. 48. Izu-Bonin anomaly. Legend same as Fig. 5. This slab is well imaged in the UU-P07 model and shows a clear dip trend. Relative amplitude strength, lateral extent and vertical extent are very different between models.

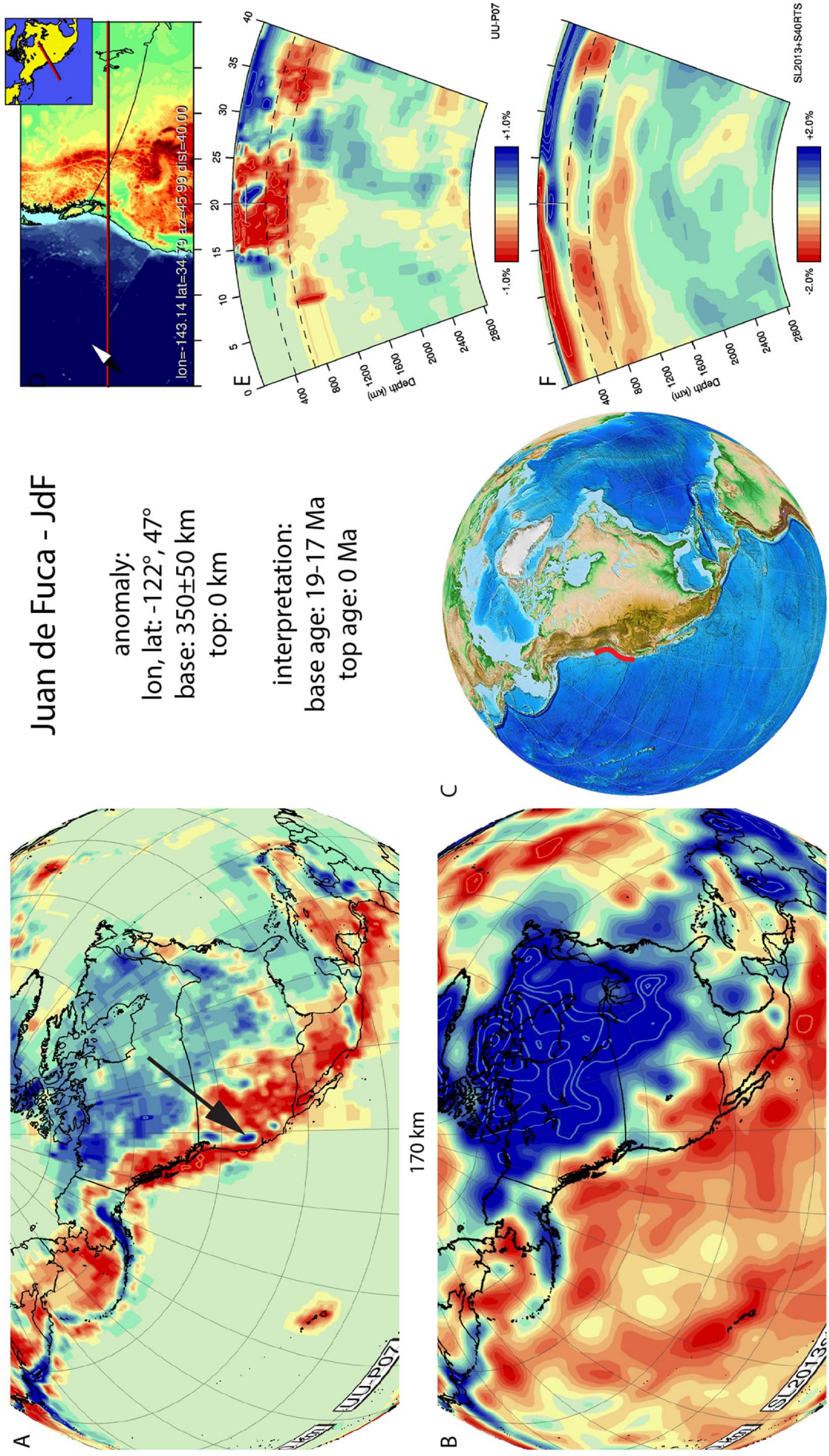

Fig. 49. Juan de Fuca anomaly. Legend same as Fig. 5. This slab is well imaged in the UU-P07 model and shows a clear dip trend. Relative amplitude strength, lateral extent and vertical extent are very different between models.

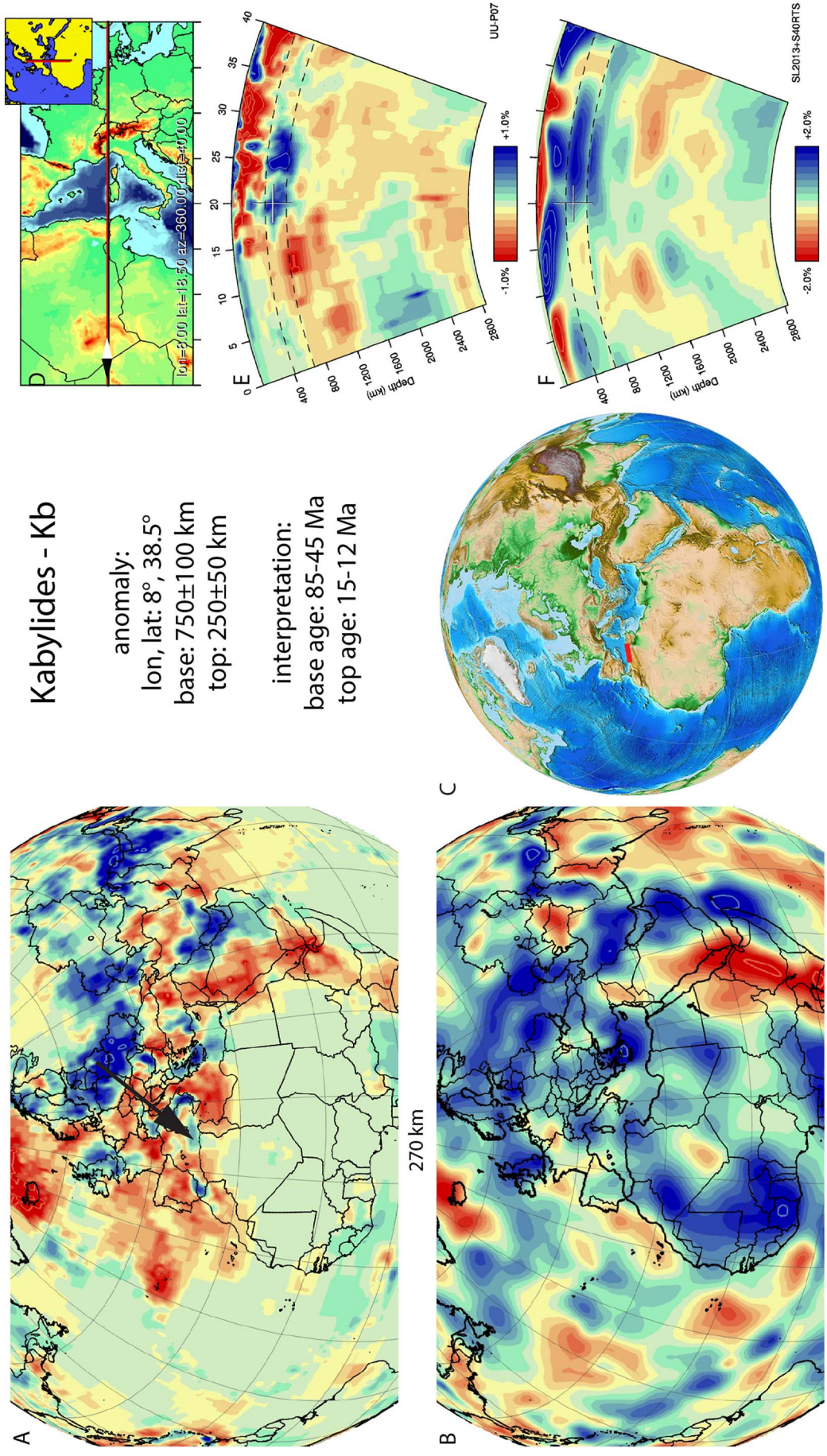

Fig. 50. Kabylides anomaly. Legend same as Fig. 5. This slab is well imaged in the UU-P07 model and there is a similar relative amplitude strength, lateral extent and vertical extent are very different between models. This slab has a dip in the upper mantle, but appears to flat-lying in the shallow lower mantle.

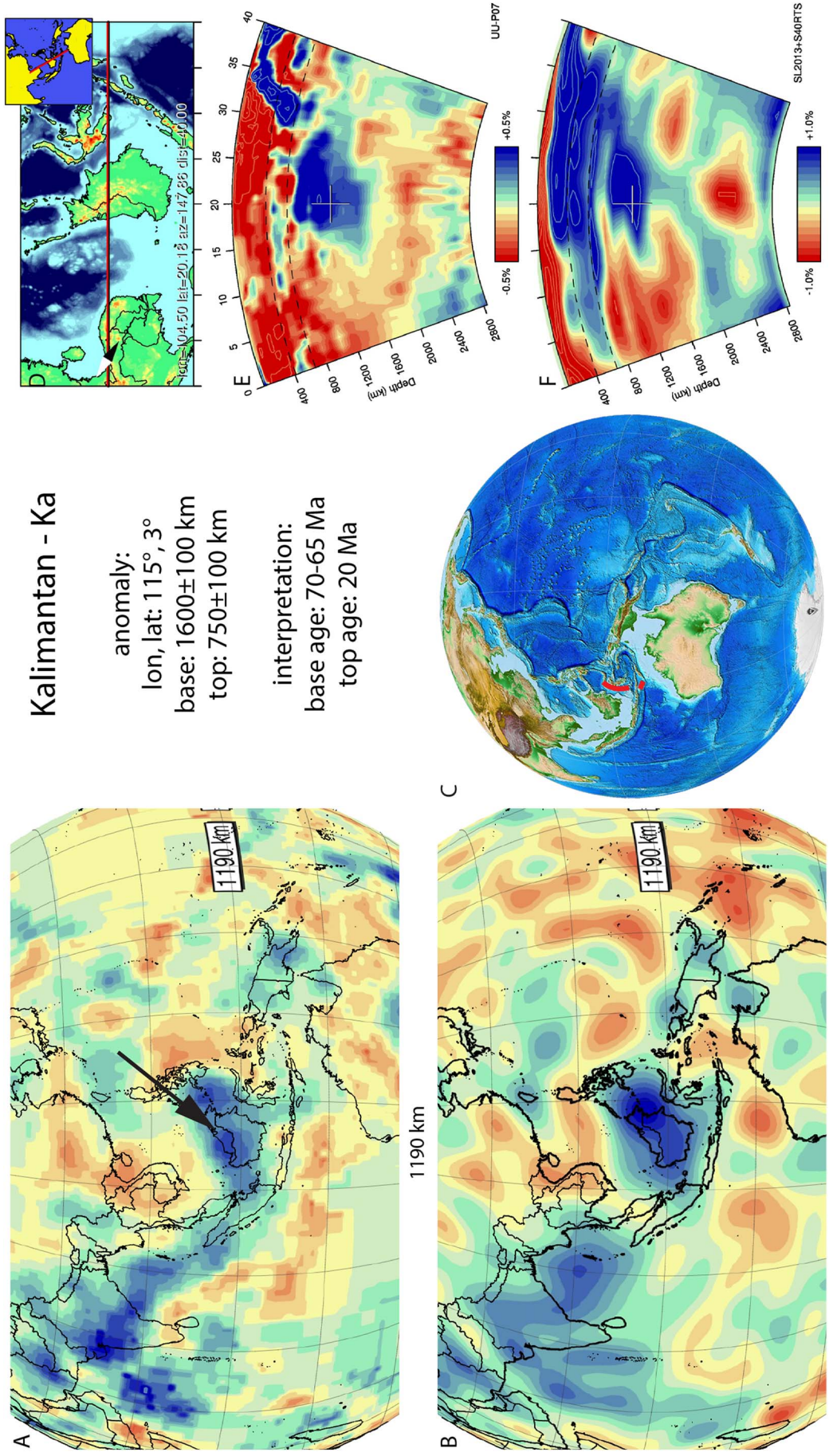

Fig. 51. Kalimantan anomaly. Legend same as Fig. 5. Relative amplitude strength, vertical and lateral extent are very similar between tomographic models. The slab does not have a dip trend.

Hall and Spakman (2015) suggested that the Kalimantan anomaly may host of two separate slabs, whereby the upper part of the anomaly represents subducted proto-South China Sea lithosphere that subducted southeastward beneath North Borneo and the Cagayan arc, now southeast of Palawan, between 45 and 20 Ma. This interpretation was adapted by Wu et al. (2016), where the western part of the anomaly was marked as Proto South China Sea and the east as one of two western East Asian Sea anomalies, subducting between 45 and 35 Ma and 50–20 Ma respectively. Wu et al., 2016 distinguished another slab in between these anomalies and named it Molucca Sea West, being a continuation of the slab in the upper mantle, with an interpreted start of subduction at 30 Ma. In the UU-P07 model it is not possible to confidently distinguish the boundary between these two or three slabs, and we adopt an age range of subduction of 70–65 to 20 Ma for the composite the Kalimantan slab(s).

3.48. Kamchatka-Kuriles - Kc

The Kamchatka-Kuriles anomaly (Fig. 52) is located below the Sea of Okhotsk and is interpreted to represent a slab that is still subducting at the Kamchatka-Kuriles subduction zone, penetrating down to the upper part of the lower mantle. We previously named it the Kamchatka slab (van der Meer et al., 2010) but renamed it to include the widely used Kuriles slab (Spakman et al., 1989; Van der Hilst et al., 1991; Gorbatov et al., 2000; Jiang et al., 2009; Koulakov et al., 2011). It represents northwestward-subducted Pacific oceanic lithosphere. The part of the slab below 660 km discontinuity was interpreted to have an age of at least 65–55 Ma (Gorbatov et al., 2000). Nokleberg et al. (2000) and Golonka et al. (2003) proposed that the onset of westward subduction below Kamchatka started earlier and formed the Olyutorka arc since the middle to Late Cretaceous. van der Meer et al. (2010) followed that latter interpretation. Following the more recent tectonic models of Konstantinovskaia (2001), Hourigan et al. (2009), and Shapiro and Solov'ev (2009), accretion of the intra-oceanic Aichayam-Valangskyi ophiolite terrane including the Olyutosky arc to the Asian continental margin followed upon a phase of SW-ward subduction that ended around 52 Ma (Konstantinovskaia, 2001; Hourigan et al., 2009), which we correlate to the Agattu slab (Section 3.2). This was followed by a subduction polarity reversal and onset of NW-ward subduction of Pacific lithosphere during the Middle Eocene (Konstantinovskaia, 2001; Shapiro and Solov'ev, 2009), simultaneously with the Aleutian slab (Section 3.3) to the northeast, which we interpret to as the age of the base of the Kamchatka-Kuriles slab.

3.49. Komsomolets - Km

The Komsomolets anomaly (Fig. 53) is located below northernmost Asia within the deep mantle and was not previously defined. It is E–W trending and its shallowest and easternmost location it may connect to the Chukchi slab (Section 3.28). Based on the Chukchi slab as well as the Mongol-Kazakh slab to the south (Section 3.63), we interpret the anomaly as a Lower Mesozoic slab subducted in the paleo-Arctic region. In the Arctic, a record of mid-Mesozoic subduction, along a continental margin, is preserved in the form of the Svyatoy-Nos arc located in northernmost Siberia (Nokleberg et al., 2000). According to Nokleberg et al. (2000) and Sokolov (2010) this arc was active in the Late Jurassic to Early Cretaceous and was part of a south dipping subduction zone, subducting South Anyui oceanic lithosphere. We date the subduction of the Komsomolets slab by this arc. In the reconstruction of Shephard et al. (2013) the Svyatoy-Nos arc is not modelled as such but would be located as the time-equivalent continuation of the Oloy subduction zone in between Siberia and Baltica.

3.50. Lake Eyre - LE

The Lake Eyre anomaly (Fig. 54) was defined by Schellart and Spakman (2015). It is located at 800–1200 km depth in the upper part of the lower mantle below southern Australia. There is no record of Mesozoic or Cenozoic subduction within Australia, and pointing at a rapid northward absolute plate motion of Australia suggested by hotspot reference frames, Schellart and Spakman (2015) suggested that the geological record of subduction of the Lake Eyre slab is best sought along the northern Australian margin. Those authors correlated the slab to a period of northward intra-oceanic subduction that started ~70 Ma ago north of Australia. This phase terminated when Australian continental lithosphere arrived in the trench. Relics of the overriding oceanic lithosphere are now found as ophiolites on Papua New Guinea and the Pocklinton Trough area. The end of their emplacement onto the Australian margin occurred around 50 Ma and was suggested as timing of slab break-off (Schellart and Spakman, 2015). Subsequently, Australia moved northward and overrode the detached slab.

3.51. Lougheed - Lo

The Lougheed anomaly (Fig. 55) is located below northernmost North America within the mid-mantle. It is N–S to NNW–SSE trending and at its southern end lies close to, but is separate from the NW-SE trending Hudson anomaly that is correlated to the Stikinia arc in northwest Canada (Section 3.41). The Lougheed slab should thus correlate to circum-Arctic subduction to the north of the Stikinia terrane. Nokleberg et al. (2000) documented the Koyukuk arc in this area and interpreted this as the result of subduction of Angayucham and Goodnews Ocean lithosphere below North American continental lithosphere. The Koyukuk arc is mainly of Late Jurassic to Early Cretaceous age. In the plate motion model of Shephard et al. (2013), these different elements were brought together. They concluded that subduction below the Koyukuk and the adjacent Nutesyn arcs was active between 160 and 120 Ma, which we adopt for the subduction age range of the anomaly.

3.52. Maldives - Md

The Maldives anomaly (Fig. 56) is located below the northwestern Indian Ocean from the deep mantle up to the upper part of the lower mantle. In previous tomographic studies it has been referred to as the eastern part of the III anomaly (Van der Voo et al., 1999b) or as the IO anomaly (Hafkenscheid et al., 2006), and was interpreted to result from northward subduction within the Neotethys ocean. We now distinguish the deeper NW-SE trending Maldives anomaly from the shallower SW-NE Carlsberg slab (Section 3.22) (Gaina et al., 2015), which were previously considered a single feature (van der Meer et al., 2010). van der Meer et al. (2010) interpreted an onset of subduction of this anomaly to occur as early as the Late Triassic comparing to reconstructions of Stampfli and Borel (2004), which we now consider unlikely given the adjacent Carlsberg, India (Section 3.43), and Arabia (Section 3.9) slabs that subducted in Cretaceous time. More recently, the age of the Maldives slab was interpreted from geological evidence of intra-oceanic subduction from ophiolites found in the Indus-Yarlung suture zone, thrust on the Tibetan Himalaya (e.g., Spontang and Xigaze ophiolites) (Hébert et al., 2012). These were suggested to have formed at equatorial latitudes based on paleomagnetic data (Abrajevitch et al., 2005), and were interpreted to have thrust onto the Tibetan Himalaya around 70 Ma based on arrival of mafic debris in the Tibetan Himalayan stratigraphy around that time (Searle et al., 1997; Corfield et al., 2001). Because paleomagnetic data of the Tibetan Himalaya also show equatorial latitudes around 70 Ma (Patzelt et al., 1996), van Hinsbergen et al. (2012) linked the record of the Himalayan ophiolites to the Maldives anomaly.

Recently, however, Garzanti and Hu (2015) demonstrated that the ~70 Ma mafic debris in the Tibetan Himalaya is not ophiolite-derived, but related to plume volcanism, perhaps from early-stage volcanics of the Deccan traps. Ophiolite-derived debris did not arrive in the Tibetan Himalayan stratigraphy until the Early Eocene instead. In

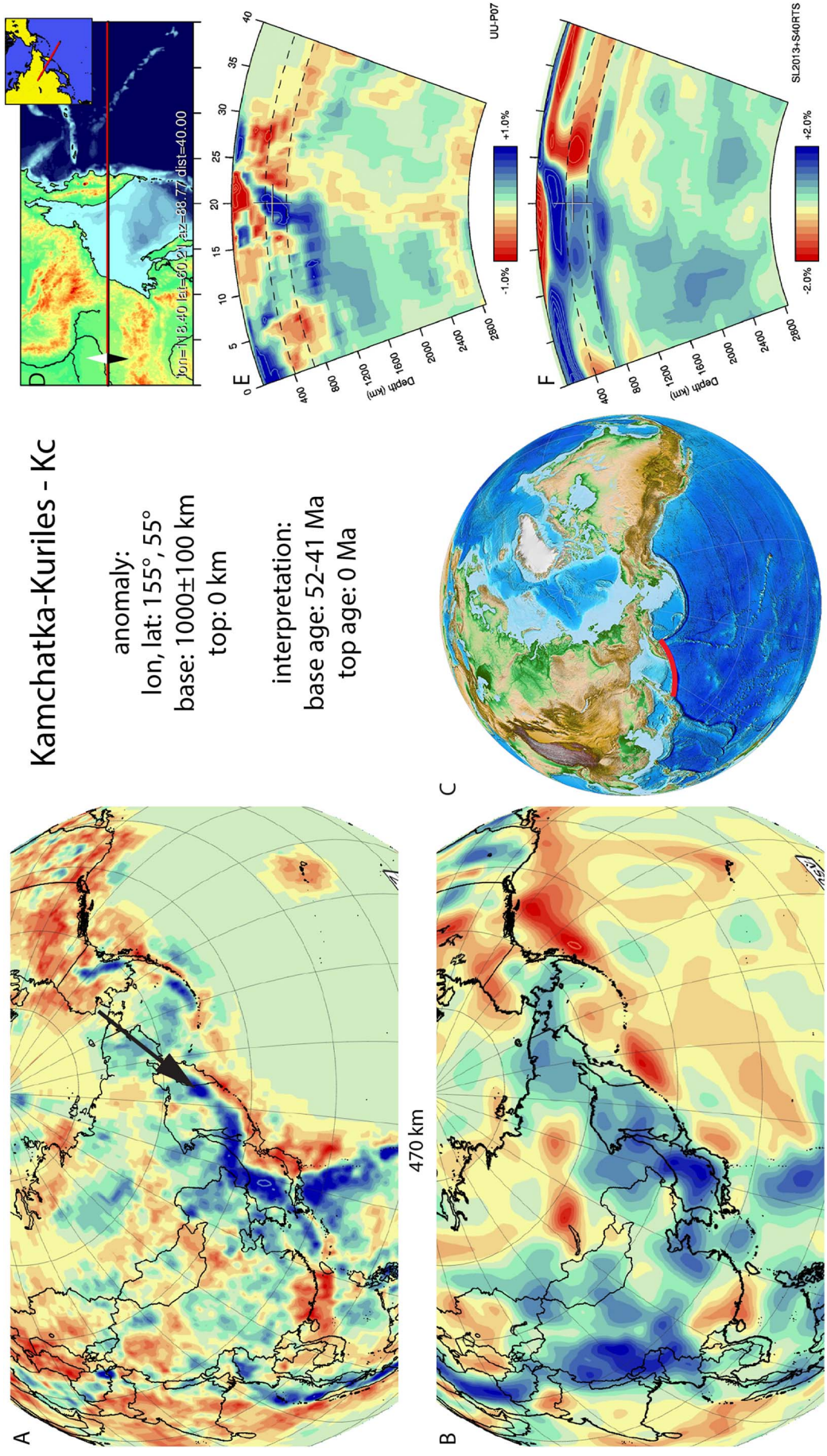

Fig. 52. Kamchatka-Kuriles anomaly. Legend same as Fig. 5. This slab is well imaged in the UU-P07 model and there is a similar Relative amplitude strength, lateral extent and vertical extent are very different between models. This slab appears to flat-lying on top of the transition zone.

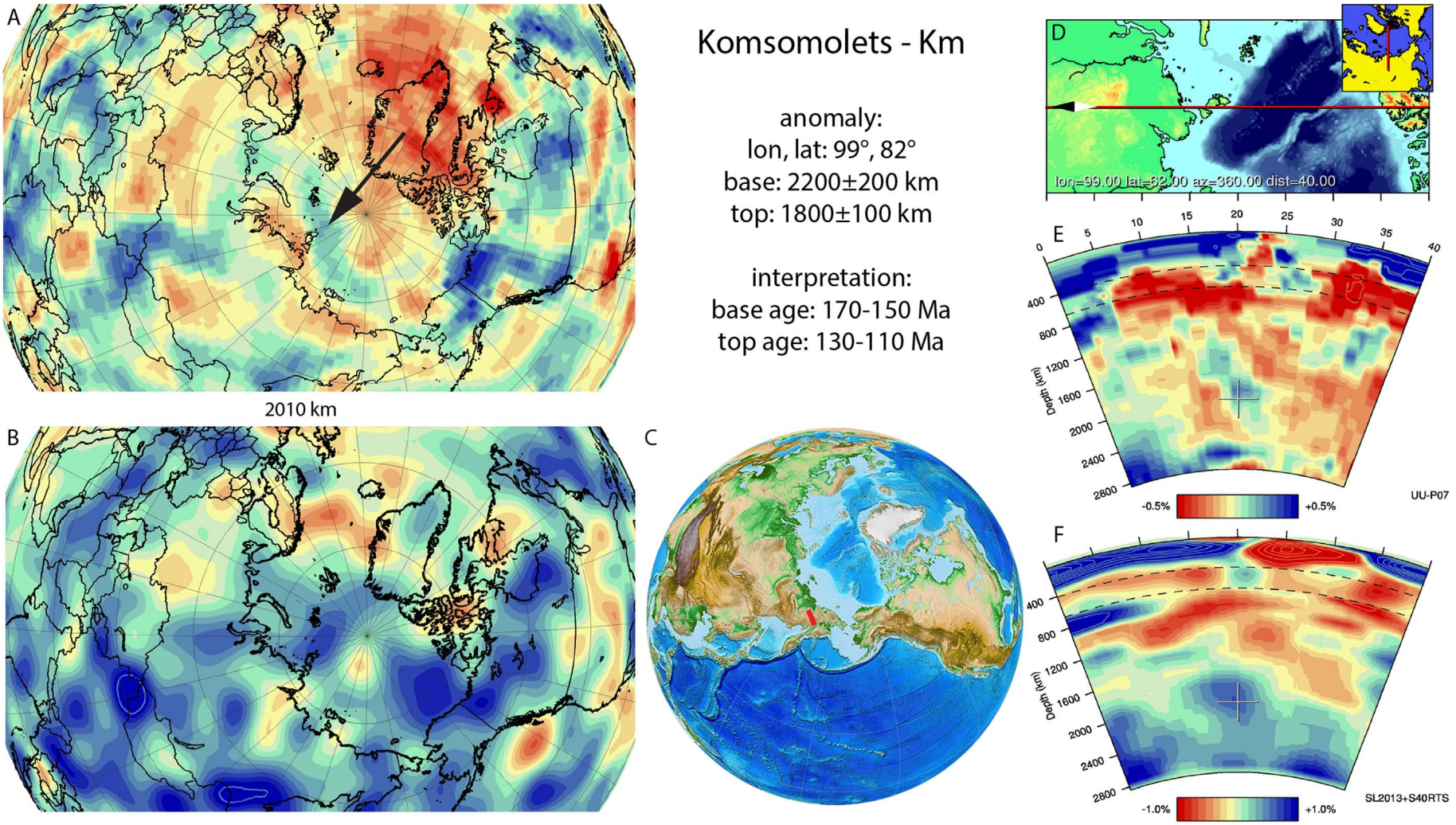

Fig. 53. Komsomolets anomaly. Legend same as Fig. 5. Positive anomalies are identified in the same location in both tomographic models with a similar vertical extent. Relative amplitude strength and lateral extent differ between tomographic models.

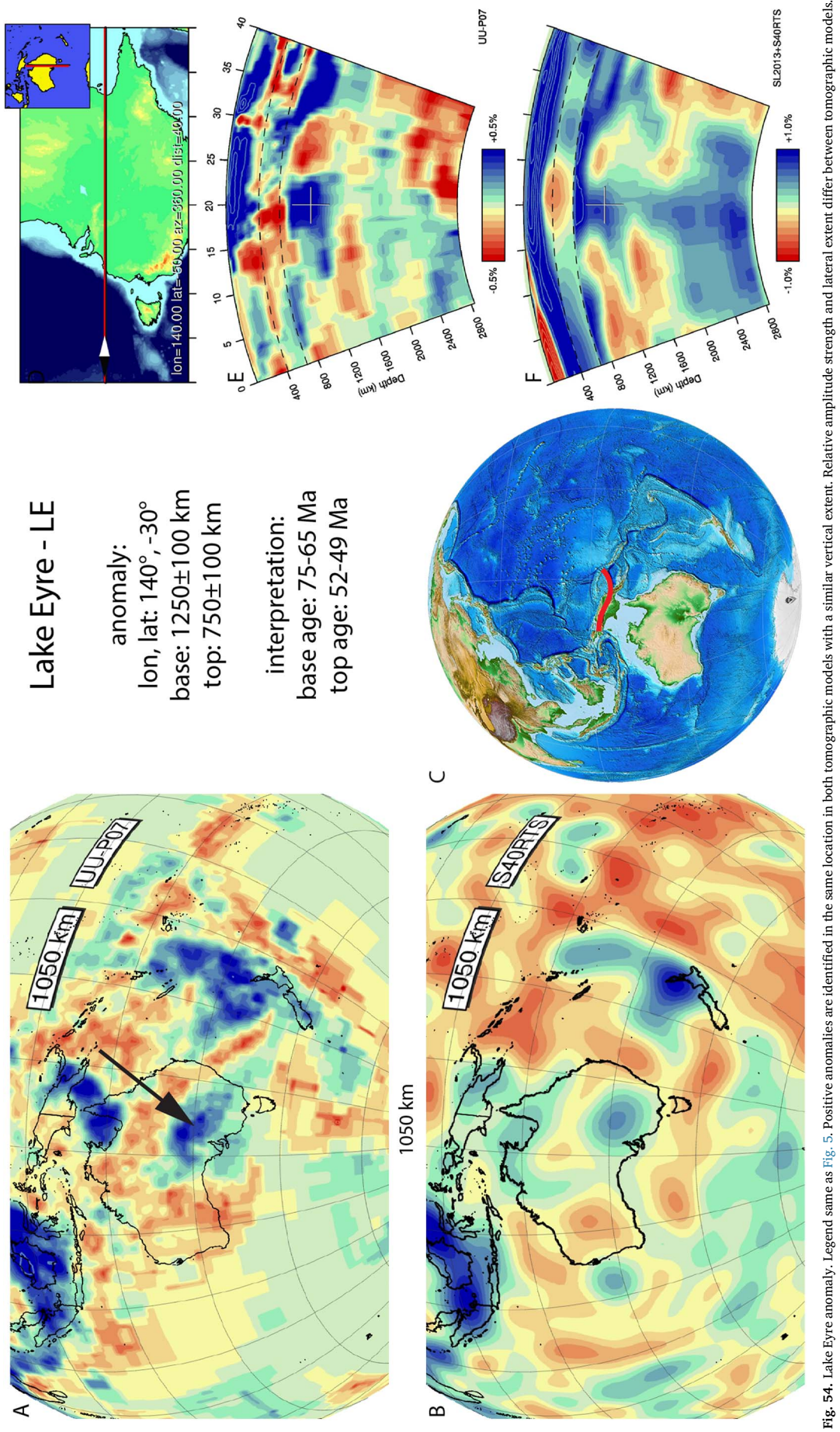

Fig. 54. Lake Eyre anomaly. Legend same as Fig. 5. Positive anomalies are identified in the same location in both tomographic models with a similar vertical extent. Relative amplitude strength and lateral extent differ between tomographic models.

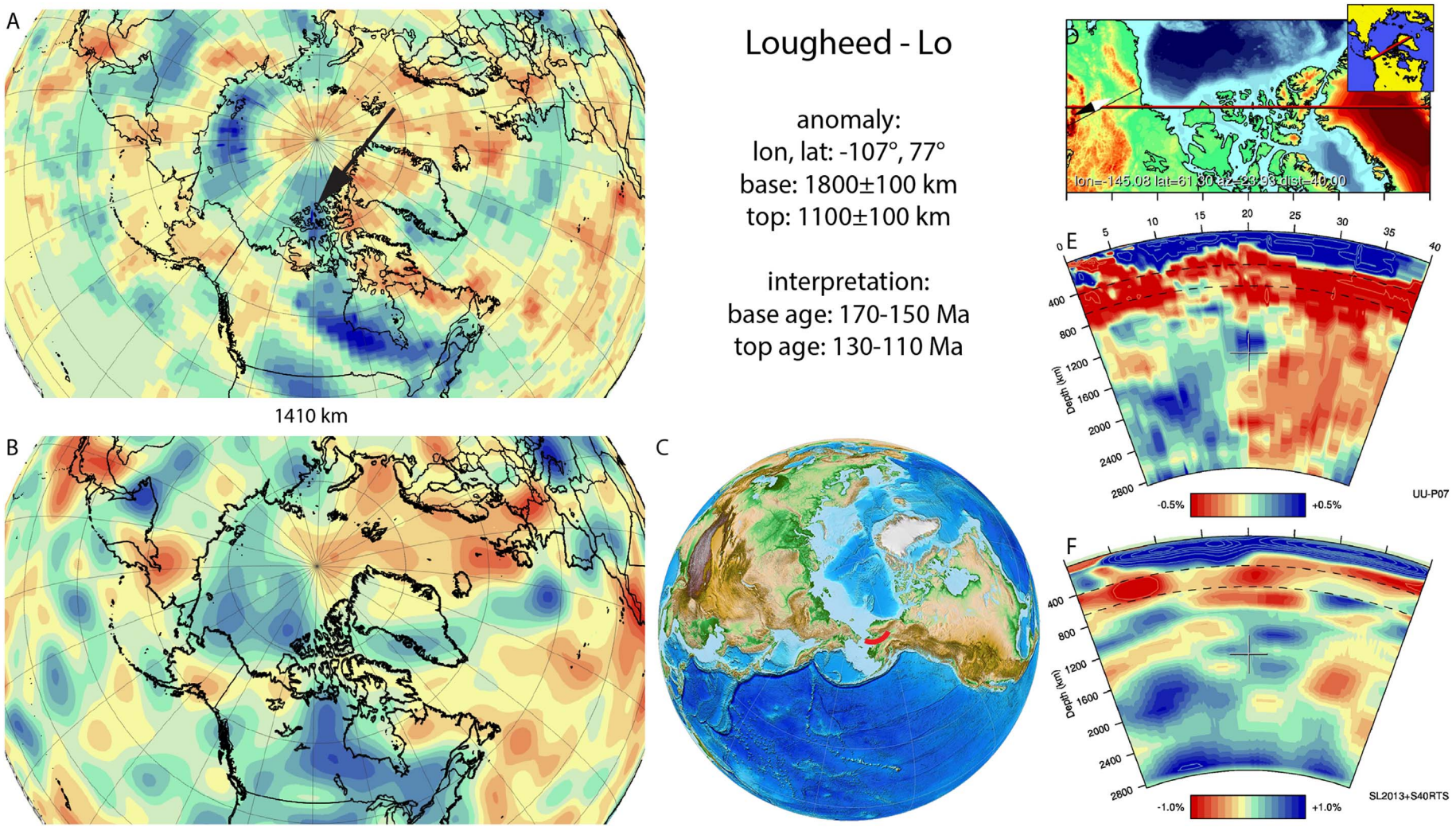

Fig. 55. Lougheed anomaly. Legend same as Fig. 5. Positive anomalies are identified in the same location in both tomographic models with a similar vertical, lateral extent and Relative amplitude strength.

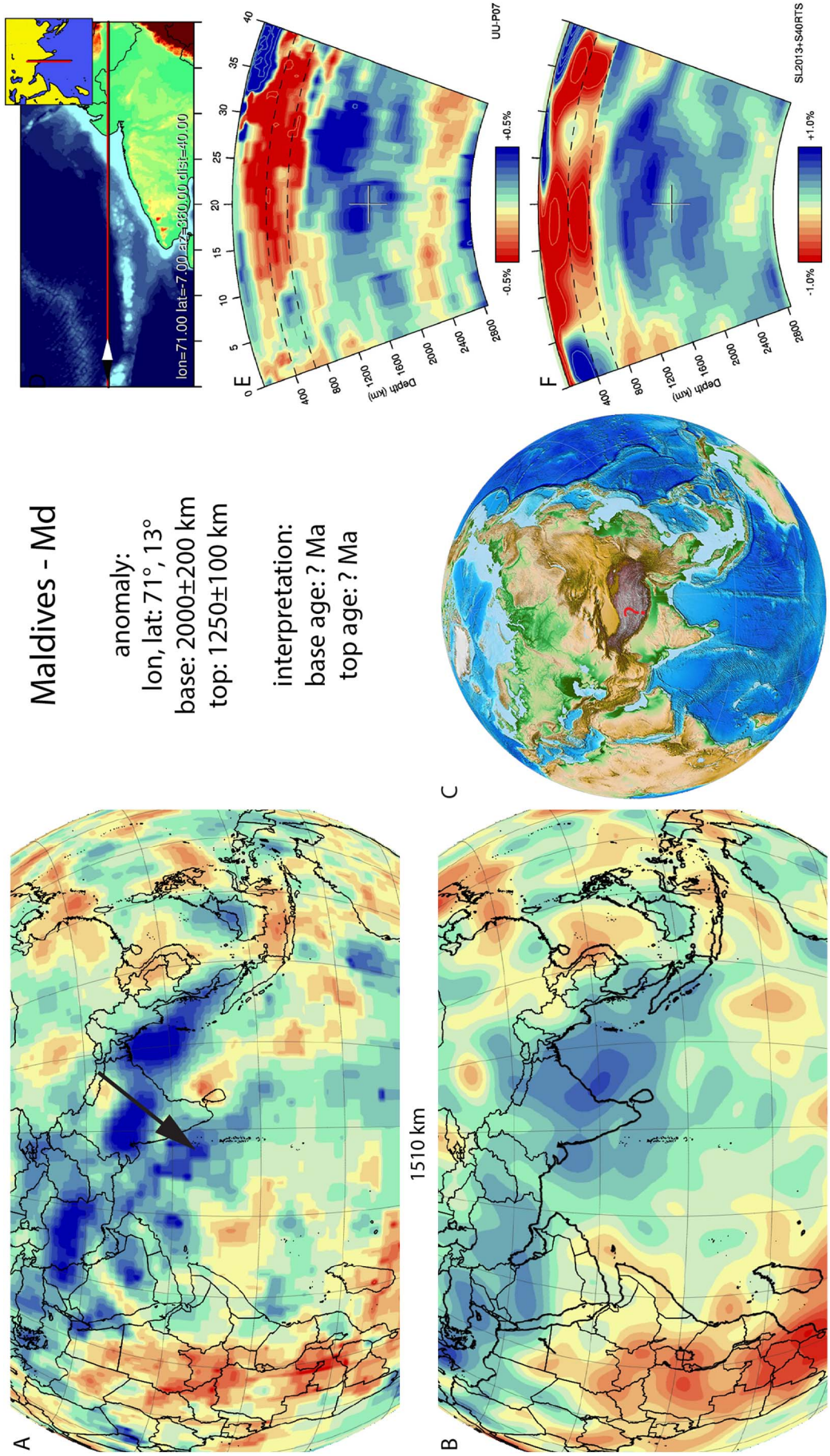

Fig. 56. Maldives anomaly. Legend same as Fig. 5. Positive anomalies are identified in the same location in both tomographic models with a similar vertical extent. Relative amplitude strength and lateral extent differ between tomographic models.

addition, Huang et al. (2015) showed that the Xigaze ophiolites are unconformably overlain by Tibet-derived forearc sediments with ages very close to the formation ages of the ophiolite (~130–125 Ma). In addition, they showed that the previous paleomagnetic data of Abrajevitch et al. (2005) were strongly affected by compaction-induced inclination shallowing, and provided a ~16.5°N paleolatitude for these ophiolites instead, i.e. immediately adjacent to the south Tibetan margin. Its current depth in the mantle is consistent with Cretaceous subduction, and when the global plate circuit (e.g., Seton et al., 2012) is cast in a hotspot reference frame (e.g., Doubrovine et al., 2012), the Maldives anomaly is located within the Neotethys ocean below the India-Arabia plate boundary. At this plate boundary, there is evidence of subduction farther south, culminating in obduction of the Waziristan-Khost ophiolite onto Arabia around 80 Ma (e.g., Gaina et al., 2015). The nearest record of intra-oceanic subduction may be the Kohistan arc, and Jagoutz et al. (2015) argued for a low latitude of Cretaceous subduction below this arc. Borneman et al. (2015), however, documented Asia-derived detritus from Cretaceous sandstones within the Kohistan stratigraphy, arguing against such a scenario. At this stage, we therefore refrain from interpreting a geological record of subduction for the Maldives anomaly.

3.53. Malpelo - Mp

The Malpelo anomaly (Fig. 57) is located below the western Panama Basin and NW South America in the mid-mantle. It is NW-SE trending and above 1175 km it is close to the Venezuela slab to the east (Section 3.90) as well as the Cocos slab to the north (Section 3.29) and Brasilia slab to the south (Section 3.18). The anomaly we here define as the Malpelo slab was previously interpreted by Taboada et al. (2000) to represent subducted Farallon plate lithosphere (labelled FaP in their figures), beneath the Panama-Costa Rican Arc and the Choco terrane in northwest South America. Meschede and Frisch (1998) proposed that this subduction zone extended to the north, and connected to the subduction zone below the Guerrero terrane and Chortis block, which are now located in present day Honduras, Guatemala, and Mexico. Because the Malpelo slab appears to have a slight westward dip, van der Meer et al. (2010, 2012) followed models of Dickinson and Lawton (2001) proposed for the Guerrero arc and interpreted the slab as the result of westward subducting Mezcalera ocean lithosphere, followed by a collision with the North American margin in the Late Cretaceous, followed by a subduction polarity switch resulting in eastward subducting Farallon lithosphere at around 1040 km depth.

The Malpelo slab, however, extends to the south into a position directly west of, and at a similar depth as the Venezuela slab (Section 3.90). This slab is interpreted to result from westward subduction of Proto-Caribbean lithosphere below the Caribbean plate (van der Meer et al., 2010; Pindell et al., 2012; van Benthem et al., 2013). Placing the kinematic reconstruction of Boschman et al. (2014) in the slab-fitted mantle reference frame of van der Meer et al. (2010) places the eastern margin of the Caribbean plate above the Venezuela slab, but the western Caribbean margin above the Malpelo slab: there is little space for a westward subducting ocean to the East of the Malpelo slab. We therefore consider it more likely that the Malpelo slab originated from eastward subduction west of the Caribbean plate.

The oldest reported evidence of subduction in Central America is arc volcanics of only ~75 Ma (Buchs et al., 2010; Wegner et al., 2011), and Pindell et al. (2012) suggested that the modern subduction zone below the eastern Caribbean region may have started ~90–85 Ma. This subduction zone, however, is still active whilst the Malpelo slab is detached. We consider it more likely that the current phase of subduction generated the slab above and slightly east of the Malpelo slab. This slab is visible in a narrow depth interval around 1000–900 km, above which a prominent slab gap is present that coincides with the location of and may be caused by the subduction of the Cocos-Nazca ridge. Given its narrow range, we have not defined this body as a separate slab.

The Guerrero arc of Mexico may be a better candidate to date the Malpelo slab. This arc formed at a paleolatitude coinciding with the northern portion of the Malpelo slab. The history of the Guerrero arc is complex, but is seen as an intra-oceanic arc that was separated from Mexico by a back-arc region that closed in Early Cretaceous time (Centeno-Garcia et al., 2011). Bajocian–Cenomanian arc assemblages of the Guerrero terrane (Talavera-Mendoza et al., 2007; Martini et al., 2011, 2013) and Callovian to Valanginian volcanic sulphides (Mortensen et al., 2008) suggest that the arc was active from ~170–165 to ~95–90 Ma. We adopt this as age range for the formation of the slab. We note, however, that our interpretation suggests that the Guerrero arc would have continued far to the south, to the west of the Caribbean plate. Currently, there is no geological evidence to support this interpretation and the interpretation of the geological record of the Malpelo slab may need revision in the future.

3.54. Manchuria - Mc

The Manchuria anomaly (Fig. 58), also referred to as Japan anomaly (Obayashi et al., 2009) was interpreted as a slab that dips down westward from the Japan subduction zone at surface, drapes the transition zone below east Asia and penetrated the upper part of the lower mantle in the west (van der Hilst et al., 1991; Fukao et al., 2001; Miller and Kennett, 2006; Abdelwahed and Zhao, 2007; Zhao and Ohtani, 2009; Lei, 2012; Chen et al., 2017). In the uppermost mantle it has a N–S trend and is connected at depths of < 300 km with the SW-NE trending Kamchatka-Kuriles slab (Section 3.48) towards the north and NNW-SSE trending Izu-Bonin slab (Section 3.44) towards the south. It has previously been associated with westward subduction of the Pacific and Philippine Sea plate starting around 40–45 Ma (van der Hilst et al., 1991; Abdelwahed and Zhao, 2007). This timing was based on the evolution of the Philippine Sea plate only, whereas the Manchuria slab is in fact located north of the Philippine Sea plate subduction zones. In van der Meer et al. (2010), we considered an earlier, Late Cretaceous start of Pacific plate subduction more likely, indicated by a Late Cretaceous-Eocene (110–50 Myr) magmatic phase in the Korean peninsula (Sagong et al., 2005).

The complications of dating this slab might be related to two ridges subducting underneath Japan as documented by Isozaki et al. (2010); first the Izanagi–Kula ridge around 120–110 Ma and then the Kula-Pacific ridge around 70–60 Ma. Ren et al. (2002) documented tectonic inversion in the Songliao Basin (NE China) at 77–67 Ma, which may date the onset of renewed subduction following ridge subduction, followed by widespread regional extension and transtension as a result of roll-back. More recently Seton et al. (2015) and Honda (2016) have the Izanagi-Pacific ridge subducting between ~60–50 Ma. On the basis of the Korean inversion and the recently modelled subduction of the last subducted ridge,we interpret the onset of Manchuria slab subduction to start at 77–50 Ma and associate this timing with the base and westernmost extent of this slab.

3.55. Manila - Ml

The Manila anomaly (Fig. 59) is located below the northewestern Phillipine Sea in the upper mantle. The Manila anomaly dips down towards the transition zone at the base of the upper mantle and has previously been imaged in several regional and global tomographic studies (Rangin et al., 1999; Lallemand et al., 2001; Zhao and Ohtani, 2009; Zheng et al., 2013; Koulakov et al., 2014; Wu et al., 2016), named South China Sea slab (Rangin et al., 1999; Lallemand et al., 2001), or Eurasian slab (Zheng et al., 2013; Zhao and Ohtani, 2009; Wu et al., 2016). It is interpreted as eastward dipping South China Sea oceanic lithosphere of the Eurasian plate still subducting at the Manila trench below the Luzon arc. In the north, continental lithosphere of the South China block has entered the trench, which led to an arc-continent collision with the Luzon arc, creating the Taiwan fold-thrust belt (Sibuet

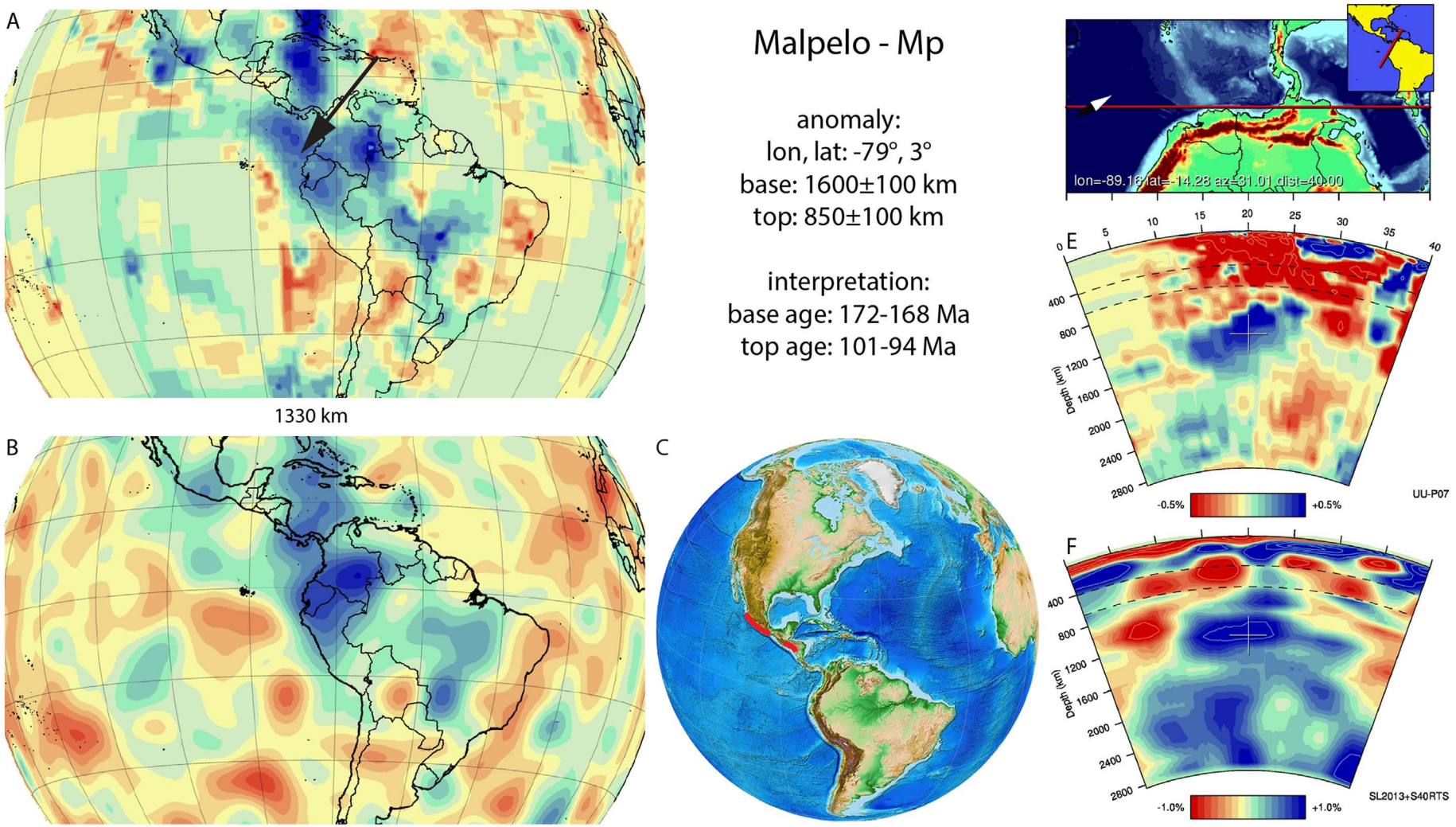

Fig. 57. Malpelo anomaly. Legend same as Fig. 5. Positive anomalies are identified in the same location in both tomographic models with a similar relative amplitude and vertical extent. Lateral extent differs between tomographic models. The slab appears to have a dip towards the SW in UU-P07.

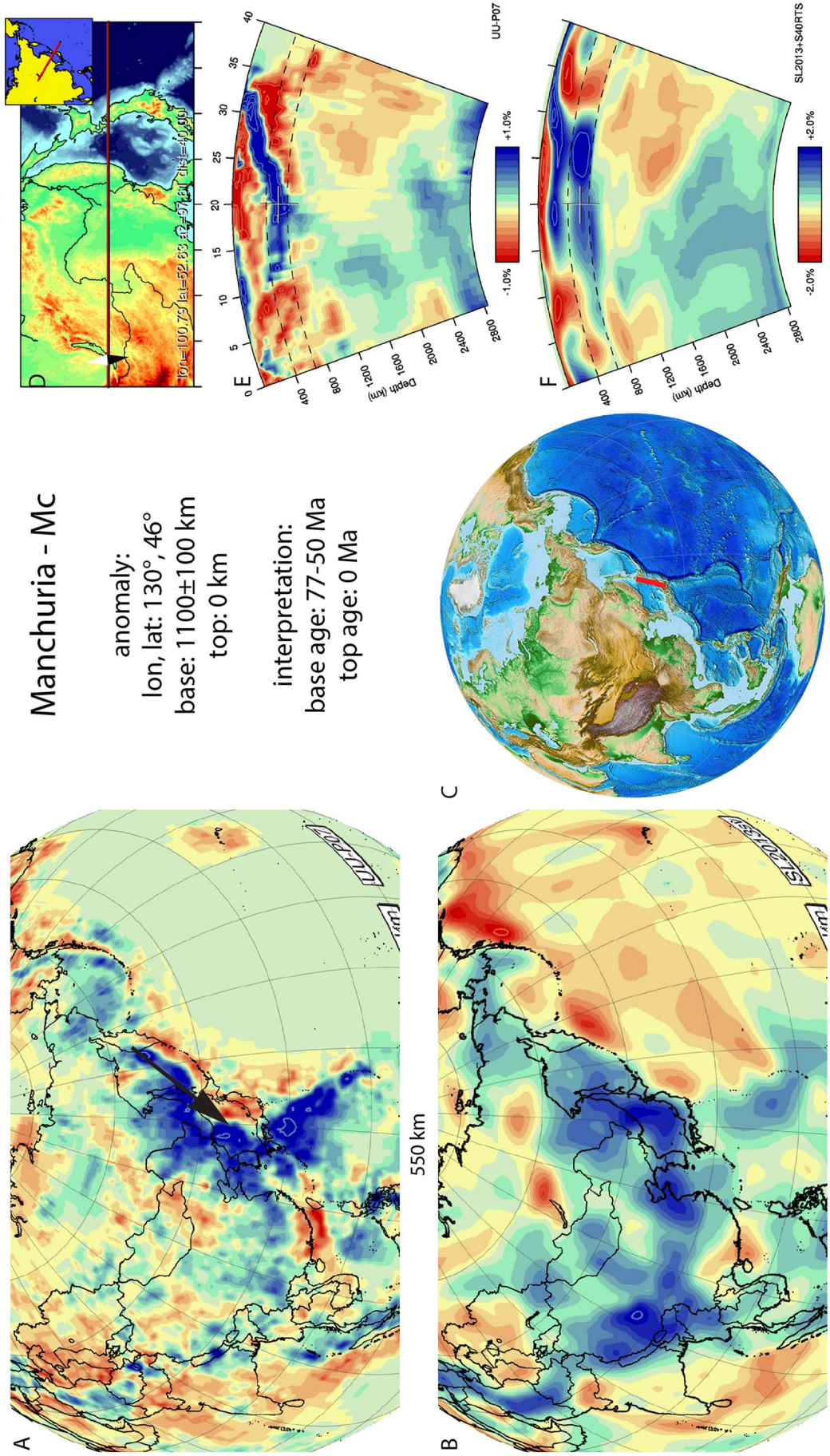

Fig. 58. Manchuria anomaly. Legend same as Fig. 5. This slab is well imaged in the UU-P07 model and there is a similar relative amplitude strength, lateral extent and vertical extent between models. This slab appears to mostly flat-lying on top of the transition zone.

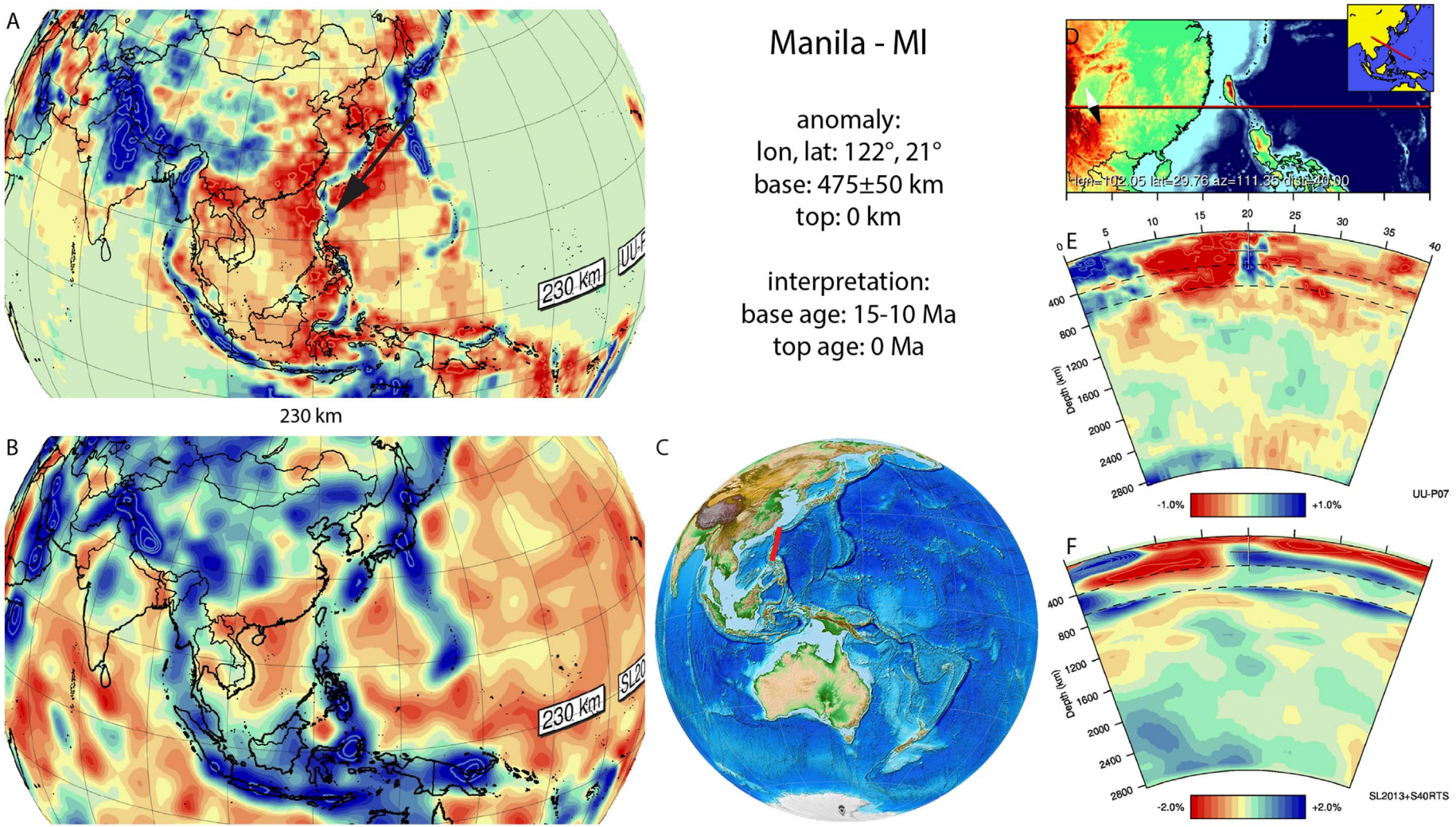

Fig. 59. Manila anomaly. Legend same as Fig. 5. This upper mantle slab is well imaged in the UU-P07 model and there is a similar relative amplitude strength, lateral extent. Vertical extent is different between models. This slab near-vertical in the upper mantle.

and Hsu, 2004; Huang et al., 2014). Due to Pliocene arc-continent collision, subduction in northern Taiwan is terminating and slab break-off is currently going on, whereby the Ryukyu subduction zone is propagating westwards, accommodating a subduction polarity flip (e.g., Ustaszewski et al., 2012). Estimates for the onset of Eurasian plate subduction below the Luzon arc are 15–10 Ma (Sibuet and Hsu, 2004; Hall, 2012), which we adopt for the age of the base of the Manila slab.

3.56. Maracaibo - Ma

The Maracaibo anomaly (Fig. 60) is located in the upper mantle below northern South America. It was first tomographically imaged by van der Hilst and Mann (1994), and was later recognized in tomographic models by Taboada et al. (2000), Bezada et al. (2010), and van Benthem et al. (2013). van Benthem et al. (2013) shows that the Maracaibo slab has a shallow dip, and is at least 900 km long from the surface to the base of the upper mantle. Another 300 km may horizontally overlie the 660 km discontinuity.

The Maracaibo subduction zone is interpreted as actively subducting Caribbean plate lithosphere that is overridden by the South American continent moving roughly W to WNW relative to the Caribbean plate, leading to oblique convergence along the NW South American continent (Kellogg and Bonini, 1982). Originally, the onset of Maracaibo subduction was estimated as ~45 Ma (Kellogg and Bonini, 1982), but recently, Ayala et al. (2012) showed that sedimentary basins in NW South America became fragmented because of uplift and deformation of the Maracaibo block as early as 58–55 Ma. Plate kinematic restorations of the Caribbean region (Pindell et al., 2012; Boschman et al., 2014) also show an onset of convergence across the Maracaibo margin around 60 Ma, and predict ~1200 km of subduction. This is consistent with the UU-P07 seismic tomographic image of van Benthem et al. (2013) if the anomaly overlying the 660 km discontinuity is assumed to be part of the Maracaibo slab. We thus assign a 60–55 Ma age for the base of the Maracaibo slab.

3.57. Mariana - Mr

The Mariana anomaly (Fig. 61) was first shown in seismic tomography by Spakman et al. (1989) and Van der Hilst et al. (1991). In subsequent tomographic models, the Mariana anomaly, which is an steeply westward dipping, N–S trending anomaly that connects to the Mariana trench and the slab is thus interpreted to represent still-subducting Pacific lithosphere. It was imaged to penetrate the lower mantle down to 1000–1200 km depth (Bijwaard et al., 1998; Widiyantoro et al., 1999; Gorbatov and Kennett, 2003; Huang and Zhao, 2006; Rost et al., 2008; Fukao and Obayashi, 2013; Jaxybulatov et al., 2013; Obayashi et al., 2013; Zahirovic et al., 2014; Wu et al., 2016). To the north along the same subduction zone, it is connected in the upper 300–400 km to the Izu-Bonin slab (Section 3.44). Below that depth, however, the Mariana and Izu-Bonin slabs are disconnected through a tear fault that may have formed at the subducted Marcus–Necker Ridge and the Ogasawara Plateau, with the Izu-Bonin slab lying horizontally on the 660 km discontinuity and the Mariana slab penetrating through (Miller et al., 2004, 2005). To the south, the Mariana slab is also bounded by a tear (Miller et al., 2006). Previous reconstructions estimated subduction of the Mariana-Izu Bonin subduction zone to have started at 48 Ma (Seno and Maruyama, 1984) to 50 Ma (Wu et al., 2016). Prior to 50 Ma, Wu et al. postulate that a western Pacific plate boundary already existed but this may have been characterised by highly oblique subduction or transforms. After 50 Ma, Pacific plate motions changed and fast subduction began (Wu et al., 2016).

The Mariana-Izu Bonin forearc has been instrumental in the development of models linking geochemical evolution of subduction-related magmas in a forearc position to subduction initiation (Stern and Bloomer, 1992; Dewey and Casey, 2011; Stern et al., 2012). U/Pb and $^{40}Ar/^{39}Ar$ ages of the oldest forearc lavas that are believed to have formed during subduction initiation are consistently 51–52 Ma (Ishizuka et al., 2011; Reagan et al., 2013), which we adopt as age for the onset of subduction of the Mariana slab.

3.58. Mayn - Mn

The Mayn anomaly (Fig. 62) is located below northeastern Siberia in the upper mantle and uppermost part of the lower mantle. It is N–S trending and towards the south it touches the Bering Sea slab (Section 3.15). It was previously imaged by Gorbatov et al. (2000) and Zhao et al. (2010). The tectonic evolution and upper mantle structure of the region leads us to interpret the Mayn anomaly as a separate slab. The location of the slab is consistent with subduction along the Shirshov Ridge in western Bering Sea. This ridge is generally interpreted to represent a Cenozoic intra-oceanic arc (Nokleberg et al., 2000; Chekhovich et al., 2012). In the tectonic model of Chekhovich et al. (2012), the Shirshov ridge underwent to a period of imbricate thrusting between 30 and 15 Ma, which we adopt as the period of subduction.

3.59. Mendocino - Mdc

The Mendocino anomaly (Fig. 63), is located in the lower mantle below the northeastern Pacific Ocean, west of the North American continental margin, west of the Hudson (Section 3.41), Hatteras (Section 3.37) and Idaho slabs (Section 3.42) and south of the North Pacific slab (Section 3.68). It was named 'X' by Sigloch (2011) and and later Cascadia Root 2 (CR2) by Sigloch and Mihalynuk (2013). van der Meer et al. (2012) interpreted it as an (unnamed) slab remnant at 2300–1700 km depth in east-Panthalassa Ocean marginal subduction zones in the UU-P07 model (Amaru, 2007). Sigloch and Mihalynuk (2013), on the basis of a regional tomographic model of Sigloch (2011) interpreted the slab to extend to the top of the lower mantle. The age of subduction is poorly constrained from geological data. Sigloch and Mihalynuk (2013) interpreted subduction to have occurred between 140 and 75 Myr on the basis of plate tectonic reconstruction. The shallowest occurrence of the slab is close to the North American continental margin, suggesting terrane accretion might have occurred in Cenozoic times. This is consistent with the inferences of Sigloch (2011) and Sigloch and Mihalynuk (2013), who indicated final terrane accretions (Siletzia, Pacific Rim) at 55–50 Myr. However as discussed at the Idaho slab, the Siletzia terrane is mostly an oceanic plateau (Wells et al., 2014) and is not related to arc volcanism. We interpret the Idaho and Mendocino slab to be genetically linked and both resulting from intra-oceanic subduction at the Talkeetna-Bonanza arcs. Based on their present-day relative locations between these two slabs and arcs, we tentatively we suggest that the Mendocino slab is correlated with the Alaskan Talkeetna arc. This Alaskan arc was formed from 202 to 201 Ma onwards (Clift et al., 2005; Rioux et al., 2007). On the basis of rapid exhumation and deposition of the coarse clastic Naknek formation Clift et al. (2005) suggested it was possibly amalgamated between 160 and 125 Ma in the greater Wrangellia terrane. We here interpret these events to represent amalgation with the Bonanza and Gravina arcs, and correlated with the Idaho slab (Section 3.42).

3.60. Mesopotamia - Me

The Mesopotamia anomaly (Fig. 64) is located below the Zagros mountain belt at the Arabia-Eurasia plate boundary from the deep mantle up to mid-mantle and connects upward to the Zagros anomaly residing in the upper mantle. In previous studies it has been referred to as the western part of the II anomaly Van der Voo et al. (1999b), as the SI and AI anomalies Hafkenscheid et al. (2006), or as the Sb1 anomaly in Agard et al. (2011). In van der Meer et al. (2010), we interpreted this anomaly as a slab resulting from intra-oceanic subduction within the Neotethys culminating in the obduction of e.g. the Semail ophiolite of Oman. Closer inspection of the tomographic images below Arabia

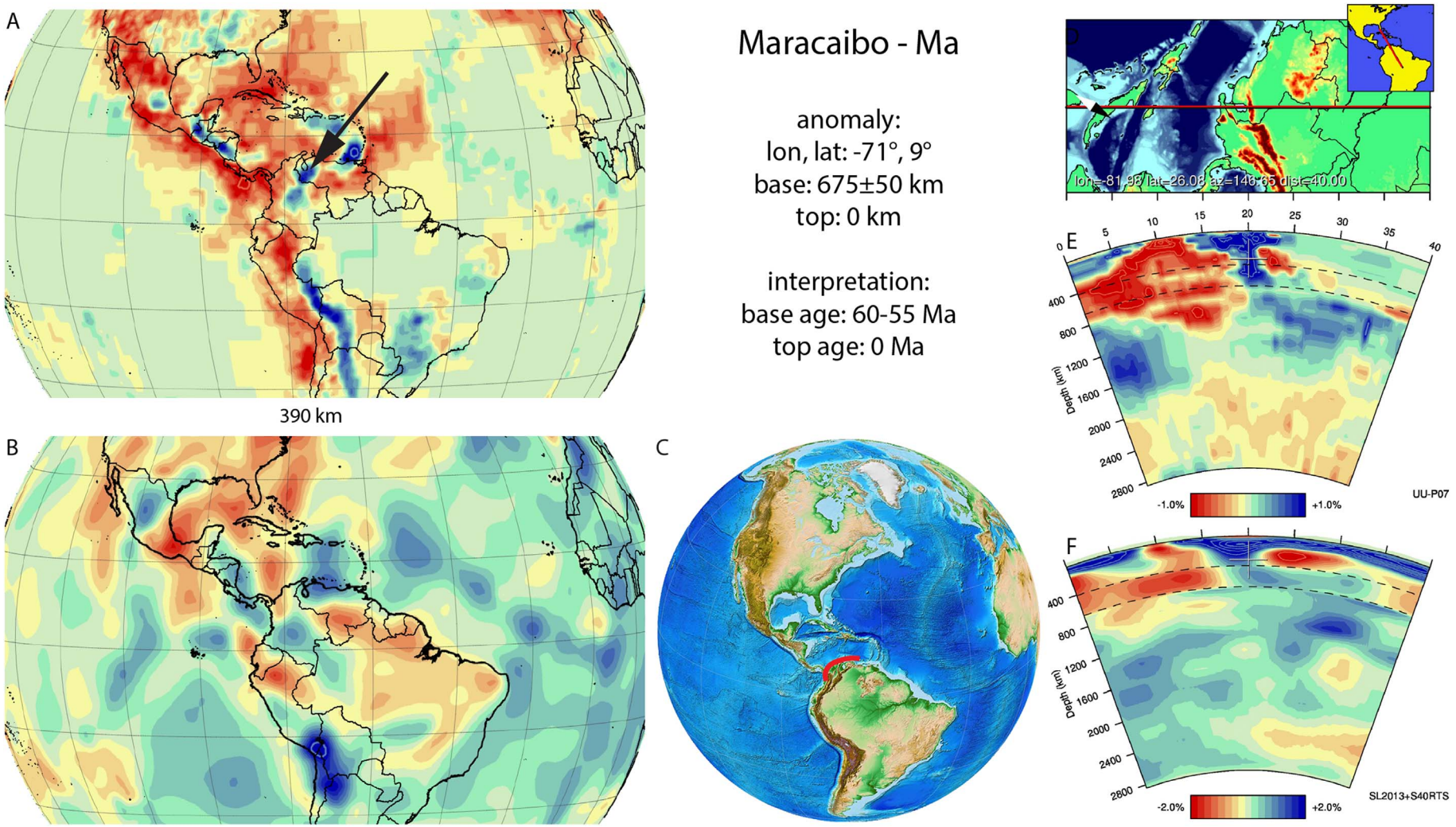

Fig. 60. Maracaibo anomaly. Legend same as Fig. 5. This slab is well imaged in the UU-P07 model and has near-vertical dip trend. Relative amplitude strength, lateral extent and vertical extent are different between models.

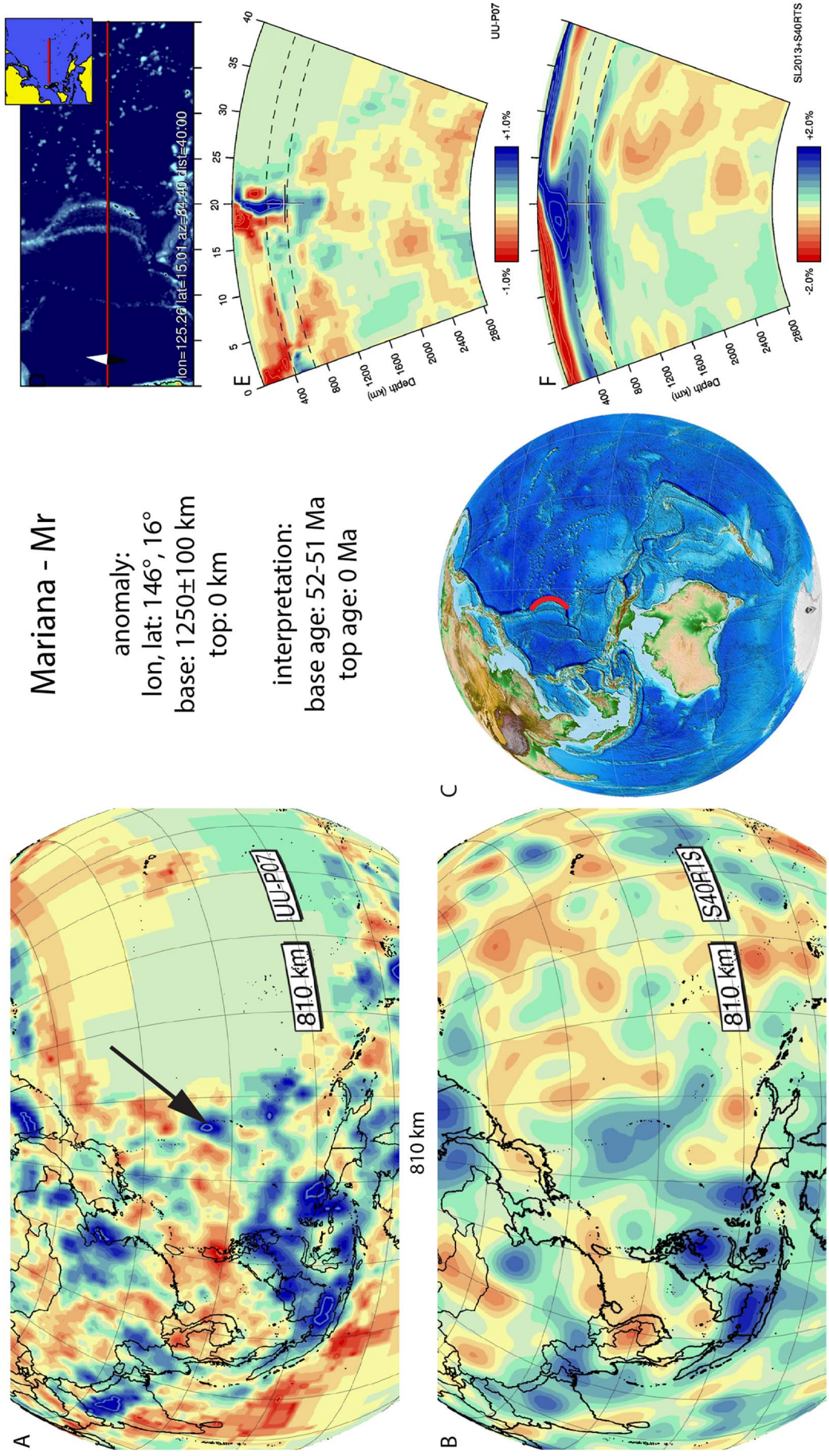

Fig. 61. Mariana anomaly. Legend same as Fig. 5. This slab is well imaged in the UU-P07 model and there is a similar relative amplitude strength and vertical extent between models. This slab is near-vertical in the upper mantle and top lower mantle.

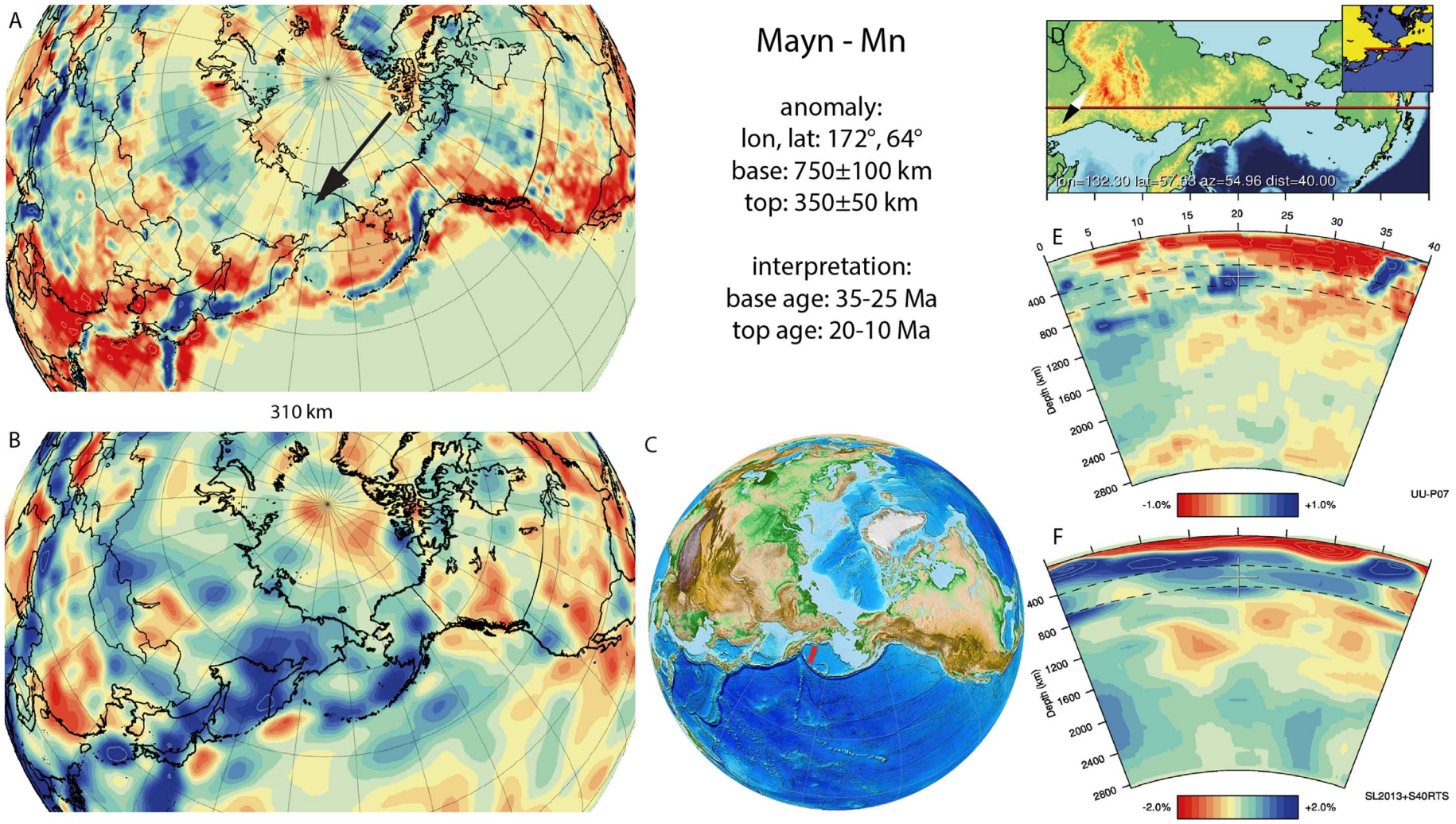

Fig. 62. Mayn anomaly. Legend same as Fig. 5. Positive anomalies are identified in the same location in both tomographic models with similar downward vertical extent. Lateral extent and relative amplitude strength, are different. There is not a visible dip trend.

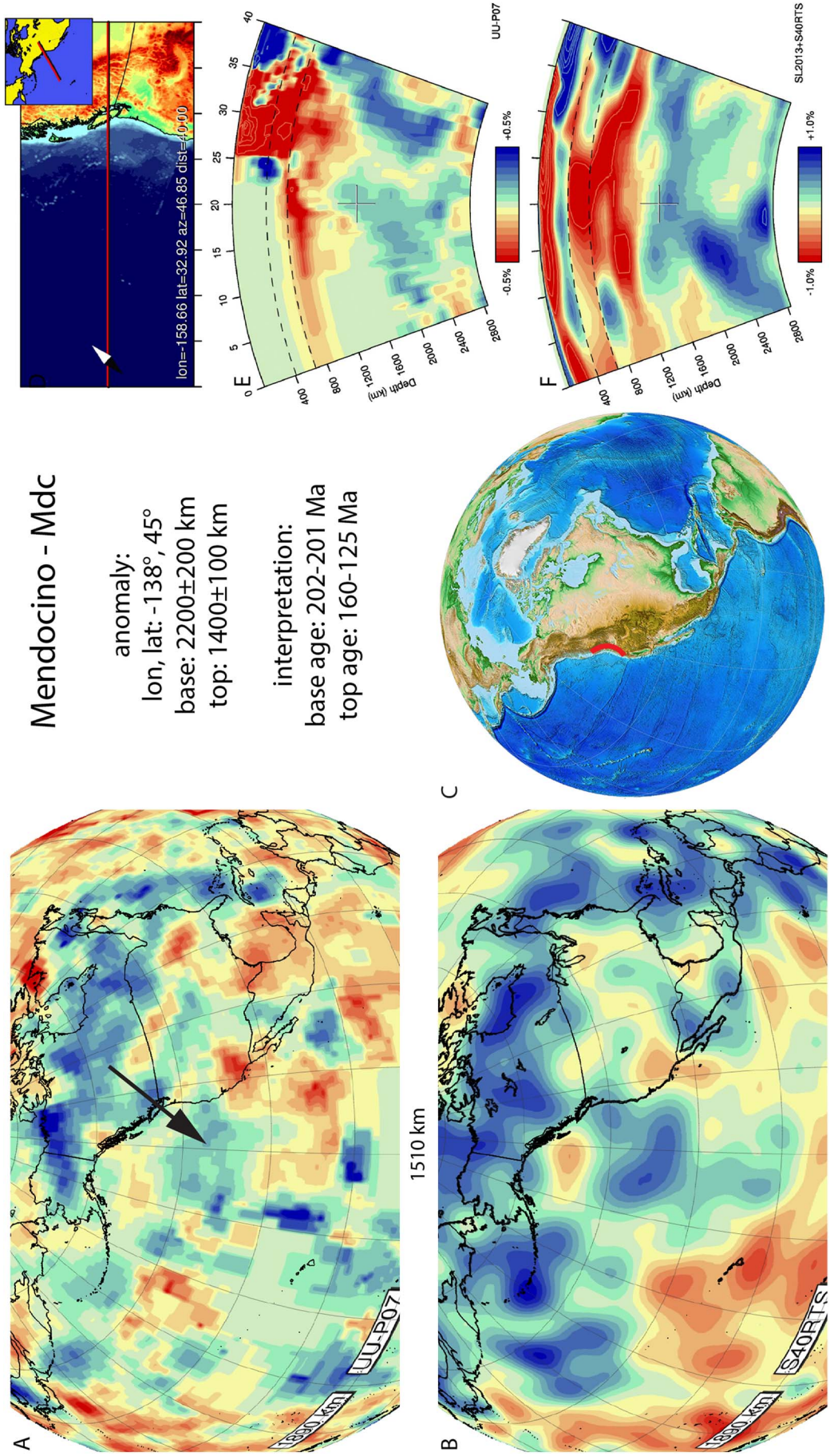

Fig. 63. Mendocino anomaly. Legend same as Fig. 5. Positive anomalies are identified in the same location in both tomographic models with a similar lateral extent. Relative amplitude strength and vertical extent differ between tomographic models.

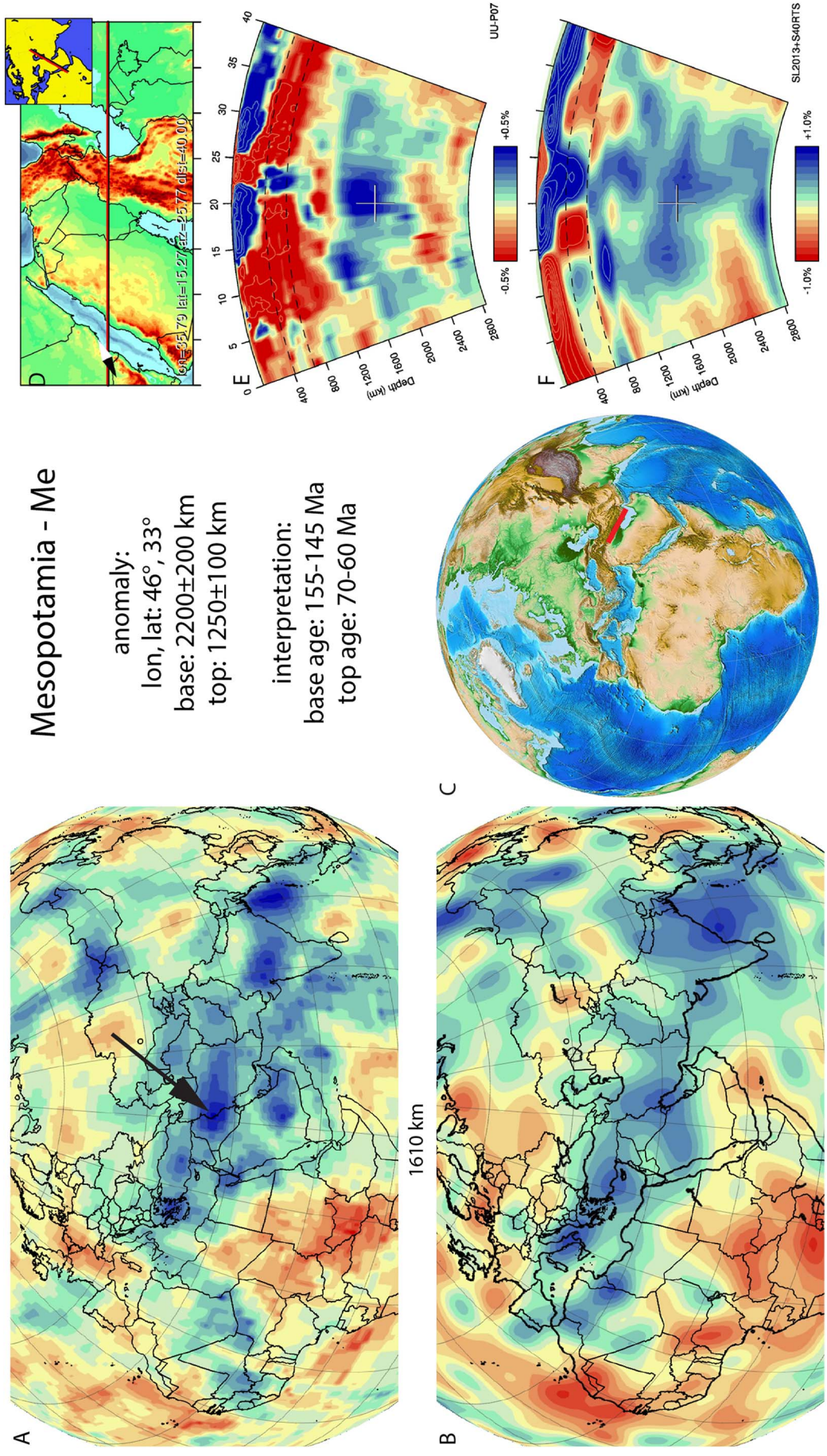

Fig. 64. Mesopotamia anomaly. Legend same as Fig. 5. Positive anomalies are identified in the same location in both tomographic models with a similar vertical extent. Relative amplitude strength and lateral extent differ between tomographic models.

shows, however, that the Mesopotamia slab at depths of 1100–1300 km is separated from a second slab to the SW (now named Arabia slabs following Hafkenscheid et al., 2006, see Section 3.9) that is a better candidate to result from subduction below the ophiolites of Oman and Iran. The Mesopotamia slab more likely relates to subduction below the Eurasian margin of Iran (Agard et al., 2011). The oldest geological evidence for subduction below the Iranian continental fragments, which collided with Eurasia in the Triassic (Muttoni et al., 2009) is the Sanandaj-Sirjan magmatic arc, active since ~150 Ma (Agard et al., 2011), providing a probable age for the base of the Mesopotamia slab. Towards the top, the slab appears to be disconnected from the upper mantle portions of slabs (see Zagros slab, Section 3.94). Agard et al. (2011) suggested, based on the age of rapid exhumation of HP-LT metamorphic rocks in the Zagros Mountains that there may have been a phase of slab break-off in the latest Cretaceous to Paleogene, ~65 ± 5 Ma which we adopt as the age of the top of the Mesopotamia slab.

3.61. Mississippi - Mi

The Mississippi anomaly (Fig. 65) is part of the set of anomalies commonly, and also in our previous compilation in van der Meer et al. (2010), interpreted as the Farallon slab as originally defined by Grand et al. (1997). The NW-SE trending Mississippi anomaly has a central position within the family of Farallon anomalies and is located in the mid-mantle below Central North America and the northern Caribbean region. At its base it connects with the top of the N–S trending Hatteras slab (Section 3.37). At its top it is close to the Great Basin slab (Section 3.35). The Mississippi anomaly corresponds to the SF3 anomaly of Sigloch and Mihalynuk (2013), who interpreted the transition of the Hatteras to the Mississippi slab to have happened when the South Farallon trench stepped westward after accretion of Shatsky Rise Conjugate plateau. This led to a slab window with Sonora volcanism including the Tarahumara ignimbrite province (85–65 Myr ago). We have adopted this as the start of subduction of the Mississippi slab. In the upper mantle, the slab disintegrates into smaller, dispersed fragments, which have been associated with subduction during the Laramide orogeny (80–40 Ma) (van der Lee and Nolet, 1997; Sigloch et al., 2008; Liu and Stegman, 2011). We have taken the end of the Laramide orogeny (40 Ma) as end of subduction of the slab.

3.62. Mongolia - Mg

The Mongolia anomaly (Fig. 66) is located below northeast Asia within the mid-mantle. In previous studies it was interpreted as a Pacific slab (Van der Voo et al., 1999a). In van der Meer et al. (2010), we used the Kamchatka-Kuriles and Manchuria slabs (shallower in the mantle, Sections 3.48 and 3.54) and Mongol-Kazakh slab (deeper in the mantle, Section 3.63) to infer that the Mongolia anomaly represents (westward) subducted Pacific lithosphere with a Middle to Late Mesozoic subduction age range. Nokleberg et al. (2000) and Golonka et al. (2003) inferred westward subduction of Pacific lithosphere at the north-eastern margin of Asia associated with the continental margin Khingan arc. This arc consists of mainly Barremian (130.8–126.3 Ma) to Cenomanian (100.5–93.9 Ma) andesites and basalts and related intrusives (Nokleberg et al., 2000), which we previously used to date the slab. Further south in the Songliao and neighbouring basins (Ren et al., 2002) documented an earlier start of volcanism, between 155 and 140 Ma. We therefore now adopt a somewhat wider age range of subduction with onset and end at 155–126.3 Ma and 100.5–93.9 Ma, respectively.

3.63. Mongol-Kazakh - MK

The Mongol-Kazakh anomaly (Fig. 67) is located below northern Siberia from the core-mantle boundary up to the mid-mantle. The anomaly is widely known in the literature as the Mongol-Okhotsk anomaly (Van der Voo et al., 1999a) and is interpreted to represent lithosphere of the Mongol-Okhotsk Ocean, which has been inferred to have subducted until the latest Jurassic-earliest Cretaceous, based on paleomagnetic and geological data (Van der Voo et al., 1999a, 2015). We renamed the slab after its present-day location, whereby the midpoint lies below the borders between Mongolia, Kazakhstan, China, and Russia, because we consistently name slabs after their present location rather than their interpreted geological history. The base of the slab merges with the graveyard of slabs under Asia at the base of the mantle (Van der Voo et al., 1999a). The southern part of the *Z*-shaped Mongol-Kazakh slab sensu (Van der Voo et al., 1999a, 2015) was redefined by van der Meer et al. (2010) as the Central China slab (Section 27) and may (also) consist of Paleotethyan lithosphere, as suggested by Stampfli and Borel (2004). Subduction of and within the Mongol-Okhotsk Ocean started well before the Mesozoic (Tomurtogoo et al., 2005; Donskaya et al., 2013) and pre-Mesozoic lithosphere may not be visible any longer in the slab graveyard above the core-mantle boundary. Van der Voo et al. (2015) noted that the deepest part of the Mongol-Kazakh slab is trending N–S, consistent with Triassic (~250–220 Ma) orientations of the Mongol-Okhotsk subduction zone, whereas upwards the slab kinks and eventually becomes oriented ~W-E, similar to the trend of the Mongol-Okhotsk suture zone. These authors argued that the shape of the slab is consistent with an oroclinal closure of the Mongol-Okhotsk Ocean suggested by the geological structure of Mongolia and southern Siberia. The shape of the slab may thus suggest a ~250–220 Ma age of the deepest, NS striking part of the slab (below ~2000 km). Closure of the Mongol-Okhotsk Ocean follows from paleomagnetic constraints from the North China and Amurian blocks and Siberia, and is slightly younger than we previously assumed: 140 ± 10 Ma (Cogne et al., 2005; Van der Voo et al., 2015).

Recently Shephard et al. (2014) performed mantle convection modelling, suggesting that the Mongol-Kazakh slab underwent as much as 60 longitude degrees westward motion through the mantle during its descent to the core-mantle boundary, and should thus be found not further east than 35°E, instead of 60–100°E preferred here, and in Van der Voo et al. (1999a, 2015). Our correlation philosophy, also used in van der Meer et al. (2010, 2012) in linking slabs to their geological record assumes that slabs do not significantly move laterally relative to each other which, when viewed globally, implies a preference for slab remnants to sink vertically as was recently corroborated by Domeier et al. (2016). In other words, the modern distribution of slab remnants in the deep mantle can be associated with the paleo-subduction zone configuration, which was found to lead to coherent correlations of plate reconstructions with mantle structure for the last 250–300 Ma (van der Meer et al., 2010, 2012, 2014). The mantle convection model of Shephard et al. (2014), and similarly Fritzell et al. (2016), predicts that the Mongol-Kazakh slab has moved > 4000 km westward through the lower mantle since it detached at ~140 Ma (i.e., at ~3 cm/year, about twice as fast as the sinking rate) relative to the Aegean slab (Section 3.1). What is driving large lateral mantle “winds” in the mantle flow modelling is not known, however, so far there has been no supporting evidence that such large mantle winds actually exist. Moreover, one would equally expect that strong mantle winds would deflect or destroy mantle plumes, which then would question the basic premise of hotspot-based absolute plate motion models that are used to drive such “slab-prediction” modelling. There is compelling evidence, however, provided by Domeier et al. (2016), that any lateral mantle flow in the past ~130 Myr did not appreciably perturb the overall radial sinking of slab and also not appreciably perturb the rising of plumes as is implied by their use of the Seton et al. (2012) absolute plate motion model. Although we believe that mantle flow modelling is on the longer term the only viable avenue to quantitatively and dynamically link plate-tectonic evolution to mantle dynamics, at present the modelling of mantle flow itself is based on uncertain data and large assumptions, e.g. mantle rheology, and thereby introduces large uncertainty and

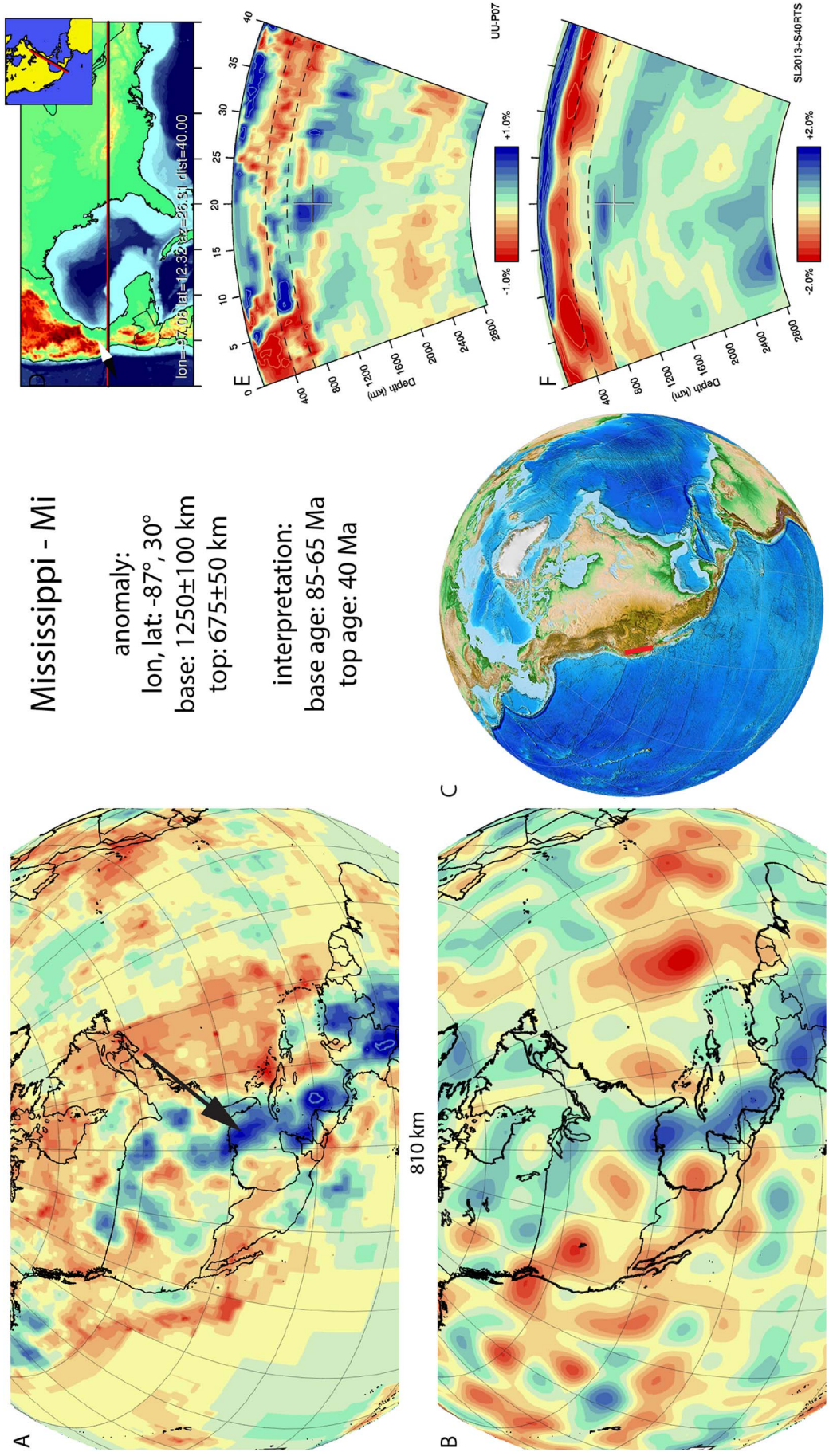

Fig. 65. Mississippi anomaly. Legend same as Fig. 5. Vertical and lateral extent are very similar between tomographic models. Relative amplitude strength differs. The slab has a clear dip trend to the NE.

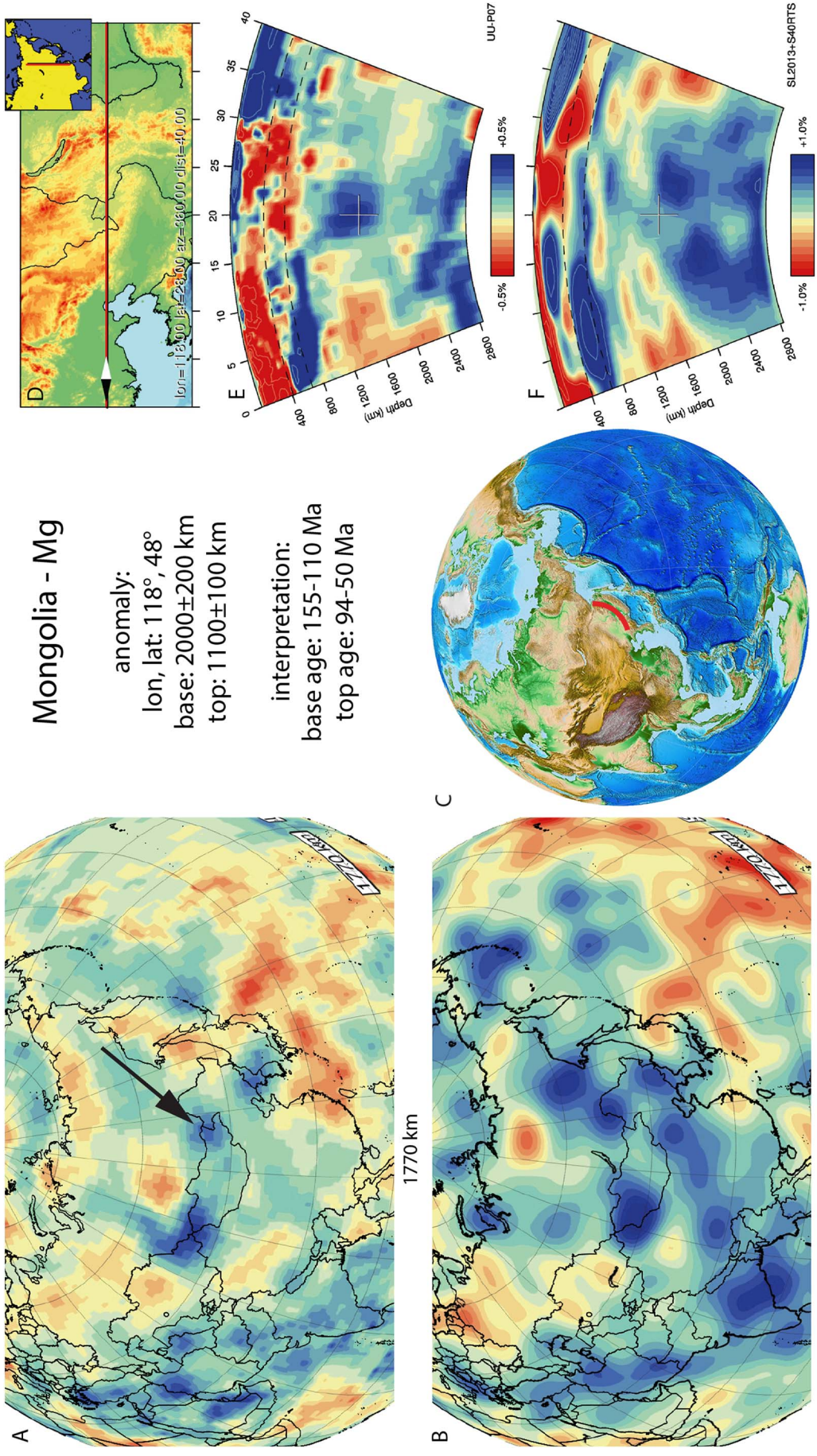

Fig. 66. Mongolia anomaly. Legend same as Fig. 5. Positive anomalies are identified in the same location in both tomographic models with a similar lateral extent. Relative amplitude strength and vertical extent differ between tomographic models.

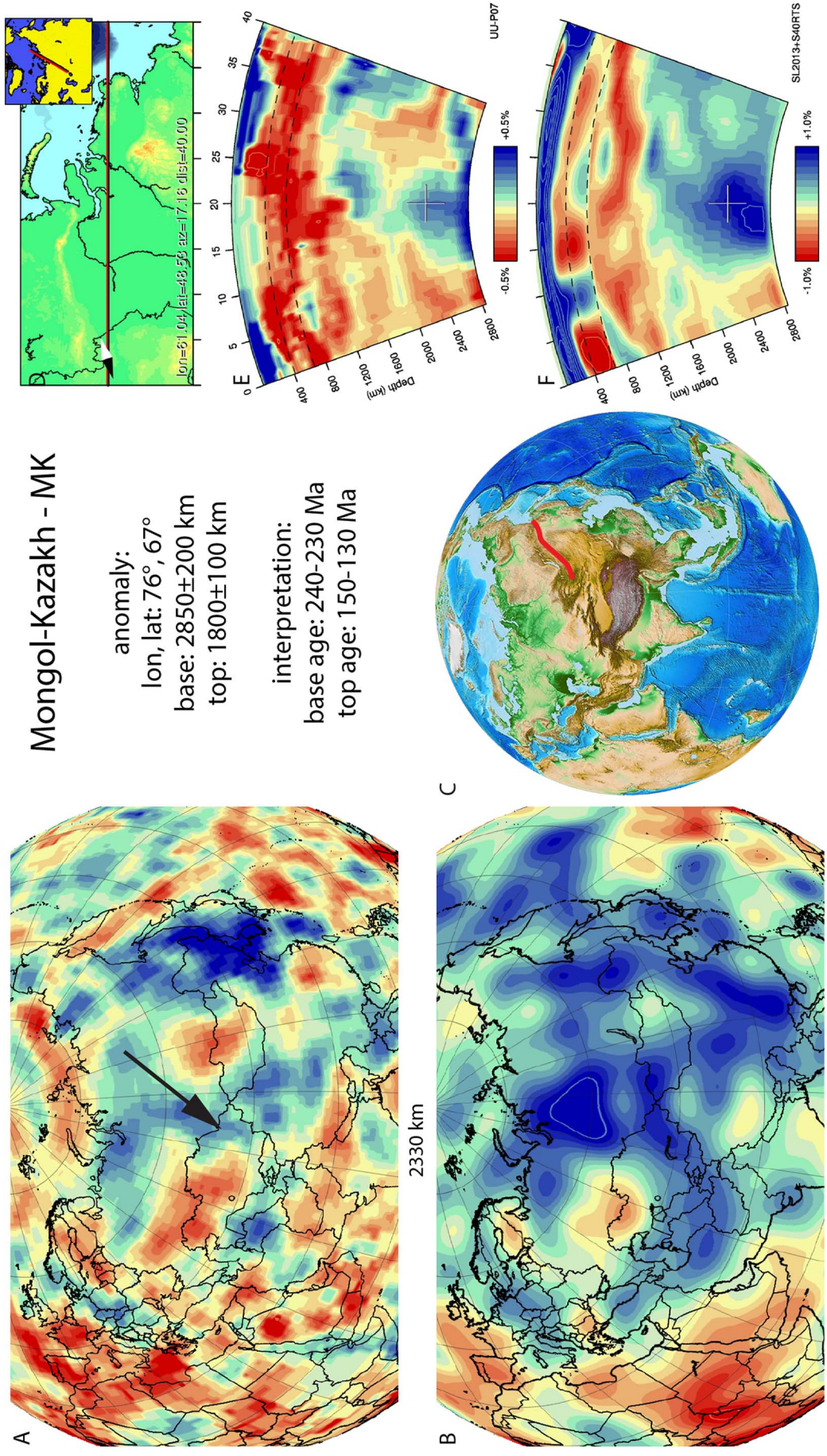

Fig. 67. Mongol-Kazakh anomaly. Legend same as Fig. 5. Positive anomalies are identified in the same location in both tomographic models with a similar vertical extent. Relative amplitude strength and lateral extent differ between tomographic models. The slab appears to be a pile on top of the CMB.

complexity to the slab identification problem it tries to solve.

3.64. Nepal - Ne

The Nepal anomaly (Fig. 68) is located in the lower mantle below the Himalaya. Its position south of the shallower part of the Mongol-Kazakh slab (Section 3.63) and north of the deeper part of the India slab (Section 3.43) suggests that the Nepal anomaly represents lithosphere that subducted during the mid-Mesozoic, and that its subduction record should be located between the Himalaya and Mongolia, i.e. in Tibet. The best candidate for its subduction location is the Bangong-Nujiang suture zone that formed in Early Cretaceous time upon collision of the Lhasa and Qiangtang terranes of the Tibetan Plateau. All other sutures in Tibet are Triassic or older in age (Yin and Harrison, 2000; Kapp et al., 2003; Zhu et al., 2013). Van der Voo et al. (2015) reconstructed the China blocks and Tibet relative to the mantle and portrayed the anomaly here identified as Nepal slab below the Bangong-Nujiang suture zone in the Early Cretaceous.

Reasonable agreement exists on the age of closure of the Bangong-Nujiang suture zone. The suture zone contains radiolarian cherts that range in age from mid Jurassic to late Early Cretaceous (130–120 Ma), flysch deposits of late Early Cretaceous age, and unconformably covering upper Albian-Aptian (~110–100 Ma) shallow marine limestones (Baxter et al., 2010; Fan et al., 2015). Calc-alkaline and adakitic magmatic rocks of 115 and 110–100 Ma were interpreted to reflect slab roll-back and break-off, respectively (Chen et al., 2014; Wu et al., 2014, 2015). The age of the top of the Nepal slab can thus be dated at ~110–100 Ma. Arc magmatic rocks on southern Qiangtang have been reported of ~168 Ma (Liu et al., 2013) and 163 Ma (Li et al., 2014b), and northward subduction below Qiangtang since late Early Jurassic (~180–170 Ma) was concluded as a result (Xu et al., 2014). Based on a detrital zircon study, subduction below Qiangtang may have started as early as 210 Ma (Zeng et al., 2015), consistent with the paleomagnetically constrained onset of northward drift of the Lhasa terrane relative to Gondwana (Li et al., 2016). We use a 210–170 Ma age range for the base of the Nepal slab.

An alternative model proposes that the Bangong-Nujiang Ocean did not subduct northwards, but southwards below the Lhasa terrane, and represented the main Paleozoic Tethyan Ocean. This model proposes that the Lhasa terrane was still connected to Gondwana in the Triassic and rifted away after the Bangong-Nujiang ocean started to subduct southward below the north Gondwana margin, opening the Neotethyan ocean as a back-arc from Triassic to Early Cretaceous time (Zhu et al., 2011, 2013). This scenario implies that the slab below the Lhasa terrane rolled back over a distance equivalent to the final dimension of the Neotethyan ocean, i.e. > 7000 km. However, we find no anomalies in the lower mantle that span such an enormous width that would support such a scenario.

3.65. New Britain - NB

The New Britain anomaly (Fig. 69) corresponds to anomaly A3 of Hall and Spakman (2002, 2004) and was previously imaged by Bijwaard et al. (1998) and Wu et al. (2016). It is a W-E trending anomaly interpreted as a slab that reaches the base of the upper mantle. It is actively subducting northward along a trench south of New Britain, consuming Solomon Sea plate lithosphere. Wu et al. (2016) separated the New Britain slab into two slabs: Solomon Sea West and Solomon Sea East. Subduction along the New Britain trench is interpreted to be a delayed response to the collision of the Ontong Java plateau with the original Melanesian subduction zone along which (part of) the Papua slab (Section 3.70) subducted below the Australian plate until approximately 26–20 Ma (Hall, 2002; Quarles van Ufford and Cloos, 2005; Knesel et al., 2008; Holm et al., 2013). The arrest of subduction of the Papua slab along the Melanesian trench was first followed by subduction of the Solomon Sea plate along the Trobriand trough (Hall, 2002; Quarles van Ufford and Cloos, 2005; Schellart et al., 2006; Knesel et al., 2008) (Welford slab, see Section 3.92), after which northward subduction started below New Britain creating the Bismarck arc since 10–5 Ma (Hall, 2002; Holm et al., 2013) or since 15 Ma (Wu et al., 2016). We adopt 15–10 the age range of the base of the New Britain slab.

3.66. New Hebrides - NH

The New Hebrides anomaly (Fig. 70) is located west of the northern termination of the Tonga trench, and is interpreted as lithosphere still subducting at the New Hebrides subduction zone. It is a NW-SE trending slab that was imaged before by Fukao et al. (2001), Hall and Spakman (2002, 2004), Schellart and Spakman (2012), Fukao and Obayashi (2013), Obayashi et al. (2013), and Wu et al. (2016). It reaches the base of the upper mantle. The NE-dipping New Hebrides subduction zone is interpreted to result from subduction polarity reversal due to the arrival of the Ontong-Java plateau into an originally contiguous Solomon-Vitiaz-Tonga-Kermadec subduction zone, around 15–10 Ma (Hall, 2002; Sdrolias et al., 2004; Schellart et al., 2006; Seton et al., 2012), which we adopt for the age of the base of the slab.

3.67. North Apennines - NA

The North Apennines anomaly (Fig. 71) is located below Corsica and Tuscany in the upper mantle. Based on early tomographic models, Spakman et al. (1993) interpreted the North Apennines anomaly as a detached slab, but subsequent models rather suggested that it is still connected to the surface (Piromallo and Morelli, 1997, 2003; Bijwaard et al., 1998; Lucente et al., 1999; Spakman and Wortel, 2004). The North Apennines slab is clearly separated from the Calabria slab by a several hundred kilometres wide gap, interpreted as the result of a lateral tear (Wortel and Spakman, 1992, 2000) or a subduction transform fault (Rosenbaum et al., 2008). Lucente et al. (1999) and Lucente and Speranza (2001) interpreted the North Apennines slab as contiguous with an anomaly lying in and below the transition zone (the Alps slab, Section 3.6) by, which would result in a 700 km long slab. Spakman and Wortel (2004), however, suggested that the North Apennines slab reaches a depth of only ~300 km, and is a separate body from the Alps slab.

Geological reconstructions of the northern Mediterranean region consistently conclude that the southward subduction zone of the Alps reached as far south as Corsica, based on the finding of a (currently) west-verging thin-skinned fold-thrust belt including high-pressure metamorphic rocks on Corsica (Brunet et al., 2000a). A transition from east- to west-dipping subduction below Corsica, coinciding with the start of the North Apennines subduction zone, is generally estimated to have occurred around 35–30 Ma (Rosenbaum et al., 2002a; Jolivet et al., 2009; Argnani, 2012; Advokaat et al., 2014b). Because the North Apennines slab is oriented at a high angle to the Africa-Europe convergence direction, almost all of its length should have been accommodated by back-arc extension in the northwest Mediterranean, which at the latitude of the North Apennines slab is on the order of 300 km (Faccenna et al., 2001; Faccenna et al., 2004). We therefore follow the interpretation of Spakman and Wortel (2004), and assign an age to the base of the North Apennine slab of 35–30 Ma.

3.68. North Pacific - NP

The North Pacific anomaly (Fig. 72) is located below the northern Pacific Ocean and southern Alaska from the mid-mantle up to upper part of the lower mantle. In previous tomographic studies it has been interpreted as Kula (Qi et al., 2007),Pacific slab (Ren et al., 2007) and was also identified as 'K' in Sigloch (2011). The Aleutian slab (Section 3.3) higher in the mantle to the north that subducted since 56–46 Ma led us to infer that the North Pacific anomaly represents Early or

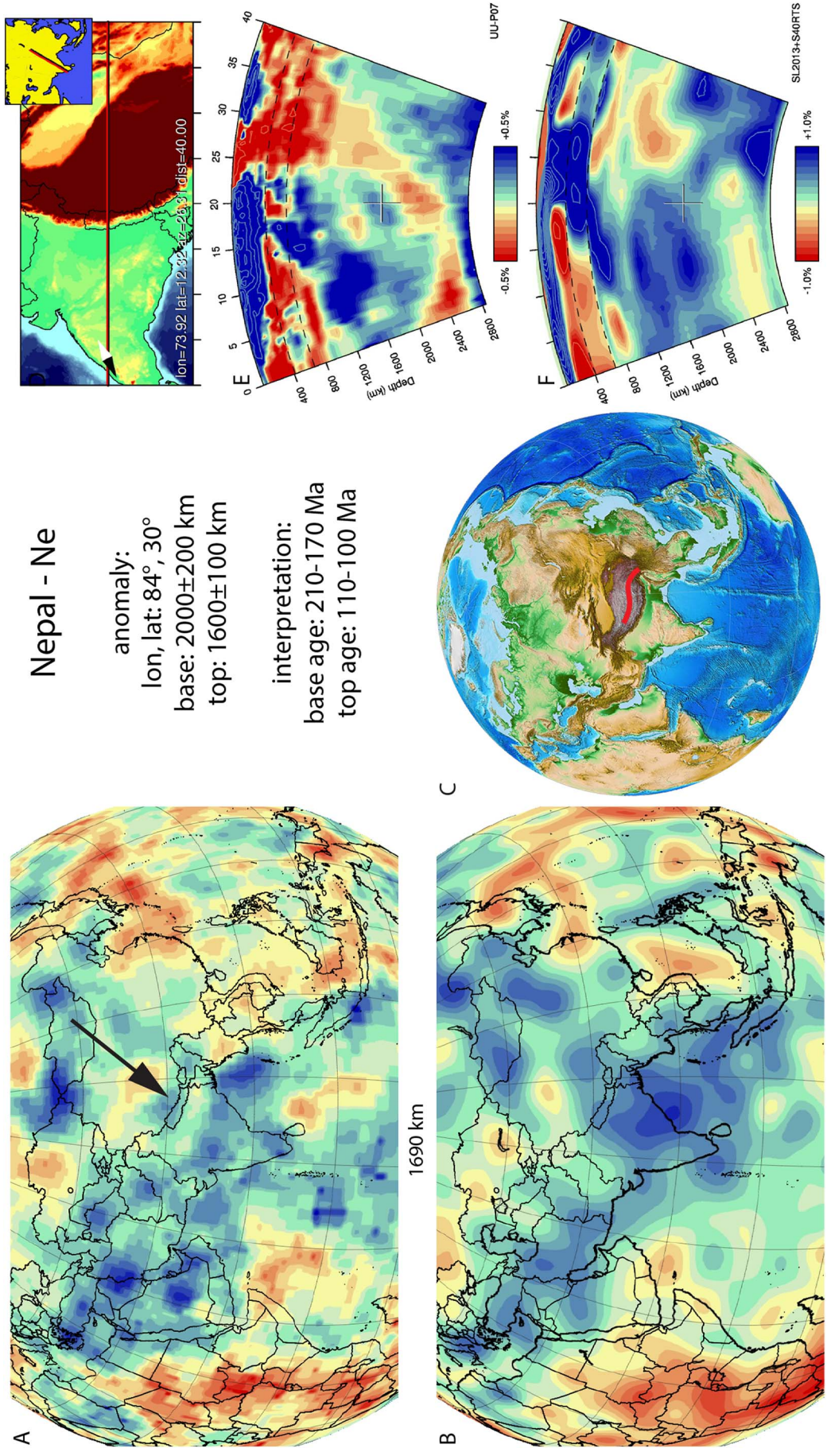

Fig. 68. Nepal anomaly. Legend same as Fig. 5. Positive anomalies are identified in the same lower mantle location in both tomographic models. Relative amplitude strength, vertical and lateral extent differ between the UU-P07 and S40RTS tomographic models.

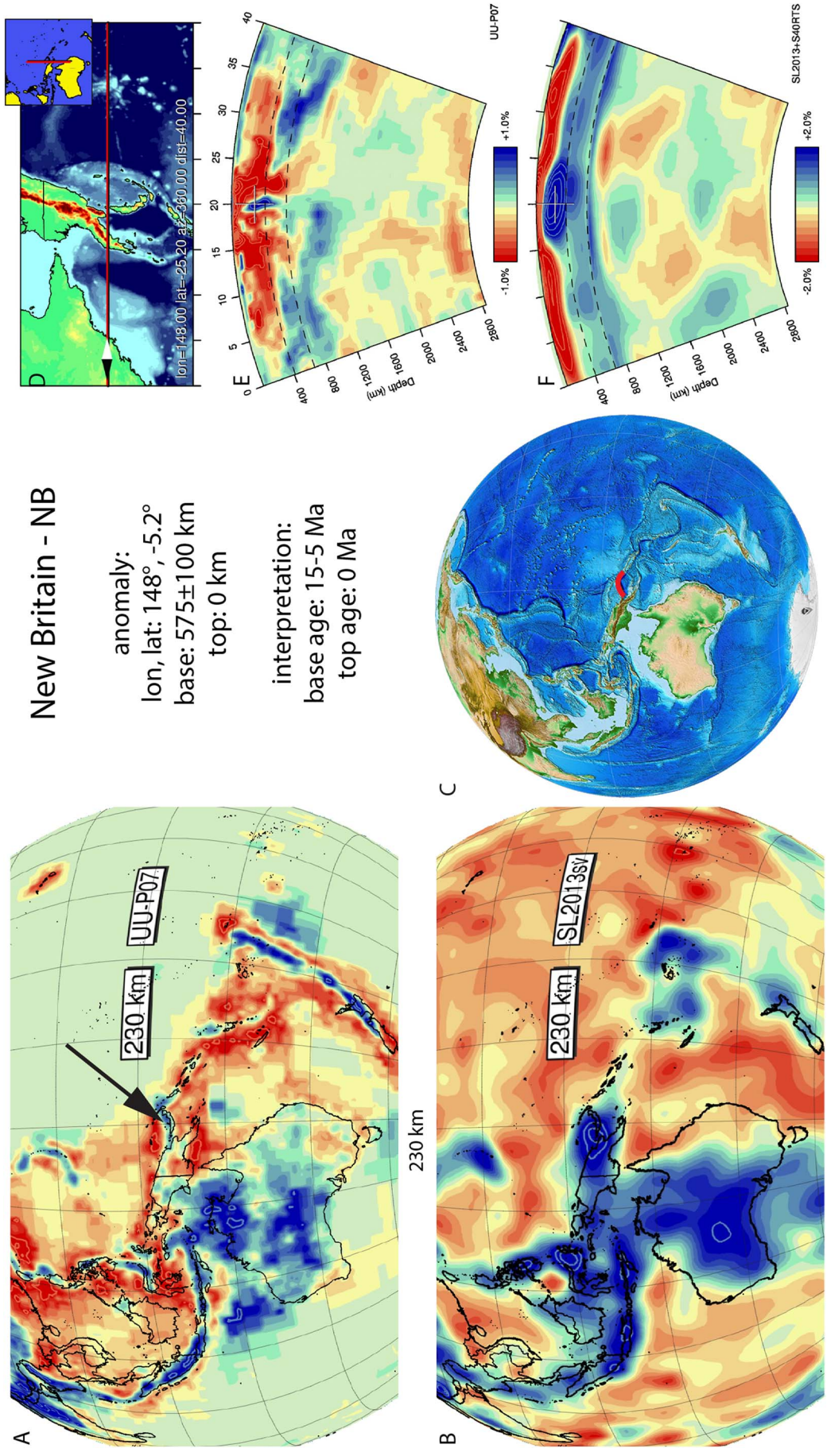

Fig. 69. New Britain anomaly. Legend same as Fig. 5. This upper mantle slab is well imaged in the UU-P07 model, but not in the SL2013 model. The dip of this slab is near-vertical.

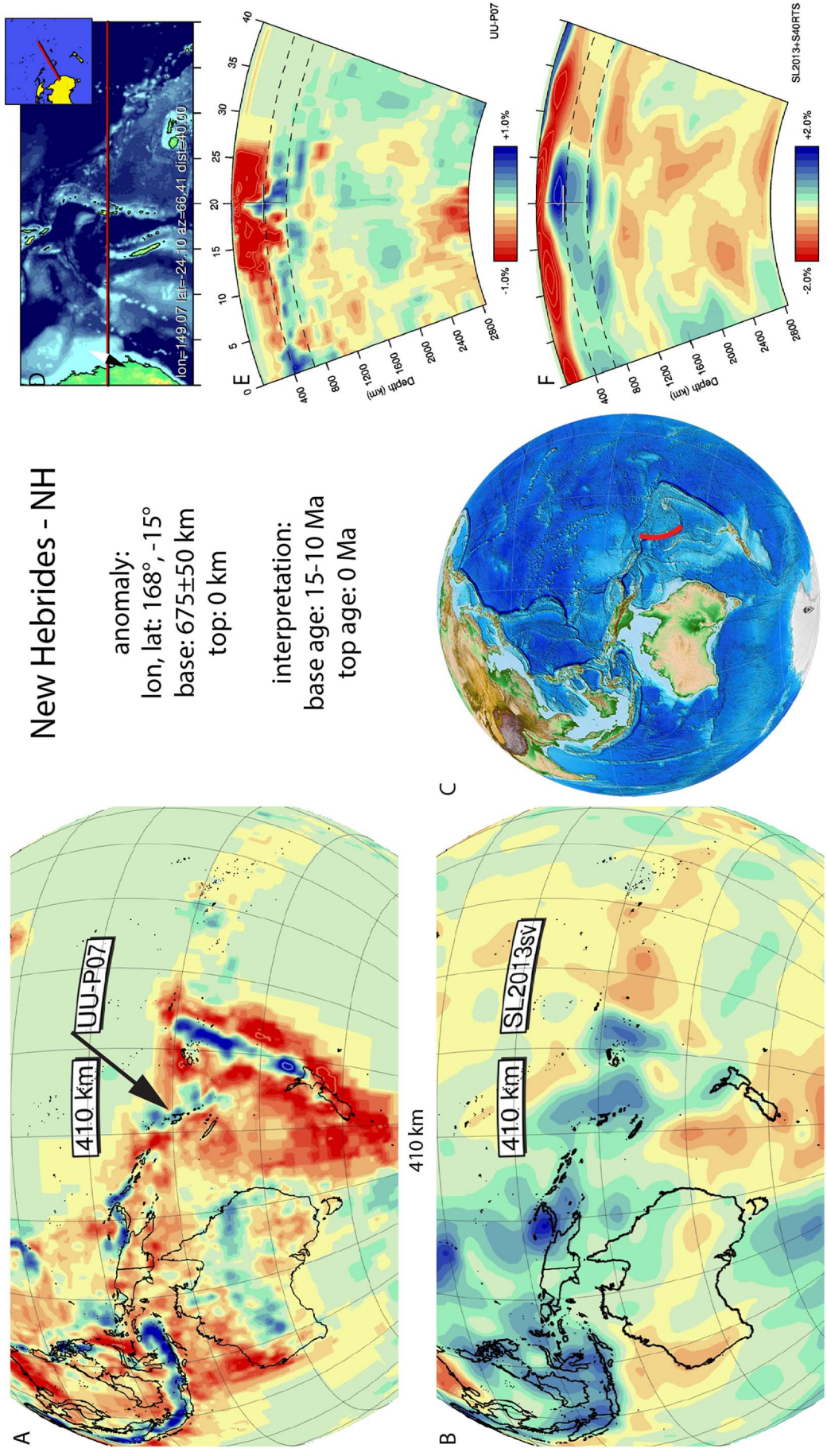

Fig. 70. New Hebrides anomaly. Legend same as Fig. 5. This upper mantle slab is well imaged in the UU-P07 model and there is a similar relative amplitude strength, lateral extent and vertical extent between models. This slab dips to the NE.

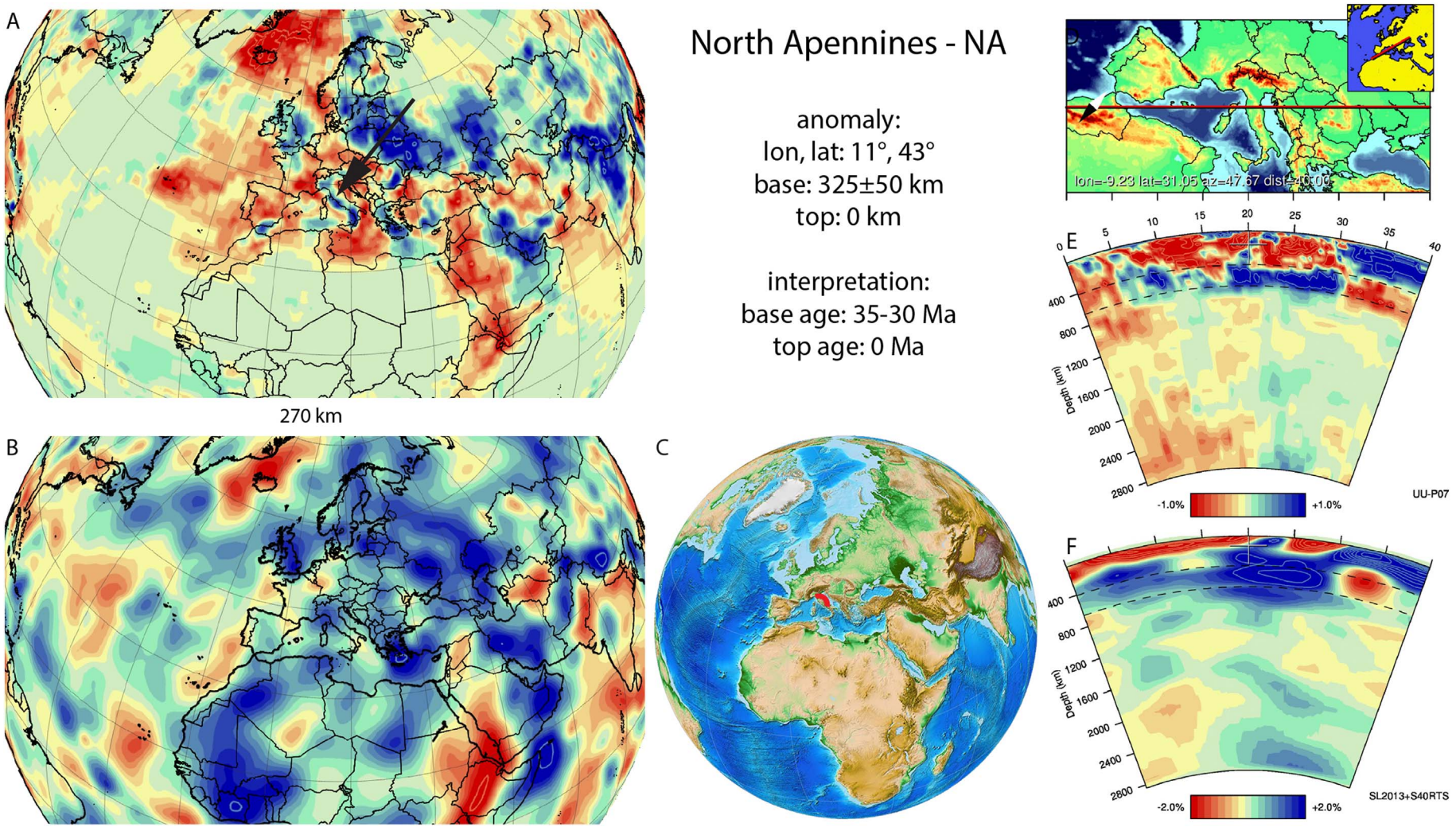

Fig. 71. North Apennines anomaly. Legend same as Fig. 5. This shallow slab is well imaged in the UU-P07 model, but not in the SL2013 model. This slab has a dip trend to the SW.

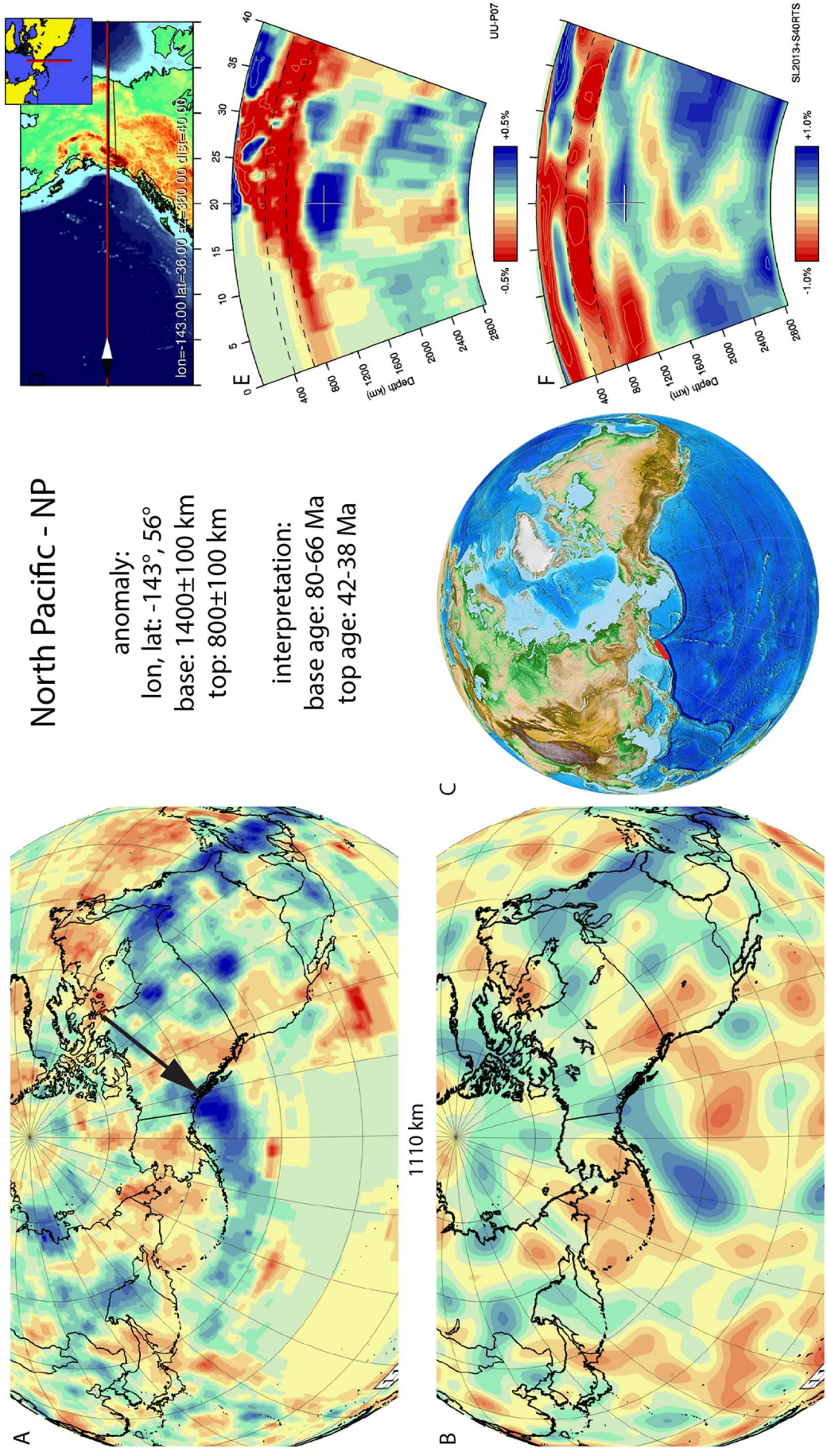

Fig. 72. North Pacific anomaly. Legend same as Fig. 5. Positive anomalies are identified in the same location in both tomographic models with a similar vertical extent. Relative amplitude strength and lateral extent differ between tomographic models.

pre-Cenozoic subducted lithosphere (van der Meer et al., 2010). Shapiro and Solov'ev (2009) inferred northward subduction of Kula oceanic lithosphere below a southward extension of the North American plate, resulting in the intra-oceanic Kronotsky-Commander arc now found in Kamchatka. This arc was dated by Levashova et al. (2000) to be active from 73 ± 7 Ma (Campanian-Maastrichtian) to 40 ± 2 Ma (Eocene), perhaps with a switch in subduction polarity in the Paleocene, resulting in subduction of North American plate.

The reconstruction of Shapiro and Solov'ev (2009), who restored the Kronotksy-Commander arc as part of the Pacific plate after its Eocene cessation, would place the arc in a positon that is in agreement with the location of the North Pacific slab. We therefore follow their interpretation and surpass our previous interpretation (van der Meer et al., 2010) which was based on an older reconstruction (Engebretson et al., 1985) of the paleo-Pacific Ocean. Following its extinction the Kronotsky-Commander arc was transported westward as an aseismic ridge to the Eurasian plate and collided with Kamchatka at ~5 Ma (Shapiro and Solov'ev, 2009).

3.69. Pamir - Pa

Subduction in the Pamir (Fig. 73) was first demonstrated by Burtman and Molnar (1993), and became evident from deep seismicity down to 250 km depth (Pegler and Das, 1998; Pavlis and Das, 2000; Koulakov, 2011; Zhang et al., 2011; Schneider et al., 2013; Sippl et al., 2013). The Pamir anomaly is interpreted to contain Asian lithosphere that subducted southward below the Pamir salient, which is a half-orocline associated with major counterclockwise rotations in the west, and a transform fault in the east – the Kashgar-Yecheng transform system (Bourgeois et al., 1997; Cowgill, 2010; van Hinsbergen et al., 2011a; Sobel et al., 2013). Seismic tomographic images of the Pamir slab reveal that its base reaches down to ~300–400 km depth (Van der Voo et al., 1999b; Negredo et al., 2007) (Fig. 77). The nature of the lithosphere of the Pamir slab is difficult to establish. The Pamir subduction zone is not associated with accretion of sediments, but instead with subduction erosion of the overriding plate (Sobel et al., 2013). Because the Pamir subduction zone is currently entirely intracontinental, the Pamir slab is generally interpreted as continental Asian lithosphere, even though it seems to behave in an oceanic manner, dipping near-vertical into the mantle (Sobel et al., 2013). Jackson et al. (2002) suggested that the Pamir slab may have represented a trapped basin of strongly attenuated continental or perhaps oceanic crust similar to the South Caspian Sea.

van Hinsbergen et al. (2011a) kinematically restored the Pamir salient and showed that the ~300–400 km of Pamir subduction is consistent with the northward motion of the northern Pamir relative to the adjacent Tarim basin, i.e. ~370 km based on estimated displacements in the western Kunlun Shan fold-thrust belt and along the Kashgar-Yecheng strike-slip system of Cowgill et al. (2003) and Cowgill (2010). Cowgill (2010) estimated the onset of activity of these structures at 30 ± 7 Ma. Sobel et al. (2013), using thermochronological data from the northern Pamir, estimated an onset of subduction around 25 Ma, at the young end of the spectrum. We conservatively keep the wide age range of Cowgill (2010) to date the base of the Pamir slab.

3.70. Papua - Pu

The Papua anomaly (Fig. 74) corresponds to the northern part of the A7 anomaly of Hall and Spakman (2002, 2004) and underlies an area from Papua New Guinea to the New Hebrides and from the east Australian margin to the Solomon islands, flat-lying at the top of the lower and base of the upper mantle. At its top it is south of the base of the New Hebrides (Section 3.66) and New Britain (Section 3.67) slabs that subducted since ~10–15 Ma. Hall and Spakman (2002, 2004) noted that the Papua anomaly is not everywhere well-defined and may in fact represent more than one slab, whereby the southwesternmost part of the slab below NW Australia (the Welford slab, Section 3.92) may be disconnected from the northern and eastern parts of the anomaly, which is the interpretation we follow here to account for the subduction records of both the Melanesian and Trobriand troughs. Hall and Spakman (2002, 2004) interpret the northern segment of the anomaly from Papua New Guinea to the New Hebrides to result from subduction at the Melanesian arc, from 45 Ma until the collision with the Ontong Java plateau, ~25 Ma, based on the reconstruction of Hall (2002). We adopt a somewhat large age range of 26–20 Ma for the collision of the Ontong Java plateau based on published estimates of Hall (2002), Quarles van Ufford and Cloos (2005), Knesel et al. (2008), and Holm et al. (2013) as estimate for the age of the top of the slab. Hall (2002), Cloos (2005) and Gaina and Müller (2007) interpreted the onset of subduction below the Melanesian arc to occur ~45 Ma ago, and Wu et al. (2016) since 50 Ma. Schellart et al. (2006) interpreted westward subduction below the Melanesian arc to have been ongoing since at least 90 Ma. We therefore adopt a large, 90–45 Ma range for the age of the base of the slab.

3.71. Reggane - Re

The Reggane anomaly (Fig. 75) is a small anomaly located in the upper part of the lower mantle below the western Sahara in the lower mantle and is resolved in both the UUP07 and S40RTS models. It was previously identified by Vissers et al. (2016). The Algeria slab directly to the east, which we correlate with Early Cretaceous ophiolite emplacement over Adria (Section 3.4) suggests that the Reggane anomaly likely represents lithosphere that subducted sometime in the Late Jurassic or Early Cretaceous in the westernmost Mediterranean region.

An Early Cretaceous phase of subduction between Iberia and southern France was postulated by Sibuet et al. (2004) based on reconstructions of the Bay of Biscay and Central Atlantic Ocean. Vissers and Meijer (2012a, 2012b) revisited the ocean basin reconstructions and reconciled these with the shortening history of the Pyrenees. They confirmed that ocean basin reconstructions require ~500 km of Early Cretaceous convergence across the Pyrenees, preceding intra-continental shortening, and advocated a short phase of subduction accommodating the counterclockwise rotation of Iberia. Paleomagnetic data confirm the ~35–40° of counterclockwise rotation of Iberia relative to Eurasia predicted from ocean basin reconstructions and constrain the timing of rotation, and hence Pyrenean subduction, to ~125–110 Ma (Gong et al., 2008; Ruiz-Martinez et al., 2012). Vissers and Meijer (2012b) interpreted a phase of high-temperature metamorphism that affected the central Pyrenees around 110–100 Ma as the result of slab break-off. Vissers et al. (2016) therefore dated the base and top of the Reggane slab at 126–121 Ma, corresponding to the varying ages assigned to the M0 isochron, and 105 ± 5 Ma, respectively. On the basis of refuting the paleomagnetic database of Vissers et al. and claiming the tomographic model used was inconclusive, Barnett-Moore et al. (2016) stated the Reggane slab was the result of enigmatic western Neotethys subduction instead of of Pyrenean subduction. van Hinsbergen et al. (2017a) showed that the Reggane anomaly appears in 8 tomographic models, including the ones used by Barnett-Moore et al. (2016), and showed that their criticism of Barnett-Moore et al. (2016) on the paleomagnetic database that requires Pyrenean subduction is unfounded.

3.72. Rio Negro - RN

The Rio Negro anomaly (Fig. 76) is located in the upper mantle below western Patagonia, southern South America. It is N–S trending and partly flat-lying. It has previously been interpreted to represent still-subducting Nazca lithosphere below the Andean margin (Aragón et al., 2011). We interpret a break in magmatism in the overriding plate between ~30–15 Ma to correspond with the gap between this slab and the deeper San Matias slab (Section 3.77). Aragón et al. (2011)

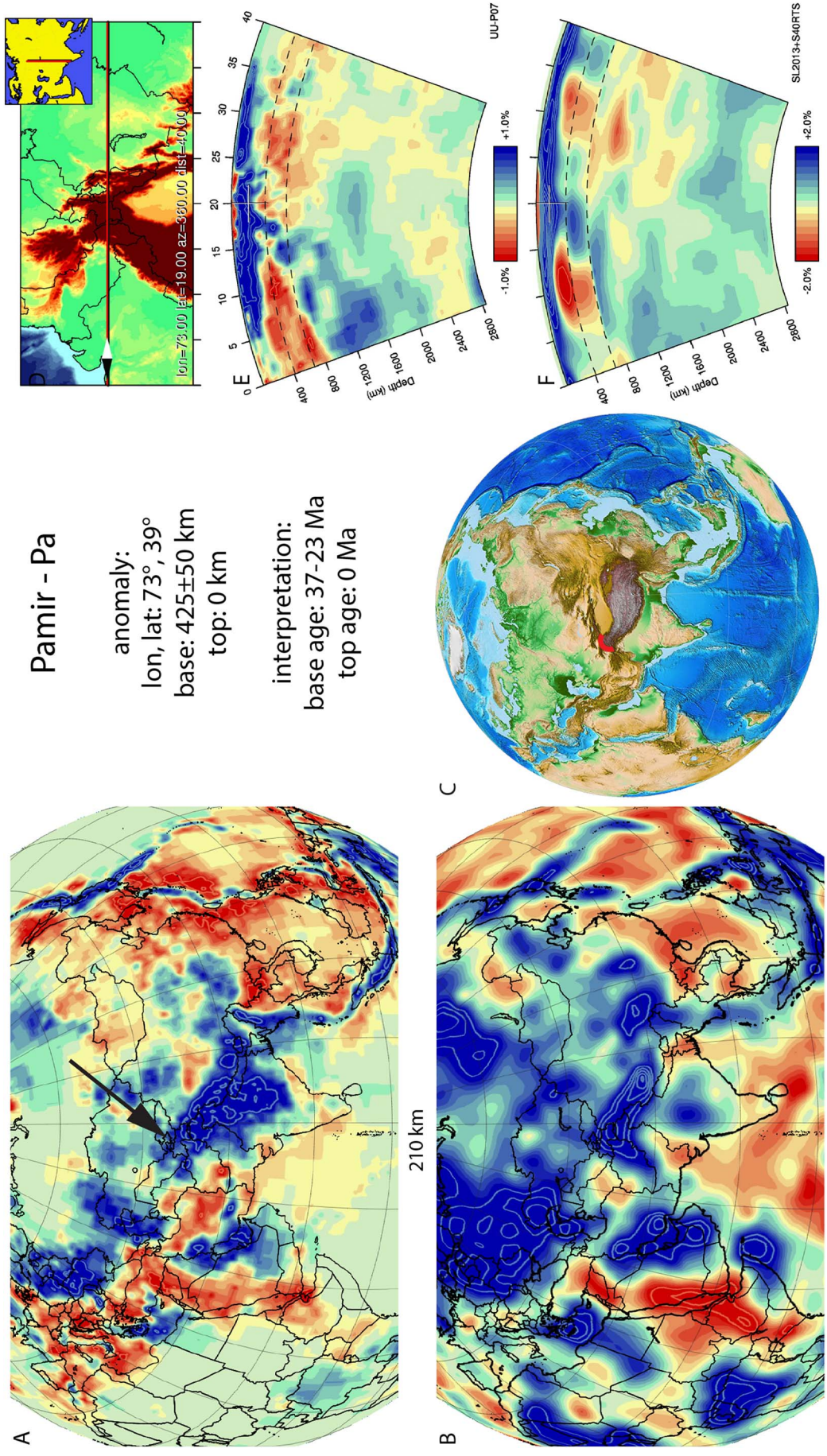

Fig. 73. Pamir anomaly. Legend same as Fig. 5. This upper mantle slab is well imaged in the UU-P07 model and there is a similar relative amplitude strength, lateral extent and vertical extent between the UU-P07 and SL2013 models. This slab dips to the SW.

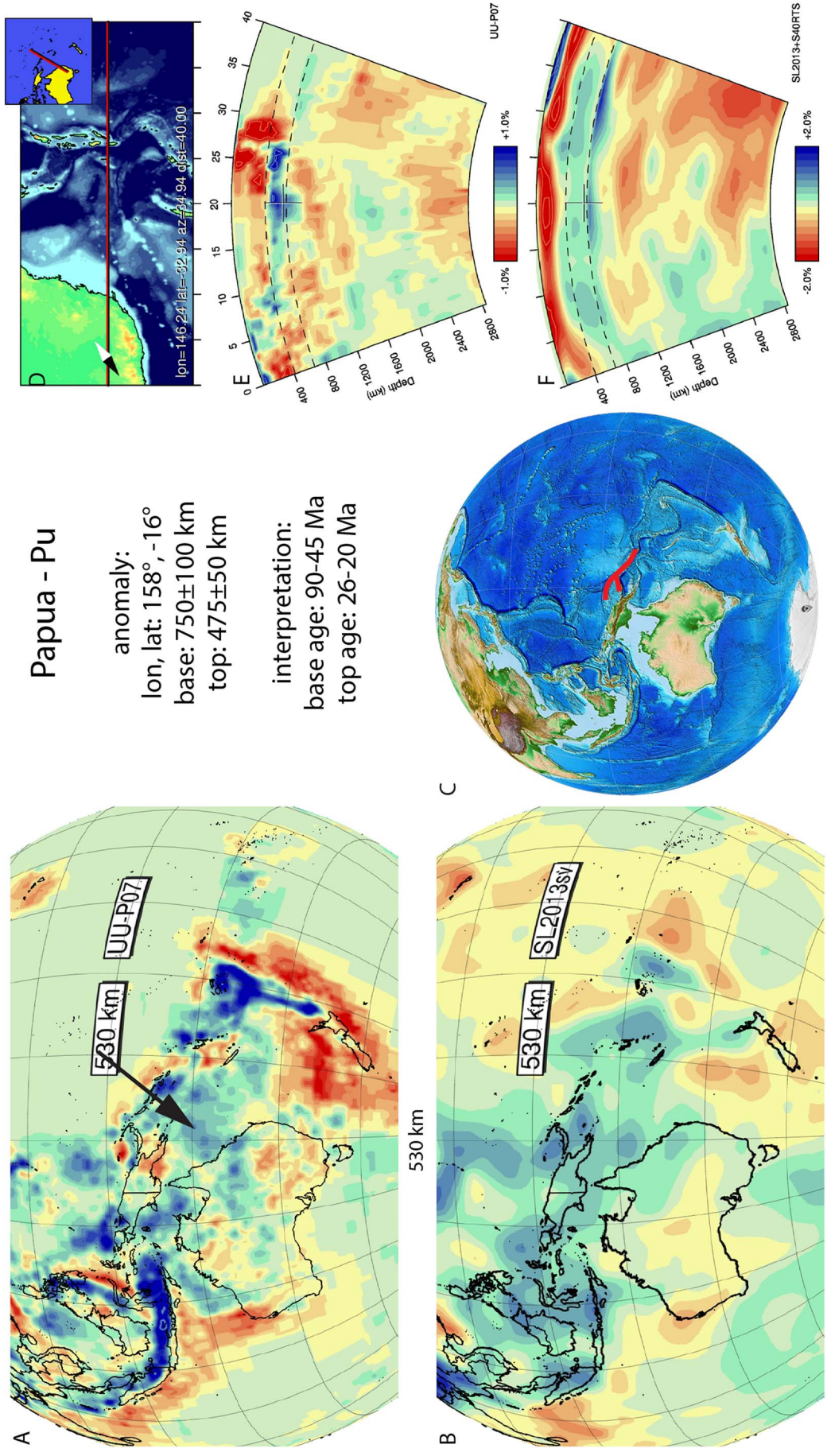

Fig. 74. Papua anomaly. Legend same as Fig. 5. Positive anomalies are identified in the same location in both tomographic models with a similar vertical extent and relative amplitude. Lateral extent is not clearly marked in the tomographic models. The slab is flat-lying on top of the transition zone.

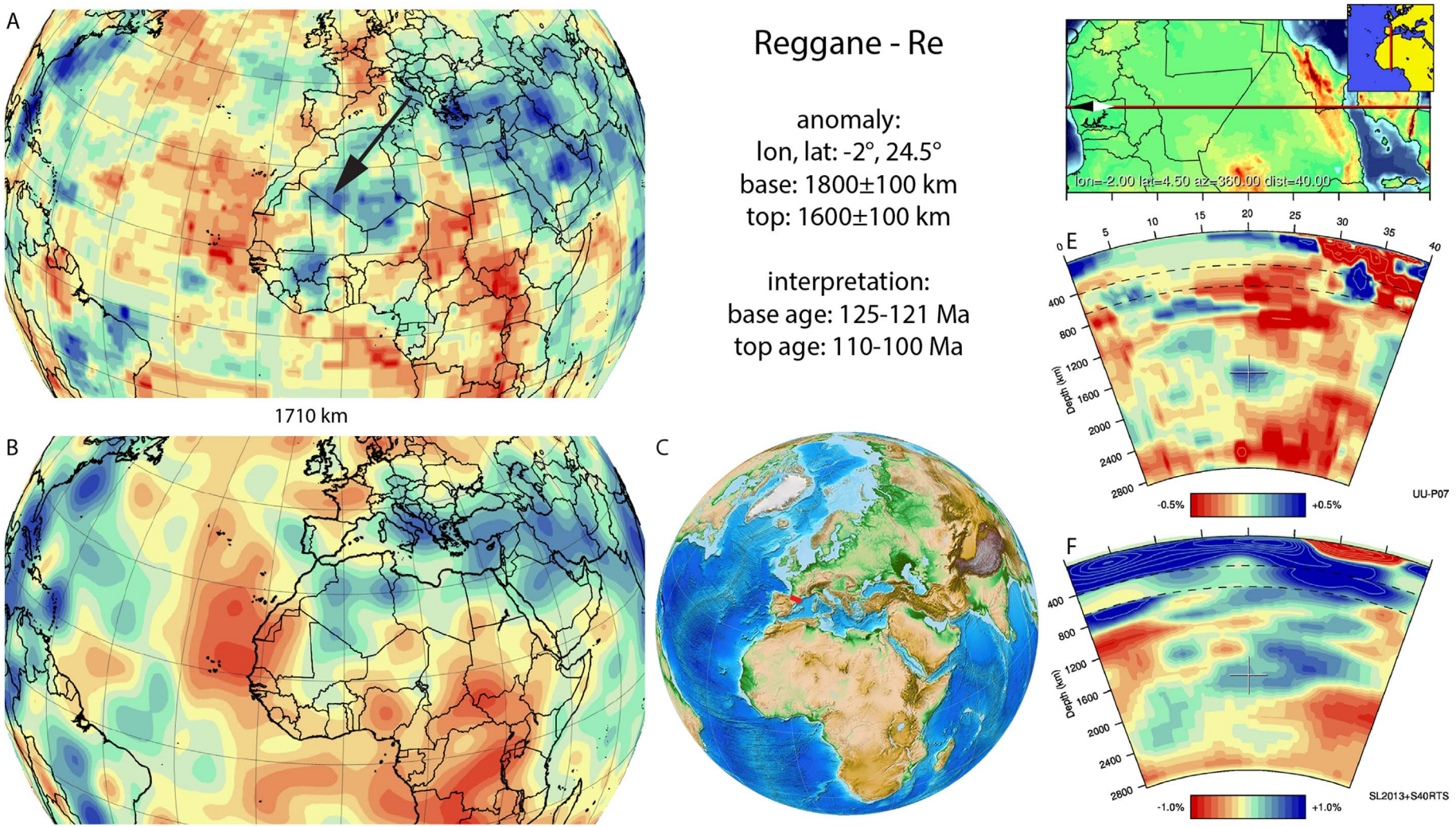

Fig. 75. Reggane anomaly. Legend same as Fig. 5. Positive anomalies are identified in the same location in both the UU-P07 and S40RTS tomographic models with a similar vertical extent and relative amplitude. Lateral extent differs. The slab does not have dip.

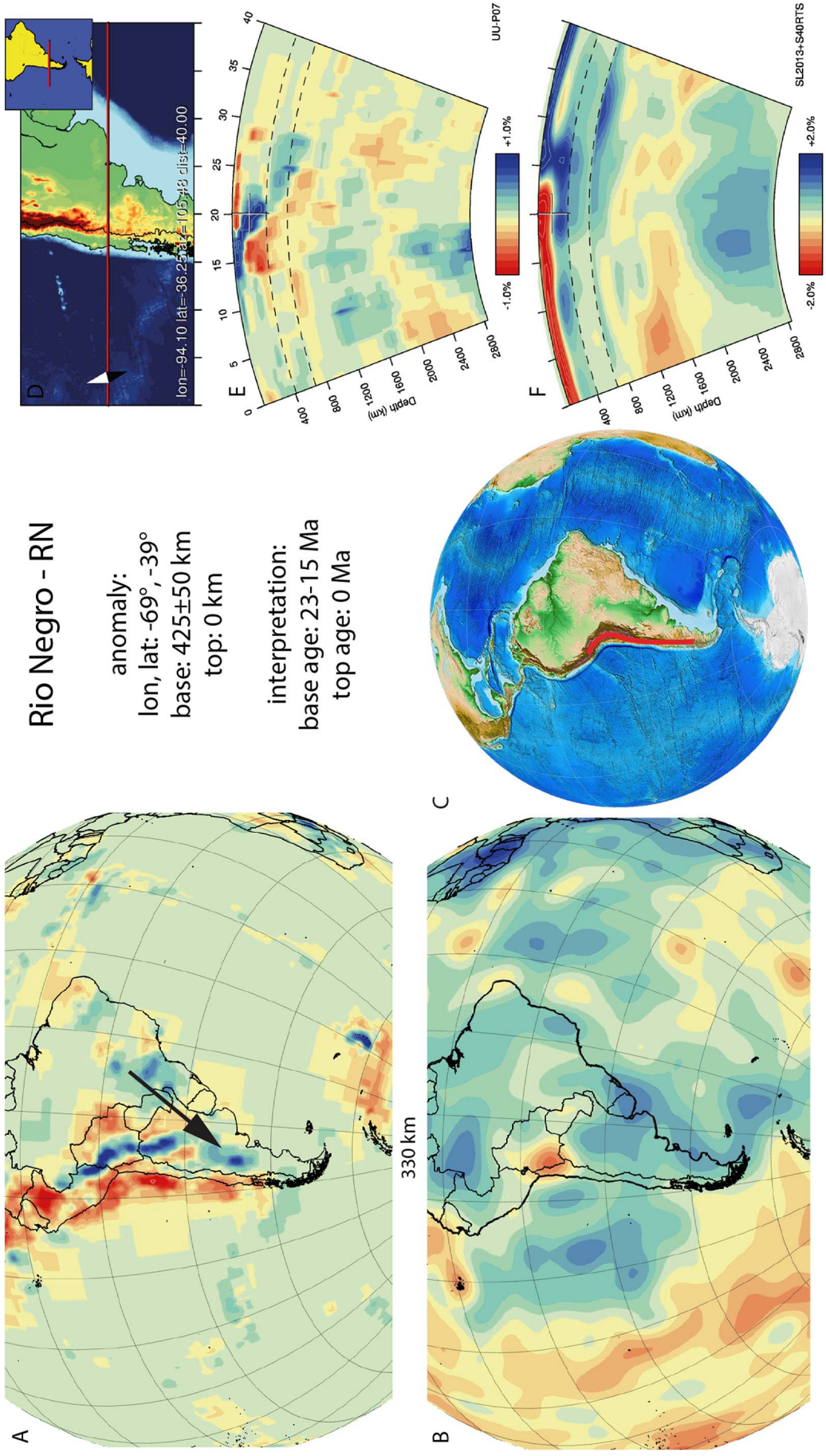

Fig. 76. Rio Negro anomaly. Legend same as Fig. 5. This upper mantle slab is well imaged in the UU-P07 model and there is a similar relative amplitude strength, lateral extent and vertical extent between the UU-P07 and SL2013 models. This slab dips to the NE.

estimated that subduction was re-established by ~23 Ma ago. Arc magmatism was re-established at around 15 Ma (Munizaga et al., 2002). We adopt the 23–15 Ma age range date the base of the slab.

3.73. Rockall - Ro

The Rockall anomaly (Fig. 77) is located west of the British Isles under the eastern North Atlantic Ocean and lies on the core-mantle boundary. It was first identified in van der Meer et al. (2010). The Mongol-Kazakh slab (Section 3.63) to the east, the Wichita slab (Section 3.91) to the west and the Balkan slab (Section 3.12) to the southeast were used by van der Meer et al. (2010) to interpret the anomaly as the Rockall slab that resulted from Early Mesozoic subduction between Siberia and Laurussia in the paleo-Arctic Ocean. The paleogeographic location is similar to the Upper Triassic-Lower Cretaceous continental margin Kony Murgal arc (Nokleberg et al., 2000). Shephard et al. (2013) renamed this to the Koni-Taigonous arc and narrowed its age range down to (Late) Triassic-Late Jurassic, which we adopt as age range for the Rockall slab.

3.74. Ryukyu - Ry

The Ryukyu anomaly (Fig. 78) is located in eastern Asia below the East China Sea in the upper mantle. The Ryukyu slab has previously been imaged in numerous regional and global tomographic models (Bijwaard et al., 1998; Lallemand et al., 2001; Zhao and Ohtani, 2009; Zheng et al., 2013; Koulakov et al., 2014; Wu et al., 2016). The slab is connected to the surface at the Ryukyu arc-Okinawa trench subduction zone, and is interpreted as Philippine Sea plate lithosphere that is still subducting northward below the South China block of the Eurasian plate. Towards the northeast it is interacts with the Izu-Bonin and Manchuria (Japan) slabs (Sections 3.44 and 3.54, respectively) at a trench-trench-trench triple junction. Towards the southwest, the trench is propagating westwards south of the island of Taiwan, where subduction of the southeastward dipping Manila slab (Section 3.55) is coming to a halt due to collision of the Philippine Sea plate with the South China block (e.g., Ustaszewski et al., 2012). According to the kinematic restoration of SE Asia of Hall (2002), subduction along the Ryukyu trench started at ~25 Ma, whereas in the reconstruction of Wu et al., 2016, subduction started at ~15 Ma. In the central Ryukyu arc, volcanism started at ~21 Ma (Chung et al., 2000), and we adopt a 25–21 Ma age range for the base of the Ryukyu slab.

3.75. Sakhalin - Sa

The Sakhalin anomaly (Fig. 79) is located below northeast Asia within the upper part of the lower mantle. In previous tomographic studies it has been interpreted to as a subducted slab of the Okhotsk plate (Gorbatov et al., 2000). On the basis of the Kamchatka slab to the east and shallower in the mantle, van der Meer et al. (2010) inferred that the Sakhalin slab likely subducted in Late Mesozoic to Early Cenozoic times. In the tectonic model of Nokleberg et al. (2000) subduction of Okhotsk lithosphere initiated at the continental margin below the East Sikhote-Alin arc in the Late Cretaceous. The Sikhote arc consists of Cenomanian-Danian arc volcanics, which we adopt as the age range for the Sakhalin slab. Subduction ended in the Late-Cretaceous-Paleocene due to accretion of the Okhotsk block, resulting in an eastward jump to form the Kamchatka-Kuriles arc and slab (Section 3.47).

3.76. Sangihe - Sn

The Sangihe anomaly (Fig. 80) was imaged by Widiyantoro and van der Hilst (1997), Bijwaard et al. (1998), Rangin et al. (1999), and Hall and Spakman (2002, 2004, 2015), and Wu et al. (2016) and is interpreted as one of the two actively subducting slabs attached to the Molucca Sea plate, the other one being the Halmahera slab (Section 3.36). The Sangihe slab dips to the NW below the island of Sulawesi and the Sangihe arc and reaches the base of the upper mantle. At shallow upper mantle levels the slab is separated into several slabs (Hall and Spakman, 2015; Wu et al., 2016), from north to south including the Philippine Trench slab, Molucca Sea West slab, Sulu and Celebes Sea South slab (Wu et al., 2016). The deepest part of the Sangihe slab, named Molucca Sea West slab in Wu et al. (2016) possibly penetrates into the lower mantle, where it merges with the large Kalimantan anomaly (Section 3.48). In the reconstruction of Hall (2002), subduction below the Sangihe arc started ~25 Ma, whereas the reconstruction of Wu et al., 2016 assume a start at ~30 Ma. We therefore use 30–25 Ma as age for the base of the slab.

3.77. San Matias - SM

The San Matias anomaly (Fig. 81) is located below southeastern South America, offshore Patagonia, at the top lower mantle and at the base of the upper mantle. It is a N–S trending anomaly and has previously been interpreted to have subducted eastward below South America, followed by its detachment due to the arrival of the Farallon-Aluk ridge at the Andean margin (Aragón et al., 2011). This led to a break in magmatism between ~30–15 Ma, which we interpret to correspond with the slab window between this slab and the shallower Rio Negro slab. We interpret the onset of subduction of the slab to correspond with the Paleocene–Eocene Pilcaniyeu belt with an age of 68–49 Ma (Giacosa and Heredia, 2004).

3.78. Sao Francisco - SF

The Sao Francisco anomaly (Fig. 82) is located below eastern South America, within the deepest mantle and resting on the core-mantle boundary. It is NE-SW trending at the core-mantle-boundary and changes to N–S trending at shallower levels. It is disconnected from and lies eastward of the Brasilia slab (Section 3.18). At the CMB, it connects northward with the Atlantis slab (Section 3.11) suggesting a possible common origin. As we interpreted the Atlantis slab to result from Triassic Panthalassa Ocean subduction along southwestern Laurentia, we infer the Sao Francisco slab to have formed at the northwestern Gondwana (South American) continental margin.

At this location, which would fit the NE-SW slab trend, Triassic metamorphism (243–225 Ma) affected granites, basalts and sedimentary rocks in the Tahamí Terrane, interpreted to have taken place in an Andean-type orogeny on the western side of Pangea as part of an orogenic belt (Restrepo et al., 2011). We connect this record to the subduction of the Sao Francisco slab and use it to date the Sao Francisco slab.

3.79. Scotia - Sc

The Scotia anomaly (Fig. 83) was first documented in the tomographic model of Bijwaard et al. (1998). It is interpreted to represent still-subducting South American plate lithosphere consumed at the South Sandwich subduction zone, and dips westward below the Scotia Sea. Resolution tests show that the deeper part of the anomaly is poorly resolved, and our interpretation is therefore tentative. The cause of formation of the Scotia subduction zone is puzzling. It formed within the South American plate, south of the Falkland plateau, even though the South American plate and Antarctic plate were in an extensional phase at that time and the spreading between South America and Antarctica was being accommodated at the mid-oceanic ridge in the Weddell Sea. Because subduction of the Scotia slab was for most of its history not associated with plate convergence but is fully accommodated by extension in the Scotia and South Sandwich basins, the age for the onset of subduction is best estimated from the age of the onset of extension in the overriding plate. Oceanic lithosphere in the South Sandwich back-arc is Late Miocene and younger, and in the Scotia Sea is

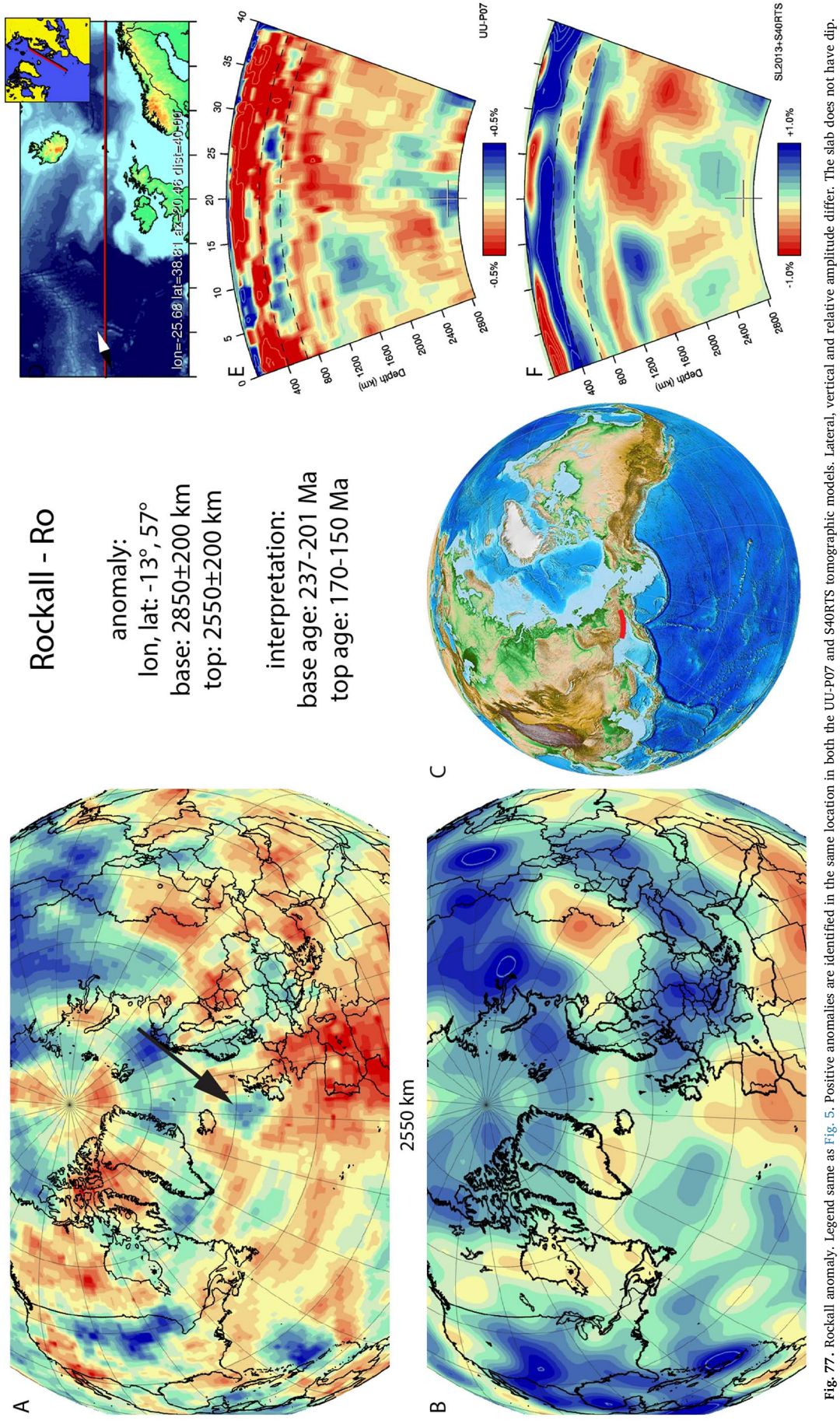

Fig. 77. Rockall anomaly. Legend same as Fig. 5. Positive anomalies are identified in the same location in both the UU-P07 and S40RTS tomographic models. Lateral, vertical and relative amplitude differ. The slab does not have dip.

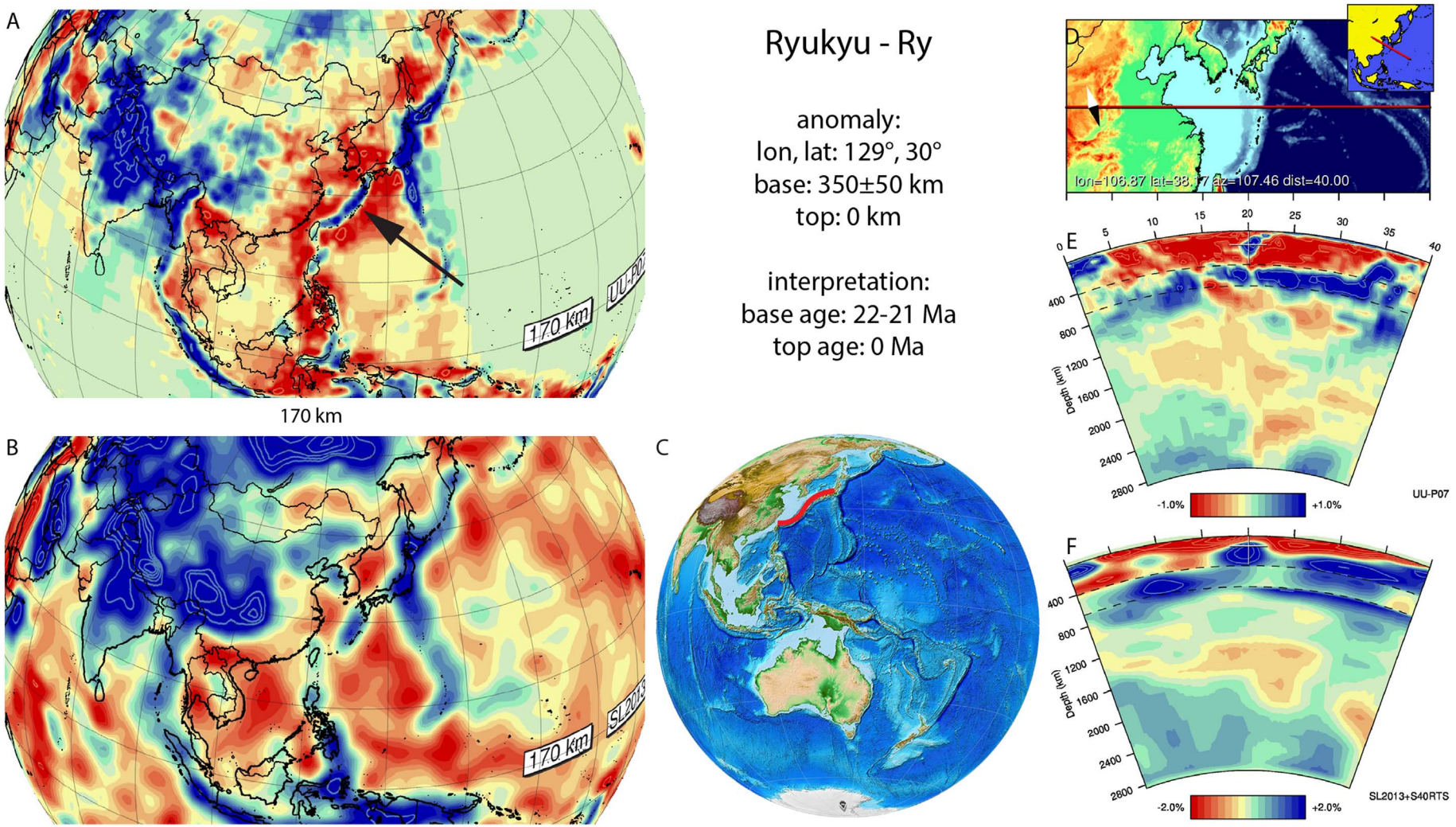

Fig. 78. Ryukyu anomaly. Legend same as Fig. 5. This upper mantle slab is well imaged in the UU-P07 model and there is a similar relative amplitude strength, lateral extent and vertical extent between the UU-P07 and SL2013 models. This slab dips to the NW.

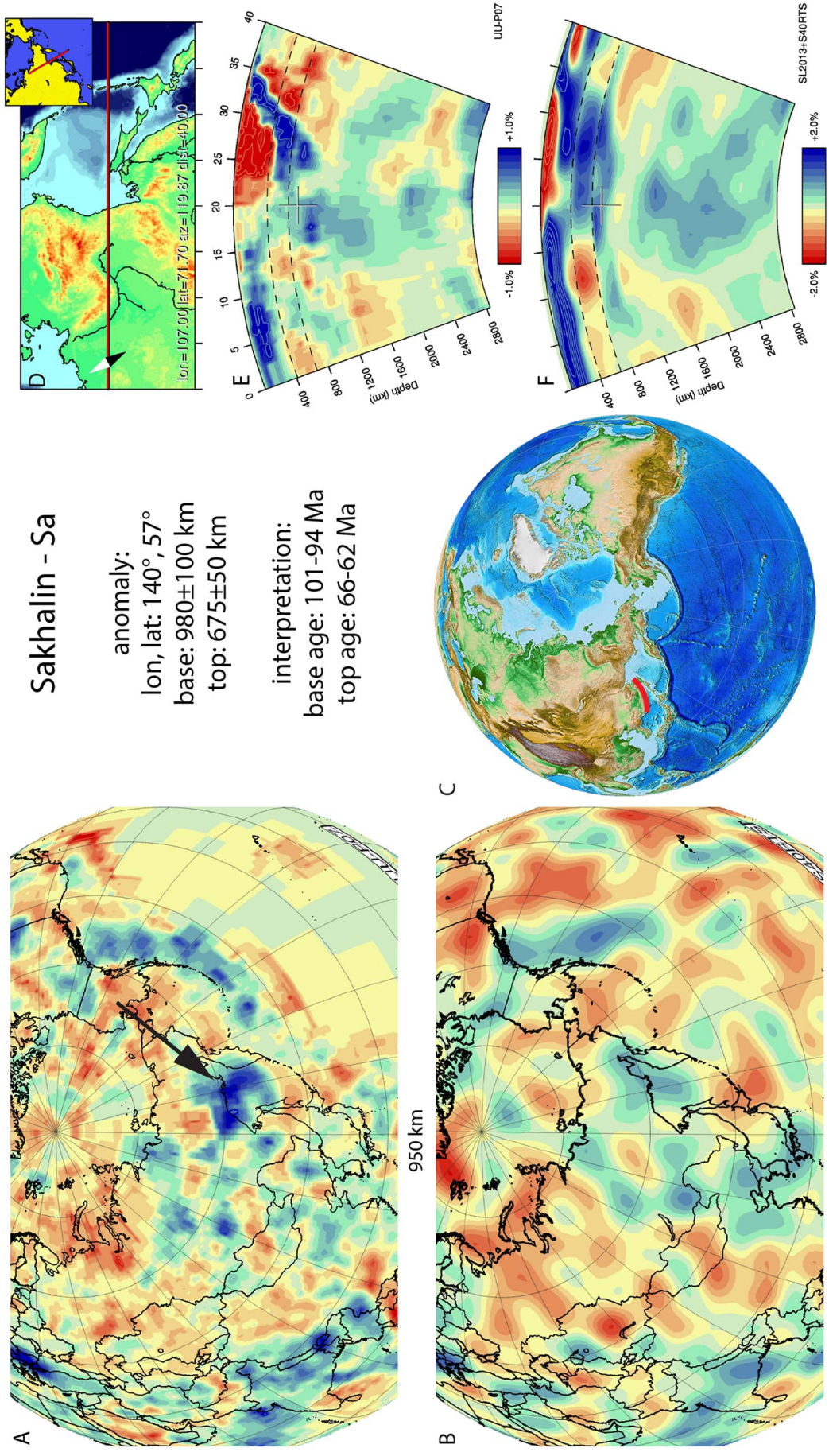

Fig. 79. Sakhalin anomaly. Legend same as Fig. 5. Positive anomalies are identified in the same location in both the UU-P07 and S40RTS tomographic models. Lateral, vertical extent and relative amplitude differ. The slab does not have dip.

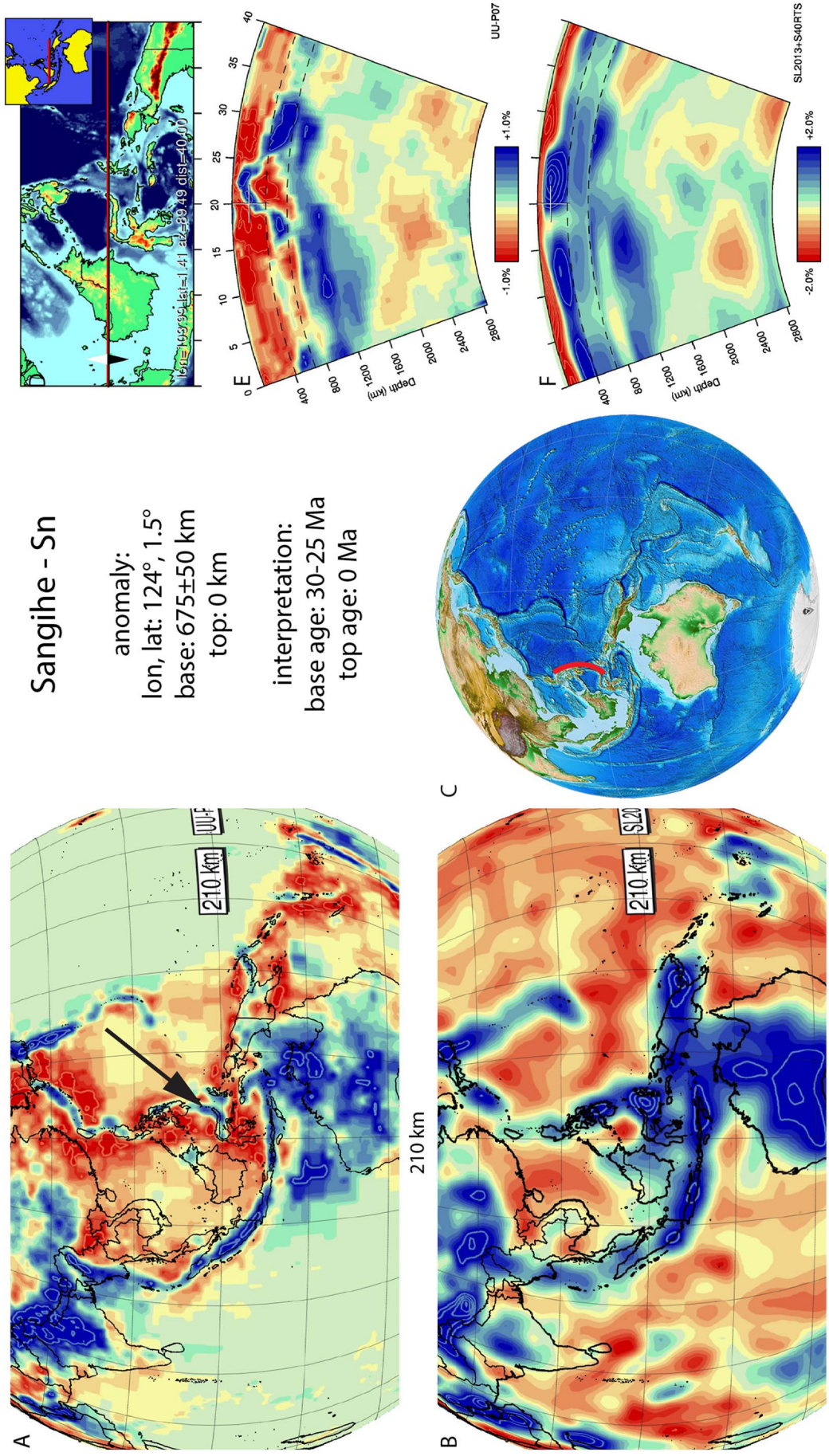

Fig. 80. Sangihe anomaly. Legend same as Fig. 5. This shallow slab is well imaged in the UU-P07 model, but not in the SL2013 model. This slab has a dip trend to the NW.

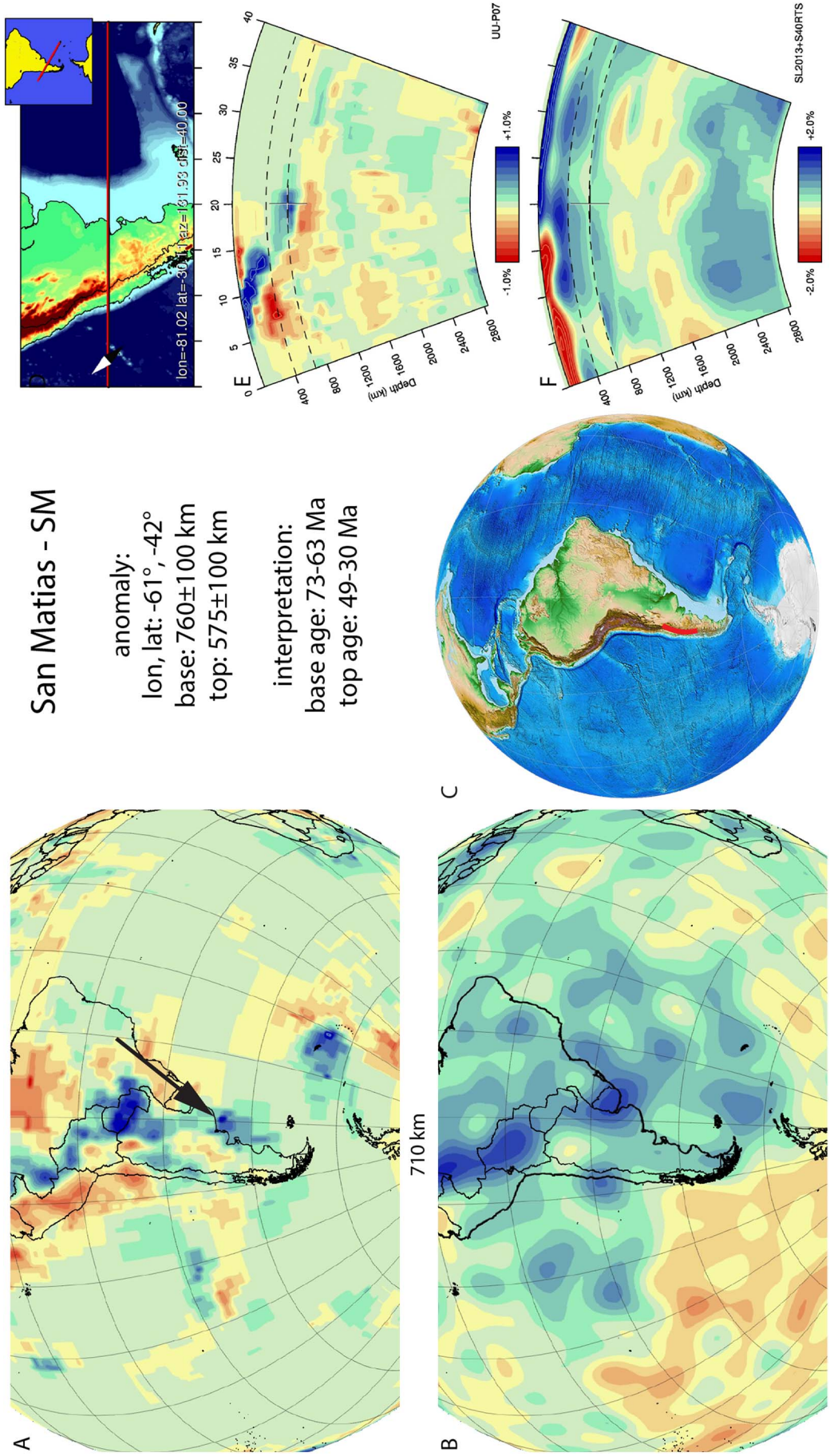

Fig. 81. San Matias anomaly. Legend same as Fig. 5. Positive anomalies are identified in approximate locations in both the UU-P07 and SL2013-S40RTS tomographic models. Lateral, vertical extent and relative amplitude differ. In the UU-P07 model, the slab is either flat-lying at the transition zone, or may have a dip to the SE.

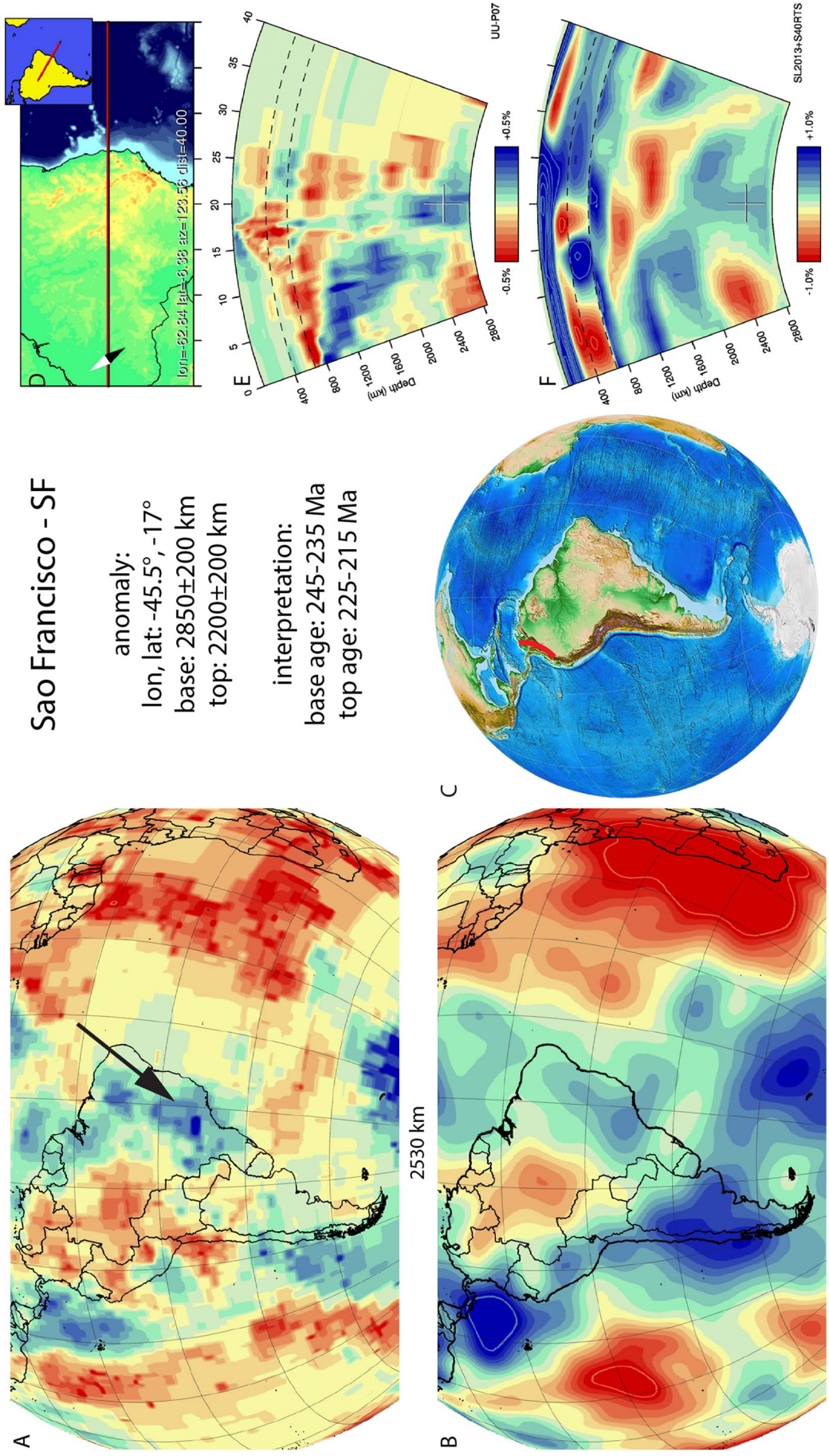

Fig. 82. Sao Francisco anomaly. Legend same as Fig. 5. Positive anomalies are identified in the same location in both the UU-P07 and S40RTS tomographic models. Lateral, vertical extent and relative amplitude are similar. The slab is vertical in the deep mantle and seems to be piling up at the CMB.

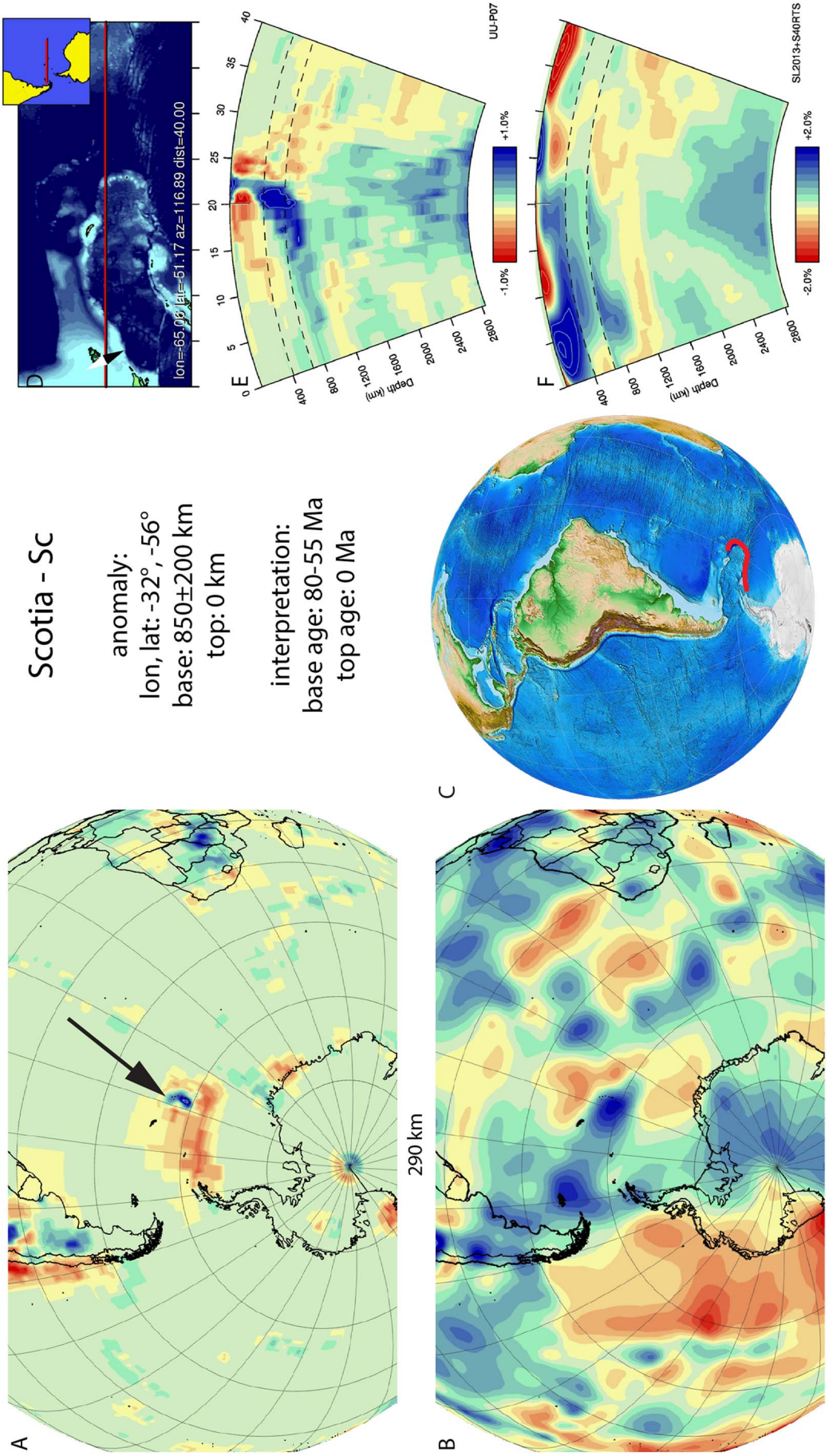

Fig. 83. Scotia anomaly. Legend same as Fig. 5. Positive anomalies are identified in the same location in both the UU-P07 and S40RTS tomographic models in the lower mantle, but differ considerably in the upper mantle between the UU-P07 and SL2013 model. In the lower mantle, lateral, vertical extent and relative amplitude are similar. The slab is dipping to the west, and is flat-lying at the top of the lower mantle.

interpreted as ~27 Ma and younger (Eagles, 2005; Lodolo et al., 2006). Closing these basins juxtaposes continental fragments along the southern fringes of the Scotia Sea (e.g., the South Orkney microcontinent) with the southern margin of the Falkland Plateau, suggesting that basin formation started within the Mesozoic passive margin of the Falkland plateau that formed during the breakup of South America and Antarctica in the Late Jurassic or Early Cretaceous. This suggests that oceanization in the Scotia Sea at 27 Ma was preceded by a period of pre-drift extension. Estimates for the onset of extension in this area from Tierra de Fuego is Eocene (~55–45 Ma) (Ghiglione et al., 2008), by which time subduction of the Scotia slab must have been active (Eagles et al., 2006; Livermore et al., 2007; Dalziel et al., 2013; Nerlich et al., 2013). This episode was preceded by a phase of slow convergence between West Antarctica and Patagonia concluded from marine magnetic anomalies of the Atlantic and Antarctic oceans, which likely date the onset of subduction (e.g., König and Jokat, 2006; Eagles, 2010; Eagles and Jokat, 2014). We adopt an 80–55 Ma age range for the base of the Scotia slab. The anomalies in the Weddell Sea become younger towards the north, and are youngest at the fault zone that bounds the South Orkney microcontinent from the Weddell Sea, where they are ~10 Ma old (Müller et al., 2008). This may indicate that the originally E–W trending portion of the Scotia subduction zone to the south of the South Orkney microcontinent became inactive due to the migration of the subduction zone to the Weddell Sea ridge and consequent slab break-off, leaving the west-dipping South Sandwich subduction zone as the only active portion of the system.

3.80. Sisimut - Si

The Sisimut anomaly (Fig. 84) is located below northernmost North America and Greenland within the mid-mantle. It is NW-SE trending and does not have a neighbouring slab in close vicinity. van der Meer et al. (2012) suggested that the slab may result from paleo-Arctic subduction and loosely inferred the anomaly we now define as Sisimut slab to be of Early Cretaceous age. It was recently studied in detail by Shephard et al. (2016) who named it the Greenland anomaly. Within the region of the Sisimut slab, Nokleberg et al. (2000) documented southward subduction of Angayucham and Anyui lithosphere below the continental-margin Nutesyn arc. This arc is Late Jurassic to Early Cretaceous in age (Nokleberg et al., 2000; Parfenov et al., 2009). In the plate motion model of Shephard et al. (2013), these different elements were integrated and they concluded that subduction below the Koyukuk and Nutesyn arcs was active between 160 and 120 Ma, which we adopt for ages for the top and bottom of the slab, in line with Shephard et al. (2016).

3.81. Sistan - St

The Sistan anomaly (Fig. 85) is a N–S striking anomaly below eastern Iran and western Afghanistan in the upper part of the lower mantle. Given its orientation, its position to the west of the India slab (Section 3.43), northeast of the Mesopotamia slab (Section 3.60) and northwest of the Carlsberg slab (Section 3.22), the Sistan anomaly is best explained by subduction that terminated with the formation of the Sistan suture that currently still overlies this slab. The Sistan suture is N–S trending and separates the Lut Block of central Iran and the Helmand Block of Afghanistan (Camp and Griffis, 1982; Tirrul et al., 1983). This suture formed at the expense of an Early Cretaceous oceanic basin (Babazadeh and De Wever, 2004) that was in an overriding plate position relative to the Mesopotamia slab (Section 3.60). Eclogite and blueschist rocks in melanges of the Sistan suture (Fotoohi Rad et al., 2005) were originally suggested to have formed in Early Cretaceous time (~125 Ma) based on $^{40}Ar/^{39}Ar$ thermochronology with large age uncertainties of > 10 Myr (Fotoohi Rad et al., 2009). A recent re-dating of these rocks by $^{40}Ar/^{39}Ar$, Rb/*Sr* and U/Pb geothermochronology was not able to reproduce these Early Cretaceous ages and rather produced a tight clustering of ages between 83 and 89 Ma (Bröcker et al., 2013), by which time subduction must have been underway to produce pressures in excess of 20 kbar (Fotoohi Rad et al., 2005). Given the stratigraphic ages of Albian-Aptian in the HP mélange of the Sistan suture (~125–100 Ma) we adopt an onset of subduction of the Sistan Ocean of 100–90 Ma. An ~59 Ma granite in the Sistan suture has a geochemistry consistent with arc magmatism (Delavari et al., 2014), ~46–25 Ma magmatism in the area is interpreted as post-collisional, perhaps reflecting delamination and asthenospheric inflow that may have been triggered by slab break-off (Rezaei-Kahkhaei et al., 2010; Pang et al., 2013; Mohammadi et al., 2016). We adopt a 59–46 Ma end of the subduction of the Sistan slab.

3.82. Socorro - So

The Socorro anomaly (Fig. 86) is located below western North America within the mid-mantle. It was first described in van der Meer et al. (2010) and corresponds to anomaly CR-3 of Sigloch and Mihalynuk (2013). The Idaho slab (Section 3.42) and the Socorro anomaly cover similar depth ranges and dips, and have a more westerly location than the Hatteras and Cocos slabs of the Farallon family (Section 3.37, and Section 3.29, respectively). Similar to the Idaho slab we therefore interpreted an intra-oceanic, Jurassic-Cretaceous origin for this slab. The Wrangellia superterrane of the northwestern North American margin contains terranes derived from both northerly and near-equatorial paleolatitudes according to paleomagnetic data (Nokleberg et al., 2000). In conjunction with our interpretation of the Idaho slab, we associate eastward subduction of Panthalassa/Farallon lithosphere below the southern part of the Wrangellia terranes to have formed the Socorro slab, starting in the Early to Middle Jurassic. Accretion of the terrane to Laurentia started in the Late Jurassic (Trop et al., 2005) and ended in the Early to Late Cretaceous (Nokleberg et al., 2000). Sigloch and Mihalynuk (2013) inferred that the Socorro slab was overridden by the continental margin at 55–50 Myr, culminating in the Siletzia and Pacific Rim terrane accretions, which we adopt as the age of breakoff.

3.83. South loyalty basin - SLB

The NW-SE trending South Loyalty Basin anomaly (Fig. 87) is located below the Tasman Sea within the upper part of the lower mantle. It was first identified by Schellart et al. (2009). In the east, the flat-lying South Loyalty Basin anomaly is difficult to distinguish from the steeply dipping Tonga-Kermadec-Hikurangi anomaly (Section 87), which makes estimating the depth of its base difficult. We follow the suggestion of Schellart et al. (2009) and Schellart and Spakman (2012), and assign a 1000 to 1200 km depth range for the anomaly, which we interpret as the South Loyalty Basin slab.

Its position west of the Tonga-Kermadec-Hikurangi slab (Section 87) requires a subduction location between the Tonga-Kermadec trench and Australia, where the geological record of the New Caledonia subduction zone (Schellart et al., 2009) is the only candidate for correlation. Schellart et al. (2006) estimated that this subduction zone was active from 50 to 45 Ma until 30–20 Ma. Matthews et al. (2015) suggested that subduction halted earlier, 45 Ma. The New Caledonia subduction zone terminated with the obduction of an ophiolite derived from the overriding plate forearc over a Paleozoic to Mesozoic volcano-sedimentary complex belonging to the Gondwana-derived Zealandia microcontinent (Luyendyk, 1995; Bache et al., 2013) on the island of New Caledonia. The ophiolite is underlain by high pressure, high-temperature amphibolites interpreted as a metamorphic sole, which was dated with $^{40}Ar/^{39}Ar$ on hornblende and U/Pb dating of zircons at ~56 Ma (Cluzel et al., 2012); sheeted dykes in the New Caledonia ophiolite have 53 Ma ages (Cluzel et al., 2006). This shows a somewhat earlier onset of New Caledonia subduction than previously interpreted, likely a few million years before the ages derived from the sole. We adopt a 60–56 Ma

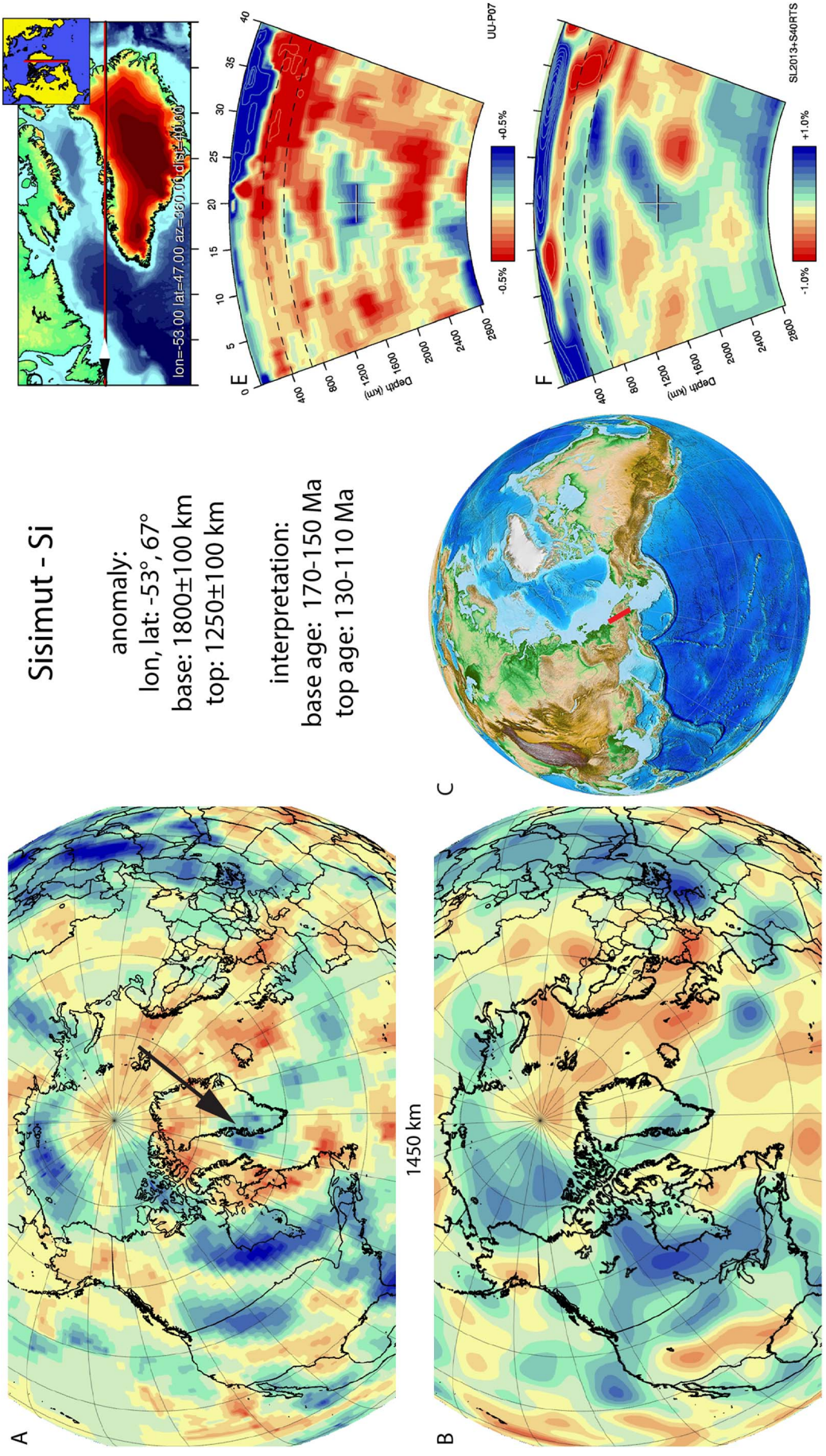

Fig. 84. Sisimut anomaly. Legend same as Fig. 5. Positive anomalies are identified in the same location in both the UU-P07 and S40RTS tomographic models. Lateral, vertical extent difer and relative amplitude is similar. The shape of the slab is unclear in UU-P07, but appears to be dipping to the south in the S40-RTS model.

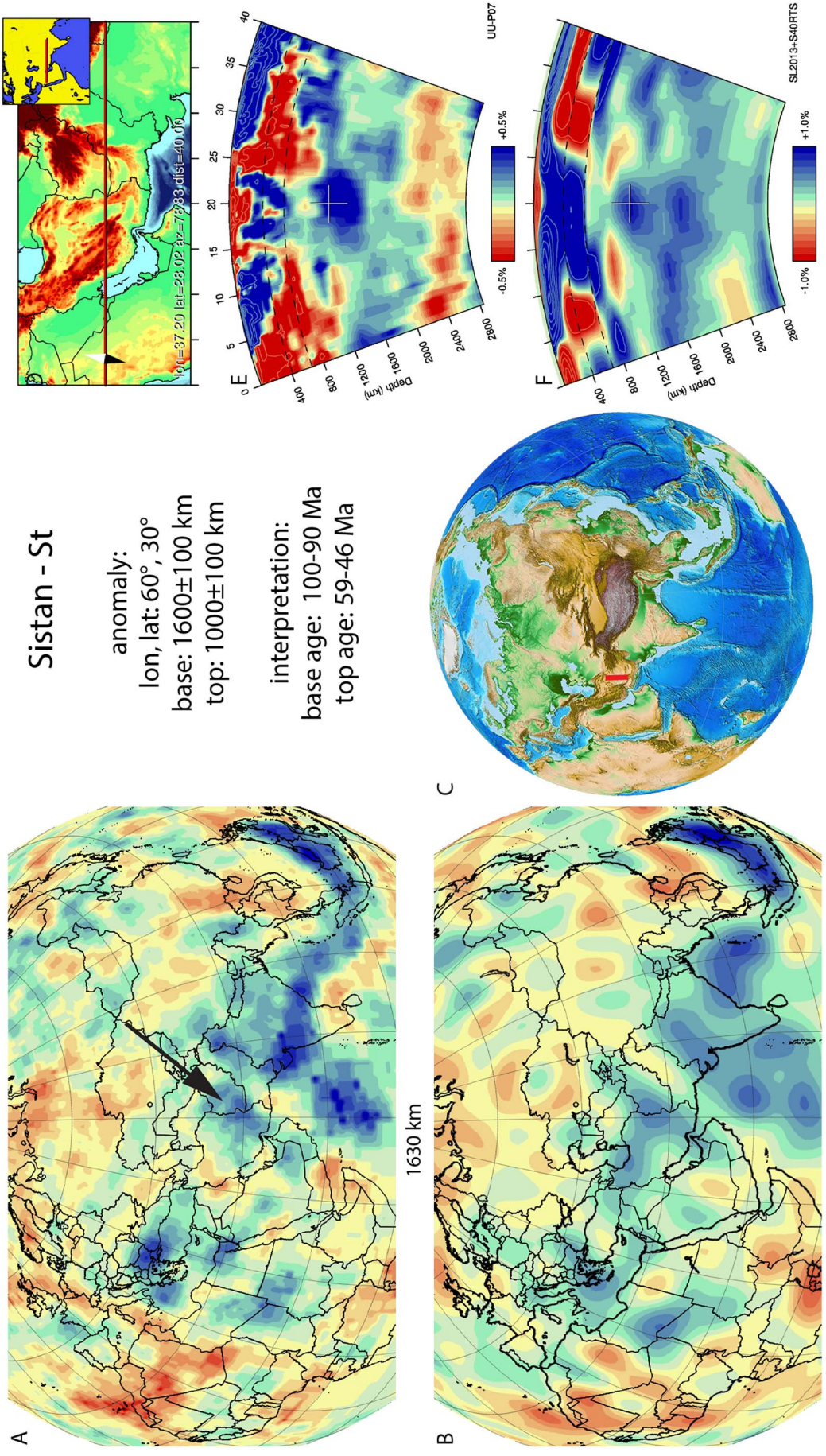

Fig. 85. Sistan anomaly. Legend same as Fig. 5. Vertical and lateral extent are very similar between tomographic models. Relative amplitude strength differs and is stronger in UU-P07. The slab has no dip trend.

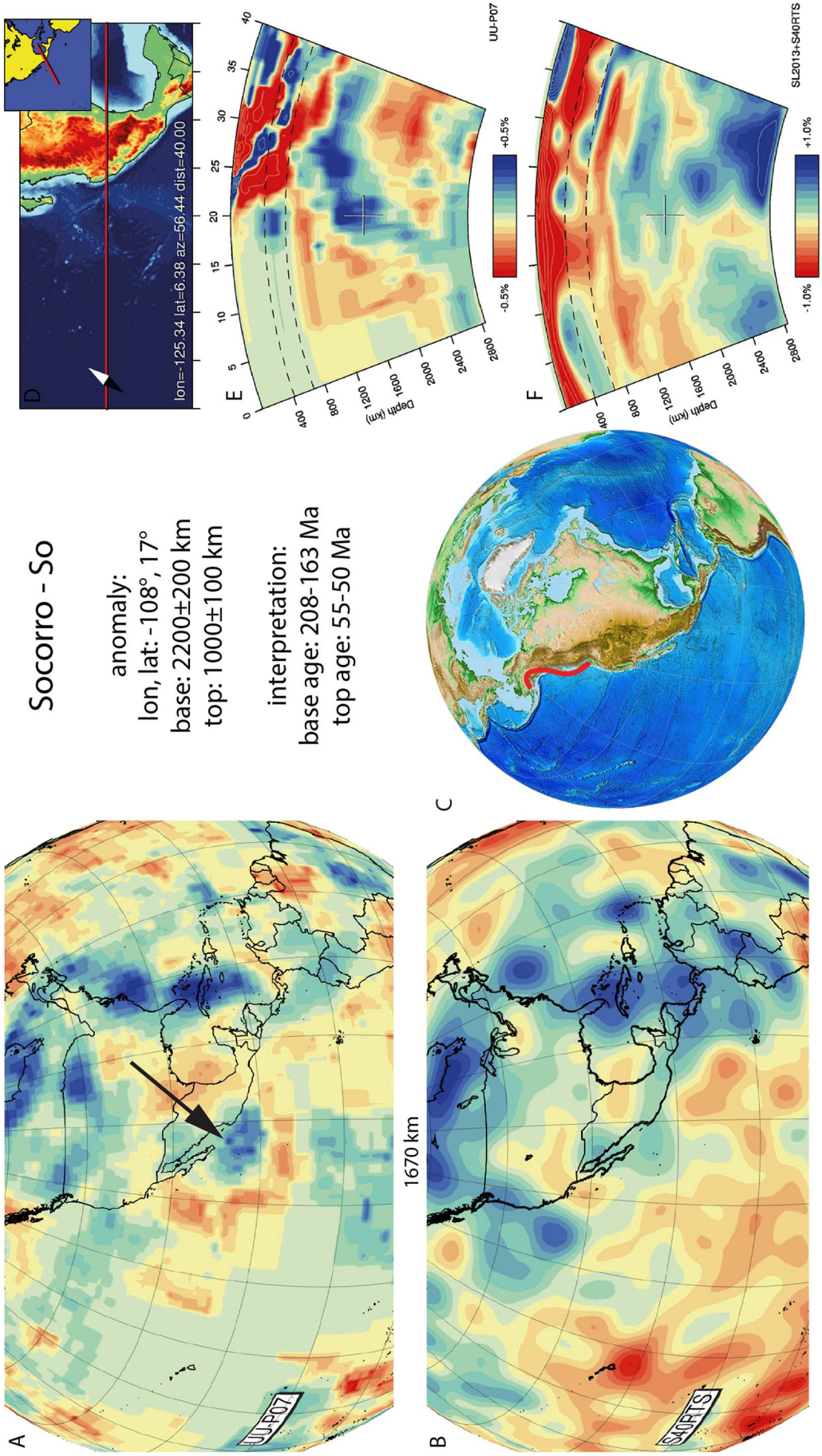

Fig. 86. Socorro anomaly. Legend same as Fig. 5. Positive anomalies are identified in the same location in both the UU-P07 and S40RTS tomographic models. Lateral extent is similar, but vertical extent and relative amplitude differ. The dip of the slab is to the SW in UU-P07.

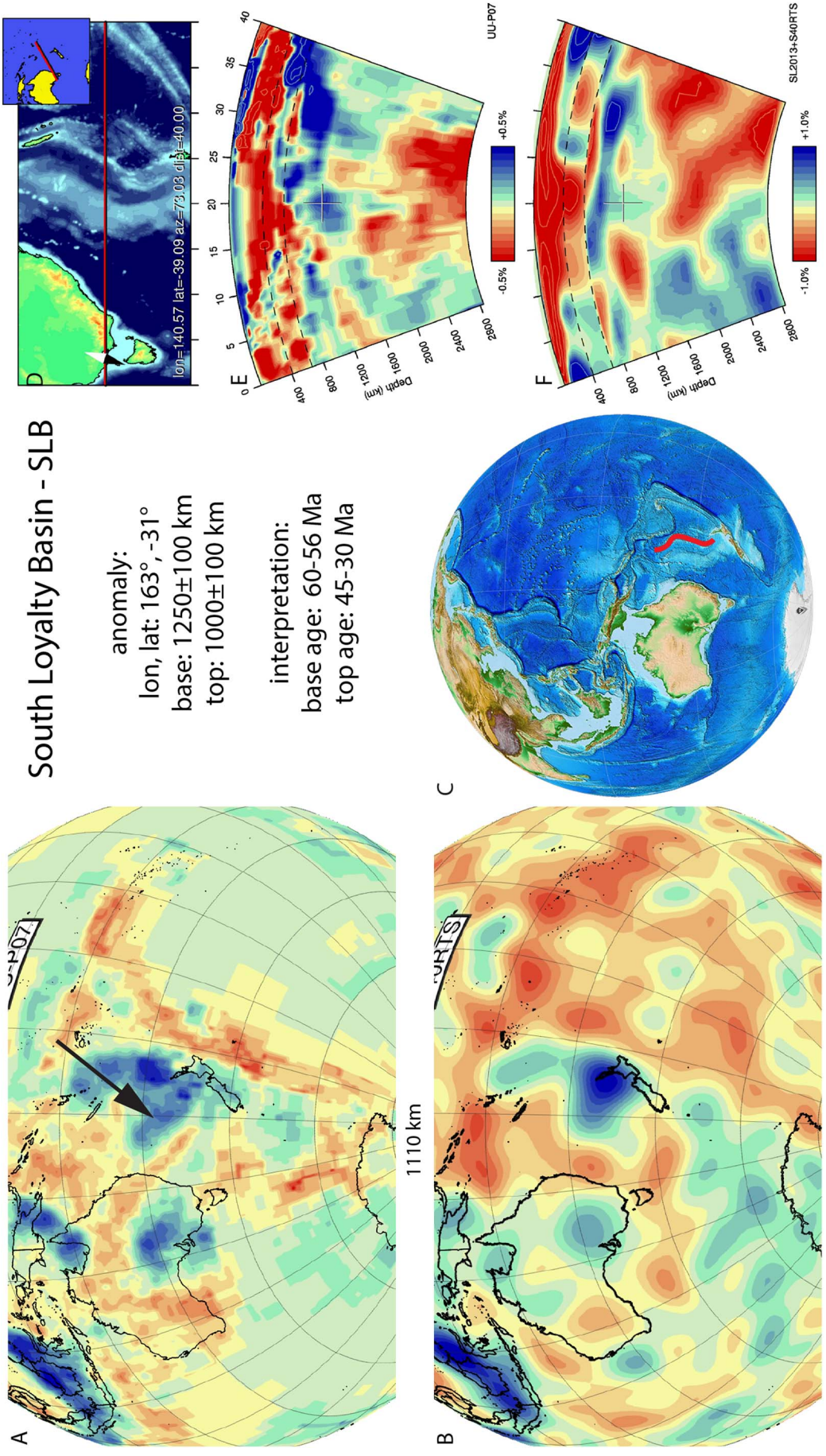

Fig. 87. South Loyalty Basin anomaly. Legend same as Fig. 5. Positive anomalies are identified in the same location in both the UU-P07 and S40RTS tomographic models. Lateral extent is similar, but vertical extent and relative amplitude differ. There is no clear dip of the slab.

subduction initiation age and a 45–30 Ma break-off age in conjunction with the recent kinematic restoration of van de Lagemaat et al. (2017).

3.84. South Orkney Island - SOI

The South Orkney Island anomaly (Fig. 88) is NW-SE trending and is located in the mid-mantle, from below southeastern Patagonia to below the Weddell Sea. Based on the shallower Scotia slab (Section 79), it most likely represents paleo-Pacific lithosphere that subducted at the proto-Andean or Gondwanide margin. Martin (2007) interpreted break-up of the Gondwanide margin by slab rollback and back-arc basin spreading to occur from the Early-Middle Jurassic (190–175 Myr) to the Middle Cretaceous. Subduction rollback was terminated by the Palmer Land tectonic event in West Antarctica from 113 to 103 Ma and by the inversion of the Rocas Verdes/Magallanes Basin in Patagonia around 94 Ma (Vaughan et al., 2002; Fildani and Hessler, 2005), which we interpret to represent the end of the subduction of the slab.

3.85. Sunda - Su

The Sunda anomaly (Fig. 89) was previously imaged by Fukao et al. (1992), Puspito and Shimazaki (1995), Puspito et al. (1993), Widiyantoro and van der Hilst (1996, 1997), Bijwaard et al., 1998; Replumaz et al. (2004), Spakman and Hall (2010), Pesicek et al. (2010), Widiyantoro et al. (2011), Koulakov (2013), Fukao and Obayashi (2013), Zahirovic et al. (2014), Hall and Spakman (2015), and Wu et al. (2016). It is interpreted as Australian and Indian plate lithosphere that is actively subducting northward below Sundaland, along the Sumatra and Java trenches. To the northwest it is disconnected through a slab window below the Andaman Islands from the Burma slab (Section 3.19). In the East it connects to the Banda slab (Section 3.13). In the west, tomographic images show that the Sunda slab reaches the base of the upper mantle, but does not connect with deeper anomalies. In the east, however, the Sunda slab merges with the SW-NE trending Kalimantan anomaly (Section 3.48) and several authors (e.g. Replumaz et al., 2004; Zahirovic et al., 2014) suggested that these slabs may be contiguous. The different orientation of the Kalimantan slab from the Sunda slab, however, suggests that these slabs result from separate subduction events instead (Hall and Spakman, 2015; Wu et al., 2016). For the Kalimantan anomaly (Section 3.47) the kinematic restoration of Hall (2012) combined with the interpretation of mantle structure by Hall and Spakman (2015) suggests a NW-ward subduction event below western Sulawesi from the latest Cretaceous to the middle Eocene. This same reconstruction suggested that the Sunda trench was in Late Cretaceous to Paleocene time a transform boundary, which became inverted as a subduction zone ~50–45 Ma ago upon the onset of Australia-Eurasia convergence, subducting Indo-Australian oceanic crust towards the NE. We adopt this as the age for the base of the Sunda slab. Disagreement between these reconstructions exists for the eastern extent of the Sunda slab. This subduction either continued as northward subduction of Indo-Australian oceanic lithosphere, offset by a dextral transfer zone (Hall and Spakman, 2015) or as southward subduction of the western part of an East Asian Sea (Wu et al., 2016).

3.86. Telkhinia slabs - Te

A north–south trending belt of positive wave-speed anomalies under the central Pacific Ocean has been interpreted to represent a series of Triassic-Jurassic intra-oceanic subduction zones, called the Telkhinia subduction zones by van der Meer et al. (2012) (Fig. 90). These anomalies are detected in both the UUP07 model and S40RTS model in the lower mantle at depths > 1500 km. Three distinct intra-oceanic subduction zones were correlated to these anomalies. At these positions in the lower mantle seismic scatterers have been detected, interpreted to be caused by remnants of subducted and folded former oceanic crust under the central Pacific Ocean by Kaneshima and Helffrich (2010) and Ma et al. (2016) and under the northern Pacific Ocean by Schumacher and Thomas (2016). The tomographic analyses of van der Meer et al. (2012) and waveform modelling of He and Wen (2009) showed that the top of the Pacific LLSVP was essentially split as a result of sinking slabs. In both P and S-wave tomographic models, the amplitudes of the anomalies are weaker than for other slabs identified at equivalent depths associated with circum-Pangaea subduction zones. This may be explained by the proximity of the slabs to the hotter LLSVP (van der Meer et al., 2012). Subsequent tomographic studies corroborated the presence of central-Pacific lower mantle anomalies (Simmons et al., 2012; French and Romanowicz, 2014; Suzuki et al., 2016) or improved the imaging of the genetically related intra-oceanic Mendocino slab (Section 59) to the east (Sigloch and Mihalynuk, 2013).

The Telkhinia slabs were correlated to exotic Triassic to Lower Cretaceous volcanic arcs now accreted in the far east Asian margin, currently incorporated in the Kolyma-Omolon and Andyr-Koryak arcs in Siberia, and the Oku-Niikappu arc in northern Japan (van der Meer et al., 2012). For this correlation, van der Meer et al. (2012) used the sinking rate of slabs of van der Meer et al. (2010) to interpret the Telkhinia slabs as the result of Early-Mid Mesozoic subduction, consistent with the age of these exotic arc relics. Paleomagnetic and paleontological constraints from these arcs provided an indication of their paleolatitude, and van der Meer et al. (2012) inferred their paleolongitude relative to the mantle by connecting them to the Telkhinia slabs. To avoid circular reasoning, we have not included the inferred ages of tops and bottoms of the Telkhinia slabs in our compilation used to constrain sinking rates of slabs in the mantle.

3.87. Tonga-Kermadec-Hikurangi - TKH

The Tonga–Kermadec–Hikurangi anomaly (Fig. 91) is located below the south Fiji Basin in the upper mantle and the upper part of the lower mantle up to a depth of ~1200 km. It was interpreted in the uppermost lower mantle as a single N–S trending slab by van der Hilst (1995), Bijwaard et al. (1998), Fukao et al. (2001), Hall and Spakman (2002, 2004), Gorbatov and Kennett (2003), Schellart et al. (2009), Schellart and Spakman (2012), and Fukao and Obayashi (2013). In the south, the Kermadec section of the slab penetrates almost straight through the 660 km discontinuity, but northward, a horizontal section of the slab, overlying the 660 km discontinuity becomes prominent. This is explained by increased eastward roll-back of the slab towards the north around an Euler pole relative to the mantle close to the southern tip of the slab in the Hikurangi segment (Schellart and Spakman, 2012).

The onset of subduction along the Tonga-Kermadec-Hikurangi subduction zone is debated. Hall (2002) suggested a 45 Ma onset based on the onset of Pacific-Australia convergence, whereas Schellart et al. (2006) suggested that westward subduction along the Tonga subduction zone had been ongoing since at least 85 Ma. Recently Wu et al. (2016) suggested 50 Ma as a start and on the basis of the LLNL-G3Dv3 tomographic model of Simmons et al. (2012) that the Tonga-Kermadec Hikurangi slab at ~1000 km depth may be connected with the central Mariana slab. Prior to 50 Ma Wu et al. postulate that a western Pacific plate boundary already existed but was this may have been characterised by highly oblique subduction or transforms. After 50 Ma, Pacific plate motions changed and fast subduction began below the Philippine Sea Plate (Wu et al., 2016). Geochemical analysis of dredge samples from the Tonga forearc found the first evidence of arc magmatism around 50 Ma (Meffre et al., 2012), although these may be interpreted to reflect the initiation of the New Caledonia subduction zone, correlated to the South Loyalty Basin slab (Schellart et al., 2009) (Section 3.83). In a recent plate kinematic analysis, van de Lagemaat et al. (2017) showed that when subduction of the South Loyalty Basin slab along the New Caledonia trench is taken into account, there is no or little convergence across the Tonga Trench until as young as 30 Ma, and argued that correlating the onset of Tonga-Kermadec subduction to subduction initiation at the Philippine Sea Plate at 52–51 Ma, or to the

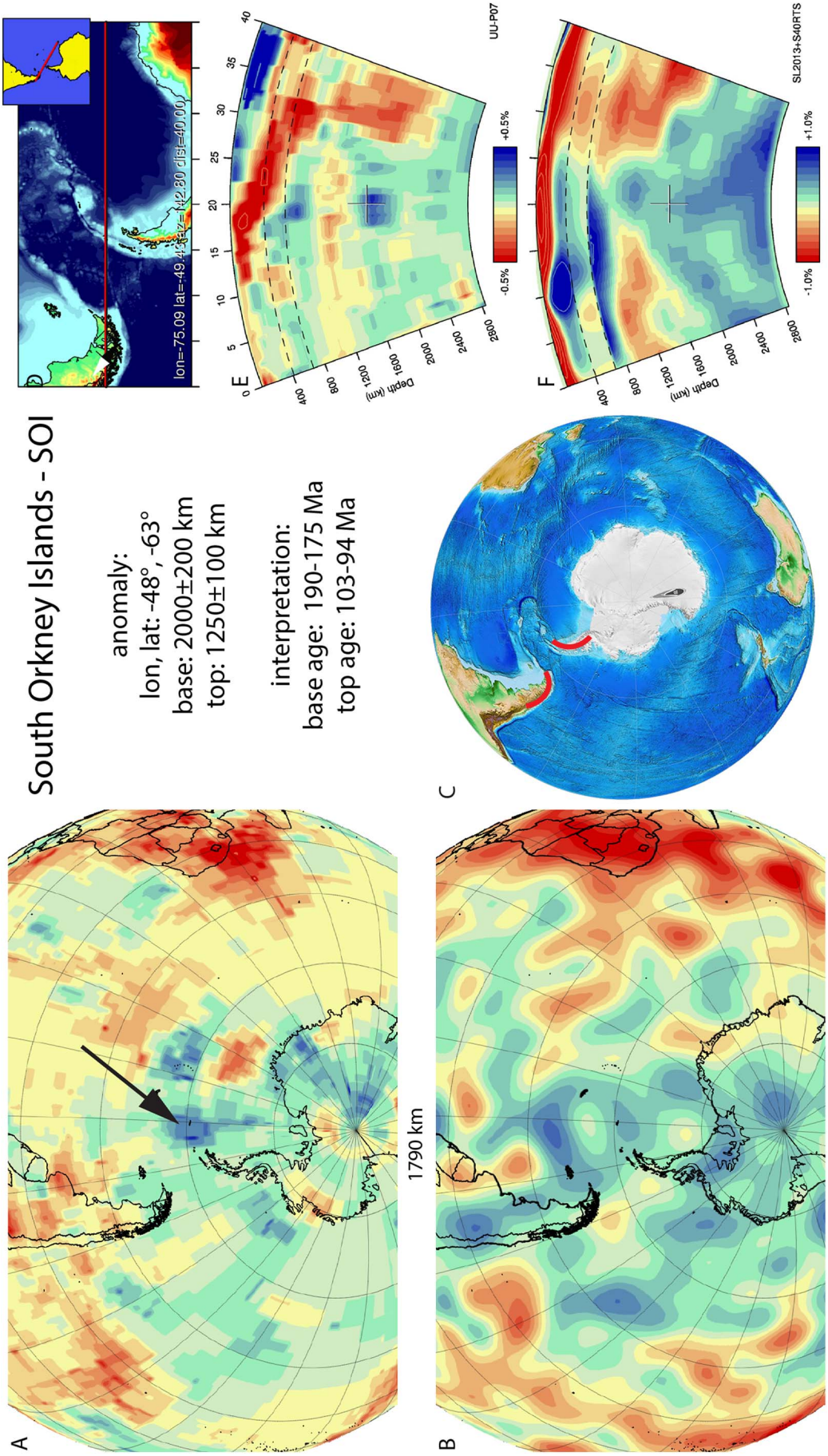

Fig. 88. South Orkney Island anomaly. Legend same as Fig. 5. Positive anomalies are identified in the same location in both the UU-P07 and S40RTS tomographic models. Lateral extent and relatrive amplitude is similar, but vertical extent differs. There is no clear dip of the slab.

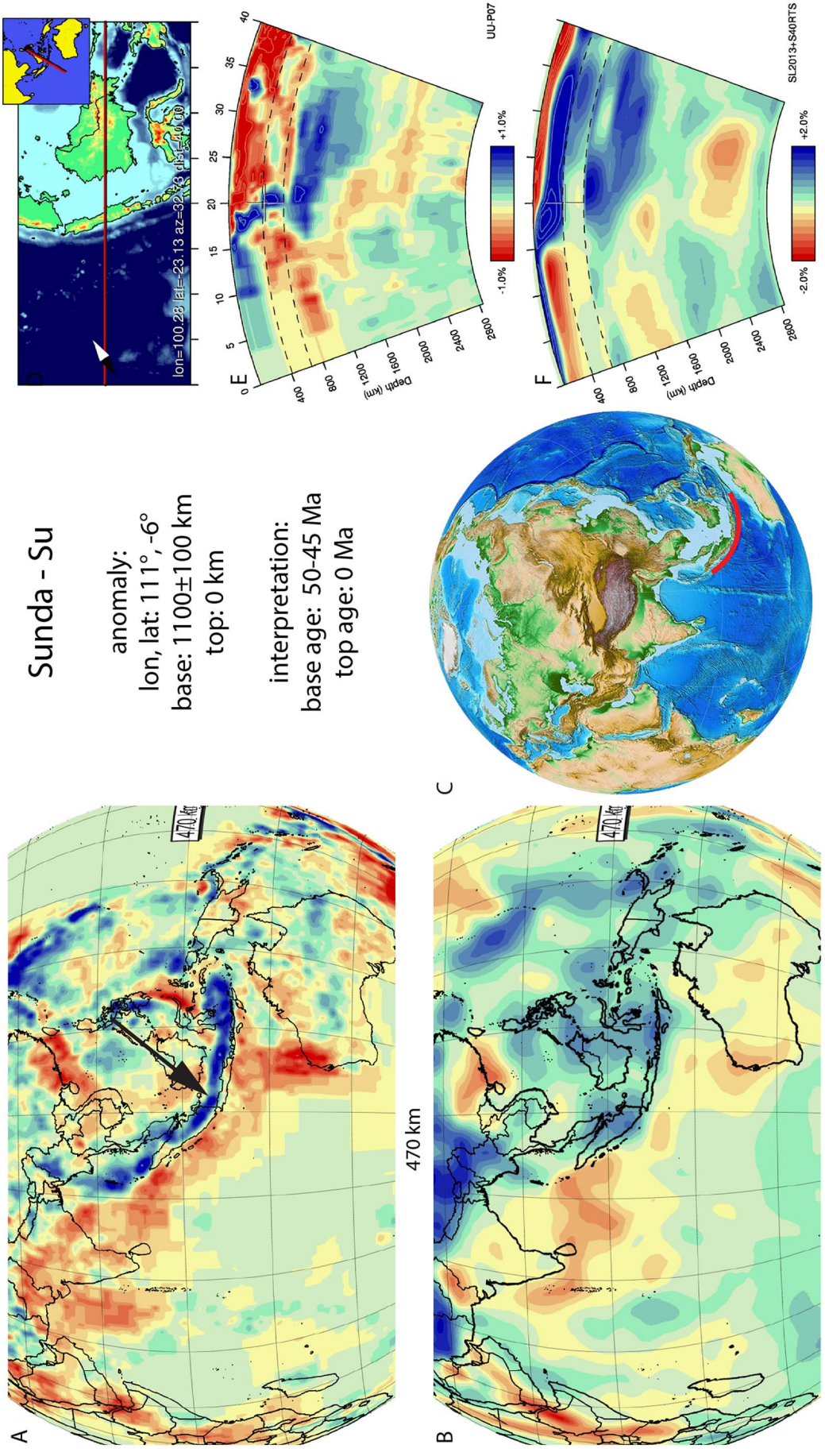

Fig. 89. Sunda anomaly. Legend same as Fig. 5. Positive anomalies are identified in the same location in both the UU-P07 and S40RTS tomographic models in the lower mantle, but differ considerably in the upper mantle between the UU-P07 and SL2013 model. In the lower mantle, lateral, vertical extent and relative amplitude are similar. The slab is dipping to the northeast, and is flat-lying at the top of the lower mantle.

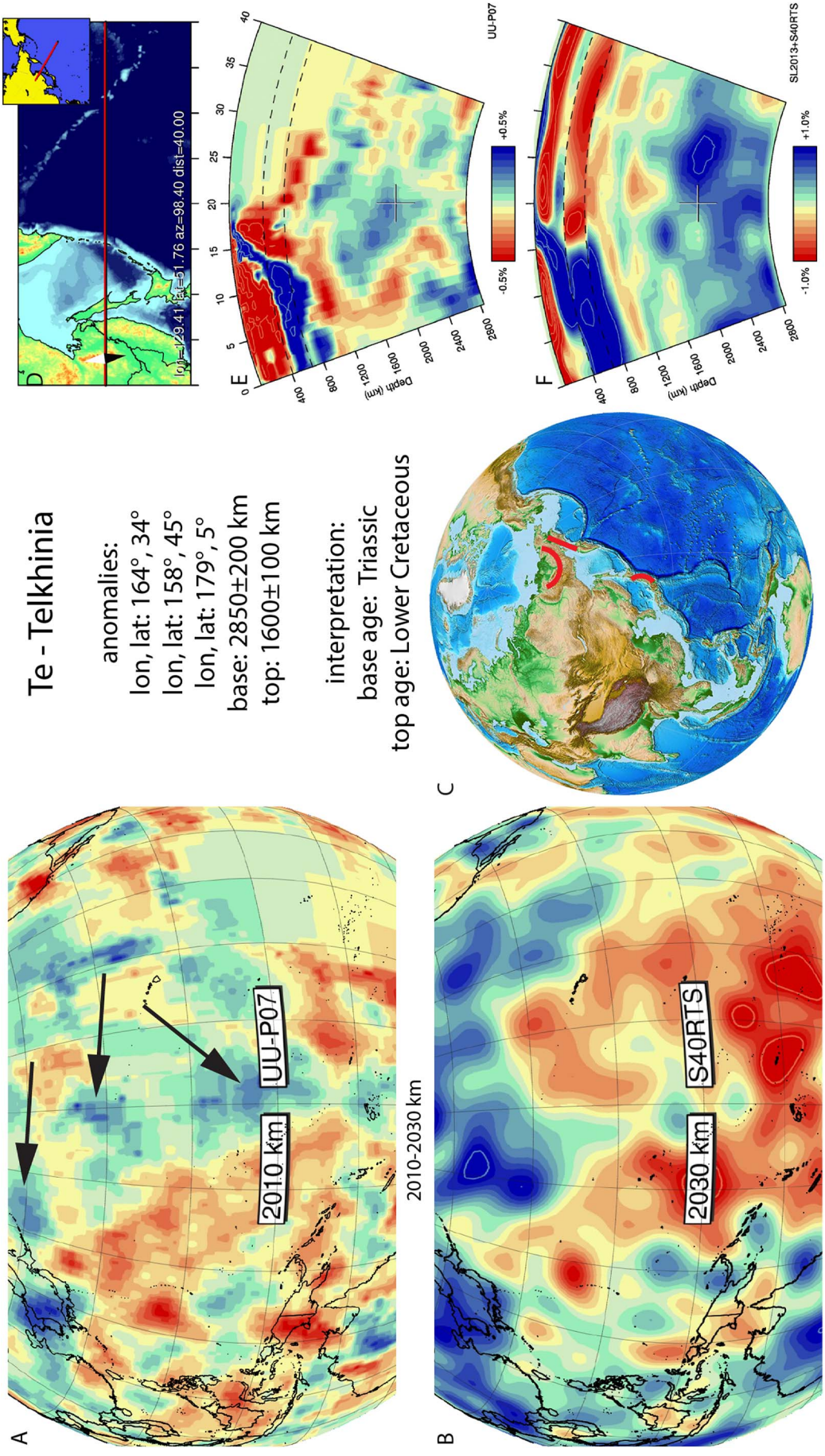

Fig. 90. Telkhinia anomalies, legend same as Fig. 5. Positive anomalies are identified in the same locations in both UUP-07 and S40RTS tomographic models. Lateral and vertical extent and relative amplitude differ.

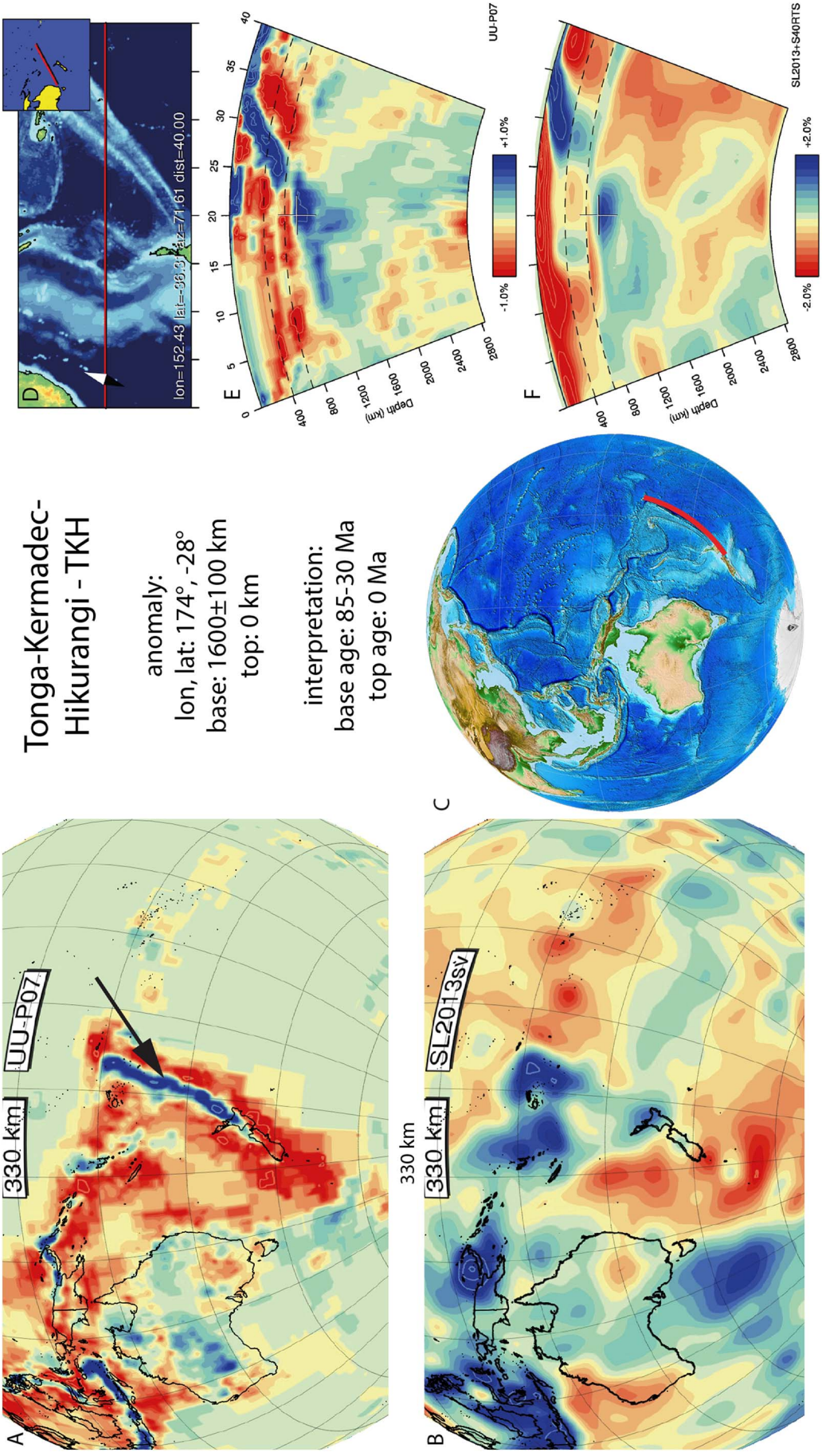

Fig. 91. Tonga-Kermadec-Hikurangi anomaly. Legend same as Fig. 5. The upper mantle part of this slab is well imaged in the UU-P07 model but is less continuous in SL2013 and S40RTS. Overall there is a similar relative amplitude strength and vertical extent between the UU-P07 and SL2013 models. Lateral extent differs between models. This slab dips to the SW.

onset of Pacific-Australia convergence at 45 Ma is kinematically unlikely. Given the ongoing debate on the age of subduction initiation, we adopt a wide age range of 85–30 Ma for the onset of the Tonga-Kermadec-Hikurangi subduction zone.

3.88. trans-Americas - TA

The Trans-Americas anomaly (Fig. 92) is located below the Cocos plate and Central America from the core-mantle boundary up to the deep mantle. It has been detected in previous seismological (Niu and Wen, 2001; Thomas et al., 2004; Hutko et al., 2006; Kito et al., 2007, 2008) and tomographic studies (van der Hilst et al., 2007; Ko et al., 2017). We infer by correlation to the base of the Cocos slab (Section 3.29) to the northeast and the base of the Idaho slab (Section 3.42) to the north that the Trans-Americas anomaly represents lithosphere that subducted during the Middle Mesozoic or before. van der Meer et al. (2010) previously interpreted the Trans-Americas slab to result from subduction of Farallon/Panthalassa lithosphere in the Permian to Triassic associated with the Sonoma orogeny at the western margin of Laurentia (Ziegler, 1989; Ward, 1995; Cawood and Buchan, 2007). Alternatively, and perhaps more likely, the slab may have an early Mesozoic intra-oceanic origin with its associated arc accreting to the western North American margin during the Middle Mesozoic. The Stikinia-Quesnellia arc may fit such a scenario. This arc initiated in the Middle-Late Triassic and accreted to Laurentia in the Early-Middle Jurassic (Nokleberg et al., 2000; Johnston and Borel, 2007). However, the location of the Stikinia-Quesnellia terrane, currently extending over 1200 km (Nokleberg et al., 2000), is poorly constrained and may in fact represent more intra-oceanic arcs of varying ages and paleo-locations. As pointed out by Shephard et al. (2013), other slabs (e.g., Wichita, Hudson, Sections 3.91, and 3.41, respectively), would have been correlated as well with this arc. Alternatively, Boschman and van Hinsbergen (2016) suggested that the Trans-Americas slab may have detached as a result of triple junction migration at the Izanagi-Farallon plate boundary, which culminated through instable triple junction formation in the 190 Ma birth of the Pacific plate. Further research on this topic may require us to revise the age of the slab, which we now tentatively place between 233 and 166 Ma covering the age of Stikinia-Quesnellia subduction (see Wichita slab, Section 3.91) as well as the birth of the Pacific plate.

3.89. Ushky - Ush

The Ushky anomaly (Fig. 93) is located below northeast Asia in the upper mantle and uppermost part of the lower mantle. It is E–W trending and at ~920 km depth it connects to the N–S trending Sakhalin slab (Section 3.75) in the west, and the NE-SW trending Kamchatka-Kuriles slab (Section 3.48) in the east. The anomaly's location is consistent with the inferred paleo-position of the continental margin Okhotsk-Chukotka arc. According to Nokleberg et al. (2000), the arc started activity in the Cenomanian-Santonian and ended in the Miocene. In recent model of Shephard et al. (2013), the arc was presumed to be active in the middle-Late Cretaceous (108–67.1 Ma), based on the studies of Layer et al. (2001), Stone et al. (2009), Akinin et al. (2009) and Vishnevskaya and Filatova (2012), which we adopt as the age range of the slab. This was followed by the accretion of the Okhotsk block to Siberia, followed by an eastward jump of subduction to the Kamchatka-Kuriles trench (Section 3.49).

3.90. Venezuela - Ve

The Venezuela anomaly (Fig. 94) is located below northern South America from the mid-mantle up to the upper part of the lower mantle. It was first identified in van der Meer et al. (2010). It was interpreted as the sGAC slab (Southern Great Arc of the Caribbean) by van Benthem et al. (2013), who inferred a Cretaceous to Eocene subduction period for this slab. Subduction of the Venezuela slab is likely associated with volcanic arc rocks in the southern Caribbean region (Boschman et al., 2014), which on e.g. Tobago date back to ~130 Ma (Neill et al., 2012). Pindell et al. (2012) suggested that subduction of the Venezuela slab started sometime before the geological records mentioned above formed, and estimated an onset of subduction of 135 Ma. Arrest of the southern Caribbean arcs in the latest Cretaceous (Neill et al., 2011), and subsequent overriding of South America over the Venezuela slab in kinematic reconstructions (Pindell and Kennan, 2009; Boschman et al., 2014) suggests that break-off of the Venezuela slab occurred around 65 ± 5 Ma, after which the northern part of the slab (Hispaniola slab, see Section 3.40) retreated farther northward (see also van Benthem et al., 2013).

3.91. Wichita - Wc

The Wichita anomaly (Fig. 95) is located below central North America from the core-mantle boundary up to deep mantle. It was first described in van der Meer et al. (2010), where we interpreted the anomaly as the Wichita slab that is the result of intra-oceanic subduction consuming Panthalassa lithosphere, creating the Mesozoic part of the intra-oceanic Paleozoic-Mesozoic Stikinia-Quesnellia arc. This arc consists of an extensive suite of mainly Late Triassic and Early Jurassic volcanic and granitic plutonic rocks, each extending for a distance of about 1200 km (Nokleberg et al., 2000). Based on the long extent, another part of this arc is perhaps associated with the Trans-Americas slab, Section 3.88). van der Meer et al. (2012) highlighted this slab as effectively forming the separation between the Slide Mountain and Thalassa Oceans. The interpretation of this deep slab and the Trans Americas slab was to some extent corroborated by the plate model of Shephard et al. (2013), who also identified material lying along the core-mantle boundary at these locations using six tomographic models. They tentatively suggested that the Wichita slab could represent Cache Creek Ocean and/or Farallon lithosphere that subducted along the Talkeetna– Bonanza and Gravina arcs, or alternatively an older remnant of Slide Mountain Ocean lithosphere subducted below earlier Stikinia-Quesnellia arcs. Johnston and Borel (2007) interpreted a two-stage process, a first involving intra-oceanic subduction and arc formation and accretion forming Stikinia-Quesnellia between 230 Ma to 150 Ma within the (eastern) Panthalassa. In a second stage, from 150 Ma to 55 Ma, this arc migrated towards North America, collided, and moved northward parallel to the continental margin. We correlate stage one with the Wichita slab and stage two with subduction leading to the Hudson slab (Section 3.41). Barresi et al. (2015) analysed the lower Hazelton Group in central Stikinia, which comprises three volcanic-intrusive complexes that nconstitute almost 16 km of volcanic stratigraphy. U–Pb zircon ages indicate that volcanism initiated by ca. 204 Ma (latest Triassic). Detrital zircon populations from the basal conglomerate contain abundant 205–233 Ma zircons, derived from regional unroofing of older Triassic intrusions. They also linked the spatial co-occurrence of Hazelton Group volcanic rocks with a belt of economic Cu–Au porphyry deposits (ca. 205–195 Ma) throughout northwestern Stikinia. Strata in the upper Hazelton Group) with a U–Pb zircon age of 178.90 ± 0.28 Ma represent waning island-arc volcanism. Milidragovic et al. (2016) incorporated the above results and included the absolute dating of the Hickman (222–220 Ma) and Three Sisters plutons (172 ± 6 Ma) and as the first and final evidence of volcanism in the Mesozoic Stikinia terrane. Based on these studies above, we adopt a 233–220 Ma start of subduction and 178–166 Ma as the end defining the ages of the base and top of the Wichita slab respectively.

3.92. Welford - We

The Welford anomaly (Fig. 96) corresponds to the southwestern part of the A7 anomaly of Hall and Spakman (2002, 2004) and underlies NE

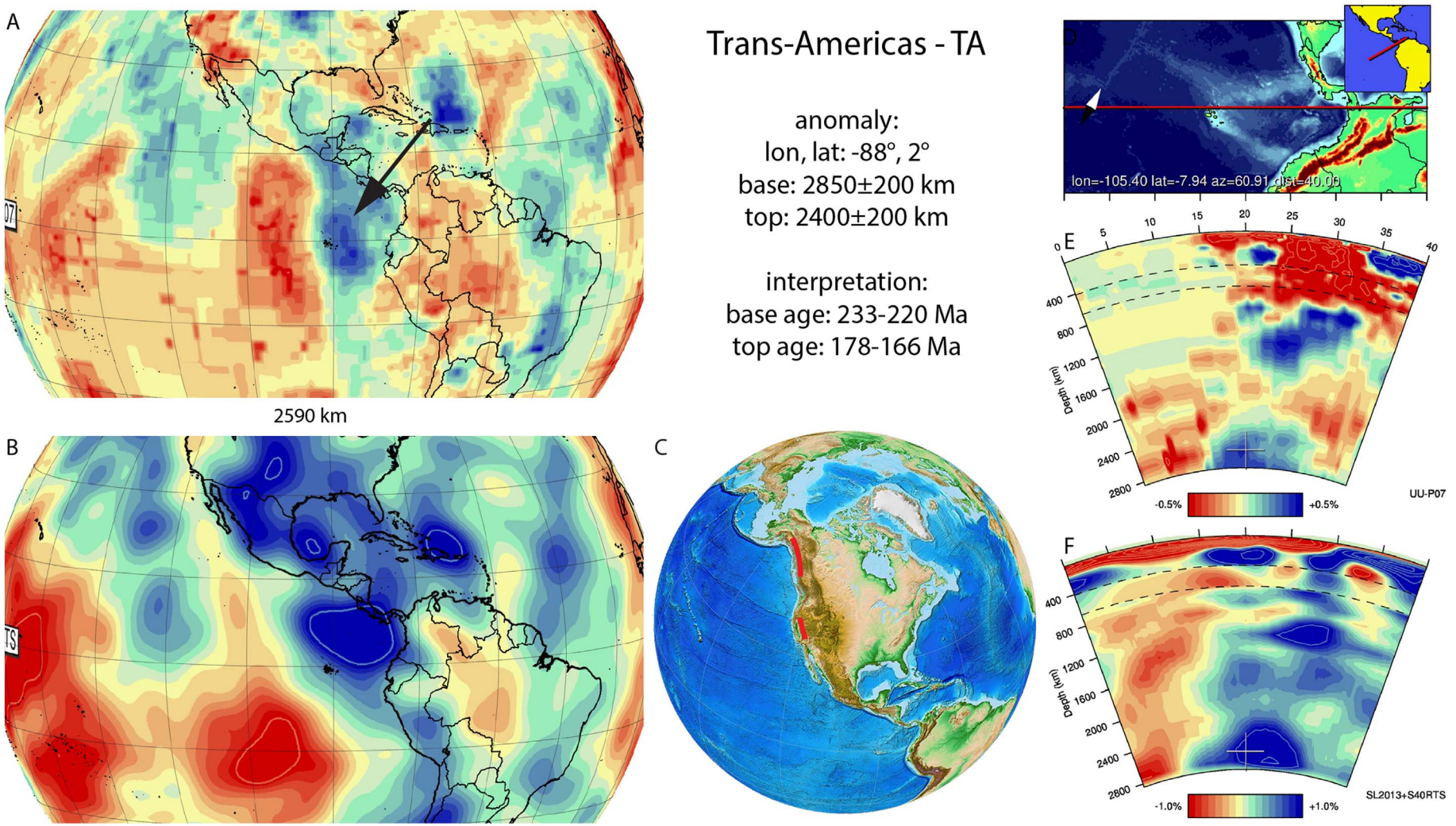

Fig. 92. Trans-Americas anomaly. Legend same as Fig. 5. A broad positive anomaly ise identified in the same location in both UUP-07 and S40RTS tomographic models with similar lateral, vertical extent and relative amplitude. The slab is piling up above the CMB.

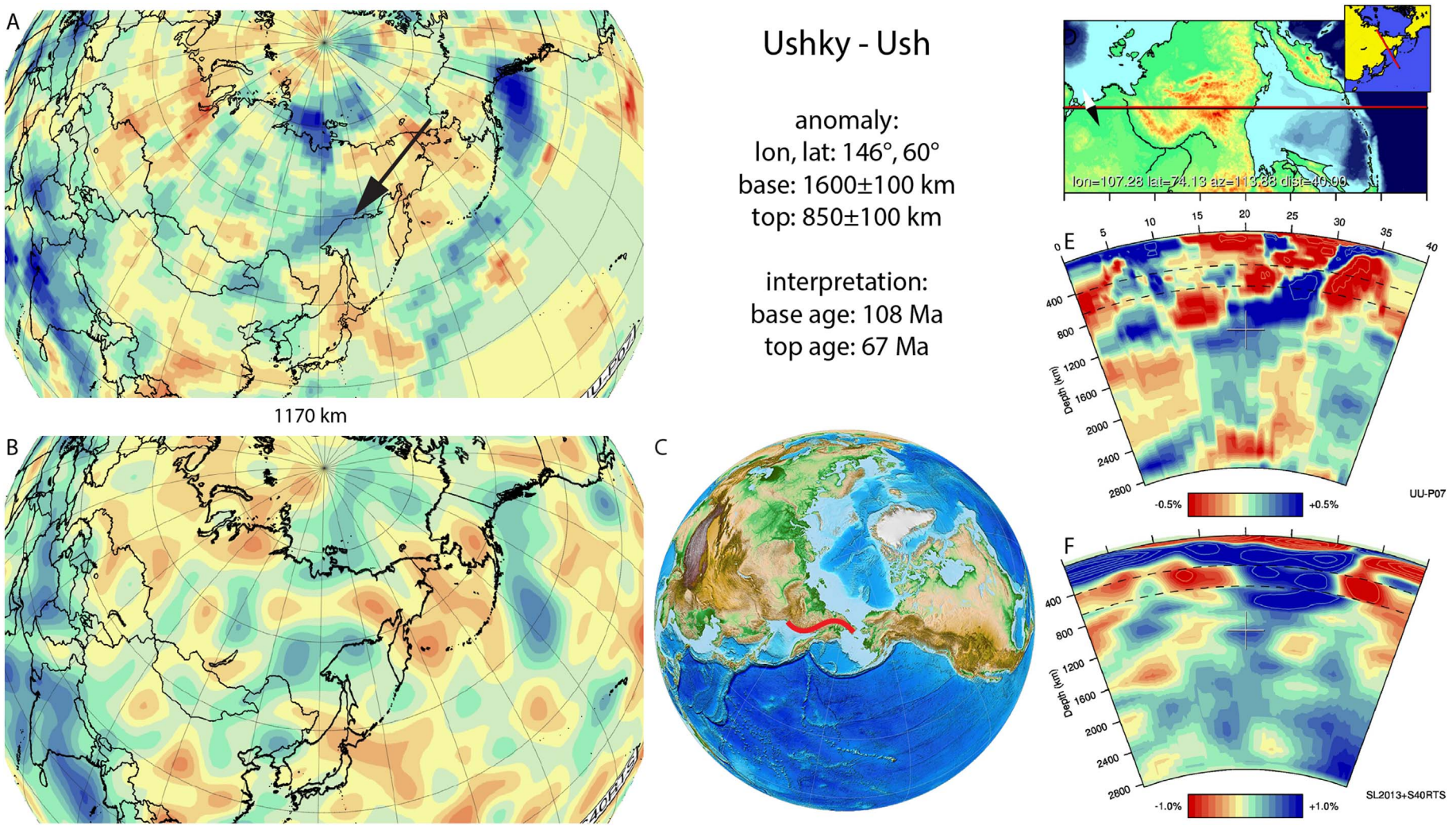

Fig. 93. Ushkhy anomaly. Legend same as Fig. 5. Positive anomalies are identified in the same locations in both UUP-07 and S40RTS tomographic models. Lateral, vertical extent and relative amplitude are similar.

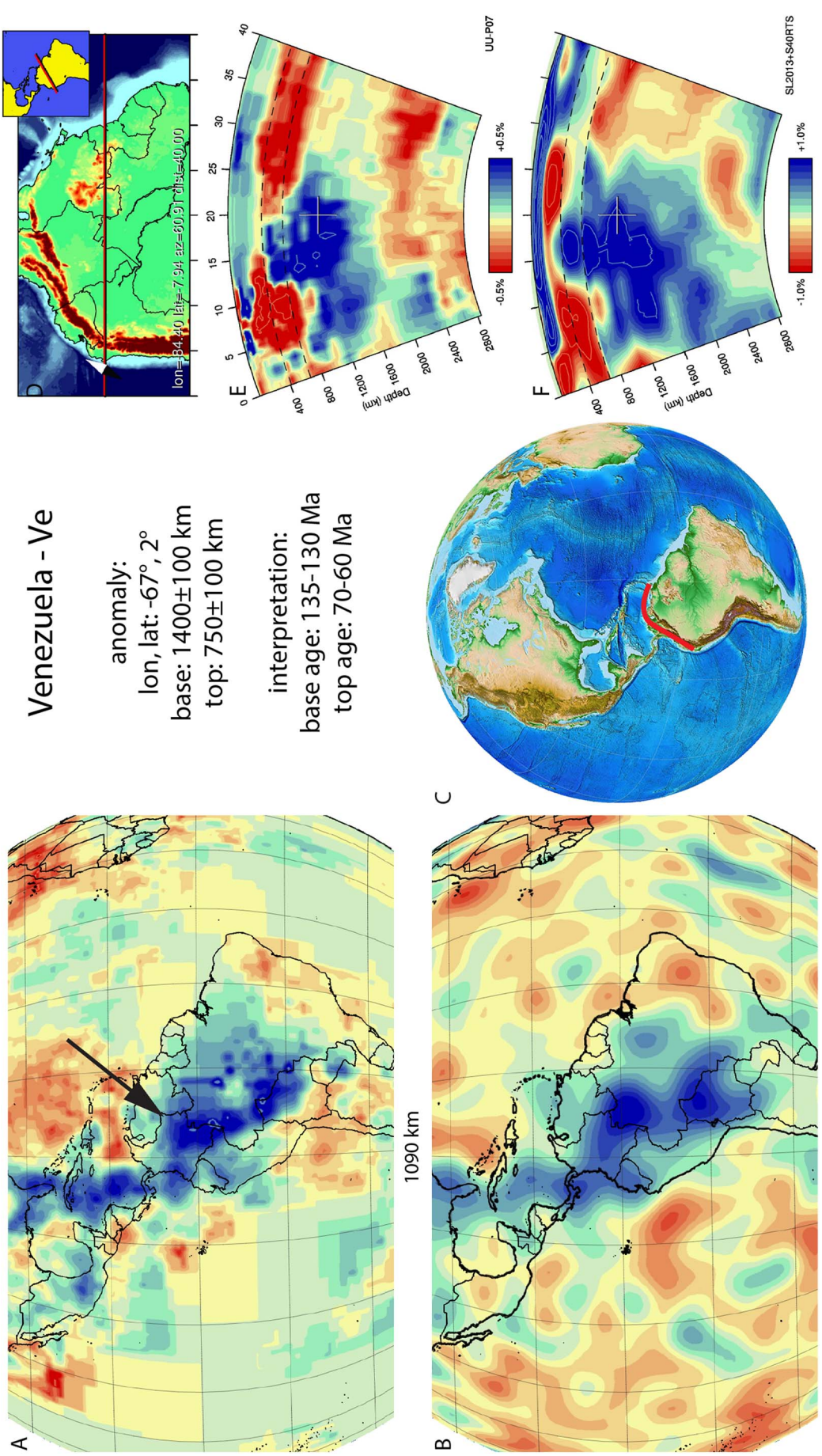

Fig. 94. Venezuela anomaly. Legend same as Fig. 5. A broad positive anomaly is identified in the same locations in both UUP-07 and S40RTS tomographic models. Lateral, extent and relative amplitude are similar. Vertical extent differs between models.

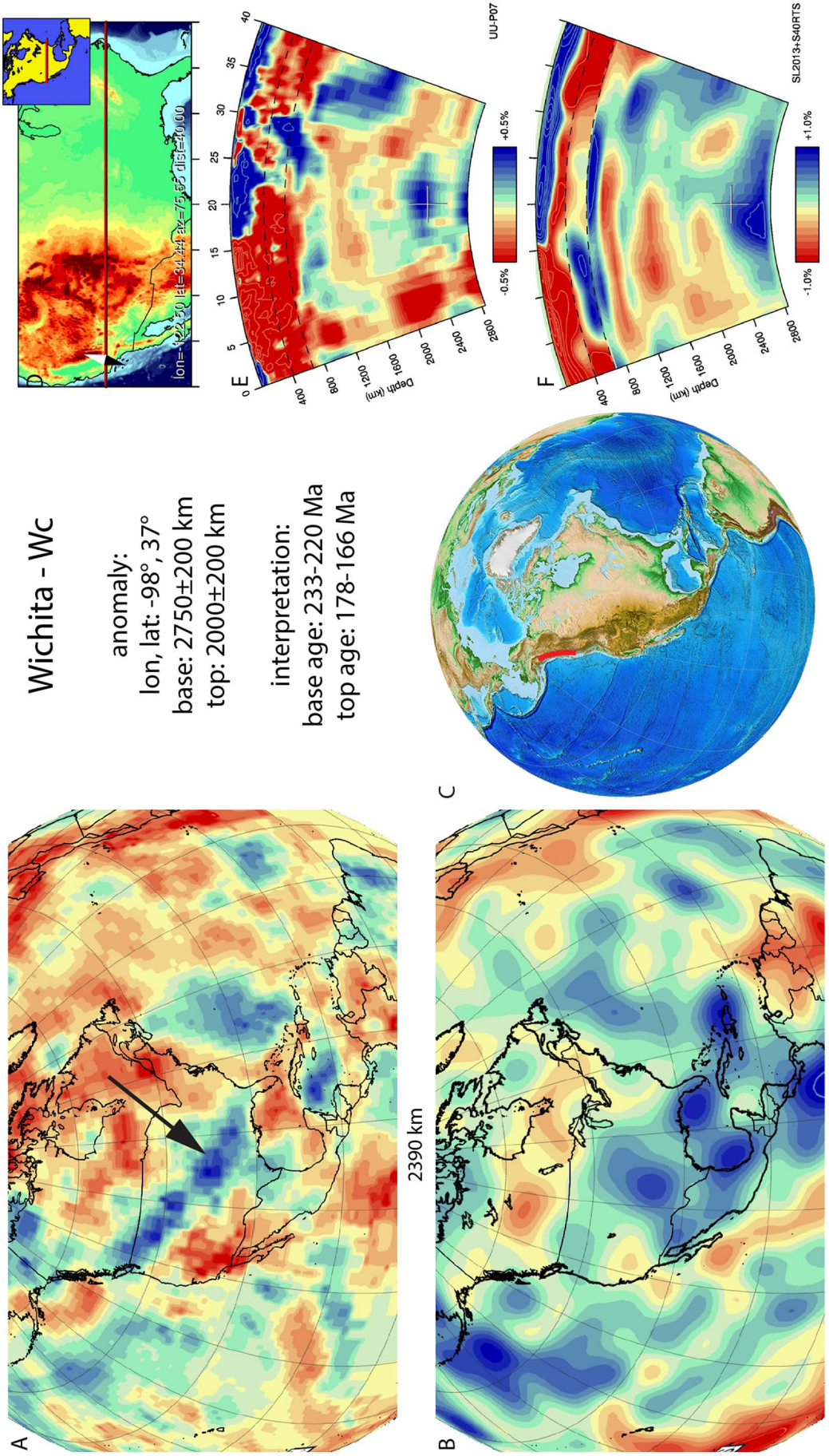

Fig. 95. Wichita anomaly. Legend same as Fig. 5. Positive anomalies are identified in the same locations in both UUP-07 and S40RTS tomographic models. Relative amplitude is similar. Lateral and vertical extent differ between models.

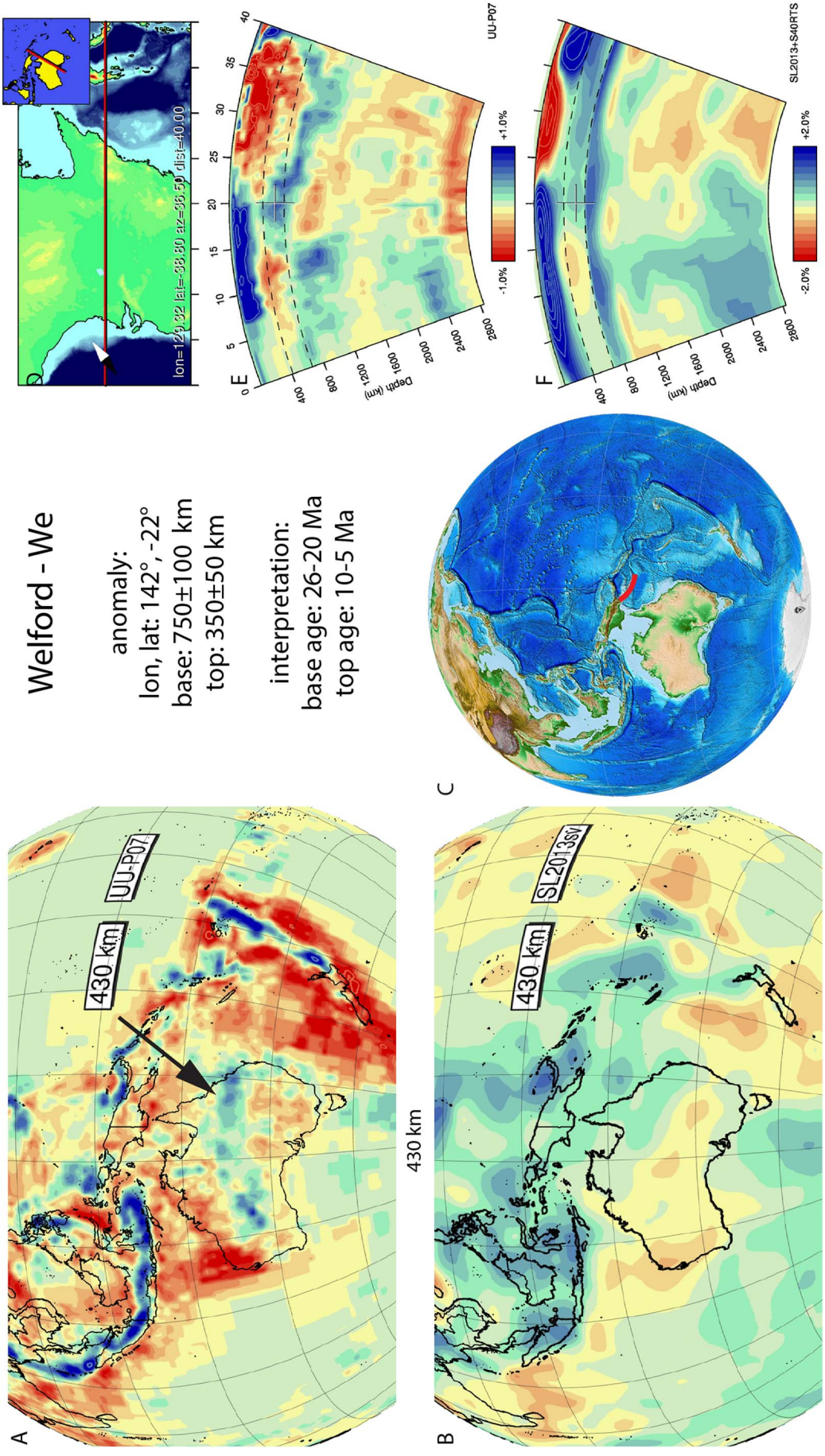

Fig. 96. Welford anomaly. Legend same as Fig. 5. The upper mantle part of this slab slab is well imaged in the UU-P07 model but is less continuous in SL2013 and S40RTS. Overall there is a similar relative amplitude strength, but lateral and vertical extent differ between tomographic models. This slab dips to the NE.

Australia, flat-lying at the top of the lower and base of the upper mantle. Hall and Spakman (2002, 2004) note that their A7 anomaly is not everywhere well-defined and may in fact represent more than one slab, whereby the northern part of the slab below NW Australia (the Papua anomaly, Section 70) may be disconnected from the southwestern parts of the anomaly, which is the interpretation we follow here.

Kinematic reconstructions of the region NE of Australia consistently interpret a southwestward Trobriand subduction zone to form as far-field response to collision of the Ontong Java plateau with the Melanesian arc at 26–20 Ma (Hall, 2002; Quarles van Ufford and Cloos, 2005; Knesel et al., 2008). This trench would have been active until ~10 Ma, after which northward subduction of the New Britain slab (Section 3.65) created the Bismarck arc since 10–5 Ma (Hall, 2002; Holm et al., 2013), accommodating northward absolute plate motion of Australia.

3.93. Yukon - Yuk

The Yukon anomaly (Fig. 97) is located below northwestern North America and is within the upper part of the lower mantle. Previously, van der Meer et al. (2010) interpreted it to be part of the North Pacific slab (Section 3.68). By closely examining the tectonic evolution and upper mantle structure of the region we now prefer an interpretation that these are separate slabs. The Yukon slab is E–W trending, and at ~900–1100 km it connects to the SW-NE trending North Pacific slab.

The location of the slab is in agreement with the location of the Upper Cretaceous-Lower Tertiary continental margin Kluane arc in the reconstructions of Nokleberg et al. (2000) and Shapiro and Solov'ev (2009). We prefer this connection over the previous interpretation of van der Meer et al. (2010), which was based on an older reconstruction of the paleo-Pacific Ocean of Engebretson et al. (1985).

(Trop and Ridgway, 2007) infers that the Kluane arc is of Campanian-Maastrichtian (83–66 Ma) age. In the Late Maastrichtian- Early Paleocene (68–61 Ma) the continental margin was uplifted and a regional unconformity developed (Trop and Ridgway, 2007). We consider this the best estimate for the moment of slab detachment and use this to infer the age of the top of the slab.

3.94. Zagros - Za

A northward dipping anomaly is located below the Zagros mountains of Iran in the upper mantle and in the upper part of the lower mantle (Hafkenscheid et al., 2006; Zor, 2008; Chang et al., 2010; Agard et al., 2011; Koulakov, 2011) (Fig. 98). The anomaly is interpreted as the Zagros slab, disconnected from the deeper Mesopotamia slab (Section 3.60) by a gap that likely corresponds to a phase of slab break-off. Along most of the Zagros mountain range, the Zagros slab is no longer connected to the surface, and displays a clear gap suggesting a recent phase of slab break-off. Agard et al. (2011) suggested, based on the age of rapid exhumation of HP-LT metamorphic rocks found in the Zagros suture zone that there may have been a phase of slab break-off in the latest Cretaceous to Paleogene, ~65 ± 5 Ma. We inferred that this corresponds to the age of the top of the Mesopotamia slab (Section 3.60), and we also use this age as the maximum age of subduction of the base of the Zagros slab. The most recent phase of slab break-off occurred in the last ~10 Myr (Agard et al., 2011), which we adopt for the age of the top of the slab.

4. Sinking of slabs in the lower mantle and implications for the lower mantle viscosity profile

As a first application and illustration of the potential use of our Atlas of the Underworld we explore the sinking and deformation history of slab remnants in the mantle and the consequences thereof for depth variation of mantle viscosity involved in sinking of slab in the lower mantle.

4.1. Variable sinking of slabs in the lower mantle

The more than three-fold increase of age-depth relations for tops and bases of slabs in comparison to those of the 28 slabs of van der Meer et al. (2010) enables us to search for age-depth trends in average sinking velocity. Fig. 99a shows the results of our age-depth compilation and Fig. 99b displays the average sinking velocities that are derived from the age-depth relations. All pertaining numbers and uncertainties are listed in Table 1. In Figs. 100 and 101 these results are split into depth intervals for the slab tops. A straight line connects the top and base symbols for each slab in these Figures. The first observation from Fig. 99a is that sinking of slab remnants occurred across the entire mantle during the past ~300 Myr and that there is no long-term (> 60 Myr) stagnation (e.g., Fukao et al., 2001, 2009; Fukao and Obayashi, 2013) visible in this downward flow, neither in the upper mantle transition zone, nor in the top of the lower mantle, suggesting a single layer convective system for the mantle. Long-term (> 60 Myr) stagnation would lead to a flattening of the sinking pattern of Fig. 99a in a particular depth range. We infer that all subduction zones that were confined to Mesozoic times are associated with slab remnants that now reside in the lower mantle. The deepest slab we identify required between ~200 Myr (Rockall and Trans-Americas slabs) and ~300 Myr (Atlantis, Balkan, Georgia Islands slabs) to reach the core-mantle boundary (CMB) (Fig. 99a). The average whole-mantle sinking rate (mantle thickness/transit time) we determine from our global compilation is 12.0 ± 2.5 mm/yr (Fig. 99a, b), similar to, or within range of previous estimates (van der Meer et al., 2010; Butterworth et al., 2014; Domeier et al., 2016). However, we also identify depth trends in average sinking rate.

The fastest slabs reach the base of the upper mantle at ~660 km within ~10 Myr while some slabs reside in the upper mantle until ~75 Myr since start of subduction (Fig. 99a). This spread of about ~65 Myr in subduction age can be attributed to a variety of subduction behavior comprising slow and fast subduction or slab retreat leading to slab flattening in the upper mantle transition zone where the flat slab meets resistance to entering the lower mantle (e.g. Goes et al., 2008). This spread in subduction age increases to 80–110 Myr across the top 800–900 km of the lower mantle, associated with what has been interpreted as a slab stagnation zone (Fukao et al., 2001, 2009; Fukao and Obayashi, 2013). From the depth of 1500–1700 km until the CMB, this spread in subduction age stays rather constant. Inspection of Fig. 100 shows that slabs with tops in the lower mantle sink with comparable rates suggested by the more or less parallel lines connecting top and base of each slab (Fig. 100c-f). We therefore suggest that the lower mantle spread in subduction ages at each depth is largely inherited from that acquired in the upper mantle. The much-reduced variation in average sinking velocities in the lower mantle, particularly below ~1500 km retains this sinking pattern. The implication is that the position of a sinking slab in Fig. 99a translates for each slab into a first-order indication regarding the upper mantle speed of paleo-subduction to be slow, fast, or intermediate, which puts qualitative constraints on for instance plate tectonic reconstructions, or the geodynamic context of mountain building, or informs independently on the possibility of e.g. large trench retreat leading to a flat slab at the base of the upper mantle that strongly decreases the net average sinking rate.

Generally, we observe a deceleration of the average sinking rate with increasing depth. The bases of the majority of actively subducting slabs (Fig. 101a) show a much smaller average sinking rate than the present-day convergence velocity at the trench. The latter is plotted at the surface as an instantaneous estimate of average sinking rate. A few slabs with currently small subduction speed at the trench show the opposite trend but the average sinking of their bases is not anomalously high. By far most detached slabs (Fig. 101b–f) show deceleration with depth implying that the slab top is sinking faster than the slab base and thus that the slab must be thickening, either by bulk deformation or by buckling. One particular exception is the detached Himalayas slab (Hi;

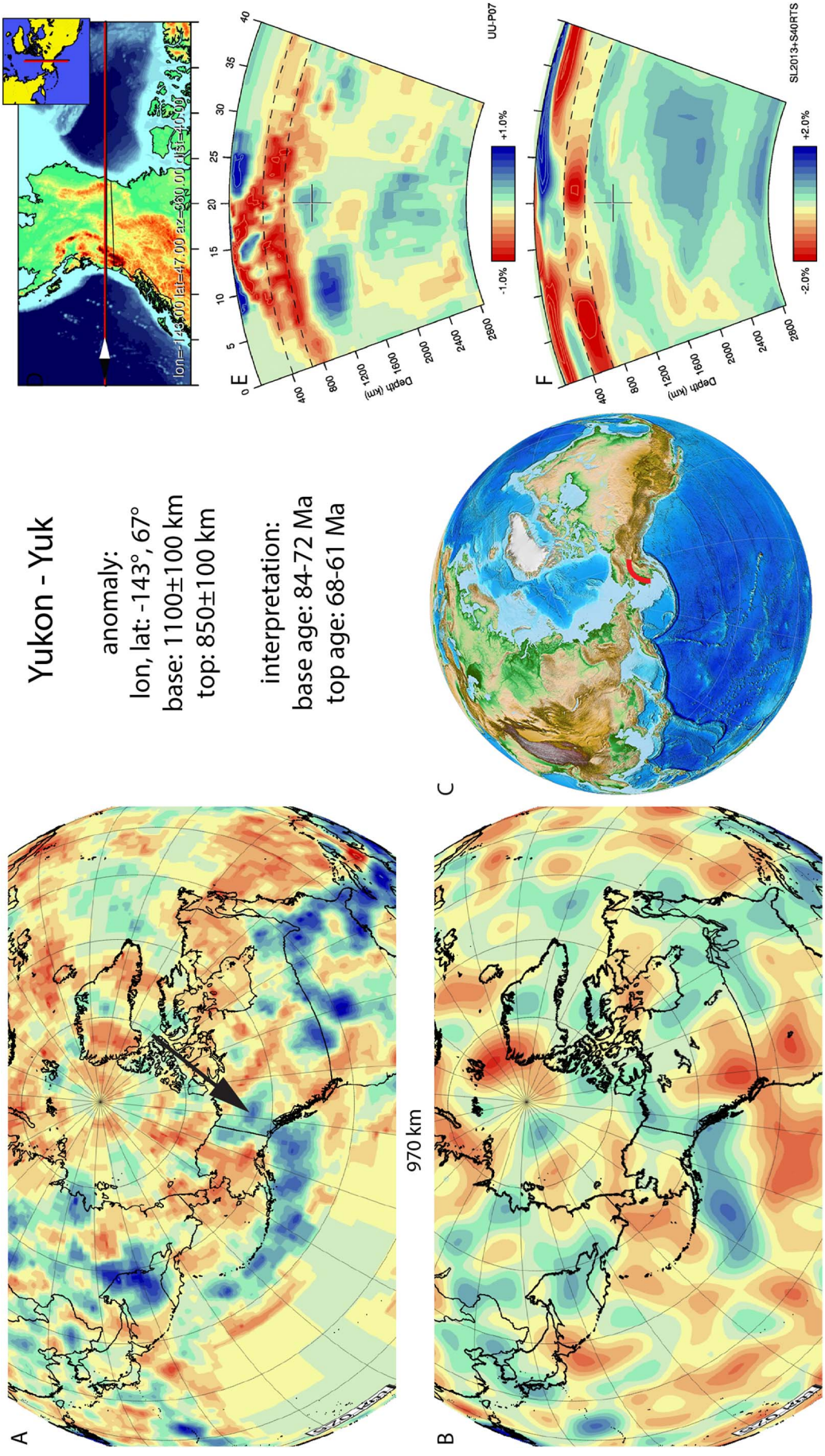

Fig. 97. Yukon anomaly. Legend same as Fig. 5. Positive anomalies are identified in the same locations in both UUP-07 and S40RTS tomographic models. Relative amplitude and vertical extent is similar. Lateral extent differs between models.

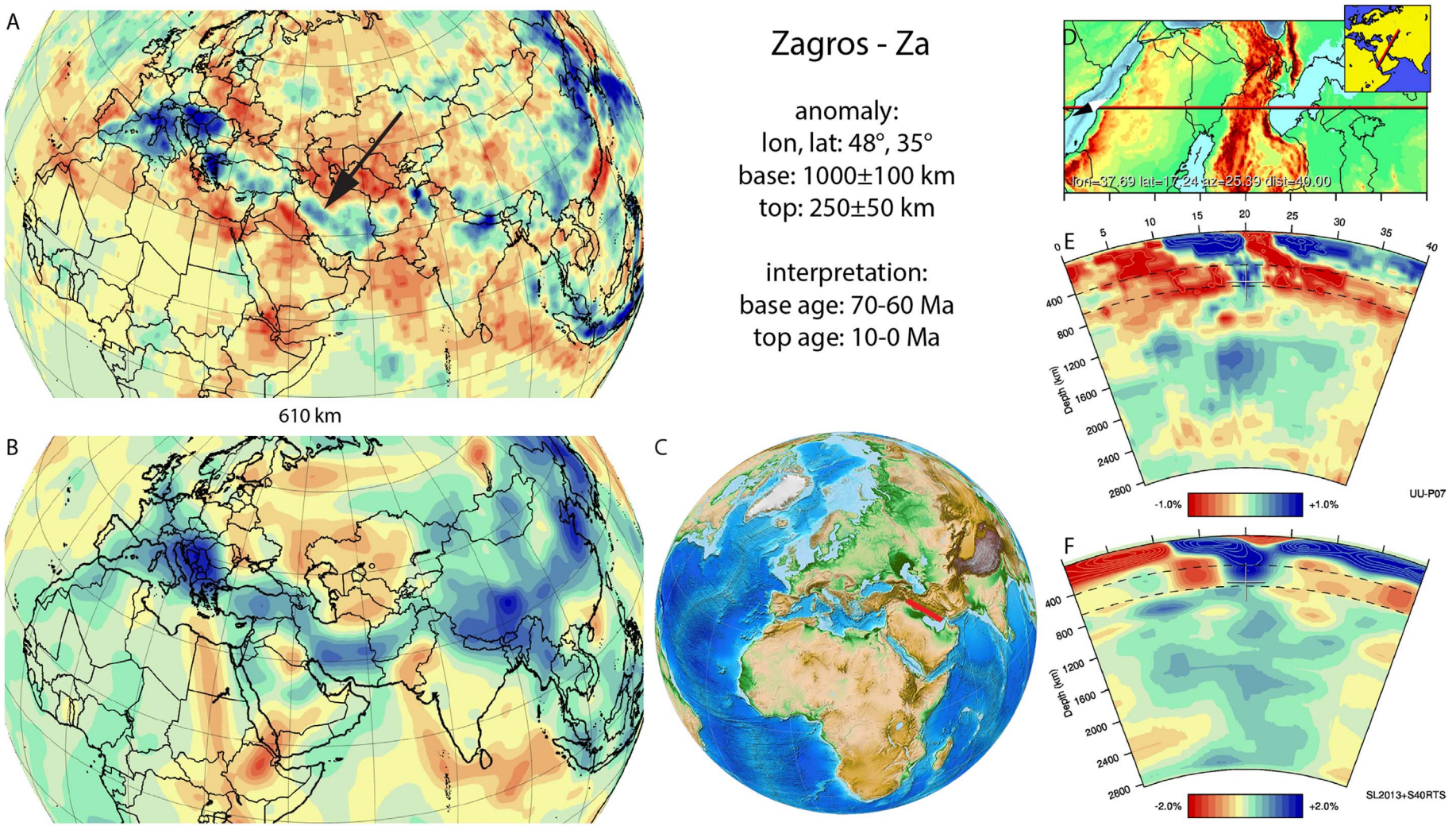

Fig. 98. Zagros anomaly. Legend same as Fig. 5. The upper mantle part of this slab slab is well imaged in the UU-P07 model but is broader in SL2013 and S40RTS. Overall there is a similar relative amplitude strength and vertical extent. Lateral extent differs between tomographic models. This slab dips to the NE in the upper mantle and appears flat-lying at the top of the lower mantle.

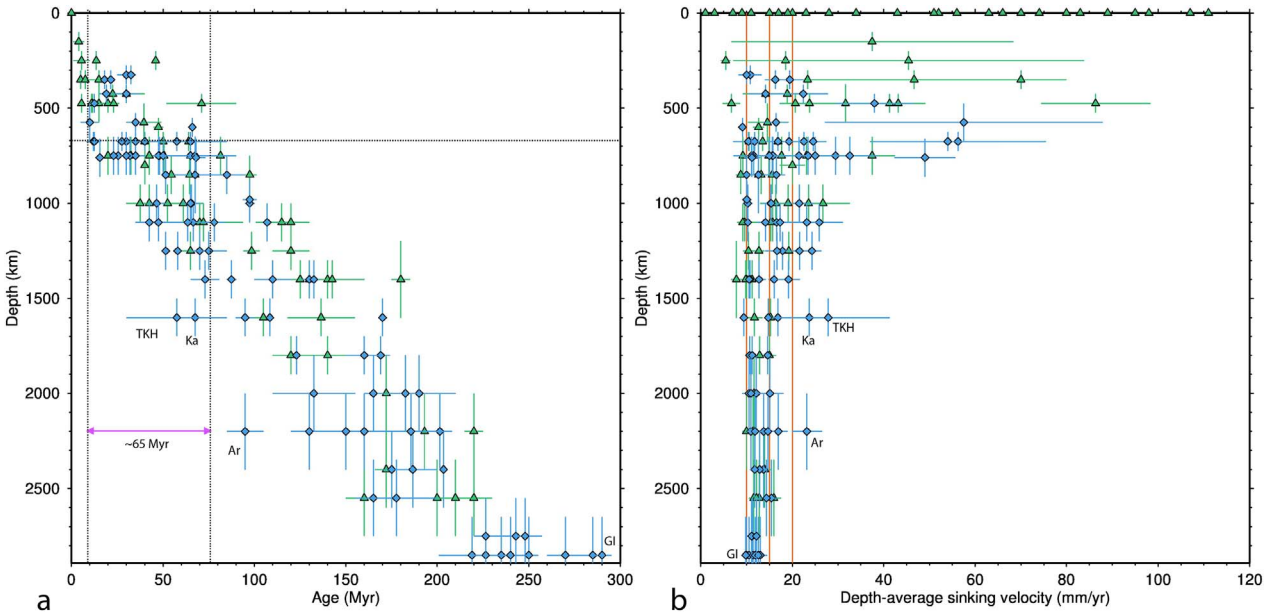

Fig. 99. Age-depth relations and corresponding average sinking rates of tops and bases of slabs: **a**) Age-depth relations for the top (green triangles) and base (blue diamonds) of tomographically imaged slabs determined in the *Atlas of the Underworld*. Depth is determined from the tomographic model UU-P07 and the age information corresponds for the top of a slab anomaly to the end of subduction/slab detachment and for the anomaly base to the start of subduction with depth and age uncertainties derived from the tomographic models and from the pertinent geological literature, respectively. Anomalous slabs: Ar = Arabia; Ka = Kalimantan; TKh = Tonga–Kermadec–Hikurangi; GI = Georgia Islands **b**) The average sinking rate of the top and base of slabs determined from the age-depth data of a) as $V_{av}(depth) = depth/age$. Velocity uncertainties are determined from the combined age and depth uncertainties in a). The depth uncertainty is the same as in a).”Slab-top”-symbols at the surface represent present-day subduction velocities as an instantaneous estimate of average sinking velocity. The three orange vertical lines at 10, 15 and 20 mm/yr are plotted for identifying subtle depth-trends.

Section 3.38, Fig. 101b), which may accelerate because of the proposed strong slab suction due to sinking of the lower-mantle Tethys slab remnants underneath (Faccenna et al., 2013). We note, however, that the interpretation of the age range of subduction of the Himalaya slab is based on its apparent volume (Replumaz et al., 2010b; van Hinsbergen et al., 2017b), and few independent geological constraints exist. We will argue in a following section that the general deceleration trend results from an increase in viscosity accommodating slab sinking in the first half of the lower mantle, where the spread in average sinking rates decreases from 10 to 40 mm/yr near the top to 10–15 mm/yr in the mid-mantle, below which there is not much change. Further, the spread in sinking rates at a particular depth may reflect differences in forced (Himalaya example) or free sinking, or lateral differences in mantle viscosity, e.g. due to long-term mantle plume activity in regions near the edges of long-lived Large Low Shear Velocity Provinces (LLSVPs) (e.g. Torsvik et al., 2008a, 2008b, 2010).

Figs. 99–101 also allow identifying outlying slabs. Three exceptionally fast sinking slabs have reached depths below 1500 km (Fig. 99a,b) of which only the Tonga–Kermadec–Hikurangi (TKH) slab is still actively subducting and may therefore still be influenced by upper mantle subduction. However, the fast sinking of two detached slabs (Arabia, Kalimantan) requires a different cause. These fast sinking lower mantle slabs occur in regions of mantle upwelling associated with ‘Plume Generation Zones’ at the edges of the deep LLSVPs (e.g. Torsvik et al., 2008a, 2008b, 2010). The Arabia slab sinks close to the well-known Afar upwelling at the NE-edge of the African LLSVP; the Kalimantan slab sinks in mantle that has reduced seismic velocities associated with the Hainan upwelling that branches of the western edge of the Pacific LLSVP (Hall and Spakman, 2015). Although we cannot exclude an effect of active subduction we note that the Tonga-Kermadec slab, with an average sinking velocity as high as 28 mm/yr, also sinks in an overall slow seismic-velocity mantle associated with the Samoan plume (Chang et al., 2016) above the southern edge of the Pacific LLSVP. Two particularly slowly sinking slabs identifiable in Fig. 100e and c are the Georgia Islands slab (GI) and the Malpelo slab (Mp). In case of the GI slab the delayed sinking may be due to early plume-slab interaction at a time when the slab may have been flat in the upper mantle (Section 3.33) in which case plume rise may have stalled sinking, while the interpretation of the Mp slab is stated to be uncertain (Section 3.53). Other slabs that stand out are the Cocos (Co, Section 3.29) and Brasilia (Ba, Section 3.18) slabs (Figs. 100a, 101a) that we propose are still connected to active subduction and constitute the longest slabs on Earth.

4.2. Average versus in situ slab sinking rates

While previously we only estimated a lower mantle averaged slab sinking rate of 12 ± 3 mm/yr from a much smaller slab catalogue (van der Meer et al., 2010), a major finding here is the depth variation of depth-average sinking rates $V_{av}(d)$ (Fig. 99b; Fig. 101) in the lower mantle as a function of depth d, as described qualitatively in the previous section. First, we like to emphasize that the $V_{av}(d)$ sinking rates are an integral measure of the actual slab sinking rates $V(d,t)$ at depth d and geological time t. For instance, the average sinking rate of the base of the Calabria slab (Section 3.20) is 10 mm ± 3 mm/yr, but because it is temporarily flat-lying on the 660 km discontinuity (e.g. Spakman and Wortel, 2004) its actual sinking velocity is possibly $V(660,t) \approx 0$ mm/yr. Generally, such temporal aspects of the sinking of slab are unknown and therefore we approximate $V(d,t)$ by the time-stationary in situ sinking velocity $\widehat{V}(d)$, which represents the time-averaged $V(d,t)$ at each mantle depth d. This allows us to define the relation $V_{av}(d) = \frac{1}{d}\int_0^d \widehat{V}(z)dz$, which after differentiating leads to $\widehat{V}(d) = V_{av}(d) + d\,V'_{av}(d)$. From this equation, the in situ time-stationary sinking velocity $\widehat{V}(d)$ can be obtained for a given profile $V_{av}(d)$ of average sinking velocity for a particular (fictitious) slab. We note that we see no use yet for solving the integral equation for $\widehat{V}(d)$ by some method of geophysical inversion. The lateral scatter in $V_{av}(d)$ at fixed depth may relate to, as indicated earlier, forcing by regional mantle flow or to slabs subject to different mantle viscosities during their downward journey. The number and limited geographical spread of $V_{av}(d)$ estimates does not allow yet for solving for regional differences

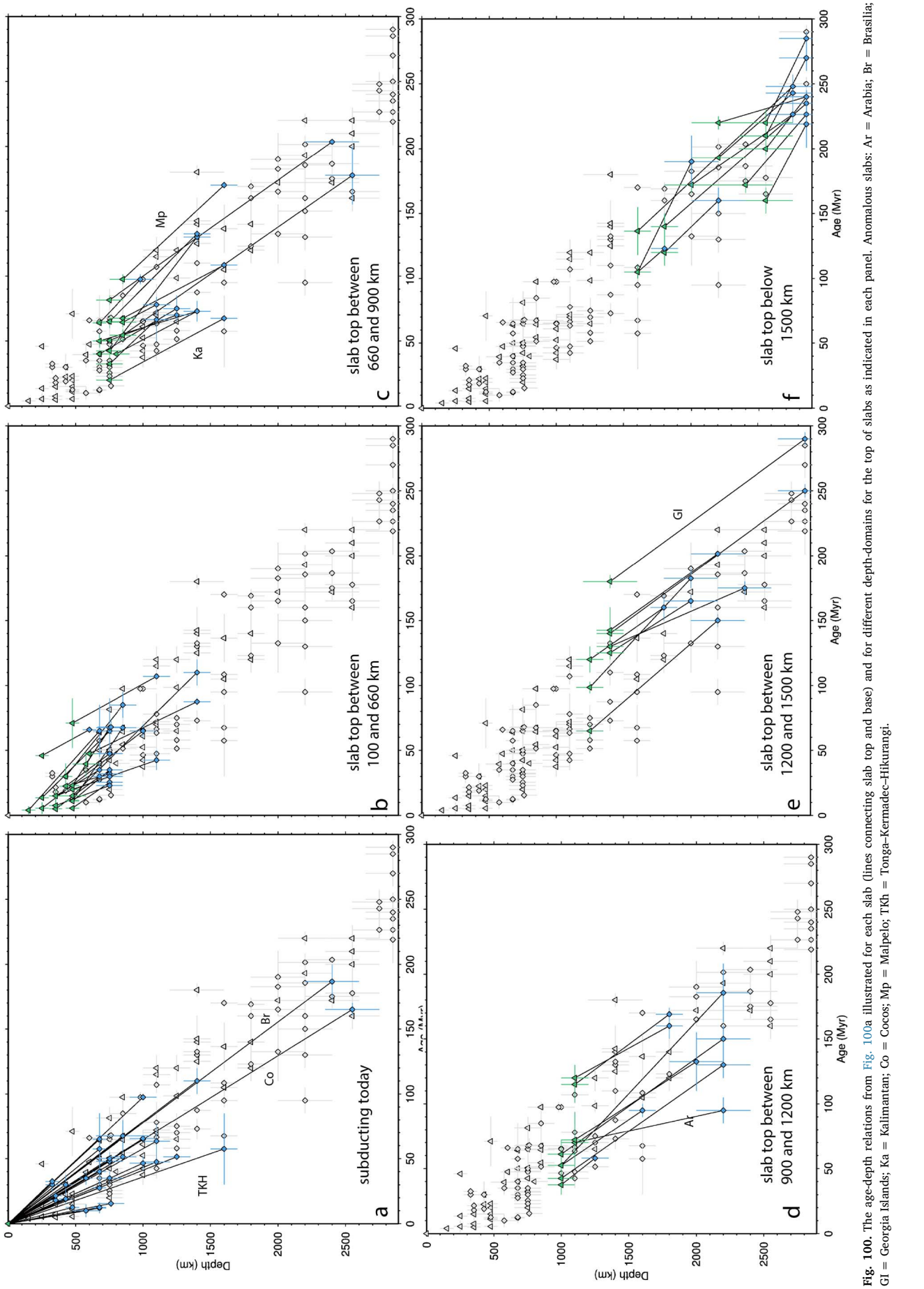

Fig. 100. The age-depth relations from Fig. 100a illustrated for each slab (lines connecting slab top and base) and for different depth-domains for the top of slabs as indicated in each panel. Anomalous slabs: Ar = Arabia; Br = Brasilia; Gl = Georgia Islands; Ka = Kalimantan; Co = Cocos; Mp = Malpelo; TKh = Tonga–Kermadec–Hikurangi.

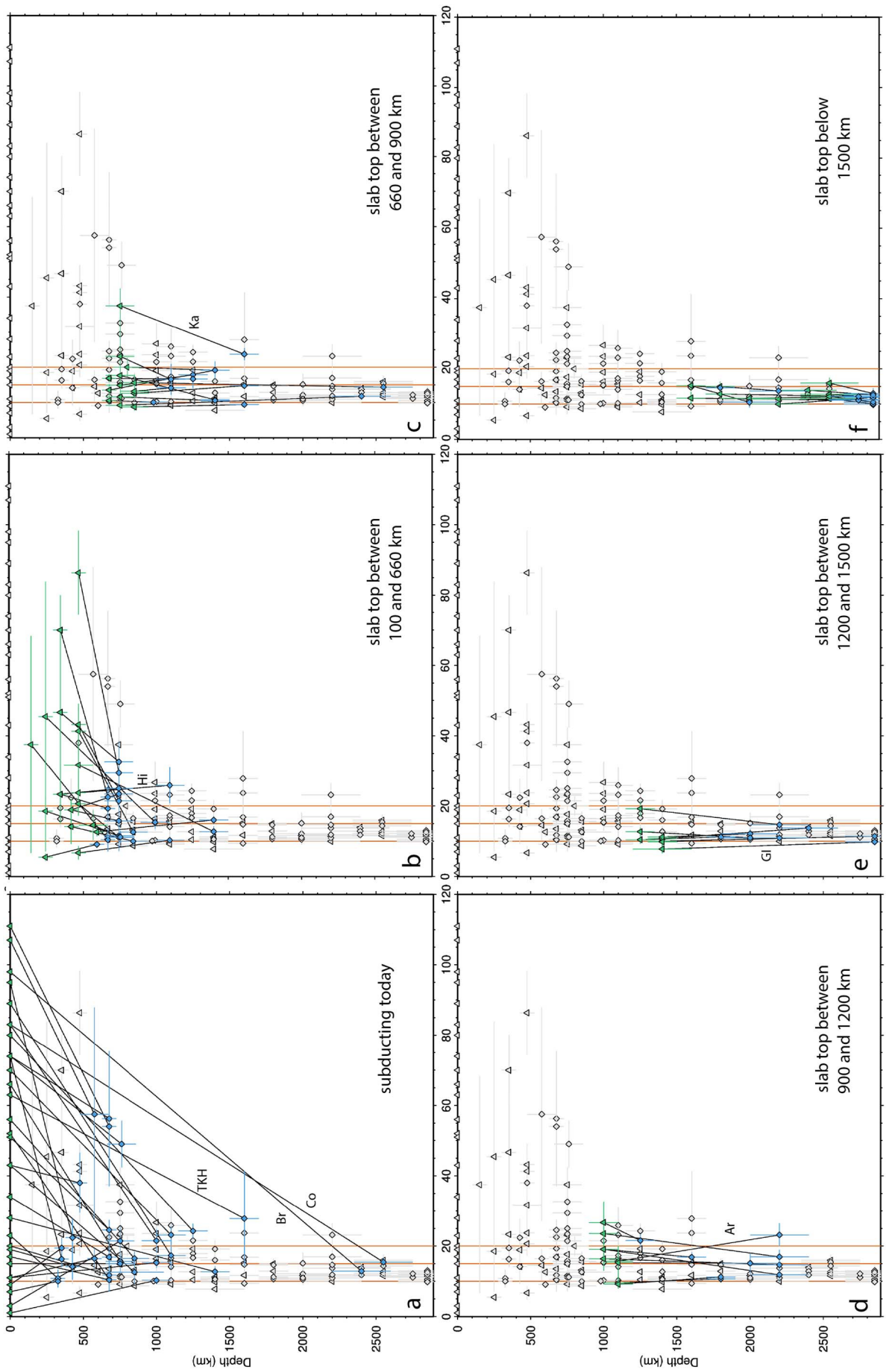

Fig. 101. Average sinking rate to depth relations for Fig. 100b. Illustrated for each slab (lines connecting slab top and base and for different depth-domains for the top of slabs as indicated in each panel. Anomalous slabs: Ar = Arabia; Br = Brasilia; Gl = Georgia Islands; Ka = Kalimantan; Co = Cocos; TKh = Tonga–Kermadec–Hikurangi.

in the $\widehat{V}(d)$ profile yielding a formal inversion of the integral equation fairly meaningless because of the large uncertainties expected.

Therefore, we adopt a forward approach in which we configured several slab-sinking profiles of $V_{av}(d)$ for fictitious slabs for which we calculated the corresponding time-stationary sinking rates $\widehat{V}(d)$. The results are summarized in Fig. 102. We conducted three batches of calculations to illustrate the sensitivity of $\widehat{V}(d)$ for smooth changes in $V_{av}(d)$. Fig. 102a shows 8 fictitious $V_{av}(d)$ profiles for slabs that assume a constant sinking rate of 12 mm/yr below ~1700 km while at the depth of 660 km $V_{av}(660)$ is designed to start from 10 mm/yr to 24 mm/yr in steps of 2 mm/yr. The smooth variation in the top part mimics the different sinking trends of slabs observed in Fig. 101, while the bottom part simulates the near constant $V_{av}(d)$ in deeper half of the lower mantle. The corresponding in situ sinking rates $\widehat{V}(d)$ (Fig. 102d) shows that generally slab sinking occurs at speeds < 15 mm/yr and decelerating slabs in particular with speeds < 10 mm/yr. We note that at the CMB, V_{av} is lowered to 11.25 mm/yr to satisfy that $\widehat{V}(CMB) = 0$ mm/yr. Slightly accelerating $V_{av}(d)$-profiles lead to a modest speed up of the slab while the deceleration leads to slow-down to as small as 4–5 mm/yr. The deceleration occurs from 660 km to ~1300 km. The lowest sinking rates occur in a depth range of about 300 km centred around 1300 km, which will take these slabs about 60 Myr to transit. Assuming incompressible deformation, the vertical shortening rates are approximated by the factor $\widehat{V}(660)/\widehat{V}(d)$ while the horizontal surface area of a slab is extended reciprocally. The vertical shortening for each of the 8 slabs is plotted in Fig. 102g and shows shortening with factors up to ~4. Shortening factors between 2 and 3 have been proposed for lower mantle slabs in the Tethyan realm (Hafkenscheid et al., 2006) which would change the plate-like character of upper mantle slab into laterally extended amorphous "blobs" in the lower mantle, as observed with tomography. Below this slab deceleration zone, slab anomalies can partially stretch because of increasing sinking rate, but will not assume their plate-like shape. Figs. 102 b, e, h, show results from a similar batch of experiments with the only difference that $V_{av} = 14$ mm/yr below the depth of 1700 km and $V_{av}(CMB) = 13.12$ mm/y. The larger deep-mantle average sinking rate causes a general increase in rates $\widehat{V}(d)$ of a few mm/yr while the thickening factor stays below 2.5 because deceleration is smaller.

In the last batch of experiments, Fig. 102c, f, i, we probe into the sensitivity of $\widehat{V}(d)$ to extreme as well as middle-of-the road V_{av}-profiles including small variations in these trends. As a whole, this experiment encompasses the full range of our dataset, with the exception of the three outliers (Ar, Ka, TKH) discussed above. The small variations we made in the V_{av}-profiles of each subset of three profiles serve forging that a minimum of $\widehat{V}(d) > 4$ mm/yr occurs in the depth range from 900 to 1500 km. Choices made for V_{av} above ~1700 km also determine the small variations in V_{av} below this depth such that V_{av} stays within limits of the age-depth relations of Fig. 99a. Obtaining a minimum in $\widehat{V}(d)$ requires that all V_{av}-profiles are decelerating in the top of the lower mantle. A small drop in V_{av} below 2750 km of 0.5–0.7 mm/yr suffices to satisfy the 0 mm/yr sinking rate at the CMB.

The resulting $\widehat{V}(d)$-profiles of Fig. 102f show in situ velocities decelerating from 12 to 22 mm/yr at the top of the lower mantle to ~4–8 mm/yr at particular depths between 1000 and 1500 km. Below the particular depth were the minimum in $\widehat{V}(d)$ occurs all profiles speed up to rates between 10 and 15 mm/yr in the deeper mantle in order to satisfy the average velocity $V_{av}(d)$ below ~1700 km, i.e. to keep within the inferred spread of age-depth relations (Fig. 99a). The corresponding shortening factors (Fig. 102j) range generally between 2 and 3.5 with excursions to factors larger than 5 for two extremely fast deceleration profiles. A factor of 5 would shorten a 660 km long upper mantle slab to a ~130 km thick "pancake" in the depth range 1000–1250 km. Although this cannot be excluded, such strong shortening has so far not been suggested from tomography or numerical modelling of subduction. Note that even slabs that sink with a minimum V_{av}-profile (darker green profiles in Fig. 102i) in which V_{av} reduces from 12 to 13 mm/yr at the top of the lower mantle to only 9 mm/yr around 1250 km, lead to a slab deceleration with shortening factors larger than 3. However, slab that subducts slowly in the upper mantle does not need to thicken strongly in the lower mantle. An example is the Aegean slab that, as observed in tomography, seems to transit the deceleration zone without considerable thickening. Differences in upper mantle subduction speed may thus explain why some slab seems to stagnate while others do not, as noted previously by Fukao and Obayashi (2013). These results show generally, and expectedly, that a gentle decrease in $V_{av}(d)$ between 660 km and 1500 km corresponds to a much more pronounced decrease in the in situ sinking rate $\widehat{V}(d)$ of a slab leading to vertical shortening. Similarly, a smooth 30% increase in $V_{av}(d)$ from 9 mm/yr to 12 mm/yr from 1600 km to 2750 km corresponds to an almost 100% increase of $\widehat{V}(d)$ from 8 mm/yr to 15 mm/yr.

Based on the average sinking velocities obtained from the Atlas (Fig. 99b), we suggest that in situ sinking rates $\widehat{V}(d)$ generally decrease in the top few hundred kilometres of the lower mantle from 10 to 25 mm/yr to 4–7 mm/yr somewhere in the depth range 1000–1500 km. Corresponding vertical shortening factors are between 2 and 3.5 but could be larger for more rapid deceleration. A minimum sinking rate of ~5–10 mm/yr across a 200–300 km depth interval where slab sinking is impeded most in the top 900 km of the lower mantle, would predict a slab transit time between 20 and 60 Myr. Such gradual transition in sinking is not easily inferred from the age-depth relations of Fig. 99a, but would explain the increase in horizontal spread in these relations from ~65 Myr at the base of the upper mantle to roughly 80–110 Myr. Flat slab in the upper-mantle transition zone will sink in the lower mantle within ~65 Myr or earlier while the continuous flow of slabs from the top to the bottom of the lower mantle excludes long-term (e.g. > 100 Myr) stagnation due to compositional buoyancy effects (Morra et al., 2010; Ballmer et al., 2015). Below ~1500 km in situ sinking rates are below 15 mm/yr for most lower mantle slabs. Only few slabs are exceptionally faster than the above range, which we have discussed in the previous section.

4.3. Towards constraining the radial profile of lower mantle viscosity associated with slab sinking

The vertical shortening and lateral thickening of slab explains the primary tomographic observations that led to the proposition of the slab stagnation zone between 660 and 1000 km (Fukao et al., 2001, 2009; Fukao and Obayashi, 2013) or down to 1500 km (Morra et al., 2010). Recent explanations of lateral slab thickening vary from a gradual increase in mantle viscosity in the top of the lower mantle, or a sudden viscosity increase near or below 1000 km, to compositional effects raising slab buoyancy (Morra et al., 2010; Marquardt and Miyagi, 2015; Rudolph et al., 2015; Ballmer et al., 2015). Despite these and other investigations there is, however, still no consensus on the particular shape of the lower mantle viscosity profile (Karato, 2010; King, 2016a, 2016b).

The continuous through-flow of slab demonstrates that the "slab stagnation zone" is rather a "slab deceleration zone" that requires a gradual increase in mantle viscosity associated with slab sinking below 660 km until ~1500 km. A rheological origin for the underlying increase of mantle viscosity across the depth range of 660–1500 km, matching with our deceleration pattern, was recently identified as a gradual increase in the strength of ferropericlase (Marquardt and Miyagi, 2015), which is the weakest mineral accommodating lower mantle deformation (Karato, 2010; Girard et al., 2016). The same authors note that below ~1500 km the increase in viscosity becomes smaller while in the deeper mantle viscosity can even reduce resulting from the Fe-spin crossover. The latter may even cause a mid-mantle minimum in viscosity (Shahnas et al., 2017). Our patterns of $V_{av}(d)$ and $\widehat{V}(d)$ below ~1500–1700 km implicitly support these predictions in terms of a slight acceleration in in situ sinking speeds for those slabs that initially decelerate in the top of the lower mantle (Fig. 102). We

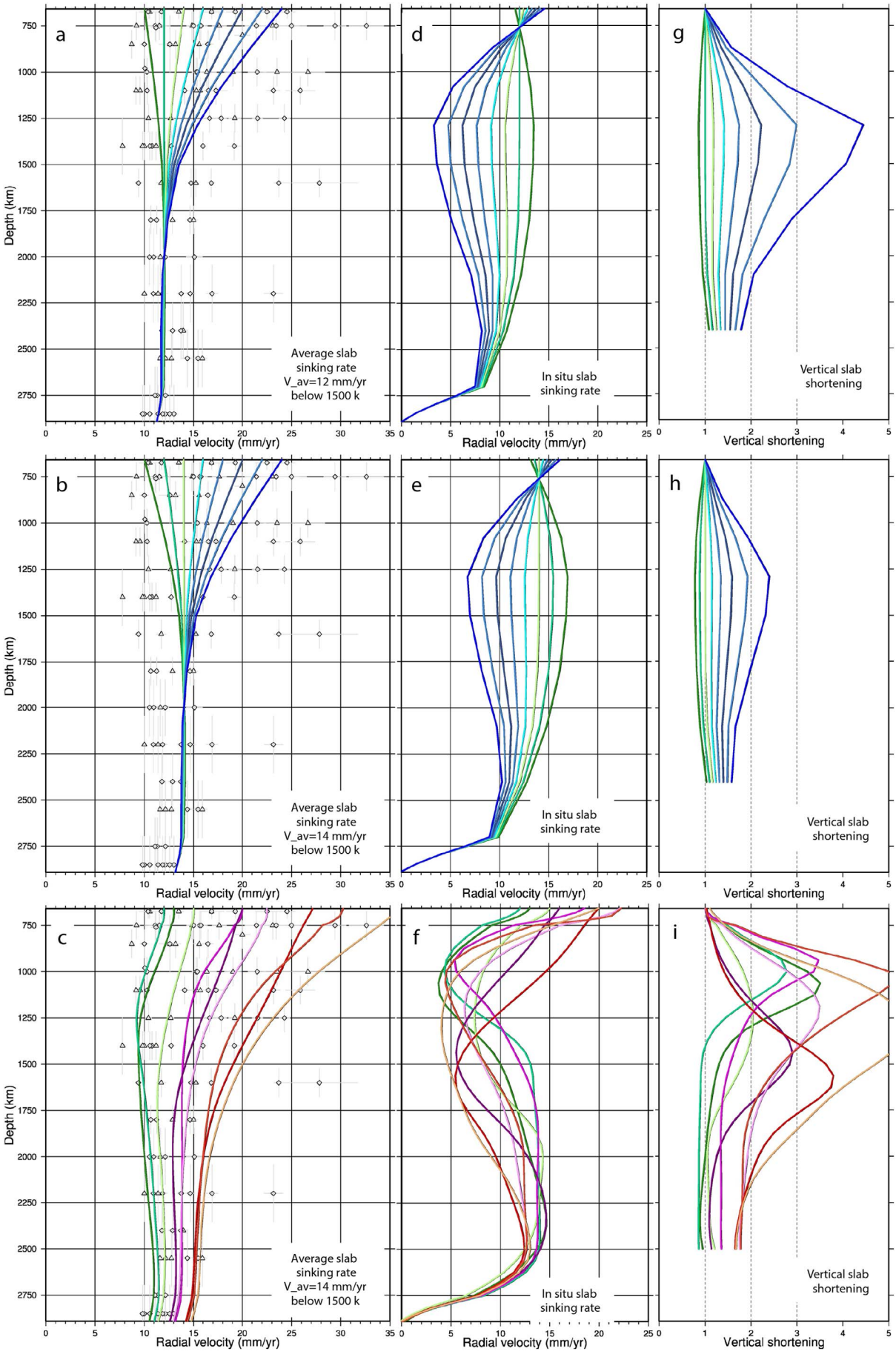

(caption on next page)

Fig. 102. Average sinking velocity converted to in situ sinking rate, vertical slab shortening factors. **a)** Configured lower mantle sinking profiles $V_{av}(d)$ for 8 fictitious slabs (dashed lines). Below 2000 km $V_{av}(d) = 12$ mm/yr is assumed which is reduced below 2750 km to reach 0 mm/yr in situ sinking at the CMB. At 660 km the starting value of $V_{av} = 10$ mm/yr (left curve) incremented in steps of 2 mm/yr to 24 mm/year (right curve). Grey symbols correspond to the age-depth data of Fig. 99a; **b)** As a) but for a constant average sinking velocity of 14 mm/yr below 2000 km; **c)** Configured lower mantle sinking profiles $V_{av}(d)$ for 9 fictitious slabs for slowly sinking slabs (green curves) fast sinking slabs (red/orange curve), or following the average depth trend (magenta curves). These curves where constrained by a minimum sinking speed of ~4 mm/yr above 1500 km and were furthermore configured to illustrate the sensitivity of in situ sinking rates $\widehat{V}(d)$ for systematic as well as small changes in the average sinking rates $V_{av}(d)$. Below 2750 km the $V_{av}(d)$ profiles where artificially reduced by 0.5–0.7 mm/yr to match 0 mm/yr vertical sinking at the CMB in line with the trend in the age-depth relations of Fig. 99a (grey symbols); **d–f)** in situ time-stationary sinking velocity $\widehat{V}(d)$ corresponding (color) to the average sinking velocity curves of a–c). **g–i)** vertical shortening factors $\widehat{V}(660)/\widehat{V}(d)$ corresponding to the in situ sinking curves d–f).

note for depths below 1600 km a small increase of the minimum average sinking rates from 9 to 12 mm/yr (Fig. 99b), which may possibly be attributed to the Fe spin crossover lowering mantle viscosity (Shahnas et al., 2017). Concurrently, any decrease in thermal expansivity and slow but progressive thermal assimilation of the slab remnant with increasing residence time would gradually lower the density contrast between slab remnant and ambient mantle and thus reduce the amplitude of the negative slab buoyancy. This would seemingly promote slower sinking, but to still match the inferred sinking trends (Fig. 99; Fig. 102) such buoyancy decrease will actually require a reduction in mantle viscosity in the deeper mantle. Any compositional contribution to the deceleration (Morra et al., 2010; Ballmer et al., 2015) is insufficient to cause long-term (> 100 Myr) stagnation, as this is not observed (Fig. 99a).

To investigate the implication of the in situ sinking profiles (Fig. 102b, f, j) for the depth variation in lower mantle viscosity we assume, considering the very low Reynolds number, that detached slab sinks with a depth-dependent terminal velocity equal to the in situ velocity $\widehat{V}(d)$. To estimate viscosity from terminal viscosity we follow the work of Kerr and Lister (1991) on sinking of ellipsoidal olivine grains in magma. This is done for an ellipsoidal slab with a temperature difference of 250 K estimated from seismic anomaly amplitudes (Goes et al., 2004), and with a vertical axis of 600 km, a long horizontal axis (trench-length) of 1000 km, and a short horizontal axis (slab width) of 80 km. Details are given in the appendix. The calculation includes depth-dependent thermal expansivity (Steinberger and Calderwood, 2006), but ignores effects of thermal assimilation, as these are difficult to incorporate. An approximation for the effect of slab shape change resulting from deceleration/acceleration is made by shortening/extending the principal axes. Fig. 103 shows the results of converting the $\widehat{V}$-sinking profiles of Fig. 102d–f into viscosity profiles. Because of several assumptions and uncertainties (Appendix), the viscosity profiles computed serve primarily to be indicative of the general depth trend of lower mantle viscosity related to slab sinking. The general observation is that slab decelerating in the top half of the lower mantle experiences increasing viscosity. The viscosity peaks in the top half of the lower mantle depending on sinking profile. Below 1500–1600 km viscosity slowly decreases due to reducing density contrasts resulting from decreasing thermal expansivity and increasing background density. Any reduction of the temperature contrast by diffusive heat transport would only enhance this decreasing trend. Most important is that the total variation in viscosity with depth is rather limited and does not depend on the slab shape, more extensive calculations show. We note that the variability we model via our choices for average sinking profiles (Fig. 102a–c) could possibly reflect the effect of global lateral differences in temperature dependence of viscosity, e.g. slab sinking in plume regions versus relatively sinking in relatively cold mantle.

Lower mantle viscosity associated with the sinking of slabs varies by less than a factor of 6 with depth, our results suggest. This is much less variation than seen in most of the published viscosity profiles of which a subset is shown in Fig. 103. Viscosity profiles that are explicitly constrained by the average rate of slab sinking are the A- and B-profiles (CA and CB in Fig. 103a) of Cízková et al. (2012). These resulted primarily from searching for viscosity profiles that cause slabs to transit the mantle within 250–300 Myr, i.e. with an average sinking rate of 12 mm/yr, while allowing for depth variability in viscosity. Our results agree best with their A-family of profiles. Also viscosity profiles EX2 and EX4 of Bower et al. (2013) match this transit time constraint. In contrast to this work, all other published viscosity profiles have been estimated from observations distinctly different from slab sinking rates. This concerns observations of the global dynamic response to redistribution of ice-water surface loads, gravity observations being linked to mantle structure, mantle dynamics, and Earth-rotational dynamics, constrained by mineral physics (e.g. Hager et al., 1984; Ricard et al., 1993, Lambeck et al., 1998, 2014; Peltier, 1998; Peltier and Drummond, 2010; Čadek and Fleitout, 2003; Mitrovica and Forte, 2004; Steinberger and Calderwood, 2006; Argus et al., 2014; Rudolph et al., 2015; Lau et al., 2016; Shahnas et al., 2017; King, 2016b). These studies probe the bulk viscosity field assuming a linear material response to volumetrically distributed forcing of mantle flow. Most studies suggest a clear depth variation while others suggest a more constant lower mantle viscosity. These differences may depend on the type of data constraint used or simply on the detail of depth parameterization adopted. In contrast, our inferences of slab sinking speeds pertain to the mantle rheology surrounding sinking slabs. There can be a difference if lower mantle rheology can be stress-dependent, as is recently suggested (Girard et al., 2016), and if slab sinking can generate the differential stresses required to activate such rheology. This, however, needs to be further investigated.

Recent seismic tomography imaging of mantle plumes suggest that broad vertically rising plumes change character by deflecting or thinning above ~1000 km (French and Romanowicz, 2015). This concurs with upward decreasing mantle viscosity, alike the viscosity trends in reverse direction suggested here for slab sinking, allowing for more plume mobility and thinning of the plume diameter, which is also confirmed by 3-D numerical models (e.g. Leng and Gurnis, 2012; Rudolph et al., 2015). This suggests that viscosity trends shown here are of wider relevance than slab sinking only and may also pertain to the bulk mantle.

Lastly, we note that proper assessment of lower mantle viscosity based on the sinking rate findings should involve work similar to that of Cízková et al. (2012), while mantle convection simulations can compare their prediction of average and in situ sinking rates to those found here.

5. Concluding remarks

In the preceding paragraphs 94 positive wave speed anomalies in the mantle have been interpreted as subducted slabs. We only considered P-wavespeed anomalies that were also imaged, although at a different resolution, in two S-wavespeed models: SL2013sv for the upper mantle and S40RTS for the lower mantle. A preliminary comparison with recently constructed voting maps from 14 recent P- and S-tomography models (Shephard et al., 2017) reveals that the majority of features identified in the voting maps match those identified here in the Atlas of the Underworld (G. Shephard, personal communication). We identified the Cocos (Co) and Brasilia (Ba) slabs as the longest slabs on Earth.

The strategy we followed for associating slab anomalies to geological evidence for subduction is based on a regional-continental scale interpretation of geological records relative to each other involving slab anomalies that are found with a similar spatial distribution at depth in the mantle. This only assumes vertical sinking of detached slab remnant, which was recently corroborated by Domeier et al. (2016). The interpretation of the start and end of subduction was based on geological information with age ranges encompassing the estimates given in

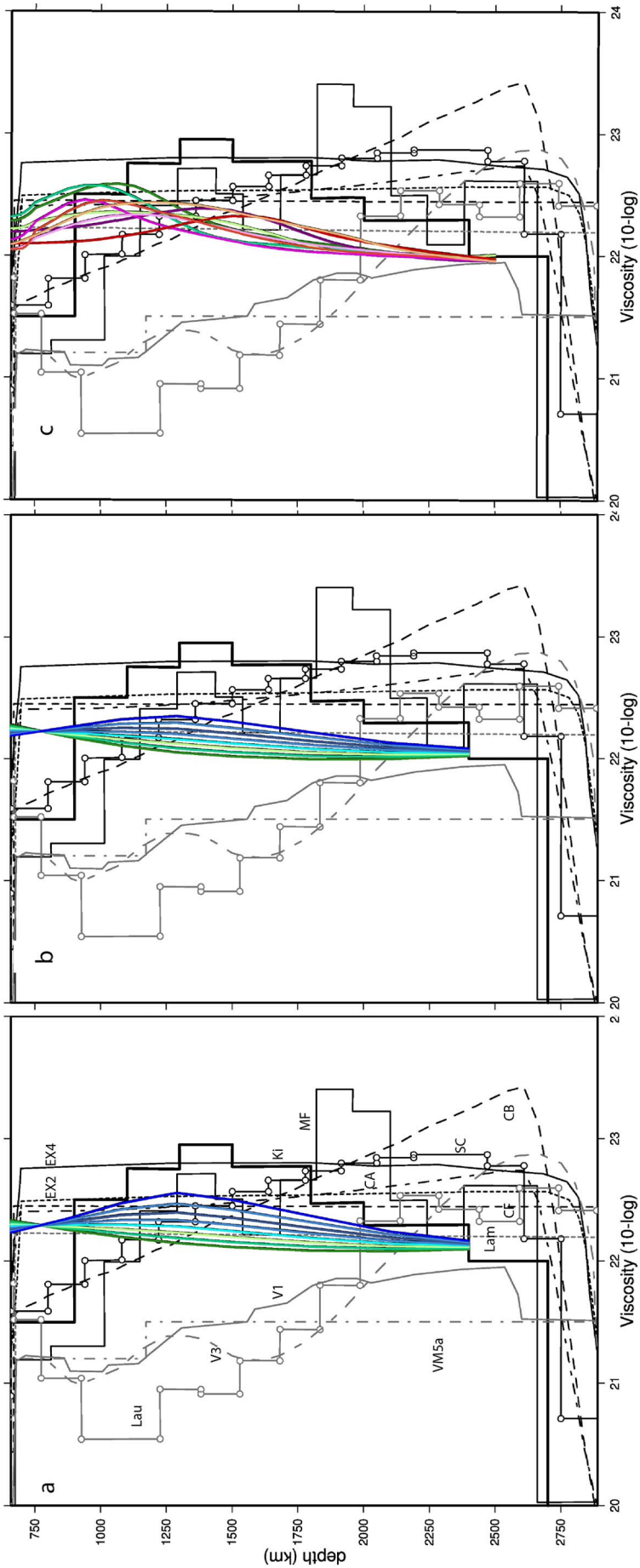

Fig. 103. Viscosity profiles (coloured) corresponding to the in situ sinking profiles of Fig. 102d, e and f, respectively, for an ellipsoidal shaped slab with a vertical axis length of 600 km, a width of 2000 km, a thickness of 80 km and a temperature contrast of 250 K that sinks from the top of the lower mantle. See Section 4.3 en the Appendix for further explanation. The grey and black curves in the background are published mantle viscosity profiles shown for comparison: **CA, CB** the prefered A- and B-profiles of Cízková et al. (2012); **CF** (Čadek and Fleitout, 2003); **EX2** and **EX4** (Bower et al., 2013); **Ki** (King, 2016b); **Lam** (Lambeck et al., 2014); **Lau** (Lau et al., 2016); **MF** (Mitrovica and Forte, 2004); **SC** (Steinberger and Calderwood, 2006); model **VM5a** from Argus et al. (2014); models **V1** and **V2** from Shahnas et al. (2017).

the pertinent literature. Where geology implied distinctly different subduction events in a particular region, this allowed for inspecting any internal lateral structure in large lower mantle slab anomalies. For example, lateral structure in the huge Farallon slab anomaly has led to a subdivision into several subduction segments: the Cocos, Hatteras and Hudson slabs, resulting from different subduction zones. By treating these separately also enables a clearer discussion on their tectonic origins for which proposed solutions differ between the Farallon Ocean plate subducting underneath the American continental margin (i.e. Grand et al., 1997; Bunge and Grand, 2000), or subduction of several Panthalassa Ocean plates dominantly under the continental margin (van der Meer et al., 2010, 2012), or dominantly at intra-oceanic subduction zones (Sigloch and Mihalynuk, 2013). Future, more accurate, plate tectonic models relative to the mantle will be needed to converge to one of these scenarios or combinations thereof. In this context, we emphasize again that in the construction of the Atlas of the Underworld no assumptions were made about slab sinking rates. Only for the interpretation of the enigmatic Maldives and Malpelo slab anomalies we cross-checked with predictions from tectonic reconstructions cast in an absolute plate motion frame, but for the vast majority of our orogen-slab associations we did not use any guidance from absolute plate motion models, particularly not to allow the Atlas to become a source of information for constructing a mantle frame based on subduction (van der Meer et al., 2010).

Under the Indo-Australian realm, many lower mantle slabs anomalies are imaged, presumably of Mesozoic origin (van der Meer et al., 2012; Simmons et al., 2015). In plate tectonic reconstructions these would be located in the transition of the Tethys to Panthalassa Oceans, which remains poorly reconstructed. The mantle structure below the Pacific and East Asia may provide an unprecedented means to interpret the Panthalassa plate kinematic history back to the Triassic, linking the few presumed relics of intra-Panthalassa and Panthalassa-Tethys junction subduction that accreted around the Pacific to subducted slab remnants.

We did not identify slabs that correlate to subduction zones older than ~300 Myr. This is perhaps because much older subduction remnants may have been thermally assimilated in the hot thermal boundary layer overlying the CMB. In addition, at the base of the mantle the occurrence of rheologically weaker post-perovskite phase, mantle viscosities are considerably lower (Fig. 103) allowing for lateral advection and strong deformation of some slab material.

The Atlas includes several slabs that appear to have interacted with the two large low shear wave velocity bodies (LLSVPs) on the core-mantle boundary. The LLSVPs are generally assumed to have been long-lived, stable features along which edges plumes may have been generated throughout the Phanerozoic or beyond (e.g., Burke et al., 2008; Torsvik et al., 2008a, 2008b, 2010, 2014). The Atlas documents that the modern shapes of both LLSVPs appear to have been influenced by subducted slabs. The Pacific LLSVP contains positive seismic velocity bodies in its centre that we correlated to Telkhinia slabs (van der Meer et al., 2012). The Perm Anomaly below Siberia was recently assumed to have migrated ~1500 km along the CMB as a function of subduction in the Paleopacific realm (Flament et al., 2017), but our correlations suggest a more straightforward solution in which it was separated from the large African LLSVP by the Balkan slab that we correlated to Permian subduction in the Urals. In this scenario, the Perm anomaly may well have acted as generation zone for the Siberian Traps (e.g., Torsvik et al., 2008a, 2008b, 2010).

The age-depth trend of slab sinking (Figs. 99a, 100) and average sinking speeds (Figs. 99b, 101) we derived from the Atlas suggest significant depth variability and possibilities to retrieve the speed of subduction in the upper mantle for slab that are now in the lower mantle. All slabs sink to the CMB. In the slab deceleration zone (660 km − 1500 km), slab requires less than ~60 Myr to cross a depth range of ~300 km where sinking speed is lowest (4–10 mm/yr). Differences in the speed of subduction in the upper mantle may explain why some slabs thicken strongly while others thicken only moderately. Our results do not agree with long-term stagnation due to compositional buoyancy effects. The spread in sinking rates may reflect lateral heterogeneity in the lower mantle viscosity as we identified some fast sinking slabs in regions of long-term plume activity. Estimated in situ time-stationary sinking rates generally decrease in the upper 900 km of the lower mantle depending on the assumed average-sinking speed profile and then show increase below ~1500 km. Conversion to mantle viscosity profiles show generally a viscosity increase somewhere between 660 km and 1500 km, while below 1500 km viscosity tends to slowly decrease. Generally our estimated profiles show a depth-variation in viscosity far less than one order in magnitude. The mismatch we find with many published viscosity profiles is puzzling if lower mantle rheology around sinking slabs is not stress dependent. The depth trend in viscosity we qualitatively infer agrees with that implied by the observed morphology change of rising plumes and recent experimental finding regarding the rheological behavior of ferropericlase.

In conclusion, this Atlas of the Underworld aims to provide a global starting point, or framework for linking plate tectonic history of the past ~300 Myr to present-day mantle structure. This also shows great potential to provide novel constraints on lower mantle viscosity associated with the sinking of slab remnants. Advances, corrections, and extensions are expected from more detailed tomographic models and better dating of paleo-subduction evolution. We aimed at brief descriptions per slab also to welcome post-peer review input on our Atlas via the website: http://www.atlas-of-the-underworld.org/.

Author contributions

DvdM and DvH constructed the Atlas of the Underworld. WS provided the analysis of sinking rates and mantle viscosity.

Acknowledgements

The seed for this research and its predecessor van der Meer et al. (2010) was planted during a sabbatical visit of Rob van der Voo to Utrecht University in 1999 and the granting of the M.C. Escher prize for DvdM's MSc. thesis in 2002. DvdM acknowledges Nexen for granting study leave to work on this research. DJJvH acknowledges ERC Starting Grant 306810 (SINK) and NWO Vidi grant 864.11.004. WS acknowledges support from the Research Council of Norway through its Centres of Excellence funding scheme, project number 223272, and support from the Netherlands research centre for Integrated Solid Earth Science (ISES). We thank Thomas van der Linden for developing the Atlas-of-the-underworld.org website. Bernard Steinberger, Jeroen Ritsema, John Hernlund, Wouter Schellart, Patrick Cordier, Hana Cízková, Arie van den Berg are thanked for discussions on slab sinking and mantle rheology.

Appendix A. Supplementary data

Supplementary data associated with this article can be found in the online version, at https://doi.org/10.1016/j.tecto.2017.10.004. These data include the Google map of the most important areas described in this article.

References

Abdelwahed, M.F., Zhao, D., 2007. Deep structure of the Japan subduction zone. Phys. Earth Planet. Inter. 162, 32–52.
Abrajevitch, A.V., Ali, J.R., Aitchison, J.C., Badengzhu, Davis, A.M., Liu, J., Ziabrev, S.V., 2005. Neotethys and the India–Asia collision: insights from a palaeomagnetic study of the Dazhuqu ophiolite, southern Tibet. Earth Planet. Sci. Lett. 233, 87–102.
Acharya, S.K., Mitra, N.D., 1986. Regional geology and tectonic setting of northeast India and adjoining region. Mem. Geol. Surv. India 6–12.
Advokaat, E.L., van Hinsbergen, D., Kaymakci, N., Vissers, R.L.M., Hendriks, B.W.H., 2014a. Late Cretaceous extension and Palaeogene rotation-related contraction in Central Anatolia recorded in the Ayhan-Büyükkışla basin. Int. Geol. Rev. 56,

1813–1836.
Advokaat, E.L., van Hinsbergen, D., Maffione, M., Langereis, C.G., Vissers, R.L.M., Cherchi, A., Schroeder, R., Madani, H., Columbu, S., 2014b. Eocene rotation of Sardinia, and the paleogeography of the western Mediterranean region. Earth Planet. Sci. Lett. 401, 183–195.
Agard, P., Jolivet, L., Vrielynck, B., Burov, E., Monié, P., 2007. Plate acceleration: the obduction trigger? Earth Planet. Sci. Lett. 258, 428–441.
Agard, P., Omrani, J., Jolivet, L., Whitechurch, H., Vrielynck, B., Spakman, W., Monié, P., Meyer, B., Wortel, M.J.R., 2011. Zagros orogeny: a subduction-dominated process. Geol. Mag. 148, 692–725.
Akinin, V.V., Miller, E.L., Wooden, J.L., 2009. Petrology and geochronology of crustal xenoliths from the Bering Strait region: linking deep and shallow processes in extending continental crust. In: Miller, R.B., Snoke, A.W. (Eds.), Crustal Crosssections from the Western North American Cordillera and Elsewhere: Implications for Tectonic and Petrologic Processes. Special Paper, 456. The Geological Society of America, Boulder, Colorado.
Al-Riyami, K., Robertson, A.H.F., Dixon, J.E., Xenophontos, C., 2002. Origin and emplacement of the Late Cretaceous Baer–Bassit ophiolite and its metamorphic sole in NW Syria. Lithos 65, 225–260.
Amaru, M.L., 2007. Global travel time tomography with 3-D reference models. Geol. Ultraiect. 274 174 p.
Anczkiewicz, R., Platt, J.P., Thirlwall, M.F., Wakabayashi, J., 2004. Franciscan subduction off to a slow start: evidence from high-precision Lu–Hf garnet ages on high grade-blocks. Earth Planet. Sci. Lett. 225, 147–161.
Aragón, E., D'Eramo, F., Castro, A., Pinotti, L., Brunelli, D., Rabbia, O., Rivalenti, G., Varela, R., Spakman, W., Demartis, M., Cavarozzi, C.E., Aguilera, Y.E., Mazzucchelli, M., Ribot, A., 2011. Tectono-magmatic response to major convergence changes in the North Patagonian suprasubduction system; the Paleogene subduction–transcurrent plate margin transition. Tectonophysics 509, 218–237.
Arculus, R.J., Ishizuka, O., Bogus, K.A., Gurnis, M., Hickey-Vargas, R., Aljahdali, M.H., Bandini-Maeder, A.N., Barth, A.P., Brandl, A., Drab, L., do Monte Guerra, R., Hamada, M., Jiang, F., Kanayama, K., et al., 2015. A record of spontaneous subduction initiation in the Izu–Bonin–Mariana arc. Nat. Geosci. 8, 728–733.
Argnani, A., 2012. Plate motion and the evolution of Alpine Corsica and Northern Apennines. Tectonophysics 579, 207–219.
Argus, D.F., Peltier, W.R., Drummond, R., Moore, A.W., 2014. The Antarctica component of postglacial rebound model ICE-6G_C (VM5a) based on GPS positioning, exposure age dating of ice thicknesses, and relative sea level histories. Geophys. J. Int. 198 (1), 537–563.
Avdeev, B., Niemi, N.A., 2011. Rapid Pliocene exhumation of the central Greater Caucasus constrained by low-temperature thermochronometry. Tectonics 30. http://dx.doi.org/10.1029/2010TC002808.
Ayala, R.C., Bayona, G., Cardona, A., Ojeda, C., Montenegro, O.C., Montes, C., Valencia, V., Jaramillo, C., 2012. The paleogene synorogenic succession in the northwestern Maracaibo block: tracking intraplate uplifts and changes in sediment delivery systems. J. S. Am. Earth Sci. 39, 93–111.
Babazadeh, S.A., De Wever, P., 2004. Early Cretaceous radiolarian assemblages from radiolarites in the Sistan Suture (eastern Iran). Geodiversitas 26, 185–206.
Bache, F., Mortimer, N., Sutherland, R., Collot, J., Rouillard, P., Stagpoole, V., Nicol, A., 2013. Seismic stratigraphic record of transition from Mesozoic subduction to continental breakup in the Zealandia sector of eastern Gondwana. Gondwana Res. 26, 1060–1078.
Bailey, W.R., Holdsworth, R.E., Swarbrick, R.E., 2000. Kinematic history of a reactivated oceanic suture: the Mammonia Complex Suture Zone, SW Cyprus. J. Geol. Soc. Lond. 157, 1107–1126.
Ballmer, M.D., Schmerr, N.C., Nakagawa, T., Ritsema, J., 2015. Compositional mantle layering revealed by slab stagnation at ~1000-km depth. Sci. Adv. 1 (11) (p.e1500815).
Barboza-Gudiño, J.R., Orozco-Esquivel, M.T., Gómez-Anguiano, M., Zavala-Monsiváis, A., 2008. The Early Mesozoic volcanic arc of western North America in northeastern Mexico. J. S. Am. Earth Sci. 25, 49–63.
Barnett-Moore, N., Hosseinpour, M., Maus, S., 2016. Assessing discrepancies between previous plate kinematic models of Mesozoic Iberia and their constraints. Tectonics 35, 1843–1862.
Barresi, T., Nelson, J.L., Dostal, J., Friedman, R., 2015. Evolution of the Hazelton arc near Terrace, British Columbia: stratigraphic, geochronological, and geochemical constraints on a Late Triassic–Early Jurassic arc and Cu–Au porphyry belt. Can. J. Earth Sci. 52 (7), 466–494.
Baxter, A.T., Aitchison, J.C., Ali, J.R., Zyabrev, S., 2010. Early cretaceous radiolarians from the spongtang massif, Ladakh, NW India: implications for Neo-Tethyan evolution. J. Geol. Soc. Lond. 167, 511–517.
Bertrand, G., Rangin, C., 2003. Tectonics of the western margin of the Shan plateau (central Myanmar): implication for the India–Indochina oblique convergence since the Oligocene. J. Asian Earth Sci. 21, 1139–1157.
Bezada, M.J., Levander, A., Schmandt, B., 2010. Subduction in the southern Caribbean: images from finite-frequency P wave tomography. J. Geophys. Res. 115. http://dx.doi.org/10.1029/2010JB007682. (B12333–19).
Bezada, M.J., Humphreys, E.D., Toomey, D.R., Harnafi, M., Davila, J.M., Gallart, J., 2013. Evidence for slab rollback in westernmost Mediterranean from improved upper mantle imaging. Earth Planet. Sci. Lett. 368, 51–60.
Bijwaard, H., Spakman, W., Engdahl, E.R., 1998. Closing the gap between regional and global travel time tomography. J. Geophys. Res. 103, 30055–30078.
Biryol, C.B., Beck, S.L., Zandt, G., Özacar, A.A., 2011. Segmented African lithosphere beneath the Anatolian region inferred from teleseismic P-wave tomography. Geophys. J. Int. 184, 1037–1057.
Blanco, M.J., Spakman, W., 1993. The P-wave velocity structure of the mantle below the Iberian Peninsula: evidence for subducted lithosphere below southern Spain. Tectonophysics 221, 13–34. http://dx.doi.org/10.1016/0040-1951(93)90025-F.
Boekhout, F., Spikings, R., Sempere, T., Chiaradia, M., Ulianov, A., Schaltegger, U., 2012. Mesozoic arc magmatism along the southern Peruvian margin during Gondwana breakup and dispersal. Lithos 146–147, 48–64.
Bogdanov, N.A., Vishnevskaya, S., Kepezhinskas, K., Sukhov, A.N., Fedorchuk, A.V., 1987. Geology of the Southern Koryak Plateau [in Russian]. Nauka, Moscow.
Borneman, N.L., Hodges, K.V., Soest, M.C., Bohon, W., Wartho, J.-A., Cronk, S.S., Ahmad, T., 2015. Age and structure of the Shyok suture in the Ladakh region of northwestern India: Implications for slip on the Karakoram fault system. Tectonics 34, 2011–2033.
Boschman, L.M., van Hinsbergen, D.J., 2016. On the enigmatic birth of the Pacific plate within the Panthalassa Ocean. Sci. Adv. 2, e1600022.
Boschman, L.M., van Hinsbergen, D.J.J., Torsvik, T.H., Spakman, W., Pindell, J., 2014. Kinematic reconstruction of the Caribbean region since the Early Jurassic. Earth Sci. Rev. 138, 102–136.
Bourgeois, O., Cobbold, R., Rouby, D., Thomas, J.-C., Shein, V., 1997. Least squares restoration of Tertiary thrust sheets in map view, Tajik depression, central Asia. J. Geophys. Res. 102, 27553–27573.
Bower, D.J., Gurnis, M., Seton, M., 2013. Lower mantle structure from paleogeographically constrained dynamic Earth models. Geochem. Geophys. Geosyst. 14, 44–63.
Bröcker, M., Rad, G.F., Burgess, R., Theunissen, S., Paderin, I., Rodionov, N., Salimi, Z., 2013. New age constraints for the geodynamic evolution of the Sistan Suture Zone, eastern Iran. Lithos 170–171, 17–34.
Brunet, C., Monié, P., Jolivet, L., Cadet, J.P., 2000a. Migration of compression and extension in the Tyrrhenian Sea, insights from $^{40}Ar/^{39}Ar$ ages on micas along a transect from Corsica to Tuscany. Tectonophysics 321, 127–155.
Brunet, M.F., Spakman, W., Ershov, A.V., Nikishin, A.M., 2000b. In: Information given by the tomography on the geodynamics of the Caucasus–Caspian area. European geophysical society annual meeting. 2000. pp. 25–29.
Buchs, D.M., Arculus, R.J., Baumgartner, O., Baumgartner-Mora, C., Ulianov, A., 2010. Late Cretaceous arc development on the SW margin of the Caribbean Plate: insights from the Golfito, Costa Rica, Azuero, Panama, complexes. Geochem. Geophys. Geosyst. 11. http://dx.doi.org/10.1029/2009GC002901.
Bunge, H.P., Grand, S.P., 2000. Mesozoic plate-motion history below the northeast Pacific Ocean from seismic images of the subducted Farallon slab. Nature 405, 337–340.
Burke, K., 1988. Tectonic evolution of the Caribbean. Annu. Rev. Earth Planet. Sci. 16, 201–230.
Burke, K., Steinberger, B., Torsvik, T.H., Smethurst, M.A., 2008. Plume Generation Zones at the margins of Large Low Shear Velocity Provinces on the core–mantle boundary. Earth Planet. Sci. Lett. 265, 49–60.
Burtman, S., Molnar, P., 1993. Geological and geophysical evidence for deep subduction of continental crust beneath the Pamir. Geol. Soc. Am. Spec. Pap. 281 (76p).
Butterworth, N.P., Talsma, A.S., Müller, R.D., Seton, M., 2014. Geological, tomographic, kinematic and geodynamic constraints on the dynamics of sinking slabs. J. Geodyn. 73, 1–13. http://dx.doi.org/10.1016/j.jog.2013.10.006.
Čadek, O., Fleitout, L., 2003. Effect of lateral viscosity variations in the top 300 km on the geoid and dynamic topography. Geophys. J. Int. 152 (3), 566–580.
Camp, E., Griffis, R.J., 1982. Character, genesis and tectonic setting of igneous rocks in the Sistan suture zone, eastern Iran. Lithos 15, 221–239.
Canil, D., et al., 2013. Age, construction, and exhumation of the midcrust of the Jurassic Bonanza arc, Vancouver Island, Canada. Lithosphere 5.1, 82–91.
Carminati, E., Wortel, M., Spakman, W., Sabadini, R., 1998a. The role of slab detachment processes in the opening of the western–central Mediterranean basins: some geological and geophysical evidence. Earth Planet. Sci. Lett. 160, 651–665.
Carminati, E., Wortel, M.J.R., Meijer, T., Sabadini, R., 1998b. The two-stage opening of the western-central Mediterranean basins: a forward modeling test to a new evolutionary model. Earth Planet. Sci. Lett. 160, 667–679.
Cawood, A., Buchan, C., 2007. Linking accretionary orogenesis with supercontinent assembly. Earth Sci. Rev. 82, 217–256.
Çelik, Ö.F., Delaloyle, M.F., Feraud, G., 2006. Precise $^{40}Ar–^{39}Ar$ ages from the metamorphic sole rocks of the Tauride Belt Ophiolites, southern Turkey: implications for the rapid cooling history. Geol. Mag. 143, 213–227.
Centeno-Garcia, E., Busby, C., Busby, M., Gehrels, G., 2011. Evolution of the Guerrero composite terrane along the Mexican margin, from extensional fringing arc to contractional continental arc. Geol. Soc. Am. Bull. 123, 1776–1797.
Chang, S.-J., van der Lee, S., Flanagan, M.P., Bedle, H., Marone, F., Matzel, E.M., Pasyanos, M.E., Rodgers, A.J., Romanowicz, B., Schmid, C., 2010. Joint inversion for three-dimensional S velocity mantle structure along the Tethyan margin. J. Geophys. Res. 115, B08309 (doi: 10.1029–2009JB007204).
Chang, S.J., Ferreira, A.M., Faccenda, M., 2016. Upper-and mid-mantle interaction between the Samoan plume and the Tonga-Kermadec slabs. Nat. Commun. 7.
Chekhovich, V.D., Sukhov, A.N., Sheremet, O.G., Kononov, M.V., 2012. Cenozoic geodynamics of the Bering Sea region. Geotectonics 46, 212–231.
Chekhovich, V.D., Sheremet, O.G., Kononov, M.V., 2014. Strike-slip fault system in the Earth's crust of the Bering Sea: a relic of boundary between the Eurasian and North American lithospheric plates. Geotectonics 48 (4), 255–272.
Chen, Y., Zhu, D.-C., Zhao, Z.-D., Meng, F.-Y., Wang, Q., Santosh, M., Wang, L.-Q., Dong, G.-C., Mo, X.-X., 2014. Slab breakoff triggered ca. 113 Ma magmatism around Xainza area of the Lhasa Terrane, Tibet. Gondwana Res. 26, 449–463.
Chen, C., Zhao, D., Tian, Y., Wu, S., Hasegawa, A., Lei, J., Park, J.H., Kang, I.B., 2017. Mantle transition zone, stagnant slab and intraplate volcanism in Northeast Asia. Geophys. J. Int., p.ggw491.
Chertova, M.V., Spakman, W., van den Berg, A.P., Geenen, T., van Hinsbergen, D.J.J., 2014. Underpinning tectonic reconstructions of the western Mediterranean region through dynamic slab evolution from 3D numerical modeling. J. Geophys. Res. 119,

5876–5902.
Chu, R., Schmandt, B., Helmberger, D.V., 2012. Juan de Fuca subduction zone from a mixture of tomography and waveform modeling. J. Geophys. Res. 117. http://dx.doi.org/10.1029/2012JB009146.
Chung, S.L., Wang, S.L., Shinjo, R., Lee, C.S., Chen, C.H., 2000. Initiation of arc magmatism in an embryonic continental rifting zone of the southernmost part of Okinawa Trough. Terra Nova 12, 225–230.
Cízková, H., van den Berg, A.P., Spakman, W., Matyska, C., 2012. The viscosity of Earth's lower mantle inferred from sinking speed of subducted lithosphere. Phys. Earth Planet. Inter. 200–201, 56–62.
Clift, P.D., Pavlis, T., DeBari, S.M., Draut, A.E., Rioux, M., Kelemen, P.B., 2005. Subduction erosion of the Jurassic Talkeetna-Bonanza arc and the Mesozoic accretionary tectonics of western North America. Geology 33 (11), 881–884.
Cloos, M., 2005. Collisional delamination in New Guinea. Geol. Soc. Am. Spec. Pap. 400 (51 p).
Cluzel, D., Meffre, S., Maurizot, P., Crawford, A.J., 2006. Earliest Eocene (53 Ma) convergence in the Southwest Pacific: evidence from pre-obduction dikes in the ophiolite of New Caledonia. Terra Nova 18, 395–402.
Cluzel, D., Jourdan, F., Meffre, S., Maurizot, P., Lesimple, S., 2012. The metamorphic sole of New Caledonia ophiolite: $^{40}Ar/^{39}Ar$, U-Pb, and geochemical evidence for subduction inception at a spreading ridge. Tectonics 31. http://dx.doi.org/10.1029/2011TC003085.
Cocks, L.R.M., Torsvik, T.H., 2007. Siberia, the wandering northern terrane, and its changing geography through the Palaeozoic. Earth Sci. Rev. 82, 27–74.
Cocks, L.R.M., Torsvik, T.H., 2011. The Palaeozoic geography of Laurentia and western Laurussia: a stable craton with mobile margins. Earth Sci. Rev. 106, 1–51.
Cogne, J.P., Kravchinsky, A., Halim, N., Hankard, F., 2005. Late Jurassic-Early Cretaceous closure of the Mongol Okhotsk Ocean demonstrated by new Mesozoic palaeomagnetic results from the Trans-Baikal area (SE Siberia). Geophys. J. Int. 163, 813–832.
Corfield, R.I., Searle, M.P., Pederson, R.B., 2001. Tectonic setting, origin, and obduction history of the Spontang Ophiolite, Ladakh Himalaya, NW India. J. Geol. 109, 715–736.
Coulon, C., Fourcade, S., Maury, R.C., Bellon, H., Louni-Hacini, A., Cotten, J., Coutelle, A., Hermitte, D., 2002. Post-collisional transition from calc-alkaline to alkaline volcanism during the Neogene in Oranie (Algeria): magmatic expression of a slab breakoff. Lithos 62 (3), 87–110.
Cowgill, E., 2010. Cenozoic right-slip faulting along the eastern margin of the Pamir salient, northwestern China. Geol. Soc. Am. Bull. 122 (1–2), 145–161. http://dx.doi.org/10.1130/B26520.1.
Cowgill, E., Yin, A., Harrison, T.M., Wang, X.F., 2003. Reconstruction of the Altyn Tagh fault based on U-Pb geochronology: role of back thrusts, mantle sutures, and heterogeneous crustal strength in forming the Tibetan Plateau. J. Geophys. Res. 108 (B7), 2346 (doi: 10.1029–2002JB002080).
Cowgill, E., Forte, A.M., Niemi, N.A., Avdeev, B., Tye, A., Trexler, C., Javakhishvili, Z., Elashvili, M., Godoladze, T., 2016. Relict basin closure and crustal shortening budgets during continental collision: an example from Caucasus sediment provenance. Tectonics 35. http://dx.doi.org/10.1002/2016TC004295.
Creager, J.S., Scholl, D.W., 1973. Initial Reports of the Deep Sea Drilling Project. Printing Office, Washington, DC.
Csontos, L., Voros, A., 2004. Mesozoic plate tectonic reconstruction of the Carpathian region. Palaeogeogr. Palaeoclimatol. Palaeoecol. 210, 1–56.
Dalziel, I.W.D., Lawver, L.A., Norton, I.O., Gahagan, L.M., 2013. The Scotia Arc: genesis, evolution, global significance. Annu. Rev. Earth Planet. Sci. 41, 767–793.
de Boorder, H., Spakman, W., White, S.H., Wortel, M., 1998. Late Cenozoic mineralization, orogenic collapse and slab detachment in the European Alpine Belt. Earth Planet. Sci. Lett. 164, 569–575.
De Jonge, M.R., Wortel, M., Spakman, W., 1994. Regional scale tectonic evolution and the seismic velocity structure of the lithosphere and upper mantle: the Mediterranean region. J. Geophys. Res. 99, 12091–12108.
DeCelles, G., Ducea, M.N., Kapp, P., Zandt, G., 2009. Cyclicity in Cordilleran orogenic systems. Nat. Geosci. 2, 251–257.
Delavari, M., Amini, S., Schmitt, A.K., McKeegan, K.D., Harrison, T.M., 2014. U–Pb geochronology and geochemistry of Bibi-Maryam pluton, eastern Iran: Implication for the late stage of the tectonic evolution of the Sistan Ocean. Lithos 200–201, 197–211.
Demouy, S., Paquette, J.L., de Saint Blanquat, M., Benoit, M., Belousova, E.A., O'Reilly, S.Y., García, F., Tejada, L.C., Gallegos, R., Sempere, T., 2012. Spatial and temporal evolution of Liassic to Paleocene arc activity in southern Peru unraveled by zircon U–Pb and Hf in-situ data on plutonic rocks. Lithos 155, 183–200.
Dewey, J.F., Casey, J.F., 2011. The origin of obducted large-slab ophiolite complexes. In: Brown, D., Ryan, D. (Eds.), Arc-continent Collision. Frontiers in Earth Sciencespp. 431–444.
Dickinson, W.R., 2006. Geotectonic evolution of the Great Basin. Geosphere 2 (353–17).
Dickinson, W.R., Lawton, T.F., 2001. Carboniferous to Cretaceous assembly and fragmentation of Mexico. Geol. Soc. Am. Bull. 113, 1142–1160.
Dilek, Y., Furnes, H., 2009. Structure and geochemistry of Tethyan ophiolites and their petrogenesis in subduction rollback systems. Lithos 113, 1–20.
Dimo-Lahitte, A., Monié, P., Vergély, P., 2001. Metamorphic soles from the Albanian ophiolites: Petrology, $^{40}Ar/^{39}Ar$ geochronology, and geodynamic evolution. Tectonics 20, 78–96.
Dokuz, A., Aydınçakır, E., Kandemir, R., Karslı, O., Siebel, W., Derman, A.S., Turan, M., 2017. Late Jurassic magmatism and stratigraphy in the eastern Sakarya zone, Turkey: Evidence for the slab breakoff of Paleotethyan oceanic lithosphere. J. Geol. 125 (1), 1–31.
Domeier, M., Doubrovine, V., Torsvik, T.H., Spakman, W., Bull, A., 2016. Global correlation of lower mantle structure and past subduction. Geophys. Res. Lett. 43, 4945–4953.
Donskaya, T.V., Gladkochub, D.P., Mazukabzov, A.M., Ivanov, A.V., 2013. Late Paleozoic – Mesozoic subduction-related magmatism at the southern margin of the Siberian continent and the 150 million-year history of the Mongol-Okhotsk Ocean. J. Asian Earth Sci. 62, 79–97.
Doubrovine, P.V., Steinberger, B., Torsvik, T.H., 2012. Absolute plate motions in a reference frame defined by moving hot spots in the Pacific, Atlantic, and Indian oceans. J. Geophys. Res., 117-B09101. http://dx.doi.org/10.1029/2011JB009072.
D'Souza, R.J., Canil, D., Creaser, R.A., 2016. Assimilation, differentiation, and thickening during formation of arc crust in space and time: the Jurassic Bonanza arc, Vancouver Island, Canada. Geol. Soc. Am. Bull. 128 (3–4), 543–557.
Dziewonski, A.M., 1984. Mapping the lower mantle: determination of lateral heterogeneity in P velocity up to degree and order 6. J. Geophys. Res. 89-B7, 5929–5952.
Eagles, G., 2005. Tectonic evolution of the west Scotia Sea. J. Geophys. Res. 110, B02401–19. http://dx.doi.org/10.1029/2004JB003154.
Eagles, G., 2010. The age and origin of the central Scotia Sea. Geophys. J. Int. 183, 587–600.
Eagles, G., Jokat, W., 2014. Tectonic reconstructions for paleobathymetry in Drake Passage. Tectonophysics 611, 28–50.
Eagles, G., Livermore, R., Morris, P., 2006. Small basins in the Scotia Sea. The Eocene Drake Passage gateway. Earth Planet. Sci. Lett. 242, 343–353.
Elliot, D.H., Fanning, C.M., 2008. Detrital zircons from upper Permian and lower Triassic Victoria Group sandstones, Shackleton Glacier region, Antarctica: evidence for multiple sources along the Gondwana plate margin. Gondwana Res. 13, 259–274.
Engebretson, D.C., Cox, A., Gordon, R.G., 1985. Relative motions between oceanic and continental plates in the Pacific Basin. In: Geological Society of America Special Paper 206, (59p.).
Faccenna, C., Becker, T.W., Pio Lucente, F., Jolivet, L., Rossetti, F., 2001. History of subduction and back-arc extension in the Central Mediterranean. Geophys. J. Int. 145, 809–820.
Faccenna, C., Jolivet, L., Piromallo, C., Morelli, A., 2003. Subduction and the depth of convection in the Mediterranean mantle. J. Geophys. Res. 108, 2099 (doi:10.1029–2001JB001690).
Faccenna, C., Piromallo, C., Crespo-Blanc, A., Jolivet, L., Rossetti, F., 2004. Lateral slab deformation and the origin of the western Mediterranean arcs. Tectonics 23. http://dx.doi.org/10.1029/2002TC001488.
Faccenna, C., Bellier, O., Martinod, J., Piromallo, C., Regard, V., 2006. Slab detachment beneath eastern Anatolia: a possible cause for the formation of the North Anatolian fault. Earth Planet. Sci. Lett. 242, 85–97.
Faccenna, C., Becker, T.W., Jolivet, L., Keskin, M., 2013. Mantle convection in the Middle East: reconciling Afar upwelling, Arabia indentation and Aegean trench rollback. Earth Planet. Sci. Lett. 375, 254–269.
Faccenna, C., Becker, T.W., Auer, L., Billi, A., 2014. Mantle dynamics in the Mediterranean. Rev. Geophys. 52, 283–332.
Faccenna, C., Oncken, O., Holt, A.F., Becker, T.W., 2017. Initiation of the Andean orogeny by lower mantle subduction. Earth Planet. Sci. Lett. 463, 189–201.
Fan, J.-J., LI, C., Liu, Y.-M., Xu, J.-X., 2015. Age and nature of the late Early Cretaceous Zhaga Formation, northern Tibet: constraints on when the Bangong–Nujiang Neo-Tethys Ocean closed. Int. Geol. Rev. 57, 342–353.
Fildani, A., Hessler, A.M., 2005. Stratigraphic record across a retroarc basin inversion: Rocas Verdes–Magallanes Basin, Patagonian Andes, Chile. Geol. Soc. Am. Bull. 117 (1596–20).
Flament, N., Williams, S., Müller, R.D., Gurnis, M., Bower, D.J., 2017. Origin and evolution of the deep thermochemical structure beneath Eurasia. Nat. Commun. 8, 14164.
Forte, A.M., Cowgill, E., Bernardin, T., Kreylos, O., Hamann, B., 2010. Late Cenozoic deformation of the Kura fold-thrust belt, southern Greater Caucasus. Geol. Soc. Am. Bull. 122, 465–486.
Forte, A.M., Cowgill, E., Whipple, K.X., 2014. Transition from a singly vergent to doubly vergent wedge in a young orogen: the Greater Caucasus. Tectonics 33, 2077–2101.
Fotoohi Rad, G.R., Droop, G.T.R., Amini, S., Moazzen, M., 2005. Eclogites and blueschists of the Sistan Suture Zone, eastern Iran: a comparison of P–T histories from a subduction mélange. Lithos 84, 1–24.
Fotoohi Rad, G.R., Droop, G.T.R., Burgess, R., 2009. Early Cretaceous exhumation of high-pressure metamorphic rocks of the Sistan Suture Zone, eastern Iran. Geol. J. 44, 104–116.
French, S.W., Romanowicz, B.A., 2014. Whole-mantle radially anisotropic shear velocity structure from spectral-element waveform tomography. Geophys. J. Int. 199, 1303–1327.
French, S.W., Romanowicz, B., 2015. Broad plumes rooted at the base of the Earth's mantle beneath major hotspots. Nature 525 (7567), 95–99.
Fritzell, E.H., Bull, A.L., Shephard, G.E., 2016. Closure of the Mongol–Okhotsk Ocean: insights from seismic tomography and numerical modelling. Earth Planet. Sci. Lett. 445, 1–12.
Fukao, Y., Obayashi, M., 2013. Subducted slabs stagnant above, penetrating through, and trapped below the 660 km discontinuity. J. Geophys. Res. 118, 5920–5938.
Fukao, Y., Obayashi, M., Inoue, H., Nenbai, M., 1992. Subducting slabs stagnant in the mantle transition zone. J. Geophys. Res. 97, 4809–4822.
Fukao, Y., Widiyantoro, S., Obayashi, M., 2001. Stagnant slabs in the Upper and Lower Mantle Transition Region. Rev. Geophys. 39, 291–323.
Fukao, Y., Obayashi, M., Nakakuki, T., 2009. Stagnant slab: a review. Annu. Rev. Earth Planet. Sci. 37, 19–46.
Gągała, Ł., Vergés, J., Saura, E., Malata, T., Ringenbach, J.-C., Werner, P., Krzywiec, P., 2012. Architecture and orogenic evolution of the northeastern Outer Carpathians from cross-section balancing and forward modeling. Tectonophysics 532–535, 223–241.

Gaina, C., Müller, D., 2007. Cenozoic tectonic and depth/age evolution of the Indonesian gateway and associated back-arc basins. Earth Sci. Rev. 83, 177–203.
Gaina, C., van Hinsbergen, D.J.J., Spakman, W., 2015. Tectonic interactions between India and Arabia since the Jurassic reconstructed from marine geophysics, ophiolite geology, and seismic tomography. Tectonics 34. http://dx.doi.org/10.1002/2014TC003780.
García-Casco, A., Torres-Roldan, R., Iturralde-Vinent, M.A., Trujillo, G.M., Cambra, K.E.N., Lázaro, C., Vega, A.R., 2006. High pressure metamorphism of ophiolites in Cuba. Geol. Acta 4, 63–88.
García-Casco, A., Iturralde-Vinent, M.A., Pindell, J., 2008. Latest Cretaceous collision/accretion between the Caribbean Plate and Caribeana: origin of metamorphic terranes in the Greater Antilles. Int. Geol. Rev. 50, 781–809.
Garcia-Castellanos, D., Villasenor, A., 2011. Messinian salinity crisis regulated by competing tectonics and erosion at the Gibraltar arc. Nature 480, 359–363.
Garzanti, E., Hu, X., 2015. Latest Cretaceous Himalayan tectonics: obduction, collison or Deccan-related uplift? Gondwana Res. 28, 165–178.
Gaschnig, R.M., Vervoort, J.D., Tikoff, B., Lewis, R.S., 2017. Construction and preservation of batholiths in the northern US Cordillera. Lithosphere 9 (2), 315–324.
Gehrels, G., Rusmore, M., Woodsworth, G., Crawford, M., Andronicos, C., Hollister, L., Patchett, J., Ducea, M., Butler, R., Klepeis, K., Davidson, C., 2009. U-Th-Pb geochronology of the Coast Mountains batholith in north-coastal British Columbia: constraints on age and tectonic evolution. Geol. Soc. Am. Bull. 121 (9–10), 1341–1361.
Geist, E.L., Vallier, T.L., Scholl, D.W., 1994. Origin, transport, and emplacement of an exotic island-arc terrane exposed in eastern Kamchatka, Russia. Geol. Soc. Am. Bull. 106, 1182–1194.
Ghiglione, M.C., Yagupsky, D., Ghidella, M., Ramos, A., 2008. Continental stretching preceding the opening of the Drake Passage: evidence from Tierra del Fuego. Geology 36, 643–645.
Ghose, N.C., Agrawal, O.P., Chatterjee, N., 2010. Geological and mineralogical study of eclogite and glaucophane schists in the Naga Hills Ophiolite, Northeast India. Island Arc 19, 336–356.
Giacosa, R.E., Heredia, N.C., 2004. Structure of the North Patagonian thick-skinned fold-and-thrust belt, southern central Andes, Argentina (41°–42°S). J. S. Am. Earth Sci. 18, 61–72.
Girard, J., Amulele, G., Farla, R., Mohiuddin, A., Karato, S.I., 2016. Shear deformation of bridgmanite and magnesiowüstite aggregates at lower mantle conditions. Science 351 (6269), 144–147.
Gnos, E., Immenhauser, A., Peters, T., 1997. Late Cretaceous/early Tertiary convergence between the Indian and Arabian plates recorded in ophiolites and related sediments. Tectonophysics 271, 1–19.
Gnos, E., Khan, M., Mahmood, K., Khan, A.S., Shafique, N.A., Villa, I.M., 1998. Bela oceanic lithosphere assemblage and its relation to the ReÂunion hotspot. Terra Nova 10, 90–95.
Goes, S., Cammarano, F., Hansen, U., 2004. Synthetic seismic signature of thermal mantle plumes. Earth Planet. Sci. Lett. 218 (3), 403–419.
Goes, S., Capitanio, F.A., Morra, G., 2008. Evidence of lower-mantle slab penetration phases in plate motions. Nature 451 (7181), 981–984.
Golonka, J., Bocharova, N.Y., Ford, D., Edrich, M.E., 2003. Paleogeographic reconstructions and basins development of the Arctic. Mar. Pet. Geol. 20, 211–248.
Gong, Z., Langereis, C.G., Mullender, T.A.T., 2008. The rotation of Iberia during the Aptian and the opening of the Bay of Biscay. Earth Planet. Sci. Lett. 273, 80–93.
González-León, C.M., Solari, L., Solé, J., Ducea, M.N., Lawton, T.F., Bernal, J.P., Becuar, E.G., Gray, F., Martínez, M.L., Santacruz, R.L., 2011. Stratigraphy, geochronology, and geochemistry of the Laramide magmatic arc in north-central Sonora, Mexico. Geosphere, GES00679-1.
Gorbatov, A., Kennett, B.L.N., 2003. Joint bulk-sound and shear tomography for Western Pacific subduction zones. Earth Planet. Sci. Lett. 210, 527–543.
Gorbatov, A., Widiyantoro, S., Fukao, Y., Gordeev, E., 2000. Signature of remnant slabs in the North Pacific from P-wave tomography. Geophys. J. Int. 142, 27–36.
Govers, R., Wortel, M.J.R., 2005. Lithosphere tearing at STEP faults: response to edges of subduction zones. Earth Planet. Sci. Lett. 236, 505–523.
Grand, S., van der Hilst, R.D., Widiyantoro, S., 1997. Global seismic tomography: a snapshot of convection in the earth. GSA Today 7, 1–7.
Gurnis, M., Moresi, L., Dietmar Müller, R., 2000. Models of mantle convection incorporating plate tectonics: the Australian region since the Cretaceous. In: The History and Dynamics of Global Plate Motions. Geophysical Monograph Series American Geophysical Union, Washington, D. C., pp. 211–238.
Gutiérrez-Alonso, G., Fernandez-Suarez, J., Weil, A.B., Brendan Murphy, J., Damian Nance, R., Corfu, F., Johnston, S.T., 2008. Self-subduction of the Pangaean global plate. Nat. Geosci. 1, 549–553.
Gutscher, M.A., Malod, J., Rehault, J.P., Contrucci, I., Klingelhoefer, F., Mendes-Victor, L., Spakman, W., 2002. Evidence for active subduction beneath Gibraltar. Geology 30, 1071–1074.
Hacker, B.R., 1990. Simulation of the metamorphic and deformational history of the metamorphic sole of the Oman ophiolite. J. Geophys. Res. 95, 4895–4907.
Hacker, B.R., 1994. Rapid emplacement of young oceanic lithosphere: argon geochronology of the Oman ophiolite. Science 265, 1563–1565.
Hacker, B.R., Mosenfelder, J.L., Gnos, E., 1996. Rapid emplacement of the Oman ophiolite: thermal and geochronologic constraints. Tectonics 15, 1230–1247.
Hadlari, T., Midwinter, D., Poulton, T.P., Matthews, A., 2017. A Pangean rim of fire: Reviewing the Triassic of western Laurentia. Lithosphere L643-1.
Hafkenscheid, E., Buiter, S.J.H., Wortel, M.J.R., Spakman, W., Bijwaard, H., 2001. Modelling the seismic velocity structure beneath Indonesia: a comparison with tomography. Tectonophysics 333, 35–46.
Hafkenscheid, E., Wortel, M.J.R., Spakman, W., 2006. Subduction history of the Tethyan region derived from seismic tomography and tectonic reconstructions. J. Geophys. Res. 111, B08401 (doi: 10.1029–2005JB003791).
Hager, B.H., Clayton, R.W., Richards, M.A., Comer, R.P., Dziewonski, A.M., 1984. Lower Mantle Heterogeneity, Dynamic Topography and the Geoid.
Hall, R., 2002. Cenozoic geological and plate tectonic evolution of SE Asia and the SW Pacific: computer-based reconstructions, model and animations. J. Asian Earth Sci. 20, 353–431.
Hall, R., 2012. Late Jurassic–Cenozoic reconstructions of the Indonesian region and the Indian Ocean. Tectonophysics 570–571, 1–41.
Hall, R., Spakman, W., 2002. Subducted slabs beneath the eastern Indonesia-Tonga region: insights from tomography. Earth Planet. Sci. Lett. 201, 321–336.
Hall, R., Spakman, W., 2004. Mantle structure and tectonic evolution of the region north and east of Australia. Geol. Soc. Aust. Spec. Publ. 22, 361–381.
Hall, R., Spakman, W., 2015. Mantle structure and tectonic history of SE Asia. Tectonophysics 658, 14–45.
Hall, R., van Hattum, M.W.A., Spakman, W., 2008. Impact of India–Asia collision on SE Asia: the record in Borneo. Tectonophysics 451, 366–389.
Handy, M.R., Schmid, S.M., Bousquet, R., Kissling, E., Bernoulli, D., 2010. Reconciling plate-tectonic reconstructions of Alpine Tethys with the geological–geophysical record of spreading and subduction in the Alps. Earth Sci. Rev. 102, 121–158.
Handy, M.R., Ustaszewski, K., Kissling, E., 2014. Reconstructing the Alps–Carpathians–Dinarides as a key to understanding switches in subduction polarity, slab gaps and surface motion. Int. J. Earth Sci. 104, 1–26.
He, Y., Wen, L., 2009. Structural features and shear-velocity structure of the "Pacific Anomaly". J. Geophys. Res. 114, B02309–17 (doi: 10.1029/2008JB005r814).
Hébert, R., Bezard, R., Guilmette, C., Dostal, J., Wang, C., Liu, Z.F., 2012. The Indus–Yarlung Zangbo ophiolites from Nanga Parbat to Namche Barwa syntaxes, southern Tibet: first synthesis of petrology, geochemistry, and geochronology with incidences on geodynamic reconstructions of Neo-Tethys. Gondwana Res. 22, 377–397.
Hoisch, T.D., Wells, M.L., Beyene, M.A., Styger, S., Vervoort, J.D., 2014. Jurassic Barrovian metamorphism in a western U.S. Cordilleran metamorphic core complex, Funeral Mountains, California. Geology 42, 399–402.
Holm, R.J., Spandler, C., Richards, S.W., 2013. Melanesian arc far-field response to collision of the Ontong Java Plateau: Geochronology and petrogenesis of the Simuku Igneous Complex, New Britain, Papua New Guinea. Tectonophysics 603, 189–212.
Homke, S., Verges, J., Serra-Kiel, J., Bernaola, G., Sharp, I.R., Garcés, M., Monetro-Verdu, I., Karpuz, R.H., G., M., 2009. Late Cretaceous–Paleocene formation of the proto-Zagros foreland basin, Lurestan Province, SW Iran. Geol. Soc. Am. Bull. 121, 963–978.
Honda, S., 2016. Slab stagnation and detachment under northeast China. Tectonophysics 671, 127–138.
Horvath, F., Bada, G., Szafian, P., Tari, G., Adam, A., Cloetingh, S., 2006. Formation and deformation of the Pannonian Basin: constraints from observational data. Geol. Soc. Lond. Mem. 32, 191–206.
Hourigan, J.K., Brandon, M.T., Soloviev, A.V., Kirmasov, A.B., Garver, J.I., Stevenson, J., Reiners, W., 2009. Eocene arc-continent collision and crustal consolidation in Kamchatka, Russian Far East. Am. J. Sci. 309, 333–396.
Huang, J., Zhao, D., 2006. High-resolution mantle tomography of China and surrounding regions. J. Geophys. Res. 111, B09305 (doi: 10.1029–2005JB004066).
Huang, H.-H., Wu, Y.-M., Song, X., Chang, C.-H., Lee, S.-J., Chang, T.-M., Hsieh, H.-H., 2014. Joint Vp and Vs tomography of Taiwan: implications for subduction-collision orogeny. Earth Planet. Sci. Lett. 392, 177–191.
Huang, W., van Hinsbergen, D.J.J., Maffione, M., Orme, D.A., Dupont-Nivet, G., Guilmette, C., Ding, L., Guo, Z., Kapp, P., 2015. Lower Cretaceous Xigaze ophiolites formed in the Gangdese forearc: evidence from paleomagnetism, sediment provenance, and stratigraphy. Earth Planet. Sci. Lett. 415, 142–153.
Humphreys, E., 2009. Relation of flat subduction to magmatism and deformation in the western United States. Geol. Soc. Am. Mem. 204, 85–98.
Hüsing, S.K., Zachariasse, W.J., van Hinsbergen, D.J.J., Krijgsman, W., Inceoz, M., Harzhauser, M., Mandic, O., Kroh, A., 2009. Oligocene-Miocene basin evolution in SE Anatolia, Turkey: constraints on the closure of the eastern Tethys gateway. Geol. Soc. Lond., Spec. Publ. 311, 107–132.
Hutko, A.R., Lay, T., Garnero, E.J., Revenaugh, J., 2006. Seismic detection of folded subducted lithosphere at the core-mantle boundary. Nature 441, 333–336.
Ishizuka, O., Tani, K., Reagan, M.K., Kanayama, K., Umino, S., Harigane, Y., Sakamoto, I., Miyajima, Y., Yuasa, M., Dunkley, D.J., 2011. The timescales of subduction initiation and subsequent evolution of an oceanic island arc. Earth Planet. Sci. Lett. 306, 229–240.
Isozaki, Y., Aoki, K., Nakama, T., Yanai, S., 2010. New insight into a subduction-related orogen: a reappraisal of the geotectonic framework and evolution of the Japanese Islands. Gondwana Res. 18, 82–105.
Iturralde-Vinent, M.A., Díaz-Otero, C., García-Casco, A., van Hinsbergen, D.J.J., 2008. Paleogene foreland basin deposits of North-Central Cuba: a record of arc-continent collision between the Caribbean and North American plates. Int. Geol. Rev. 50, 863–884.
Jackson, J., Priestley, K., Allen, M.B., Berberian, M., 2002. Active tectonics of the South Caspian Basin. Geophys. J. Int. 148, 214–245.
Jagoutz, O., Royden, L., Holt, A.F., Becker, T.W., 2015. Anomalously fast convergence of India and Eurasia caused by double subduction. Nat. Geosci. 8, 475–478.
Jahn-Awe, S., Froitzheim, N., Nagel, T.J., Frei, D., Georgiev, N., Pleuger, J., 2010. Structural and geochronological evidence for Paleogene thrusting in the Western Rhodopes (SW Bulgaria): elements for a new tectonic model of the Rhodope Metamorphic Province. Tectonics 29, TC3008 (doi: 10.1029–2009TC002558).
Jaxybulatov, K., Koulakov, I., Dobretsov, N.L., 2013. Segmentation of the Izu-Bonin and Mariana slabs based on the analysis of the Benioff seismicity distribution and regional

tomography results. Solid Earth 4, 59–73.
Ji, W.-Q., Wu, F.-Y., Chung, S.-L., Li, J.-X., Liu, C.-Z., 2009. Chem. Geol. 262, 229–245.
Jiang, G., Zhao, D., Zhang, G., 2009. Seismic tomography of the Pacific slab edge under Kamchatka. Tectonophysics 465, 190–203.
Jicha, B.R., Scholl, D.W., Singer, B.S., Yogodzinski, G.M., Kay, S.M., 2006. Revised age of Aleutian Island Arc formation implies high rate of magma production. Geology 34, 661–664.
Johnston, S.T., Borel, G.D., 2007. The odyssey of the Cache Creek terrane, Canadian Cordillera: implications for accretionary orogens, tectonic setting of Panthalassa, the Pacific superwell, and break-up of Pangea. Earth Planet. Sci. Lett. 253, 415–428.
Jolivet, L., Brun, J.-P., 2010. Cenozoic geodynamic evolution of the Aegean. Int. J. Earth Sci. 99, 109–138.
Jolivet, L., Faccenna, C., Piromallo, C., 2009. From mantle to crust: Stretching the Mediterranean. Earth Planet. Sci. Lett. 285, 198–209.
Jones, R.E., De Hoog, J.C.M., Kirstein, L.A., Kasemann, S.A., Hinton, R., Elliott, T., Litvak, D., EIMF, 2014. Temporal variations in the influence of the subducting slab on Central Andean arc magmas: evidence from boron isotope systematics. Earth Planet. Sci. Lett. 408, 390–401.
Jourdan, S., Bernet, M., Tricart, P., Hardwick, E., Paquette, J.L., Guillot, S., Dumont, T., Schwartz, S., 2013. Short-lived, fast erosional exhumation of the internal western Alps during the late early Oligocene: constraints from geothermochronology of pro- and retro-side foreland basin sediments. Lithosphere 5, 211–225.
Kakar, M.I., Collins, A.S., Mahmood, K., Foden, J.D., Khan, M., 2012. U-Pb zircon crystallization age of the Muslim Bagh ophiolite: enigmatic remains of an extensive pre-Himalayan arc. Geology 40, 1099–1102.
Kalyoncuoğlu, Ü.Y., Elitok, Ö., Dolmaz, M.N., Anadolu, N.C., 2011. Geophysical and geological imprints of southern Neotethyan subduction between Cyprus and the Isparta Angle, SW Turkey. J. Geodyn. 52, 70–82.
Kaneshima, S., 2013. Lower mantle seismic scatterers below the subducting Tonga slab: evidence for slab entrainment of transition zone materials. Phys. Earth Planet. Inter. 222, 35–46.
Kaneshima, S., Helffrich, G., 2010. Small scale heterogeneity in the mid-lower mantle beneath the circum-Pacific area. Phys. Earth Planet. Inter. 183, 91–103.
Kapp, P., Murphy, M.A., Yin, A., Harrison, T.M., Ding, L., Guo, J., 2003. Mesozoic and Cenozoic tectonic evolution of the Shiquanhe area of western Tibet. Tectonics 22. http://dx.doi.org/10.1029/2001TC001332.
Kapp, P., DeCelles, G., Gehrels, G.E., Heizler, M., Ding, L., 2007. Geological records of the Cretaceous Lhasa-Qiangtang and Indo-Asian collisions in the Nima basin area, central Tibet. Geol. Soc. Am. Bull. 119, 917–933.
Karamata, S., 2006. The geological development of the Balkan Peninsula related to the approach, collision and compression of Gondwanan and Eurasian units. Geol. Soc. Lond., Spec. Publ. 260, 155–178.
Karaoğlan, F., Parlak, O., Klötzli, U., Thoni, M., Koller, F., 2012. U–Pb and Sm–Nd geochronology of the Kızıldağ (Hatay, Turkey) ophiolite: implications for the timing and duration of suprasubduction zone type oceanic crust formation in the southern Neotethys. Geol. Mag. 150, 283–299.
Karaoğlan, F., Parlak, O., Klötzli, U., Thoni, M., Koller, F., 2014. U–Pb and Sm–Nd geochronology of the ophiolites from the SE Turkey: implications for the Neotethyan evolution. Geodin. Acta 25, 146–161.
Karato, S.I., 2010. Rheology of the Earth's mantle: a historical review. Gondwana Res. 18 (1), 17–45.
Kashiwagi, H., 2016. Atmospheric carbon dioxide and climate change since the Late Jurassic (150 Ma) derived from a global carbon cycle model. Palaeogeogr. Palaeoclimatol. Palaeoecol. 454, 82–90. http://dx.doi.org/10.1016/j.palaeo.2016.04.002.
Kaymakci, N., Inceöz, M., Ertepinar, P., Koç, A., 2010. Late Cretaceous to Recent kinematics of SE Anatolia (Turkey). Geol. Soc. Lond., Spec. Publ. 340, 409–435.
Kellogg, J.N., Bonini, W.E., 1982. Subduction of the Caribbean plate and basement uplifts in the overriding South American plate. Tectonics 1, 251–276.
Kerr, R.C., Lister, J.R., 1991. The effects of shape on crystal settling and on the rheology of magmas. J. Geol. 99 (3), 457–467.
Keskin, M., 2003. Magma generation by slab steepening and breakoff beneath a subduction-accretion complex: an alternative model for collision-related volcanism in Eastern Anatolia, Turkey. Geophys. Res. Lett. 30, 8046 (doi: 10.1029–2003GL018019).
Khan, I., Clyde, W., 2013. Lower Paleogene tectonostratigraphy of Balochistan: evidence for time-transgressive Late Paleocene-Early Eocene uplift. Geosciences 3, 466–501.
King, S.D., 2016a. An evolving view of transition zone and midmantle viscosity. Geochem. Geophys. Geosyst. 17, 1234–1237.
King, S.D., 2016b. Reconciling laboratory and observational models of mantle rheology in geodynamic modelling. J. Geodyn. 100, 33–50.
Kissling, E., 1993. Deep structure of the Alps—what do we really know? Phys. Earth Planet. Inter. 79, 87–112.
Kissling, E., 2008. Deep structure and tectonics of the Valais—and the rest of the Alps. Bull. Angewandte Geologie 13, 3–10.
Kissling, E., Spakman, W., 1996. Interpretation of tomographic images of uppermost mantle structure: examples from the Western and Central Alps. J. Geodyn. 21, 97–111.
Kito, T., Rost, S., Thomas, C., Garnero, E.J., 2007. New insights into the P- and S-wave velocity structure of the D″ discontinuity beneath the Cocos Plate. Geophys. J. Int. 169, 631–645.
Kito, T., Thomas, C., Rietbrock, A., Garnero, E.J., Nippress, S.E.J., Heath, A.E., 2008. Seismic evidence for a sharp lithospheric base persisting to the lowermost mantle beneath the Caribbean. Geophys. J. Int. 174, 1019–1028.
Knesel, K.M., Cohen, B.E., Vasconcelos, M., Thiede, D.S., 2008. Rapid change in drift of the Australian plate records collision with Ontong Java plateau. Nature 454, 754–757.
Ko, J.Y.T., Hung, S.H., Kuo, B.Y., Zhao, L., 2017. Seismic evidence for the depression of the D″ discontinuity beneath the Caribbean: implication for slab heating from the Earth's core. Earth Planet. Sci. Lett. 467, 128–137.
Koç, A., Kaymakci, N., van Hinsbergen, D.J.J., Vissers, R.L.M., 2016. A Miocene onset of the modern extensional regime in the Isparta Angle: constraints from the Yalvaç Basin (southwest Turkey). Int. J. Earth Sci. 434, 75–90.
Koglin, N., Kostopoulos, D., Reischmann, T., 2009. Geochemistry, petrogenesis and tectonic setting of the Samothraki mafic suite, NE Greece: trace-element, isotopic and zircon age constraints. Tectonophysics 473, 53–68.
König, M., Jokat, W., 2006. The Mesozoic breakup of the Weddell Sea. J. Geophys. Res. 111, B12102.
Konstantinovskaia, E.A., 2001. Arc-continent collision and subduction reversal in the Cenozoic evolution of the Northwest Pacifc: an example from Kamchatka (NE Russia). Tectonophysics 333, 75–94.
Koop, W., Stoneley, R., 1982. Subsidence history of the Middle East Zagros Basin: Permian to recent. Philos. Trans. R. Soc. Lond. A 305, 149–168.
Koulakov, I., 2011. High-frequency P and S velocity anomalies in the upper mantle beneath Asia from inversion of worldwide traveltime data. J. Geophys. Res. 116, B04301. http://dx.doi.org/10.1029/2010JB007938.
Koulakov, I., 2013. Studying deep sources of volcanism using multiscale seismic tomography. J. Volcanol. Geotherm. Res. 257, 205–226.
Koulakov, I.Y., Dobretsov, N., Bushenkova, N., Yakovlev, A.V., 2011. Slab shape in subduction zones beneath the Kurile–Kamchatka and Aleutian arcs based on regional tomography results. Russ. Geol. Geophys. 52, 650–667.
Koulakov, I., Zabelina, I., Amanatashvili, I., Meskhia, V., 2012. Nature of orogenesis and volcanism in the Caucasus region based on results of regional tomography. Solid Earth 3, 327–337.
Koulakov, I., Wu, Y.-M., Huang, H.-H., Dobretsov, N., Jakovlev, A., Zabelina, I., Jaxybulatov, K., Chervov, V., 2014. Slab interactions in the Taiwan region based on the P- and S-velocity distributions in the upper mantle. J. Asian Earth Sci. 79, 53–64.
Kovalenko, D.V., 2003. Paleomagnetism of geological complexes of Kamchatka and Southern Koryakia. In: Tectonic and Geophysical Interpretation [in Russian]. Nauchnyi Mir, Moscow.
Kufner, S.K., Schurr, B., Sippl, C., Schneider, F., Yuan, X., Ischuk, A., Arib, A., Murodkulov, S., Haberland, C., Mechie, J., Bianchi, M., Tilmann, F., 2014. Evidence for deeply subducting Asian lithosphere beneath the Pamir-Hindu Kush region from lithospheric imaging. Geophys. Res. Abstr. 16 (EGU2014–3412–3).
Kufner, S.-K., Schurr, B., Sippl, C., Yuan, X., Ratschbacher, L., Akbar, A.S.O.M., Ischuk, A., Murodkulov, S., Schneider, F., Mechie, J., Tilmann, F., 2016. Deep India meets deep Asia: lithospheric indentation, delamination and break-off under Pamir and Hindu Kush (Central Asia). Earth Planet. Sci. Lett. 435, 171–184.
Lallemand, S., Font, Y., Bijwaard, H., Kao, H., 2001. New insights on 3-D plates interaction near Taiwan from tomography and tectonic implications. Tectonophysics 335, 229–253.
Lambeck, K., Smither, C., Johnston, P., 1998. Sea-level change, glacial rebound and mantle viscosity for northern Europe. Geophys. J. Int. 134 (1), 102–144.
Lambeck, K., Rouby, H., Purcell, A., Sun, Y., Sambridge, M., 2014. Sea level and global ice volumes from the Last Glacial Maximum to the Holocene. Proc. Natl. Acad. Sci. 111 (43), 15296–15303.
Lau, H.C., Mitrovica, J.X., Austermann, J., Crawford, O., Al-Attar, D., Latychev, K., 2016. Inferences of mantle viscosity based on ice age data sets: radial structure. J. Geophys. Res. Solid Earth 121 (10), 6991–7012.
Layer, W., Newberry, R., Fujita, K., Parfenov, L., Trunilina, V., Bakharev, A., 2001. Tectonic setting of the plutonic belts of Yakutia, northeast Russia, based on $^{40}A/^{39}Ar$ geochronology and trace element geochemistry. Geology 29, 167–170.
Lefebvre, C., Meijers, M.J.M., Kaymakci, N., Peynircioğlu, A., Langereis, C.G., van Hinsbergen, D.J.J., 2013. Reconstructing the geometry of central Anatolia during the late Cretaceous: large-scale Cenozoic rotations and deformation between the Pontides and Taurides. Earth Planet. Sci. Lett. 366, 83–98.
Lei, J., 2012. Upper-mantle tomography and dynamics beneath the North China Craton. J. Geophys. Res. 117, B06313 (doi: 10.1029–2012JB009212).
Lei, J., Zhao, D., 2007. Teleseismic evidence for a break-off subducting slab under Eastern Turkey. Earth Planet. Sci. Lett. 257, 14–28.
Lekic, V., Cottaar, S., Dziewonski, A., Romanowicz, B., 2012. Cluster analysis of global lower mantle tomography: a new class of structure and implications for chemical heterogeneity. Earth Planet. Sci. Lett. 357–358. http://dx.doi.org/10.1016/j.epsl.2012.09.014.
Leng, W., Gurnis, M., 2012. Shape of thermal plumes in a compressible mantle with depth-dependent viscosity. Geophys. Res. Lett. 39 (5).
Levashova, N.M., 1999. Kinematics of Late Cretaceous and Cretaceous–Paleogene Oceanic Island Arcs [in Russian], Author's Abstract. (Candidate Thesis. GIN RAN).
Levashova, N.M., Shapiro, M.N., Beniamovsky, V.N., Bazhenov, M.L., 2000. Paleomagnetism and geochronology of the Late Cretaceous-Paleogene island arc complex of the Kronotsky Peninsula, Kamchatka, Russia: kinematic implications. Tectonics 19 (5), 834–851.
Li, Z.-X., Li, X.-H., 2007. Formation of the 1300-km-wide intracontinental orogen and postorogenic magmatic province in Mesozoic South China: a flat-slab subduction model. Geology 35, 179–182.
Li, C., van der Hilst, R.D., 2010. Structure of the upper mantle and transition zone beneath Southeast Asia from traveltime tomography. J. Geophys. Res. 115, B07308 (doi: 10.1029–2009JB006882).
Li, C., van der Hilst, R.D., Meltzer, A.S., Engdahl, E.R., 2008. Subduction of the Indian lithosphere beneath the Tibetan Plateau and Burma. Earth Planet. Sci. Lett. 274, 157–168.
Li, Z.-X., Li, X.-H., Chung, S.-L., Lo, C.-H., Xu, X., Li, W.-X., 2012. Magmatic switch-on and

switch-off along the South China continental margin since the Permian: transition from an Andean-type to a Western Pacific-type plate boundary. Tectonophysics 532–535, 271–290.
Li, J., Zhang, Y., Dong, S., Johnston, S.T., 2014a. Cretaceous tectonic evolution of South China: a preliminary synthesis. Earth Sci. Rev. 134, 98–136.
Li, S.-M., Zhu, D.-C., Wang, Q., Zhao, Z.-D., Sui, Q.-L., Liu, S.-A., Liu, D., Mo, X.-X., 2014b. Northward subduction of Bangong–Nujiang Tethys: insight from Late Jurassic intrusive rocks from Bangong Tso in western Tibet. Lithos 205, 284–297.
Li, Z., Qiu, J.-S., Yang, X.-M., 2014c. A review of the geochronology and geochemistry of Late Yanshanian (Cretaceous) plutons along the Fujian coastal area of southeastern China: implications for magma evolution related to slab break-off and rollback in the Cretaceous. Earth Sci. Rev. 128, 232–248.
Li, Z., Ding, L., Lippert, C., Song, P., Yue, Y., van Hinsbergen, D.J.J., 2016. Paleomagnetic constraints on the Mesozoic drift of the Lhasa terrane (Tibet) from Gondwana to Eurasia. Geology 44, 727–730.
Li, S., Guilmette, C., Ding, L., Xu, Q., Fu, J.J., Yue, Y.H., 2017. Provenance of Mesozoic clastic rocks within the Bangong-Nujiang suture zone, central Tibet: Implications for the age of the initial Lhasa-Qiangtang collision. J. Asian Earth Sci. 147, 469–484.
Liati, A., Gebauer, D., Fanning, C.M., 2004. The age of ophiolitic rocks of the Hellenides (Vourinos, Pindos, Crete): first U–Pb ion microprobe (SHRIMP) zircon ages. Chem. Geol. 207, 171–188.
Lippitsch, R., Kissling, E., Ansorge, J., 2003. Upper mantle structure beneath the Alpine orogen from high-resolution teleseismic tomography. J. Geophys. Res. 108, 2376 (doi: 10.1029–2002Jb002016).
Lister, G., Kennett, B., Richards, S., Forster, M., 2008. Boudinage of a stretching slablet implicated in earthquakes beneath the Hindu Kush. Nat. Geosci. 1, 196–201. http://dx.doi.org/10.1038/ngeo132.
Lister, G.S., White, L.T., Hart, S., Forster, M.A., 2012. Ripping and tearing the rolling-back New Hebrides slab. Aust. J. Earth Sci. 59-6, 899–911. http://dx.doi.org/10.1080/08120099.2012.686454.
Lithgow-Bertelloni, C., Richards, M.A., 1998. The dynamics of Cenozoic and Mesozoic plate motions. Rev. Geophys. 36 (1), 27–78.
Liu, L., 2014. Constraining Cretaceous subduction polarity in eastern Pacific from seismic tomography and geodynamic modeling. Geophys. Res. Lett. 41, 8029–8036.
Liu, L., Stegman, D.R., 2011. Segmentation of the Farallon slab. Earth Planet. Sci. Lett. 311, 1–10.
Liu, L., Spasojevic, S., Gurnis, M., 2008. Reconstructing Farallon Plate subduction beneath North America back to the Late Cretaceous. Science 322, 934–938.
Liu, D., Huang, Q., Fan, S., Zhang, L., Shi, R., Ding, L., 2013. Subduction of the Bangong-Nujiang Ocean: constraints from granites in the Bangong Co area, Tibet. Geol. J. 49, 188–206.
Livermore, R., Hillenbrand, C.-D., Meredith, M., Eagles, G., 2007. Drake Passage and Cenozoic climate: an open and shut case? Geochem. Geophys. Geosyst. 8. http://dx.doi.org/10.1029/2005GC001224.
Lodolo, E., Donda, F., Tassone, A., 2006. Western Scotia Sea margins: improved constraints on the opening of the Drake Passage. J. Geophys. Res. 111. http://dx.doi.org/10.1029/2006JB004361. (B06101–14).
Lonergan, L., White, N., 1997. Origin of the Betic-Rif mountain belt. Tectonics 16, 504–522.
Long, M.D., 2016. The Cascadia Paradox: mantle flow and slab fragmentation in the Cascadia subduction system. J. Geodyn. 102, 151–170.
Lucente, F.P., Speranza, F., 2001. Belt bending driven by lateral bending of subducting lithospheric slab: geophysical evidences from the northern Apennines (Italy). Tectonophysics 337, 53–64.
Lucente, F.P., Chiarabba, C., Cimini, G.B., Giardini, D., 1999. Tomographic constraints on the geodynamic evolution of the Italian region. J. Geophys. Res. 104, 20307–20327.
Lustrino, M., Morra, V., Fedele, L., Franciosi, L., 2009. Beginning of the Apennine subduction system in central western Mediterranean: constraints from Cenozoic "orogenic" magmatic activity of Sardinia, Italy. Tectonics 28, TC5016 (doi: 10.1029–2008TC002419).
Luyendyk, B.P., 1995. Hypothesis for Cretaceous rifting of east Gondwana caused by subducted slab capture. Geology 23, 373–376.
Ma, X., Sun, X., Wiens, D.A., Wen, L., Nyblade, A., Anandakrishnan, S., Aster, R., Huerta, A., Wilson, T., 2016. Strong seismic scatterers near the core–mantle boundary north of the Pacific Anomaly. Phys. Earth Planet. Inter. 253, 21–30.
Maffione, M., Thieulot, C., van Hinsbergen, D.J.J., Morris, A., Plumper, O., Spakman, W., 2015a. Dynamics of intraoceanic subduction initiation: 1. Oceanic detachment fault inversion and the formation of supra-subduction zone ophiolites. Geochem. Geophys. Geosyst. 16, 1753–1770.
Maffione, M., van Hinsbergen, D.J.J., Koornneef, L.M.T., Guilmette, C., Hodges, K., Borneman, N., Huang, W., Ding, L., Kapp, P., 2015b. Forearc hyperextension dismembered the south Tibetan ophiolites. Geology 43, 475–478.
Maffione, M., van Hinsbergen, D., de Gelder, G.I.N.O., van der Goes, F., Morris, A., 2017. Kinematics of subduction initiation in the Neo-Tethys Ocean during the Late Cretaceous reconstructed from ophiolites of Turkey, Cyprus, and Syria. J. Geophys. Res (in press).
Magganas, A., Sideris, C., Kokkinakis, A., 1991. Marginal basin—volcanic arc origin of metabasic rocks of the Circum-Rhodope Belt, Thrace, Greece. Mineral. Petrol. 44, 235–252.
Maggi, A., Priestley, K., 2005. Surface waveform tomography of the Turkish-Iranian plateau. Geophys. J. Int. 160, 1068–1080.
Mahmood, K., Boudier, F., Gnos, E., Monié, P., Nicolas, A., 1995. $^{40}Ar/^{39}Ar$ dating of the emplacement of the Muslim Bagh ophiolite, Pakistan. Tectonophysics 250, 169–181.
Marquardt, H., Miyagi, L., 2015. Slab stagnation in the shallow lower mantle linked to an increase in mantle viscosity. Nat. Geosci. 8, 311–314. http://dx.doi.org/10.1038/ngeo2393.
Martin, A.K., 2007. Gondwana breakup via double-saloon-door rifting and seafloor spreading in a backarc basin during subduction rollback. Tectonophysics 445, 245–272.
Martini, M., Mori, L., Solari, L., Centeno-García, E., 2011. Sandstone Provenance of the Arperos Basin (Sierra de Guanajuato, Central Mexico): Late Jurassic–Early Cretaceous Back-Arc Spreading as the Foundation of the Guerrero Terrane. J. Geol. 119, 597–617.
Martini, M., Solari, L., Camprubi, A., 2013. Kinematics of the Guerrero terrane accretion in the Sierra de Guanajuato, central Mexico: new insights for the structural evolution of arc–continent collisional zones. Int. Geol. Rev. 55, 574–589.
Martin-Short, R., Allen, R.M., Bastow, I.D., 2016. Subduction geometry beneath south central Alaska and its relationship to volcanism. Geophys. Res. Lett. 43. http://dx.doi.org/10.1002/2016GL070580.
Matenco, L., Bertotti, G., 2000. Tertiary tectonic evolution of the external East Carpathians (Romania). Tectonophysics 316, 255–286.
Matenco, L., Radivojević, D., 2012. On the formation and evolution of the Pannonian Basin: constraints derived from the structure of the junction area between the Carpathians and Dinarides. Tectonics 31. http://dx.doi.org/10.1029/2012TC003206.
Matenco, L., Bertotti, G., Cloetingh, S., Dinu, C., 2003. Subsidence analysis and tectonic evolution of the external Carpathian–Moesian Platform region during Neogene times. Sediment. Geol. 156, 71–94.
Matthews, K.J., Williams, S.E., Whittaker, J.M., Müller, R.D., Seton, M., Clarke, G.L., 2015. Geologic and kinematic constraints on Late Cretaceous to mid Eocene plate boundaries in the southwest Pacific. Earth Sci. Rev. 140, 72–107.
Maurin, T., Rangin, C., 2009. Structure and kinematics of the Indo-Burmese Wedge: recent and fast growth of the outer wedge. Tectonics 28, TC2010 (doi: 10.1029–2008TC002276).
Meffre, S., Falloon, T.J., Crawford, T.J., Hoernle, K., Hauff, F., Duncan, R.A., Bloomer, S.H., Wright, D.J., 2012. Basalts erupted along the Tongan fore arc during subduction initiation: Evidence from geochronology of dredged rocks from the Tonga fore arc and trench. Geochem. Geophys. Geosyst. 13. http://dx.doi.org/10.1029/2012GC004335.
Meijers, M.J.M., Kaymakci, N., van Hinsbergen, D.J.J., Langereis, C.G., Stephenson, R.A., Hippolyte, J.-C., 2010. Late Cretaceous to Paleocene oroclinal bending in the central Pontides (Turkey). Tectonics 29, TC4016 (doi: 10.1029–2009TC002620).
Meschede, M., Frisch, W., 1998. A plate-tectonic model for the Mesozoic and Early Cenozoic history of the Caribbean plate. Tectonophysics 296, 269–291.
Michard, A., Negro, F., Saddiqi, O., Bouybaouene, M.L., Chalouan, A., Montigny, R., Goffé, B., 2006. Pressure–temperature–time constraints on the Maghrebide mountain building: evidence from the Rif–Betic transect (Morocco, Spain), Algerian correlations, and geodynamic implications. Compt. Rendus Geosci. 338, 92–114.
Milidragovic, D., Joyce, N.L., Zagorevski, A., Chapman, J.B., 2016. Petrology of explosive Middle-Upper Triassic ultramafic rocks in the Mess Creek area, northern Stikine terrane. In: Geological Fieldwork 2015, British Columbia Ministry of Energy and Mines, British Columbia Geological Survey Paper 2016-1, pp. 95–111.
Miller, M.S., Kennett, B.L.N., 2006. Evolution of mantle structure beneath the northwest Pacific: Evidence from seismic tomography and paleogeographic reconstructions. Tectonics 25, 1–14.
Miller, M.S., Kennett, B.L.N., Lister, G.S., 2004. Imaging changes in morphology, geometry, physical properties of the subducting Pacific plate along the Izu–Bonin–Mariana arc. Earth Planet. Sci. Lett. 224, 363–370.
Miller, M.S., Gorbatov, A., Kennett, B.L.N., 2005. Heterogeneity within the subducting Pacific slab beneath the Izu–Bonin–Mariana arc: evidence from tomography using 3D ray tracing inversion techniques. Earth Planet. Sci. Lett. 235, 331–342.
Miller, M.S., Gorbatov, A., Kennett, B.L.N., 2006. Three-dimensional visualization of a near-vertical slab tear beneath the southern Mariana arc. Geochem. Geophys. Geosyst. 7. http://dx.doi.org/10.1029/2005GC001110.
Mills, B., Daines, S.J., Lenton, T.M., 2014. Changing tectonic controls on the long-term carbon cycle from Mesozoic to present. Geochem. Geophys. Geosyst. 15. http://dx.doi.org/10.1002/2014GC005530.
Mitrovica, J.X., Forte, A.M., 2004. A new inference of mantle viscosity based upon joint inversion of convection and glacial isostatic adjustment data. Earth Planet. Sci. Lett. 225 (1), 177–189.
Mohammadi, A., Burg, J.-P., Bouilhol, P., Ruh, J., 2016. U–Pb geochronology and geochemistry of Zahedan and Shah Kuh plutons, southeast Iran: implication for closure of the South Sistan suture zone. Lithos 248–251, 293–308.
Moix, P., Beccaletto, L., Kozur, H.W., Hochard, C., Rosselet, F., Stampfli, G.M., 2008. A new classification of the Turkish terranes and sutures and its implication for the paleotectonic history of the region. Tectonophysics 451, 7–39.
Morley, C.K., 2002. A tectonic model for the Tertiary evolution of strike–slip faults and rift basins in SE Asia. Tectonophysics 347, 189–215.
Morra, G., Yuen, D.A., Boschi, L., Chatelain, P., Koumoutsakos, P., Tackley, P.J., 2010. The fate of the slabs interacting with a density/viscosity hill in the mid-mantle. Phys. Earth Planet. Inter. 180 (3), 271–282.
Morris, A., Erson, M.W., Robertson, A.H., Al-Riyami, K., 2002. Extreme tectonic rotations within an eastern Mediterranean ophiolite (Baër–Bassit, Syria). Earth Planet. Sci. Lett. 202, 247–261.
Mortensen, J.K., Hall, B.V., Bissig, T., Friedman, R.M., Danielson, T., Oliver, J., Rhys, D.A., Ross, K.V., Gabites, J.E., 2008. Age and Paleotectonic setting of volcanogenic massive sulfide deposits in the Guerrero Terrane of Central Mexico: constraints from U-Pb age and Pb isotope studies. Econ. Geol. 103, 117–140.
Müller, R.D., Sdrolias, M., Gaina, C., Roest, W.R., 2008. Age, spreading rates, and spreading asymmetry of the world's ocean crust. Geochem. Geophys. Geosyst. 9, Q04006 (doi: 10.1029–2007GC001743).
Müller, R.D., Seton, M., Zahirovic, S., Williams, S.E., Matthews, K.J., Wright, N.M.,

Shephard, G.E., Maloney, K.T., Barnett-Moore, N., Hosseinpour, M., Bower, D.J., Cannon, J.S., 2016. Ocean basin evolution and global-scale plate reorganization events since pangea breakup. Annu. Rev. Earth Planet. Sci. 44, 107–138.
Mumladze, T., Forte, A.M., Cowgill, E.S., Trexler, C.C., Niemi, N.A., Yıkılmaz, M.B., Kellogg, L.H., 2015. Subducted, detached, torn slabs beneath the Greater Caucasus. GEORESJ 5, 36–46.
Munizaga, F., Hervé, F., Drake, R.E., Pankhurst, R.J., Brook, M., Snelling, N., 2002. Geochronology of the Lake Region of south-central Chile (39°–42°S): preliminary results. J. S. Am. Earth Sci. 1, 309–316.
Muttoni, G., Mattei, M., Balini, M., Zanchi, A., Gaetani, M., Berra, F., 2009. The drift history of Iran from the Ordovician to the Triassic. Geol. Soc. Lond., Spec. Publ. 312, 7–29.
Best, M.G., Christiansen, E.H., 1991. Limited extension during peak Tertiary volcanism, Great Basin of Nevada and Utah. J. Geophys. Res. Solid Earth 96 (B8), 13509–13528.
Natal'in, B.A., Sunal, G., Satir, M., Toraman, E., 2012. Tectonics of the Strandja Massif, NW Turkey: history of a long-lived arc at the northern margin of Paleo-Tethys. Turk. J. Earth Sci. 21, 755–798.
Negredo, A.M., Replumaz, A., Villaseñor, A., Guillot, S., 2007. Modeling the evolution of continental subduction processes in the Pamir–Hindu Kush region. Earth Planet. Sci. Lett. 259, 212–225.
Neill, I., Kerr, A.C., Hastie, A.R., Stanek, K.P., Millar, I.L., 2011. Origin of the Aves Ridge and Dutch-Venezuelan Antilles: interaction of the Cretaceous “Great Arc” and Caribbean-Colombian Oceanic Plateau? J. Geol. Soc. 168, 333–348.
Neill, I., Kerr, A.C., Hastie, A.R., Pindell, J.L., Millar, I.L., Atkinson, N., 2012. Age and petrogenesis of the Lower Cretaceous North Coast Schist of Tobago, a fragment of the Proto–Greater Antilles Inter-American Arc System. J. Geol. 120, 367–384.
Nerlich, R., Clark, S.R., Bunge, H.-P., 2013. The Scotia Sea gateway: no outlet for Pacific mantle. Tectonophysics 604, 41–50.
Niu, F., Wen, L., 2001. Strong seismic scatterers near the core-mantle boundary west of Mexico. Geophys. Res. Lett. 28, 3557–3560.
Nokleberg, W.J., Parfenov, L.M., Monger, J.W.H., Norton, I.O., Khanchuk, A., Stone, D.B., Scotese, C.R., Scholl, D.W., Fujita, K., 2000. Phanerozoic tectonic evolition of the circum-north Pacific. In: USGS Professioneal Paper. 1626. pp. 1–122.
Obayashi, M., Yoshimitsu, J., Fukao, Y., 2009. Tearing of stagnant slab. Science 324, 1173–1175.
Obayashi, M., Yoshimitsu, J., Nolet, G., Fukao, Y., Shiobara, H., Sugioka, H., Miyamachi, H., Gao, Y., 2013. Finite frequency whole mantle Pwave tomography: improvement of subducted slab images. Geophys. Res. Lett. 40, 5652–5657.
Obrebski, M., Allen, R.M., Xue, M., Hung, S.-H., 2010. Slab-plume interaction beneath the Pacific Northwest. Geophys. Res. Lett. 37. http://dx.doi.org/10.1029/2010GL043489.
Okay, A.I., Monié, P., 1997. Early Mesozoic subduction in the Eastern Mediterranean. Evidence from Triassic eclogite in northwest Turkey. Geology 25, 595–598.
Okay, A.I., Nikishin, A.M., 2015. Tectonic evolution of the southern margin of Laurasia in the Black Sea region. Int. Geol. Rev. 57, 1051–1076.
Okay, A.I., Monod, O., Monié, P., 2002. Triassic blueschists and eclogites from northwest Turkey: vestiges of the Paleo-Tethyan subduction. Lithos 64, 155–178.
Okay, A.I., Zattin, M., Cavazza, W., 2010. Apatite fission-track data for the Miocene Arabia-Eurasia collision. Geology 38, 35–38.
Okay, A.I., Noble, J., Tekin, U.K., 2011. Devonian radiolarian ribbon cherts from the Karakaya Complex, Northwest Turkey: implications for the Paleo-Tethyan evolution. C.R. Palevol 10, 1–10.
Pang, K.-N., Chung, S.-L., Zarrinkoub, M.H., Khatib, M.M., Mohammadi, S.S., Chiu, H.-Y., Chu, C.-H., Lee, H.-Y., Lo, C.-H., 2013. Eocene–Oligocene post-collisional magmatism in the Lut–Sistan region, eastern Iran: magma genesis and tectonic implications. Lithos 180–181, 234–251.
Pankhurst, R.J., Rapela, C.W., Fanning, C.M., Márquez, M., 2006. Gondwanide continental collision and the origin of Patagonia. Earth Sci. Rev. 76, 235–257.
Parfenov, L.M., Badarch, G.A., B., N., Khanchuk, A., Kuzmin, M.I., Nokleberg, W.J., Prokopiev, A.V., Ogasawara, M., Yan, H., 2009. Summary of Northeast Asia geodynamics and tectonics. In: Stephan Mueller Special Publication Series. 4. pp. 11–33.
Patzelt, A., Li, H., Wang, J., Appel, E., 1996. Palaeomagnetism of Cretaceous to Tertiary sediments from southern Tibet: evidence for the extent of the northern margin of India prior to the collision with Eurasia. Tectonophysics 259, 259–284.
Pavlis, G.L., Das, S., 2000. The Pamir-Hindu Kush seismic zone as a strain marker for flow in the upper mantle. Tectonics 19, 103–115.
Pegler, G., Das, S., 1998. An enhanced image of the Pamir-Hindu Kush seismic zone from relocated earthquake hypocentres. Geophys. J. Int. 134, 573–595.
Peltier, W.R., 1998. Postglacial variations in the level of the sea: implications for climate dynamics and solid-earth geophysics. Rev. Geophys. 36 (4), 603–689.
Peltier, W.R., Drummond, R., 2010. Deepest mantle viscosity: constraints from Earth rotation anomalies. Geophys. Res. Lett. 37 (12).
Pesicek, J.D., Thurber, C.H., Widiyantoro, S., Zhang, H., DeShon, H.R., Engdahl, E.R., 2010. Sharpening the tomographic image of the subducting slab below Sumatra, the Andaman Islands and Burma. Geophys. J. Int. 182, 433–453.
Pindell, J.L., Kennan, L., 2009. Tectonic evolution of the Gulf of Mexico, Caribbean and northern South America in the mantle reference frame: an update. Geol. Soc. Lond., Spec. Publ. 328, 1–55.
Pindell, J., Maresch, W.V., Martens, U., Stanek, K., 2012. The Greater Antillean Arc: Early Cretaceous origin and proposed relationship to Central American subduction mélanges: implications for models of Caribbean evolution. Int. Geol. Rev. 54, 131–143.
Piromallo, C., Morelli, A., 1997. Imaging the Mediterranean upper mantle by P-wave travel time tomography. Ann. Geofis. 40, 963–979.
Piromallo, C., Morelli, A., 2003. P wave tomography of the mantle under the Alpine-Mediterranean area. J. Geophys. Res. 108, 2065. http://dx.doi.org/10.1029/2002JB001757.
Platt, J.P., Allerton, S., Kirker, A., Mandeville, C., Mayfield, A., Platzman, E.S., Rimi, A., 2003. The ultimate arc: differential displacement, oroclinal bending, and vertical axis rotation in the External Betic-Rif arc. Tectonics 22, 1017 (doi:10.1029–2001TC001321).
Pownall, J.M., Hall, R., Armstrong, R.A., Forster, M.A., 2014. Earth's youngest known ultrahigh-temperature granulites discovered on Seram, eastern Indonesia. Geology 42, 279–282.
Pullen, A., Kapp, P., 2014. Mesozoic tectonic history and lithospheric structure of the Qiangtang terrane: insights from the Qiangtang metamorphic belt, central Tibet. In: Geological Society of America Special Papers. 507. pp. 71–87.
Puspito, N.T., Shimazaki, K., 1995. Mantle structure and seismotectonics of the Sunda and Banda arcs. Tectonophysics 251, 215–228.
Puspito, N.T., Yamanaka, Y., Miyatake, T., Shimazaki, K., Hirahara, K., 1993. Three-dimensional P-wave velocity structure beneath the Indonesian region. Tectonophysics 220, 175–192.
Qi, C., Zhao, D., Chen, Y., 2007. Search for deep slab segments under Alaska. Phys. Earth Planet. Inter. 165, 68–82.
Quarles van Ufford, A., Cloos, M., 2005. Cenozoic tectonics of New Guinea. AAPG Bull. 89, 119–140.
Ramos, A., 2008. Patagonia: A paleozoic continent a drift? J. S. Am. Earth Sci. 26, 235–251.
Rangin, C., Bijwaard, H., Pubellier, M., Spakman, W., 1999. Tomographic and geological constraints on subduction along the eastern Sundaland continental margin (South-East Asia). Bull. Soc. Geol. Fr. 170, 775–788.
Rawlinson, N., Spakman, W., 2016. On the use of sensitivity tests in seismic tomography. Geophys. J. Int. 205, 1221–1243. http://dx.doi.org/10.1093/gji/ggw084.
Reagan, M.K., McClelland, W.C., Girard, G., Goff, K.R., Peate, D.W., Ohara, Y., Stern, R.J., 2013. The geology of the southern Mariana fore-arc crust: implications for the scale of Eocene volcanism in the western Pacific. Earth Planet. Sci. Lett. 380, 41–51.
Ren, J., Tamaki, K., Li, S., Junxia, Z., 2002. Late Mesozoic and Cenozoic rifting and its dynamic setting in Eastern China and adjacent areas. Tectonophysics 344, 175–205.
Ren, Y., Strutzmann, E., van der Hilst, R.D., Besse, J., 2007. Understanding seismic heterogeneities in the lower mantle beneath the Americas from seismic tomography and plate tectonic history. J. Geophys. Res. 112, B01302 (doi: 10.1029–2005JB004154).
Ren, Y., Stuart, G.W., Houseman, G.A., Dando, B., Ionescu, C., Hegedus, E., Radovanovic, S., Shen, Y., Group, S.C.P.W, 2012. Upper mantle structures beneath the Carpathian–Pannonian region implications for the geodynamics of continental collision. Earth Planet. Sci. Lett. 349–350, 139–152.
Replumaz, A., Kárason, H., van der Hilst, R.D., Besse, J., Tapponnier, P., 2004. 4-D evolution of SE Asia's mantle from geological reconstructions and seismic tomography. Earth Planet. Sci. Lett. 221, 103–115.
Replumaz, A., Negredo, A.M., Guillot, S., Villasenor, A., 2010a. Multiple episodes of continental subduction during India/Asia convergence: insight from seismic tomography and tectonic reconstruction. Tectonophysics 483, 125–134.
Replumaz, A., Negredo, A.M., Guillot, S., van der Beek, P., Villaseñor, A., 2010b. Crustal mass budget and recycling during the India/Asia collision. Tectonophysics 492, 99–107.
Replumaz, A., Negredo, A.M., Villaseñor, A., Guillot, S., 2010c. Indian continental subduction and slab break-off during Tertiary collision. Terra Nova 22, 290–296.
Restrepo, J.J., Ordóñez-Carmona, O., Armstrong, R., Pimentel, M.M., 2011. Triassic metamorphism in the northern part of the TahamI Terrane of the central cordillera of Colombia. J. S. Am. Earth Sci. 32, 497–507.
Rezaei-Kahkhaei, M., Kananian, A., Esmaeily, D., Asiabanha, A., 2010. Geochemistry of the Zargoli granite: implications for development of the Sistan Suture Zone, south-eastern Iran. Island Arc 19, 259–276.
Ricard, Y., Richards, M., Lithgow-Bertelloni, C., Le Stunff, Y., 1993. A geodynamic model of mantle density heterogeneity. J. Geophys. Res. Solid Earth 98 (B12), 21895–21909.
Richards, M.A., Engebretson, D.C., 1992. Large-scale mantle convection and the history of subduction. Nature 355, 437–440. http://dx.doi.org/10.1038/355437a0.
Rioux, M., Hacker, B., Mattinson, J., Kelemen, P., Blusztajn, J., Gehrels, G., 2007. Magmatic development of an intra-oceanic arc: high-precision U-Pb zircon and whole-rock isotopic analyses from the accreted Talkeetna arc, south-central Alaska. Geol. Soc. Am. Bull. 119 (9–10), 1168–1184.
Ritsema, J., Deuss, A., van Heijst, H.J., Woodhouse, J.H., 2011. S40RTS: a degree-40 shear-velocity model for the mantle from new Rayleigh wave dispersion, teleseismic traveltime and normal-mode splitting function measurements. Geophys. J. Int. 184, 1223–1236.
Robertson, A.H.F., 2002. Overview of the genesis and emplacement of Mesozoic ophiolites in the Eastern Mediterranean Tethyan region. Lithos 65, 1–67.
Rogers, R.D., Kárason, H., van der Hilst, R.D., 2002. Epeirogenic uplift above a detached slab in northern Central America. Geology 30, 1031–1034.
Rosenbaum, G., Lister, G.S., 2004. Formation of arcuate orogenic belts in the western Mediterranean region. Geol. Soc. Am. Spec. Pap. 383, 41–56.
Rosenbaum, G., Avigad, D., Sánchez-Gómez, M., 2002a. Coaxial flattening at deep levels of orogenic belts: evidence from blueschists and eclogites on Syros and Sifnos (Cyclades, Greece). J. Struct. Geol. 24, 1451–1462.
Rosenbaum, G., Lister, G.S., Duboz, C., 2002b. Reconstruction of the tectonic evolution of the western Mediterranean since the Oligocene. J. Virtual Explor. 8, 107–130.
Rosenbaum, G., Gasparon, M., Lucente, F.P., Peccerillo, A., Miller, M.S., 2008. Kinematics of slab tear faults during subduction segmentation and implications for Italian magmatism. Tectonics 27, TC2008 (doi: 10.1029–2007TC002143).
Rost, S., Garnero, E.J., Williams, Q., 2008. Seismic array detection of subducted oceanic crust in the lower mantle. J. Geophys. Res. 113. http://dx.doi.org/10.1029/2007JB005263. (B06303–11).

Roth, J.B., Fouch, M.J., James, D.E., Carlson, R.W., 2008. Three-dimensional seismic velocity structure of the northwestern United States. Geophys. Res. Lett. 35. http://dx.doi.org/10.1029/2008GL034669. (L15304–6).
Rudolph, M.L., Lekić, V., Lithgow-Bertelloni, C., 2015. Viscosity jump in Earth's mid-mantle. Science 350 (6266), 1349–1352.
Ruiz-Martinez, V.C., Torsvik, T.H., van Hinsbergen, D.J.J., Gaina, C., 2012. Earth at 200 Ma: global palaeogeography refined from CAMP palaeomagnetic data. Earth Planet. Sci. Lett. 331–332, 67–79.
Sagong, H., Kwon, S.T., Ree, J.H., 2005. Mesozoic episodic magmatism in South Korea and its tectonic implication. Tectonics 24 (doi: 10.1029–2004TC001720, TC5002).
Sayıt, K., Göncüoglu, M.C., 2013. Geodynamic evolution of the Karakaya Mélange Complex, Turkey: a review of geological and petrological constraints. J. Geodyn. 65, 56–65.
Schaeffer, A.J., Lebedev, S., 1 July 2013. Global shear speed structure of the upper mantle and transition zone. Geophys. J. Int. 194 (1), 417–449. http://dx.doi.org/10.1093/gji/ggt095.
Schellart, W.P., Spakman, W., 2012. Mantle constraints on the plate tectonic evolution of the Tonga–Kermadec–Hikurangi subduction zone and the South Fiji Basin region. Aust. J. Earth Sci. 59, 933–952.
Schellart, W.P., Spakman, W., 2015. Australian plate motion and topography linked to fossil New Guinea slab below Lake Eyre. Earth Planet. Sci. Lett. 421, 107–116.
Schellart, W.P., Lister, G.S., Toy, V.G., 2006. A Late Cretaceous and Cenozoic reconstruction of the Southwest Pacific region: tectonics controlled by subduction and slab rollback processes. Earth Sci. Rev. 76, 191–233.
Schellart, W.P., Kennett, B.L.N., Spakman, W., Amaru, M.L., 2009. Plate Reconstructions and Tomography Reveal a Fossil Lower Mantle Slab Below the Tasman Sea. vol. 278. pp. 143–151.
Scherreiks, R., Meléndez, G., Boudagher-Fadel, M., Fermeli, G., Bosence, D., 2014. Stratigraphy and tectonics of a time-transgressive ophiolite obduction onto the eastern margin of the Pelagonian platform from Late Bathonian until Valanginian time, exemplified in northern Evvoia, Greece. Int. J. Earth Sci. 103, 2191–2216.
Schildgen, T.F., Cosentino, D., Caruso, A., Buchwaldt, R., Yıldırım, C., Bowring, S.A., Rojay, B., Echtler, H., Strecker, M.R., 2012. Surface expression of eastern Mediterranean slab dynamics: Neogene topographic and structural evolution of the southwest margin of the Central Anatolian Plateau, Turkey. Tectonics 31. http://dx.doi.org/10.1029/2011TC003021.
Schmandt, B., Humphreys, E., 2011. Seismically imaged relict slab from the 55 Ma Siletzia accretion to the northwest United States. Geology 39, 175–178.
Schmid, S.M., F genschuh, B., Kissling, E., Schuster, R., 2004. Tectonic map and overall architecture of the Alpine orogen. Eclogae Geol. Helv. 97, 93–117.
Schmid, S.M., Bernoulli, D., Fügenschuh, B., Maţenco, L., Schefer, S., Schuster, R., Tischler, M., Ustaszewski, K., 2008. The Alpine-Carpathian-Dinaridic orogenic system: correlation and evolution of tectonic units. Swiss J. Geosci. 101, 139–183.
Schneider, F.M., Yuan, X., Schurr, B., Mechie, J., Sippl, C., Haberland, C., Minaev, V., Oimahmadov, I., Gadoev, M., Radjabov, N., Abdybachaev, U., Orunbaev, S., Negmatullaev, S., 2013. Seismic imaging of subducting continental lower crust beneath the Pamir. Earth Planet. Sci. Lett. 375, 101–112.
Scholl, D.W., Vallier, T.L., Stevenson, A.J., 1989. In: Scholl, D.W., Grantz, A., Vedder, J.G. (Eds.), Geologic evolution and petroleum geology of the Aleutian Ridge, pp. 122–155 (Houston, Texas).
Schumacher, L., Thomas, C., 2016. Detecting lower-mantle slabs beneath Asia and the Aleutians. Geophys. J. Int. 205, 1512–1524.
Sdrolias, M., Müller, R.D., Gaina, C., 2004. Tectonic evolution of the southwest Pacific using constraints from backarc basins. Geol. Soc. Aust. Spec. Publ. 22, 343–359.
Searle, M.P., Cox, J.C., 2009. Tectonic setting, origin and obduction of the Oman Ophiolite. Geol. Soc. Am. Bull. 111, 104–122.
Searle, M.P., Corfield, R.I., Stephenson, B., McCarron, J., 1997. Structure of the north Indian continental margin in the Ladakh-Zanskar Himalayas: Implications for the timing of obduction of the Spontang ophiolite, India-Asia collision and deformation events in the Himalaya. Geol. Mag. 134, 297–316.
Sengör, A.M.C., Yilmaz, Y., 1981. Tethyan evolution of Turkey: a plate tectonic approach. Tectonophysics 75, 181–241.
Sengör, A.M.C., Özeren, S., Genç, T., Zor, E., 2003. East Anatolian high plateau as a mantle-supported, north-south shortened domal structure. Geophys. Res. Lett. 30, 8045 (doi: 10.1029–2003GL017858).
Seno, T., Maruyama, S., 1984. Paleogeographic reconstruction and origin of the Philippine Sea. Tectonophysics 102, 53–84.
Seton, M., Müller, R.D., Zahirovic, S., Gaina, C., Torsvik, T.H., Shephard, G., Talsma, A., Gurnis, M., Turner, M., Maus, S., Chandler, M., 2012. Global continental and ocean basin reconstructions since 200 Ma. Earth Sci. Rev. 113, 212–270.
Seton, M., Flament, N., Whittaker, J., Müller, R.D., Gurnis, M., Bower, D.J., 2015. Ridge subduction sparked reorganization of the Pacific plate-mantle system 60–50 million years ago. Geophys. Res. Lett. 42, 1732–1740.
Shahnas, M.H., Yuen, D.A., Pysklywec, R.N., 2017. Mid-mantle heterogeneities and iron spin transition in the lower mantle: implications for mid-mantle slab stagnation. Earth Planet. Sci. Lett. 458, 293–304.
Shapiro, M.N., Solov'ev, A.V., 2009. Formation of the Olyutorsky–Kamchatka foldbelt: a kinematic model. Russ. Geol. Geophys. 50, 668–681.
Shephard, G.E., Müller, R.D., Seton, M., 2013. The tectonic evolution of the Arctic since Pangea breakup: integrating constraints from surface geology and geophysics with mantle structure. Earth Sci. Rev. 124, 148–183.
Shephard, G.E., Flament, N., Williams, S., Seton, M., Gurnis, M., Müller, R.D., 2014. Circum-Arctic mantle structure and long-wavelength topography since the Jurassic. J. Geophys. Res. 119. http://dx.doi.org/10.1002/2014JB011078.
Shephard, G.E., Trønnes, R.G., Spakman, W., Panet, I., Gaina, C., 2016. Evidence for slab material under Greenland and links to Cretaceous High Arctic magmatism. Geophys. Res. Lett. 43, 3717–3726.
Shephard, G.E., Matthews, K.J., Hosseini, K., Domeier, M., 2017. On the consistency of seismically imaged lower mantle slabs. Sci. Rep. 7, 10976. http://dx.doi.org/10.1038/s41598-017-11039-w.
Sibuet, J.-C., Hsu, S.-K., 2004. How was Taiwan created? Tectonophysics 379, 159–181.
Sibuet, J.C., Srivastava, S.P., Spakman, W., 2004. Pyrenean orogeny and plate kinematics. J. Geophys. Res. 109 (doi: 10.1029–2003JB002514, B08104).
Sigloch, K., 2011. Mantle provinces under North America from multifrequency P wave tomography. Geochem. Geophys. Geosyst. 12 (doi:10.1029–2010GC003421, Q02W08).
Sigloch, K., Mihalynuk, M.G., 2013. Intra-oceanic subduction shaped the assembly of Cordilleran North America. Nature 496, 50–56.
Sigloch, K., McQuarrie, N., Nolet, G., 2008. Two-stage subduction history under North America inferred from multiple-frequency tomography. Nat. Geosci. 1, 458–462.
Simmons, N.A., Myers, S.C., Johannesson, G., Matzel, E., 2012. LLNL-G3Dv3: global P wave tomography model for improved regional and teleseismic travel time prediction. J. Geophys. Res. 117. http://dx.doi.org/10.1029/2012JB009525. (B10302).
Simmons, N.A., Myers, S.C., Johannesson, G., Matzel, E., Grand, S.P., 2015. Evidence for long-lived subduction of an ancient tectonic plate beneath the southern Indian Ocean. Geophys. Res. Lett. 42, 9270–9278. http://dx.doi.org/10.1002/2015GL066237.
Sippl, C., Schurr, B., Tympel, J., Angiboust, S., Mechie, J., Yuan, X., Schneider, F.M., Sobolev, S.V., Ratschbacher, L., Haberland, C., TIPAGE-Team, 2013. Deep burial of Asian continental crust beneath the Pamir imaged with local earthquake tomography. Earth Planet. Sci. Lett. 384, 165–177.
Skolbeltsyn, G., Mellors, R., Gok, R., Turkelli, N., 2014. Upper mantle S wave velocity structure of the East Anatolian-Caucasus Region. Tectonics 33, 207–221.
Sobel, E.R., Chen, J., Schoenbohm, L.M., Thiede, R., Stockli, D.F., Sudo, M., Strecker, M.R., 2013. Oceanic-style subduction controls late Cenozoic deformation of the Northern Pamir orogen. Earth Planet. Sci. Lett. 363, 204–218.
Sokolov, S.D., 1992. Accretionary Tectonics of the Koryak–Chukchi Segment of the Pacific Belt [in Russian]. Nauka, Moscow.
Sokolov, S.D., 2010. Tectonics of Northeast Asia: an overview. Geotectonics 44, 493–509.
Sokolov, S.D., Bondarenko, G.Y., Layer, W., Kravchenko-Berezhnoy, I.R., 2009. South Anyui suture: tectono-stratigraphy, deformations, and principal tectonic events. In: Stephan Mueller Special Publication Series. 4. pp. 201–221.
Šoštarić, S.B., Palinkaš, A.L., Neubauer, F., Cvetkovic, V., Bernroider, M., Genser, J., 2014. The origin and age of the metamorphic sole from the Rogozna Mts., Western Vardar Belt: new evidence for the one-ocean model for the Balkan ophiolites. Lithos 192–195, 39–55.
Spakman, W., 1986a. Subduction beneath Eurasia in connection with the Mesozoic Tethys. Geol. Mijnb. 65, 145–153.
Spakman, W., 1986b. In: Freeman, R., Mueller, S., Giese (Eds.), The upper mantle structure in the Central European-Mediterranean region, pp. 215–222 (Strassbourg).
Spakman, W., 1991. Delay-time tomography of the upper mantle below Europe, the Mediterranean, and Asia Minor. Geophys. J. Int. 107.2, 309–332.
Spakman, W., Hall, R., 2010. Surface deformation and slab–mantle interaction during Banda arc subduction rollback. Nat. Geosci. 3, 562–566.
Spakman, W., Nolet, G., 1988. Imaging algorithms, accuracy and resolution in delay time tomography. In: Mathematical Geophysics. Springer, Netherlands, pp. 155–187.
Spakman, W., Wortel, M.J.R., 2004. A tomographic view on western Mediterranean geodynamics. In: Cavazza, W., Roure, F., Spakman, W., Stampfli, G.M., Ziegler, P. (Eds.), The TRANSMED Atlas, The Mediterranean Region from Crust to Mantle, pp. 31–52.
Spakman, W., Wortel, M., Vlaar, N.J., 1988. The Hellenic subduction zone: a tomographic image and its geodynamic implications. Geophys. Res. Lett. 15, 60–63.
Spakman, W., Stein, S., van der Hilst, R.D., Wortel, M.J.R., 1989. Resolution experiments for NW Pacific subduction zone tomography. Geophys. Res. Lett. 16, 1097–1100.
Spakman, W., van der Lee, S., van der Hilst, R., 1993. Travel-time tomography of the European-Mediterranean mantle down to 1400 km. Phys. Earth Planet. Inter. 79, 3–74.
Stampfli, G.M., Borel, G.D., 2002. A plate tectonic model for the Paleozoic and Mesozoic constrained by dynamic plate boundaries and restored synthetic oceanic isochrons. Earth Planet. Sci. Lett. 196, 17–33.
Stampfli, G.M., Borel, G.D., 2004. The TRANSMED transects in space and time: constraints on the Paleotectonic evolution of the Mediterranean domain. In: The TRANSMED Atlas. The Mediterranean Region from Crust to Mantle. Springer Berlin Heidelberg, Berlin, Heidelberg, pp. 53–80.
Stanek, K.P., Maresch, W.V., Pindell, J.L., 2009. The geotectonic story of the northwestern branch of the Caribbean Arc: implications from structural and geochronological data of Cuba. In: Stanek, K.P., Maresch, W.V., Pindell, J. (Eds.), Geological Society, London, Special Publications 328. pp. 361–398.
Steinberger, B., Calderwood, A.R., 2006. Models of large-scale viscous flow in the Earth's mantle with constraints from mineral physics and surface observations. Geophys. J. Int. 167 (3), 1461–1481. http://dx.doi.org/10.1038/nature06824.
Steinberger, B., Torsvik, T.H., 2008. Absolute plate motions and true polar wander in the absence of hotspot tracks. Nature 452, 620–623.
Stern, R.J., Bloomer, S.H., 1992. Subduction zone infancy: examples from the Eocene Izu-Bonin-Mariana and Jurassic California arcs. Geol. Soc. Am. Bull. 104, 1621–1636.
Stern, R.J., Reagan, M., Ishizuka, O., Ohara, Y., Whattam, S.A., 2012. To understand subduction initiation, study forearc crust: to understand forearc crust, study ophiolites. Lithosphere 4, 469–483.
Stone, D.B., Layer, W., Raikevich, M.I., 2009. Age and paleomagnetism of the Okhotsk-Chukotka Volcanic Belt (OCVB) near Lake El'gygytgyn, Chukotka, Russia. In: Stephan Mueller Special Publication Series. 4. pp. 243–260.
Stoykov, S., Peytcheva, I., von Quadt, A., Moritz, R., Frank, M., Fontignie, D., 2004. Timing and magma evolution of the Chelopech volcanic complex (Bulgaria). Swiss

Bull. Mineral. Petrol. 84, 101–117.
Sugioka, H., Suetsugu, D., Obayashi, M., Fukao, Y., Gao, Y., 2010. Fast P- and S-wave velocities associated with the "cold" stagnant slab beneath the northern Philippine Sea. Phys. Earth Planet. Inter. 179, 1–6.
Suzuki, Y., Kawai, K., Geller, R.J., Borgeaud, A.F.E., Konishi, K., 2016. Waveform inversion for 3-D S-velocity structure of D″ beneath the Northern Pacific: possible evidence for a remnant slab and a passive plume. Earth Planets Space 68, 198. http://dx.doi.org/10.1186/s40623-016-0576-0.
Swarbrick, R.E., Naylor, M.A., 1980. The Kathikas melange, SW Cyprus: late Cretaceous submarine debris flows. Sedimentology 27, 63–78.
Taboada, A., Rivera, L.A., Fuenzalida, A., Cisternas, A., Philip, H., Bijwaard, H., Olaya, J., Rivera, C., 2000. Geodynamics of the northern Andes: subductions and intracontinental deformation (Colombia). Tectonics 19, 787–813.
Talavera-Mendoza, O., Ruiz, J., Gehrels, G.E., Valencia, A., Centeno-Garcia, E., 2007. Detrital zircon U/Pb geochronology of southern Guerrero and western Mixteca arc successions (southern Mexico): new insights for the tectonic evolution of southwestern North America during the late Mesozoic. Geol. Soc. Am. Bull. 119, 1052–1065.
Tankard, A., Welsink, H., Aukes, P., Newton, R., Stettler, E., 2009. Tectonic evolution of the Cape and Karoo basins of South Africa. Mar. Pet. Geol. 26, 1379–1412.
Tate, G.W., McQuarrie, N., van Hinsbergen, D.J.J., Bakker, R.R., Harris, R., Willett, S., Reiners, W., Fellin, M.G., Ganerød, M., Zachariasse, W.J., 2014. Resolving spatial heterogeneities in exhumation and surface uplift in Timor-Leste: constraints on deformation processes in young orogens. Tectonics 33, 1089–1112.
Tate, G.W., McQuarrie, N., van Hinsbergen, D.J., Bakker, R.R., Harris, R.A., Jiang, H., 2015. Australia going down under: quantifying continental subduction during arc-continent accretion in Timor-Leste. Geosphere 11, 1860–1883.
Tate, G.W., McQuarrie, N., Tiranda, H., van Hinsbergen, D.J.J., Harris, R., Zachariasse, W.J., Fellin, M.G., Reiners, W., Willett, S.D., 2017. First-order orogenic cylindricity amid locally high variability in uplift, exhumation and geometry: insights on orogenic controls from West Timor. Gondwana Res (under review).
Tekin, U.K., Göncüoğlu, M.C., 2007. Discovery of the oldest (Upper Ladinian to Middle Carnian) radiolarian assemblages from the Bornova Flysch zone in Western Turkey: implications for the evolution of the Neotethyan Izmir-Ankara ocean. Ofioliti 32, 131–150.
Tekin, U.K., Göncüoglu, M.C., Turhan, N., 2002. First evidence of Late Carnian radiolarians from the Izmir–Ankara suture complex, central Sakarya, Turkey: implications for the opening age of the Izmir–Ankara branch of Neo-Tethys. Geobios 35, 127–135.
Thomas, C., Garnero, E.J., Lay, T., 2004. High-resolution imaging of lowermost mantle structure under the Cocos plate. J. Geophys. Res. 109, B08307 (doi:10.1029–2004JB003013).
Tirrul, R., Bell, I.R., Griffis, R.J., Camp, E., 1983. The Sistan suture zone of eastern Iran. Geol. Soc. Am. Bull. 94, 134–150.
Tomurtogoo, O., Windley, B.F., Kröner, A., Badarch, G., Liu, D.Y., 2005. Zircon age and occurrence of the Adaatsag ophiolite and Muron shear zone, central Mongolia: constraints on the evolution of the Mongol-Okhotsk ocean, suture and orogen. J. Geol. Soc. 162, 125–134.
Torsvik, T.H., Müller, R.D., Van der Voo, R., Steinberger, B., Gaina, C., 2008a. Global plate motion frames: toward a unified model. Rev. Geophys. 46 (doi:10.1029–2007RG000227 RG3004).
Torsvik, T.H., Steinberger, B., Cocks, L.R.M., Burke, K., 2008b. Longitude: linking Earth's ancient surface to its deep interior. Earth Planet. Sci. Lett. 276, 273–282.
Torsvik, T.H., Burke, K., Steinberger, B., Webb, S.J., Ashwal, L.D., 2010. Diamonds sampled by plumes from the core–mantle boundary. Nature 466, 352–355.
Torsvik, T.H., Van der Voo, R., Preeden, U., MacNiocaill, C., Steinberger, B., Doubrovine, V., van Hinsbergen, D.J.J., Domeier, M., Gaina, C., Tohver, E., Meert, J.G., McCausland, J.A., Cocks, L.R.M., 2012. Phanerozoic polar wander, palaeogeography and dynamics. Earth Sci. Rev. 114, 325–368.
Torsvik, T.H., Van der Voo, R., Doubrovine, V., Burke, K., Steinberger, B., Ashwal, L.D., Tronnes, R.G., Webb, S.J., Bull, A.L., 2014. Deep mantle structure as a reference frame for movements in and on the Earth. Proc. Natl. Acad. Sci. U. S. A. 111, 8735–8740.
Torsvik, T.H., Doubrovine, P.V., Steinberger, B., Gaina, C., Spakman, W., Domeier, M., 2017. Pacific plate motion change caused the Hawaiian-Emperor Bend. Nat. Commun (in press).
Tremblay, A., Meshi, A., Deschamps, T., Goulet, F., Goulet, N., 2015. The Vardar Zone as a suture for the Mirdita ophiolites, Albania: constraints from the structural analysis of the Korabi-Pelagonia Zone. Tectonics 34. http://dx.doi.org/10.1002/2014TC003807.
Trop, J.M., Ridgway, K.D., 2007. Mesozoic and Cenozoic tectonic growth of southern Alaska: a sedimentary basin perspective. Geol. Soc. Am. Spec. Pap. 432, 55–94.
Trop, J.M., Szuch, S.A., Rioux, M., Blodgett, R.B., 2005. Sedimentology and provenance of the Upper Jurassic Naknek Formation, Talkeetna Mountains, Alaska; bearings on the accretionary tectonic history of the Wrangellia composite terrane. Geol. Soc. Am. Bull. 117, 570–588.
Ustaszewski, K., Schmid, S.M., Fügenschuh, B., Tischler, M., Kissling, E., Spakman, W., 2008. A map-view restoration of the Alpine-Carpathian-Dinaridic system for the Early Miocene. Swiss J. Geosci. 101, 273–294.
Ustaszewski, K., Wu, Y.-M., Suppe, J., Huang, H.-H., Chang, C.-H., Carena, S., 2012. Crust–mantle boundaries in the Taiwan–Luzon arc-continent collision system determined from local earthquake tomography and 1D models: implications for the mode of subduction polarity reversal. Tectonophysics 578, 31–49.
van Benthem, S., Govers, R., Spakman, W., Wortel, M.J.R., 2013. Tectonic Evolution and Mantle Structure of the Caribbean. 118. pp. 3019–3036.
van de Lagemaat, S.H.A., van Hinsbergen, D.J.J., Boschman, L.M., Kamp, J.J., 2017. Southwest Pacific absolute plate kinematic reconstruction reveals major mid – Late Cenozoic Tonga-Kermadec slab-dragging. Tectonics (submitted).
van der Hilst, R., Engdahl, R., Spakman, W., Nolet, G., 1991. Tomographic imaging of subducted lithosphere below northwest Pacific island arcs. Nature 353, 37–43.
van der Hilst, R.D., 1995. Complex morphology of subducted lithosphere in the mantle beneath the Tonga trench. Nature 374, 154–157.
van der Hilst, R.D., Mann, P., 1994. Tectonic implications of tomographic images of subducted lithosphere beneath northwestern South America. Geology 22, 451–454.
van der Hilst, R., Seno, T., 1993. Effects of relative plate motion on the deep structure and penetration depth of slabs below the Izu-Bonin and Mariana island arcs. Earth Planet. Sci. Lett. 120 (3–4), 395–407.
van der Hilst, R.D., Spakman, W., 1989. Importance of reference model in linearized tomography and images of subduction below the Caribbean plate. Geophys. Res. Lett. 16, 1093–1096.
Van der Hilst, R., Engdahl, R., Spakman, W., Nolet, G., 1991. Tomographic imaging of subducted lithosphere below northwest Pacific island arcs. Nature 353, 37–43.
van der Hilst, R.D., Widiyantoro, S., Engdahl, E.R., 1997. Evidence for deep mantle circulation from global tomography. Nature 386, 578–584. http://dx.doi.org/10.1038/386578a0.
van der Hilst, R.D., de Hoop, M.V., Wang, P., Shim, S.H., Ma, P., Tenorio, L., 2007. Seismostratigraphy and thermal structure of Earth's Core-Mantle Boundary Region. Science 315, 1813–1817.
van der Lee, S., Nolet, G., 1997. Seismic image of the subducted trailing fragments of the Farallon plate. Nature 386, 266–269.
van der Meer, D.G., Spakman, W., van Hinsbergen, D.J.J., Amaru, M.L., Torsvik, T.H., 2010. Towards absolute plate motions constrained by lower-mantle slab remnants. Nat. Geosci. 3, 36–40.
van der Meer, D.G., Torsvik, T.H., Spakman, W., van Hinsbergen, D.J.J., Amaru, M.L., 2012. Intra-Panthalassa Ocean subduction zones revealed by fossil arcs and mantle structure. Nat. Geosci. 5, 215–219.
van der Meer, D.G., Zeebe, R.E., van Hinsbergen, D.J.J., Sluijs, A., Spakman, W., Torsvik, T.H., 2014. Plate tectonic controls on atmospheric CO_2 levels since the Triassic. Proc. Natl. Acad. Sci. 111, 4380–4385.
van der Meer, D.G., van den Berg van Saparoea, A.P.H., van Hinsbergen, D.J.J., van de Weg, R.M.B., Goddéris, Y., Le Hir, G., Donnadieu, Y., 2017. Reconstructing first-order changes in sea level during the Phanerozoic and Neoproterozoic using strontium isotopes. Gondwana Res. 44, 22–34.
Van der Voo, R., Spakman, W., Bijwaard, H., 1999a. Mesozoic subducted slabs under Siberia. Nature 397, 246–249.
Van der Voo, R., Spakman, W., Bijwaard, H., 1999b. Tethyan subducted slabs under India. Earth Planet. Sci. Lett. 171, 7–20.
Van der Voo, R., van Hinsbergen, D.J.J., Domeier, M., Spakman, W., Torsvik, T.H., 2015. Latest Jurassic-earliest Cretaceous closure of the Mongol-Okhotsk Ocean: a paleomagnetic and seismological-tomographic analysis. Geol. Soc. Am. Spec. Pap. 513, 589–606.
van Hinsbergen, D.J.J., 2010. A key extensional metamorphic complex reviewed and restored: the Menderes Massif of western Turkey. Earth Sci. Rev. 102, 60–76.
van Hinsbergen, D.J.J., Hafkenscheid, E., Spakman, W., Meulenkamp, J.E., Wortel, M.J.R., 2005. Nappe stacking resulting from subduction of oceanic and continental lithosphere below Greece. Geology 33, 325–328.
van Hinsbergen, D.J.J., Kaymakci, N., Spakman, W., Torsvik, T.H., 2010. Reconciling the geological history of western Turkey with plate circuits and mantle tomography. Earth Planet. Sci. Lett. 297, 674–686.
van Hinsbergen, D.J.J., Kapp, P., Dupont-Nivet, G., Lippert, C., DeCelles, G., Torsvik, T.H., 2011a. Restoration of Cenozoic deformation in Asia, and the size of Greater India. Tectonics 30. http://dx.doi.org/10.1029/2011TC002908. (TC5003).
van Hinsbergen, D.J.J., Steinberger, B., Doubrovine, V., Gassmöller, R., 2011b. Acceleration and deceleration of India-Asia convergence since the Cretaceous: roles of mantle plumes and continental collision. J. Geophys. Res. 116. http://dx.doi.org/10.1029/2010JB008051. (B06101).
van Hinsbergen, D.J., Lippert, C., Dupont-Nivet, G., McQuarrie, N., Doubrovine, V., Spakman, W., Torsvik, T.H., 2012. Greater India Basin hypothesis and a two-stage Cenozoic collision between India and Asia. Proc. Natl. Acad. Sci. U. S. A. 109, 7659–7664.
van Hinsbergen, D.J.J., Vissers, R., Spakman, W., 2014. Origin and consequences of western Mediterranean subduction, rollback, and slab segmentation. Tectonics 33, 393–419.
van Hinsbergen, D.J.J., Peters, K., Maffione, M., Spakman, W., Guilmette, C., Thieulot, C., Plumper, O., Gürer, D., Brouwer, F.M., Aldanmaz, E., Kaymakci, N., 2015. Dynamics of intra-oceanic subduction initiation, part 2: supra-subduction zone ophiolite formation and metamorphic sole exhumation in context of absolute plate motions. Geochem. Geophys. Geosyst. 16, 1771–1785.
van Hinsbergen, D.J., Maffione, M., Plunder, A., Kaymakci, N., Ganerød, M., Hendriks, B.W.H., Corfu, F., Gürer, D., de Gelder, G.I.N.O., Peters, K., McPhee, J., Brouwer, F.M., Advokaat, E.L., Vissers, R.L.M., 2016. Tectonic evolution and paleogeography of the Kırşehir Block and the Central Anatolian Ophiolites, Turkey. Tectonics 35, 983–1014.
van Hinsbergen, D.J.J., Spakman, W., Vissers, R.L.M., van der Meer, D.G., 2017a. Comment on "Assessing discrepancies between previous plate kinematic models of Mesozoic Iberia and their constraints" by Barnett-Moore et al. Tectonics 36. http://dx.doi.org/10.1002/2016TC004418.
van Hinsbergen, D.J.J., Li, S., Lippert, P.C., Huang, W., Advokaat, E.L., Spakman, W., 2017b. Reconstructing the paleogeography and subduction geodynamics of Greater India: how to apply Ockham's Razor? Tectonophysics (under review).
Vaughan, A.P.M., Pankhurst, R.J., Fanning, C.M., 2002. A mid-Cretaceous age for the Palmer Land event, Antarctic Peninsula: implications for terrane accretion timing and

Gondwana palaeolatitudes. J. Geol. Soc. Lond. 159, 113–116.
Villagomez, D., Spikings, R., Magna, T., Kammer, A., Winkler, W., Beltrán, A., 2011. Geochronology, geochemistry and tectonic evolution of the Western and Central cordilleras of Colombia. Lithos 125, 875–896.
Vincent, S.J., Morton, A.C., Carter, A., Gibbs, S., Barabadze, T.G., 2007. Oligocene uplift of the Western Greater Caucasus: an effect of initial Arabia? Eurasia collision. Terra Nova 19, 160–166.
Vincent, S.J., Carter, A., Lavrishchev, A., Rice, S.P., Barabadze, T.G., Hovius, N., 2010. The exhumation of the western Greater Caucasus: a thermochronometric study. Geol. Mag. 148, 1–21.
Vincent, S.J., Braham, W., Lavrishchev, A., Maynard, J.R., Harland, M., 2017. The formation and inversion of the western Greater Caucasus Basin and the uplift of the western Greater Caucasus: implications for the wider Black Sea region. Tectonics 36. http://dx.doi.org/10.1002/2016TC004204.
Vishnevskaya, S., Filatova, N.I., 2012. Allochthonous Mesozoic marine sequences of northeastern Asia and western North America: correlation of stratigraphic and geodynamic depositional settings. Russ. J. Pac. Geol. 6, 189–208.
Vissers, R.L.M., Meijer, T., 2012a. Iberian plate kinematics and Alpine collision in the Pyrenees. Earth Sci. Rev. 114, 61–83.
Vissers, R.L.M., Meijer, T., 2012b. Mesozoic rotation of Iberia: subduction in the Pyrenees? Earth Sci. Rev. 110, 93–110.
Vissers, R., van Hinsbergen, D., Meijer, T., Piccardo, G.B., 2013. Kinematics of Jurassic ultra-slow spreading in the Piemonte Ligurian ocean. Earth Planet. Sci. Lett. 380, 138–150.
Vissers, R.L.M., van Hinsbergen, D.J.J., van der Meer, D.G., Spakman, W., 2016. Cretaceous slab break-off in the Pyrenees: Iberian plate-kinematics in paleomagnetic and mantle reference frames. Gondwana Res. 34, 49–59.
von Blanckenburg, F., Davies, J.H., 1995. Slab breakoff: a model for syncollisional magmatism and tectonics in the Alps. Tectonics 14, 120–131.
von Quadt, A., Moritz, R., Peytcheva, I., Heinrich, C.A., 2005. 3: Geochronology and geodynamics of Late Cretaceous magmatism and Cu–Au mineralization in the Panagyurishte region of the Apuseni–Banat–Timok–Srednogorie belt, Bulgaria. Ore Geol. Rev. 27, 95–126.
Wakabayashi, J., 2015. Anatomy of a subduction complex: architecture of the Franciscan Complex, California, at multiple length and time scales. Int. Geol. Rev. 57, 669–746.
Wakabayashi, J., Dilek, Y., 2000. Spatial and temporal relationships between ophiolites and their metamorphic soles: a test of models of forearc ophiolite genesis. Geol. Soc. Am. Spec. Pap. 349, 53–64.
Wakabayashi, J., Dumitru, T.A., 2007. $^{40}Ar/^{39}Ar$ ages from coherent, high-pressure metamorphic rocks of the Franciscan Complex, California: revisiting the timing of metamorphism of the world's type subduction. Int. Geol. Rev. 49, 1–36.
Wanke, M., Portnyagin, M., Hoernle, K., Werner, R., Hauff, F., van den Bogaard, P., Garbe-Schonberg, D., 2012. Bowers Ridge (Bering Sea): an Oligocene-Early Miocene island arc. Geology 40, 687–690.
Ward, L., 1995. Subduction cycles under western North America during the Mesozoic and Cenozoic eras. In: GSA Special Paper. 299. pp. 1–40.
Warren, C.J., Parrish, R.R., Searle, M.P., Waters, D.J., 2003. Dating the subduction of the Arabian continental margin beneath the Semail ophiolite, Oman. Geology 31, 889–892.
Wegner, W., Worner, G., Harmon, R.S., Jicha, B.R., 2011. Magmatic history and evolution of the Central American Land Bridge in Panama since Cretaceous times. Geol. Soc. Am. Bull. 123, 703–724.
Wei, W., Xu, J., Zhao, D., Shi, Y., 2012. J. Asian Earth Sci. 60, 88–103.
Wells, R.E., McCaffrey, R., 2013. Steady rotation of the Cascade arc. Geology 41, 1027–1030.
Wells, R., Bukry, D., Friedman, R., Pyle, D., Duncan, R., Haeussler, P., Wooden, J., 2014. Geologic history of Siletzia, a large igneous province in the Oregon and Washington Coast Range: correlation to the geomagnetic polarity time scale and implications for a long-lived Yellowstone hotspot. Geosphere 10 (4), 692–719.
West, J.D., Fouch, M.J., Roth, J.B., Elkins-Tanton, L.T., 2009. Vertical mantle flow associated with a lithospheric drip beneath the Great Basin. Nat. Geosci. 2, 439–444.
Widiyantoro, S., van der Hilst, R., 1996. Structure and evolution of lithospheric slab beneath the Sunda Arc, Indonesia. Science 271, 1566–1570.
Widiyantoro, S., van der Hilst, R.D., 1997. Mantle structure beneath Indonesia inferred from high-resolution tomographic imaging. Geophys. J. Int. 130, 167–182.
Widiyantoro, S., Kennett, B.L.N., van der Hilst, R.D., 1999. Seismic tomography with P and S data reveals lateral variations in the rigidity of deep slabs. Earth Planet. Sci. Lett. 173, 91–100.
Widiyantoro, S., Gorbatov, A., Kennett, B.L.N., Fukao, Y., 2000. Improving global shear wave traveltime tomography using three-dimensional ray tracing and iterative inversion. Geophys. J. Int. 141-3, 747–758. http://dx.doi.org/10.1046/j.1365-246x.2000.00112.x.
Widiyantoro, S., Pesicek, J.D., Thurber, C.H., 2011. Subducting slab structure below the eastern Sunda arc inferred from non-linear seismic tomographic imaging. Geol. Soc. Lond., Spec. Publ. 355, 139–155.
Wortel, M.J.R., Spakman, W., 1992. Structure and dynamics of subducted lithosphere in the Mediterranean region. In: Proceedings van de Koninklijke Nederlandse Academie van Wetenschappen. 95. pp. 325–347.
Wortel, M.J.R., Spakman, W., 2000. Subduction and slab detachment in the Mediterranean-Carpathian region. Science 290, 1910–1917.
Wu, H., Li, C., Hu, P., Li, X., 2014. Early Cretaceous (100–105 Ma) Adakitic magmatism in the Dachagou area, northern Lhasa terrane, Tibet: implications for the Bangong–Nujiang Ocean subduction and slab break-off. Int. Geol. Rev. 57, 1172–1188.
Wu, H., Li, C., Xu, M., Li, X., 2015. Early Cretaceous adakitic magmatism in the Dachagou area, northern Lhasa terrane, Tibet: implications for slab roll-back and subsequent slab break-off of the lithosphere of the Bangong-Nujiang Ocean. J. Asian Earth Sci. 97, 51–66.
Wu, J., Suppe, J., Lu, R., Kanda, R., 2016. Philippine Sea and East Asian plate tectonics since 52 Ma constrained by new subducted slab reconstruction methods. J. Geophys. Res. 121, 4670–4741.
Xiao, W.J., Huang, B., Han, C., Sun, S., Li, J., 2010. A review of the western part of the Altaids: a key to understanding the architecture of accretionary orogens. Gondwana Res. 18, 253–273.
Xu, M., LI, C., Zhang, X., Wu, Y., 2014. Nature and evolution of the Neo-Tethys in central Tibet: synthesis of ophiolitic petrology, geochemistry, geochronology. Int. Geol. Rev. 56, 1072–1096.
Yin, A., Harrison, T.M., 2000. Geologic evolution of the Himalayan-Tibetan orogen. Annu. Rev. Earth Planet. Sci. 28, 211–280.
Zahirovic, S., Müller, R.D., Seton, M., Flament, N., Gurnis, M., Whittaker, J., 2012. Insights on the kinematics of the India-Eurasia collision from global geodynamic models. Geochem. Geophys. Geosyst. 13. http://dx.doi.org/10.1029/2011GC003883.
Zahirovic, S., Seton, M., Müller, R.D., 2014. The Cretaceous and Cenozoic tectonic evolution of Southeast Asia. Solid Earth 5, 227–273.
Zahirovic, S., Matthews, K.J., Flament, N., Müller, R.D., Hill, K.C., Seton, M., Gurnis, M., 2016. Tectonic evolution and deep mantle structure of the eastern Tethys since the latest Jurassic. Earth Sci. Rev. 162, 293–337.
Zeng, M., Zhang, X., Cao, H., Ettensohn, F.R., Cheng, W., Lang, X., 2015. Late Triassic initial subduction of the Bangong-Nujiang Ocean beneath Qiangtang revealed: stratigraphic and geochronological evidence from Gaize, Tibet. Basin Res. 28, 147–157.
Zhang, J., Shan, X., Huang, X., 2011. Seismotectonics in the Pamir: an oblique transpressional shear and south-directed deep-subduction model. Geosci. Front. 2, 1–15.
Zhao, D., Lei, J., 2004. Seismic ray path variations in a 3D global velocity model. Phys. Earth Planet. Inter. 141 (3), 153–166.
Zhao, D., Ohtani, E., 2009. Deep slab subduction and dehydration and their geodynamic consequences: evidence from seismology and mineral physics. Gondwana Res. 16, 401–413.
Zhao, D., Hasegawa, A., Horiuchi, S., 1992. Tomographic imaging of P and S wave velocity structure beneath northeastern Japan. J. Geophys. Res. Solid Earth 97 (B13), 19909–19928.
Zhao, D., Pirajno, F., Dobretsov, N.L., Liu, L., 2010. Mantle structure and dynamics under East Russia and adjacent regions. RGG 51, 925–938.
Zheng, H.-W., Gao, R., Li, T.-D., Li, Q.-S., He, R.-Z., 2013. Collisional Tectonics Between the Eurasian and Philippine Sea Plates From Tomography Evidences in Southeast China. vol. 606. pp. 14–23.
Zhu, D.-C., Zhao, Z.-D., Niu, Y., Mo, X.-X., Chung, S.-L., Hou, Z.-Q., Wang, L.-Q., Wu, F.-Y., 2011. The Lhasa Terrane: record of a microcontinent and its histories of drift and growth. Earth Planet. Sci. Lett. 301, 241–255.
Zhu, H., Bozdağ, E., Peter, D., Tromp, J., 2012. Structure of the European Upper Mantle Revealed by Adjoint Tomography. vol. 5. pp. 493–498.
Zhu, D.-C., Zhao, Z.-D., Niu, Y., Dilek, Y., Hou, Z.-Q., Mo, X.-X., 2013. The origin and pre-Cenozoic evolution of the Tibetan Plateau. Gondwana Res. 23, 1429–1454.
Ziegler, A., 1989. Evolution of Laurussia. Kluwer Academic Publications, Dordrecht (102p).
Zimmerman, A., Stein, H.J., Hannah, J.L., Kozelj, D., Bogdanov, K., Berza, T., 2007. Tectonic configuration of the Apuseni–Banat—Timok–Srednogorie belt, Balkans-South Carpathians, constrained by high precision Re–Os molybdenite ages. Mineral. Deposita 43, 1–21.
Zor, E., 2008. Tomographic evidence of slab detachment beneath eastern Turkey and the Caucasus. Geophys. J. Int. 175, 1273–1282.